Understanding the Loss of Tropospheric Chlorine Atoms

Jordan Stewart

Doctor of Philosophy

University of York
Chemistry

August 2023

Abstract

In the pursuit of improved understanding surrounding tropospheric chemistry, and thus the ability to introduce timely and effective air quality policies, the role of atomic chlorine remains a poorly defined area. Research has indicated that chlorine could have significant roles in the control of the budgets of ozone (O_3) and nitrogen oxides (NO_x), and the determination of the lifetime of greenhouse gases such as methane (CH_4). Its overall significance in these processes, however, remains poorly understood owing to large uncertainties in global concentrations. Understanding the sources and sinks of Cl-atoms is therefore vital if we are to accurately evaluate its importance as a tropospheric oxidant.

This thesis details the development of a Chlorine Comparative Reactivity Method (Cl-CRM) instrument to directly measure the total Cl loss rate. The system was tested and calibrated using several single and mixed hydrocarbon standards, with a working range of 12 – 400 s^{-1} and an uncertainty of 30% identified. Nitrogen oxide (NO) is identified as a significant source of interference in the setup which currently prevents the field deployment of the instrument. Methods to minimise this interference are explored, and potential reactor re-designs proposed to minimise photolytic losses within the system.

Seasonal thermodynamic partitioning of chloride between the gas and particulate phase at an urban background site in the UK was also investigated. The thermodynamic model ISORROPIA II is found to underestimate particulate chloride by a factor of 2 in the summer, however this discrepancy was attributed to charge imbalance owing to a lack of concurrent metal ion measurements. Larger discrepancies were observed in the winter dataset for which the source is unknown. In contrast to previous studies, we did not find any evidence that the temperature dependence of the HCl effective equilibrium constant function used in the model is too large.

Table of Contents

List of Figures

List of Tables

Acknowledgements

I would first like to thank my supervisors Pete Edwards and Terry Dillon, not only for the opportunity to pursue this PhD, but for their constant support and guidance over the past four years. You have both always been able to find time to answer my questions, no matter how trivial, and I could not have asked for better supervision.

Next, I'd like to thank Stephen Andrews, Stuart Young, Killian Murphy, Marvin Shaw, Jim Hopkins and Martyn Ward for their technical support and advice throughout this project. In particular, I'd like to thank Stephen and Stuart for their patience towards me and my far too frequent need for Swagelok. I'd also like to thank Abigail Mortimer, Mark Roper and Stuart Murray of the Chemistry Workshop without whom the glassware and reactors used in this work would not have been possible. John 'Wes' Halfacre is someone who I would like to give a special mention to. Not only were you a great source of help throughout my PhD but your sense of humour made the lab an enjoyable place to be.

My experiences during my PhD would not have been the same without the friends I've made along the way, whether that be in WACL or through handball. A special mention must go to Luke, Dan, Ryan, David, Lucy and Jack who provided many welcome escapes from work and encouragement throughout this process. Apologies for never going climbing with you all though…

Finally, I would like to thank my mum, dad and brother who have been a constant source of support and encouragement throughout my studies. Whether it be proof reading chapters of this thesis (despite having no background in chemistry), or simply being available to chat over the phone about how things are going, you've always been there for me and I cannot thank you enough.

Author's Declaration

I declare that this thesis is a presentation of original work and I am the sole author. This work has not previously been presented for a degree or other qualification at this University or elsewhere. All sources are acknowledged as references. The HCl measurements reported in chapter 5 were conducted by Dr John Halfacre. Sources of the supporting gas and particulate phase measurements are provided in the chapter.

Chapter 1

Introduction

1.1 Motivation and History of Atmospheric Chlorine Chemistry

It is well established that climate change and air pollution are two of the greatest challenges we face in the 21st century. As reported in The Sixth Assessment Report of the Intergovernmental Panel on Climate Change, published in 2022, up to 3.6 billion people are estimated to be highly vulnerable to the impacts of climate change.[1] Accurately assessing the implications of current and future emissions is therefore vital if we are to introduce timely and effective air quality policies that will enable the extent and effects of these challenges to be minimised. To achieve this, an understanding of the chemical and physical processes by which trace gas species are removed from the atmosphere is required. It is well established that the majority of such species are removed through a series of oxidizing chemical reactions within the troposphere, with the rate at which this "self-cleansing" process occurs typically referred to as the oxidative capacity of the atmosphere. Such self-cleaning capabilities govern a number of fundamental processes that have significant impacts on the aforementioned challenges, including controlling the lifetime of greenhouse gases such as CH_4, the formation of secondary pollutants such as O_3 and secondary organic aerosols (SOA), and the deposition of chemicals into ecosystems. It is therefore clear that if we are to accurately assess the impact of trace gas emissions, we need to understand the sources and sinks of species responsible for their removal – tropospheric oxidants.

Chlorine atoms are known to be powerful oxidants of both organic and inorganic species. The importance of Cl chemistry within atmospheric oxidation chemistry was first suggested in 1974 by Stolarski and Cicerone who hypothesised that, should sources of atomic Cl exist within the stratosphere, catalytic destruction of O_3 could proceed via the formation of oxides of chlorine (ClO_x):[2]

$$Cl + O_3 \rightarrow ClO + O_2 \qquad \text{(Reaction 1.1)}$$

$$ClO + O \rightarrow Cl + O_2 \qquad \text{(Reaction 1.2)}$$

$$\text{Net:} \quad O_3 + O \rightarrow 2\,O_2$$

A prominent source of these Cl atoms was later identified by Molina and Rowland who showed that as chlorofluorocarbons (CFCs) are inert to removal mechanisms within the troposphere, they are able diffuse from the ground level into the stratosphere whereupon they are exposed to UV radiation of sufficient energy to cleave the C-Cl bond and release Cl.[3] The breakdown of CFCs was therefore expected to occur within the upper stratosphere as opposed to the lower stratosphere in which the bulk of stratospheric O_3 exists. Consequently, it was estimated that CFCs would account for 5-10% of O_3 depletion.[4] It was not until 1985, however, that the true extent of CFC involvement in O_3 destruction was fully rationalised. Based at Halley Bay, Farman *et al*. reported significant depletions in the thickness of the springtime O_3 layer above Antarctica when compared to measurements

recorded in the 1950s, a phenomenon later referred to as the "O_3 hole".[5] To explain this enhanced O_3 loss, Solomon *et al*. proposed that HCl and chlorine nitrate ($ClONO_2$), products of the reaction of ClO and Cl in the lower troposphere, could react to generate Cl_2 as outlined in reaction 1.3:

$$HCl + ClONO_2 \rightarrow HNO_3 + Cl_2 \qquad \text{(Reaction 1.3)}$$

Whilst reaction between the two species is slow in the gas phase, reactions on particle surfaces proceed at a much greater rate. It was therefore suggested that the reaction proceeded via a heterogenous mechanism on top of the surfaces of polar stratospheric clouds (PSCs), from which Cl-atoms would be generated following the photolysis of Cl_2. PSCs also provided a surface upon which reactive nitrogen could be converted into the less reactive HNO_3 following the reaction of dinitrogen pentoxide (N_2O_5) with water:[6]

$$N_2O_5 + H_2O_{(aq)} \rightarrow 2\ HNO_3 \qquad \text{(Reaction 1.4)}$$

To account for these new finding, a new mechanism for the catalytic destruction of O_3 involving the formation of a ClO-dimer was proposed by Molina and Molina:[7]

$$2\ Cl + 2\ O_3 \rightarrow 2\ ClO + 2\ O_2 \qquad \text{(Reaction 1.5)}$$

$$ClO + ClO + M \rightarrow Cl_2O_2 + M \qquad \text{(Reaction 1.6)}$$

$$Cl_2O_2 + h\nu \rightarrow Cl + ClO_2 \qquad \text{(Reaction 1.7)}$$

$$ClO_2 + h\nu \rightarrow Cl + O_2 \qquad \text{(Reaction 1.8)}$$

$$\text{Net:}\quad 2\ O_3 \rightarrow 3\ O_2$$

The growing evidence of CFC involvement in stratospheric O_3 depletion led to the signing of the Montreal Protocol in September 1987, which mandated the gradual phase-out of the production of the compounds along with several other chlorine and bromine containing O_3 depleting substances. To date, the treaty is widely considered to be one of the most successful international environmental policies to have ever been introduced.

By contrast, an understanding of the impacts of Cl atoms within the troposphere has yet to be fully established, with current estimations of its importance ranging from highly important to negligible.[8, 9] This uncertainty predominantly arises due to a lack of observational constraints that would enable the Cl chemistry to be accurately represented within simulations. It is therefore clear that this an area which requires further research and will be the focus of this work.

1.2 The Role of Chlorine in the Troposphere

1.2.1 Fundamentals of Oxidative Chemistry

Under most atmospheric conditions, the hydroxyl radical (OH) is the dominant daytime oxidant within the troposphere, with its formation predominantly driven by the photolysis of O_3:

$$O_3 + h\nu\ (\lambda < 375\ nm) \rightarrow O(^1D) + O_2 \qquad \text{(Reaction 1.9)}$$

$$O(^1D) + H_2O \rightarrow 2\ OH \qquad \text{(Reaction 1.10)}$$

Upon its formation, OH can go on to react with CO to form the hydroperoxyl radical (HO_2). This in turn can react with O_3 to reform OH in a process collectively referred to as the HO_x cycle:

$$OH + CO \rightarrow H + CO_2 \qquad \text{(Reaction 1.11)}$$

$$H + O_2 + M \rightarrow HO_2 + M \qquad \text{(Reaction 1.12)}$$

$$HO_2 + O_3 \rightarrow OH + 2\ O_2 \qquad \text{(Reaction 1.13)}$$

Another loss mechanism of OH is through reaction with volatile organic compounds (VOCs), resulting in the formation of peroxy radicals (RO_2). For example, in the case of CH_4:

$$OH + CH_4 \rightarrow CH_3 + H_2O \qquad \text{(Reaction 1.14)}$$

$$CH_3 + O_2 + M \rightarrow CH_3O_2 + M \qquad \text{(Reaction 1.15)}$$

The subsequent fate of these peroxy radicals is dependent upon the concentration of NO within the environment of interest. In instances in which the concentration of NO is very low, RO_2 can either react in a self-reaction ($RO_2 + RO_2$) or through a cross-reaction with another RO_2 radical ($RO_2 + R'O_2$). Both pathways ultimately result in the formation of HO_2, as represented by the self-reaction pathway of the methylperoxy radical formed in reaction 1.15:

$$CH_3O_2 + CH_3O_2 \rightarrow 2\ CH_3O + \text{other products} \qquad \text{(Reaction 1.16)}$$

$$CH_3O + O_2 \rightarrow HO_2 + HCHO \qquad \text{(Reaction 1.17)}$$

In the presence of NO however, reaction 1.16 in the above mechanism can be replaced with the following:

$$CH_3O_2 + NO \rightarrow CH_3O + NO_2 \qquad \text{(Reaction 1.18)}$$

HO_2 formed during the oxidation process can also react with NO to re-form OH and a molecule of NO_2, ultimately resulting in the formation of O_3 following the photolysis of the latter species:

$$NO_2 + h\nu\ (\lambda < 420\ nm) \rightarrow O(^3P) + NO \qquad \text{(Reaction 1.19)}$$

$$O(^3P) + O_2 + M \rightarrow O_3 + M \qquad \text{(Reaction 1.20)}$$

Like OH, Cl is known to react with hydrocarbons, typically via a hydrogen abstraction mechanism as outlined in reaction 1.21:

$$Cl + RH \rightarrow HCl + R \qquad \text{(Reaction 1.21)}$$

It is widely reported that Cl atoms are therefore involved in CH_4, dimethylsulfide and non-methane hydrocarbon (NMHC) oxidation.[10-14] Despite their lower abundance than OH, global model simulations conducted by Wang *et al*. and Sherwen *et al*. attribute Cl atoms to be responsible for 1 and 2% of the global oxidation of CH_4 respectively.[12, 13] For ethane, this contribution increases to 20 and 27%. These substantial contributions can be attributed to the rate coefficients for the reaction of Cl with VOCs typically being a factor of >10 greater than comparative reactions with OH.[15] Research has also provided evidence of Cl atom involvement in regional O_3 production,[16, 17] oxidation and deposition of gaseous mercury,[18, 19] and processing of reactive nitrogen species such as N_2O_5.[20, 21] The impact of these processes however, and thus the importance of Cl as an oxidant, are difficult to quantify owing to large uncertainties in global and local Cl atom concentrations. In comparison to OH for example, of which global mean concentrations are estimated to be $0.7 – 1.5 \times 10^6$ molecule cm^{-3},[22] estimations of Cl atom levels span over two orders of magnitude ($10^2 – 10^4$ atoms cm^{-3}), with the simulated global distribution depicted in Figure 1.1.[23-27] Such a large uncertainty arises from there being no observational technique currently developed that would enable direct measurements of species at the concentrations at which Cl atoms are present within the troposphere. As such, indirect methods must be employed in order to estimate their concentration although these are not without their issues. A summary of the methods currently reported in the literature is given below.

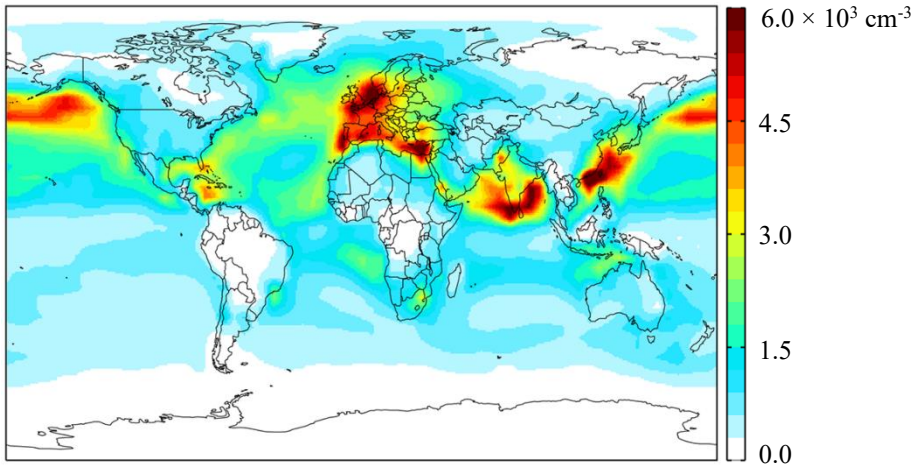

Figure 1.1. Global distribution of the annual Cl-atom concentrations simulated by the Geos-Chem global transport model. Taken from Wang et al. [13]

1.2.2 Existing Methods of Estimating Chlorine Atom Concentrations

On a global scale, average concentrations of Cl atoms have previously been inferred using isotope ratios of CH_4.[24-27] The underlying principle of this approach to estimating Cl atom concentrations is the kinetic isotope effect. Considering first the oxidation of CH_4 by OH, reaction with the more stable and prominent (99%) $^{12}CH_4$ isomer will proceed at a slightly faster rate than that with the heavier $^{13}CH_4$ isomer owing to the C-H bond in the latter being stronger.[25] Consequently, as more CH_4 is removed from the troposphere through reaction with OH, the ^{13}C / ^{12}C ratio increases. Due to the rate coefficient for the reaction between CH_4 and Cl atoms being approximately a factor of 15 greater than the analogous reaction with OH (k_{Cl} = 1.0 × 10^{-13}, k_{OH} = 6.4 × 10^{-15} at 298 K),[15] and Cl also reacting faster with the ^{12}C isomer due to this kinetic isotope effect, the observed isotope ratios would be greater in environments in which Cl atoms are present than would be predicted on the basis of simple removal of CH_4 through reaction with OH. As such, comparison of the predicted and observed isotope ratios enables the concentration of Cl atoms to be obtained. From such studies, spatially and temporally averaged concentrations within the marine boundary layer (MBL) have been reported, and are estimated to be within the range of 0.3 - 1.8 × 10^4 atoms cm^{-3}. Such concentrations are in reasonable agreement with those obtained by Singh *et al*. who used the removal rate of tetrachloroethylene (chosen due it's the large k_{Cl} / k_{OH} ratio of 365 at 275 K) to approximate the Cl atom concentration to be within the range of 0.5 – 1.5 × 10^4 atoms cm^{-3} in the MBL.[23] A key disadvantage of both of these techniques however is that they do not provide any insight into the controlling mechanisms for the formation of Cl.

A more readily used technique which enables Cl chemistry to be assessed on a regional and local scale is the examination of VOC tracer ratios. Such an approach requires the concentration of three different VOCs of similar sources to be monitored, with the species chosen such that two have comparable reaction rate coefficients for reaction with Cl and two have comparable rate coefficients for reaction with OH as depicted in Figure 1.2. The relative contribution of OH and Cl to the oxidation of the three VOCs, and thus an estimation of the Cl atom concentration, can be obtained by monitoring the ratio of the three compounds in air masses of different ages. In general, ratios of more reactive VOCs (such as the tracer ratio species given in red in Figure 1.2) are typically utilised for monitoring transportation and photochemical processes which occur on shorter timescales of hours and days, as opposed to tens of days.[28] Average concentrations obtained using this approach have ranged from 7.2 × 10^2 – 10^5 atoms cm^{-3}.[29-35] Mixing of air parcels of different photochemical ages and emission histories is a clear source of uncertainty in the factors influencing changes in the tracer VOC ratios however, provided that the difference in rate coefficients between the two VOCs comprising each ratio are significantly large, the method is still reported to yield a reasonable assessment of the degree of photochemical processing of the most reactive monitored species.[28] As reported by Young *et al*. however,[36] high sensitivity to the formation of secondary OH radicals

following the initial oxidation of VOCs by Cl is the key issue with this method. The formation of OH is driven by the reaction between HO_2 and NO as outlined in reaction 1.22:

$$HO_2 + NO \rightarrow OH + NO_2 \qquad \text{(Reaction 1.22)}$$

Consequently, the technique is only suitable for application in remote environments in which the concentration of nitrogen oxides (NO_x) is low.

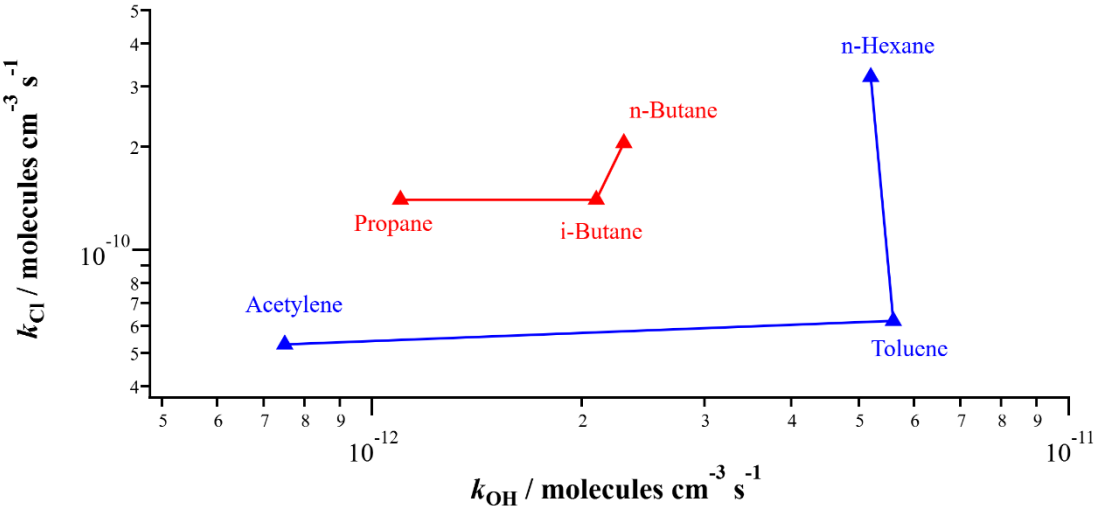

Figure 1.2. Rate constants for the reaction of Cl and OH with VOCs typically used to determine the Cl atom concentration via the tracer ratio method. Reproduction from Young et al. [36]

Mist chamber experiments have also been used for the measurement of inorganic Cl gases.[37-40] In such an approach, water-soluble species are concentrated through turbulent mixing of ambient air and an aqueous solution dispersed as a mist within a chamber. The resulting aqueous matrix is then typically analysed through ion chromatography (IC). For the measurement of Cl gases, two mist chambers are typically operated in tandem, one containing an acidic solution to sample HCl* (HCl + $ClNO_2$ + $ClNO_3$ + ClNO) and another containing a basic solution to sample Cl* (Cl + ClO + Cl_2 + HOCl). Whilst such an approach would enable the total Cl atom concentration to be determined, like the isotope ratio method, identification of the contributing species is not possible. Furthermore, the technique suffers from poor time resolution as samples are typically collected over a period greater than 2 hours.[39] It is therefore clear that new observational techniques are required if we are to reduce the uncertainty in the Cl atom concentration, and thus elucidate the importance of Cl chemistry within the troposphere. Since the atmospheric lifetime of Cl atoms is relatively short, they can be considered to be in steady state:

$$\frac{d[Cl]}{dt} = \Sigma P_{Cl} - k'_{Cl}[Cl] = 0 \qquad \text{(Equation 1.1)}$$

where:

- ΣP_{Cl} is the total rate of Cl atom production
- k'_{Cl} is the total loss rate of Cl atoms
- [Cl] is the steady state concentration of Cl

It therefore follows that if the sources and sinks of Cl atoms are simultaneously measured, the concentration of Cl atoms can be determined. Consequently, any new observational techniques developed should focus on the measurement of the sources of Cl atoms and their total loss rate.

1.3 Sources of Chlorine Reservoir Species

In order for a chlorinated compound to contribute to the oxidation processes discussed in section 1.2 they need to be able to release a Cl atom under tropospheric conditions, either through photolysis or following reaction with OH. For the vast majority of chlorinated organic compounds such as CFCs, whilst they are important sources of Cl atoms within the stratosphere as discussed in section 1.1, their contribution to tropospheric Cl atom production is negligible due to their stability with respect to tropospheric degradation processes.[41] In contrast however, inorganic gases such as HCl, nitryl chloride ($ClNO_2$), Cl_2 and hypochlorous acid (HOCl) are susceptible to degradation under such conditions and can therefore be considered as chlorine reservoir species.[42] A breakdown of the sources of these species, and their relative importance to the formation of Cl atoms, is given below.

1.3.1 Chemical Sources

The dominant global source of inorganic chlorine gases stems from the mobilisation of particulate chloride (pCl^-) present within sea spray aerosols (SSA). The formation of these SSAs occurs via a mechanical process in which wind-induced turbulence results in the formation of breaking waves at the ocean surface.[43] When such actions occur, air is entrained into the water where upon it is dispersed into bubbles that rise to the surface and burst. This bursting action results in the formation of hundreds of film drops that consist of sea salt and hydrophobic organics that are present within the sea surface microlayer (SML), with sizes ranging from the nanometre to micrometre scale.[44, 45] The transportation of the resulting SSA is determined by particle size, with the inland transport of the super-micron (diameter > 1μm) fraction negligible due to its short lifetime against deposition (~1.5 days).[46] The submicron fraction however, due to its lighter weight, has a longer lifetime of 1-2 weeks and can therefore be carried further inland beyond the immediate coastal regions.[47] Additional inland sources of pCl^- include road salt application and the combustion of biomass and biofuels.[48, 49]

A key route by which pCl^- is mobilised into the gas phase in the form of HCl is through acid displacement.[42] Whilst organic acids have been shown to play a role in this process,[50] the two most common strong acids through which this is achieved are HNO_3 and H_2SO_4 as described by reactions 1.23 and 1.24 respectively:[51, 52]

$$HNO_3 + Cl^- \rightleftharpoons NO_3^- + HCl \quad \text{(Reaction 1.23)}$$

$$H_2SO_4 + 2\,Cl^- \rightleftharpoons SO_4^{2-} + 2\,HCl \quad \text{(Reaction 1.24)}$$

HCl is the most abundant form of inorganic chlorine within the troposphere, with mixing ratios ranging from 10^1 – 10^3 parts per trillion volume (pptv) reported.[53-56] Higher concentrations of the reservoir species are typically observed in polluted coastal environments, likely owing to the enhanced anthropogenic emissions of acid gas precursors such as NO_x and SO_2. Using global 3-D modelling, the formation of HCl through acid displacement of SSA was attributed to 70% of the total reactive chlorine budget (Cl_y) by Wang *et al*.[13] Upon its formation, HCl can react with OH to liberate a Cl atom as described by reaction 1.25:

$$HCl + OH \rightarrow Cl + H_2O \quad \text{(Reaction 1.25)}$$

As the reaction is relatively slow ($k = 7.8 \times 10^{-13}$ cm^3 molecule^{-1} s^{-1} at 298 K),[57] this pathway represents a minor loss mechanism of HCl, as reflected in the aforementioned study by Wang *et al*. in which only 19% of the total HCl loss was attributed to the process.[13] Instead, the lifetime of HCl is predominantly controlled by wet and dry deposition processes.[56] It is important to note, however, that the reaction between Cl atoms and hydrocarbons re-generates HCl as discussed in section 1.2.1. As such, Cl can cycle between the two forms so long as there is sufficient concentrations of OH available for reaction. HCl can also exist in equilibrium with its hydrated form in the particle phase under typical atmospheric conditions, as described by reaction 1.26. Thermodynamic partitioning between the two states is dependent upon a number of factors including relative humidity (RH), liquid water content, particle pH and solute activity - parameters which are in turn influenced by meteorological conditions such as ambient pressure and temperature as well as the atmospheric composition.[53]

$$HCl \rightleftharpoons H^+_{(aq)} + Cl^-_{(aq)} \quad \text{(Reaction 1.26)}$$

Heterogeneous reactions on the surface of chloride containing aerosols offer an alternative route by which the relatively unreactive pCl$^-$ can be converted into a more active form. N_2O_5 is a nocturnal reservoir of NO_x formed via the reversible reaction between NO_2 and NO_3 as outlined in reactions 1.27 – 1.29:

$$NO + O_3 \rightarrow NO_2 + O_2 \quad \text{(Reaction 1.27)}$$

$$NO_2 + O_3 \rightarrow NO_3 + O_2 \quad \text{(Reaction 1.28)}$$

$$NO_2 + NO_3 \rightleftharpoons N_2O_5 \quad \text{(Reaction 1.29)}$$

Laboratory experiments conducted by Finlayson-Pitts *et al*. first identified that the reaction of N_2O_5 on aqueous chloride containing particles could generate both $ClNO_2$ and NO_3^- (reaction 1.30).[21]

Similarly, N_2O_5 can also react with water present within the particle to generate HNO_3 (reaction 1.31), thus the yield of $ClNO_2$ from the process is dependent on both the water and chloride concentrations of the particle.[58]

$$N_2O_5 + Cl^-_{(aq)} \rightarrow ClNO_2 + NO_3^- \quad \text{(Reaction 1.30)}$$

$$N_2O_5 + H_2O_{(aq)} \rightarrow 2\ HNO_3 \quad \text{(Reaction 1.31)}$$

More recently, Raff *et al*. have proposed a further surface-mediated mechanism for the formation of $ClNO_2$.[59] Initially, N_2O_5 is absorbed onto a surface whereupon it forms the complex $NO_2^+NO_3^-$ as shown in reaction 1.32. The complex can then undergo reaction with HCl to generate $ClNO_2$ and HNO_3 as outlined in reaction 1.33. A schematic representation of the two heterogenous pathways to $ClNO_2$ is given in Figure 1.3.

$$N_2O_5 \rightarrow NO_2^+ NO_3^- \quad \text{(Reaction 1.32)}$$

$$NO_2^+ NO_3^- + HCl \rightarrow ClNO_2 + HNO_3 \quad \text{(Reaction 1.33)}$$

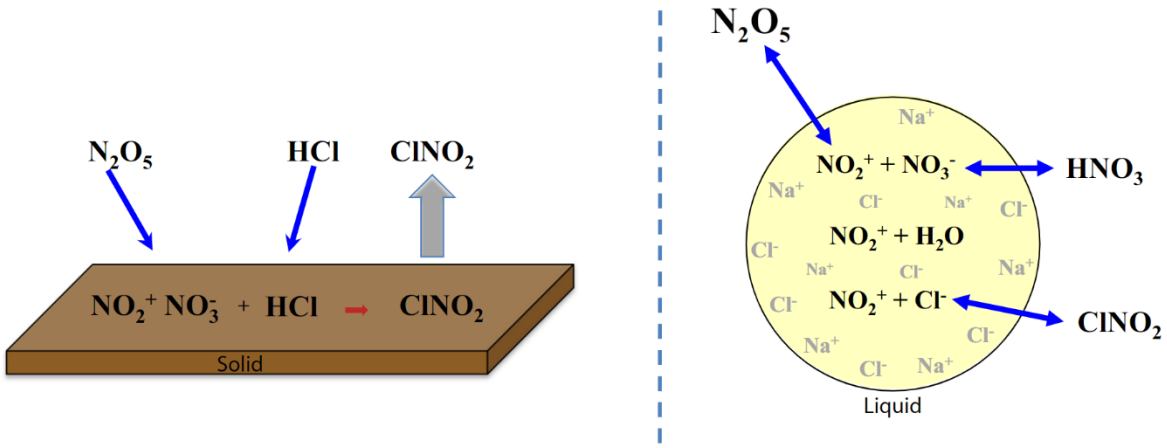

Figure 1.3. Heterogeneous pathways for the conversion of N_2O_5 into $ClNO_2$. (Left) Surface-mediated reaction between N_2O_5 and HCl as proposed by Raff *et al*.[59] (Right) The more well-established reaction of N_2O_5 with $Cl^-_{(aq)}$. Taken from Ravishankara.[60]

Whilst measurements of $ClNO_2$ via the surface-mediated mechanism were acquired at low RHs (0.5 – 25%), Raff *et al.* suggest that the mechanism could function at a greater rate at higher RHs owing to the catalytic behaviour of water observed within ab-initio calculations and experimental measurements. As noted by Ravishankara, however, higher humidities would lead to the formation of droplets with greater water content which could remove N_2O_5 as described by reaction 1.31.[60] Consequently, production of $ClNO_2$ via reaction with $Cl^-_{(aq)}$ present in aerosols is likely to dominate within the free troposphere and at a regional and global scale. The importance of the surface mediated mechanism on a localised scale will ultimately be determined by the availability of solid surfaces and sources of pCl^-. It therefore follows that surface reactions would be most prominent in highly

urbanised areas, due to their large building densities, as well as indoor environments. As reactive uptake coefficients were not reported by Raff *et al*., how effectively this mechanism would compete with the particulate pathway is unknown and thus requires further investigation.

With respect to ambient observations of $ClNO_2$, initial measurements of the reservoir species were focused on the MBL in which concentrations ranging between sub 50 pptv (below the level of detection of a CIMS instrument) and 2.1 parts per billion volume (ppbv) were recorded, the latter observed within the polluted coastal environment of Los Angeles.[61-63] In 2010, Thornton *et al*. detected $ClNO_2$ at concentrations ranging between 100 - 450 pptv near Boulder, Colorado in central North America, expanding the impact of Cl tropospheric chemistry beyond the MBL.[64] Since then, a considerable number of studies have reported $ClNO_2$ measurements in continental environments as well as polluted coastal sites.[65-73] Upon photolysis, $ClNO_2$ releases a Cl atom and NO_2 (reaction 1.35).[61, 74] Research conducted by Ghosh *et al*. demonstrated that this could result in the production of Cl within the first 3-5 hours following sunrise, a period in which the contraction of other oxidants would be low.[75]

$$ClNO_2 + h\nu \rightarrow Cl + NO_2 \qquad \text{(Reaction 1.35)}$$

Cl_2 is another photolabile chlorine reservoir species, with typical tropospheric mixing ratios on the order of 10-100 pptv reported.[62, 76, 77] The aqueous phase reaction of OH and Cl^- as described by reactions 1.35–1.39 is a minor route by which Cl_2 can be produced:[78]

$$OH_{(aq)} + Cl^- \rightleftharpoons HOCl^- \qquad \text{(Reaction 1.35)}$$

$$HOCl^- + H^+ \rightarrow H_2O + Cl \qquad \text{(Reaction 1.36)}$$

$$Cl + Cl^- \rightarrow Cl_2^- \qquad \text{(Reaction 1.37)}$$

$$2\ Cl_2^- \rightarrow Cl_{2(aq)} + 2\ Cl^- \qquad \text{(Reaction 1.38)}$$

$$Cl_{2(aq)} \rightarrow Cl_{2(g)} \qquad \text{(Reaction 1.39)}$$

A number of heterogenous reactions have also been proposed which would provide alternative pathways to the formation of Cl_2. One such route is the formation and reaction of a surface complex which is formed following the reaction of gas phase OH and Cl^-:[78-80]

$$OH_{(g)} + Cl^-_{(aq)} \rightleftharpoons OH\text{--}Cl^- \qquad \text{(Reaction 1.40)}$$

$$2\ OH\text{--}Cl^- \rightarrow Cl_{2(g)} + 2\ OH^-_{(aq)} \qquad \text{(Reaction 1.41)}$$

Heterogenous reactions with $ClNO_2$, $ClONO_2$, HOCl and hypobromous acid (HOBr) offer further routes by which chlorine activation can proceed:[77, 81]

$$ClNO_2 + Cl^-_{(aq)} \rightarrow Cl_2 + NO_2^- \quad \text{(Reaction 1.42)}$$

$$ClONO_2 + Cl^-_{(aq)} + H^+_{(aq)} \rightarrow Cl_2 + HNO_3 \quad \text{(Reaction 1.43)}$$

$$HOCl + Cl^-_{(aq)} + H^+_{(aq)} \rightarrow Cl_2 + H_2O \quad \text{(Reaction 1.44)}$$

$$HOBr + Cl^-_{(aq)} + H^+_{(aq)} \rightarrow BrCl + H_2O \quad \text{(Reaction 1.45)}$$

Analogous reactions to those described in 1.43 and 1.44 with particulate bromide are also known to act as potential sources of bromine chloride (BrCl).[82] In the aforementioned global model simulations conducted by Wang *et al.*,[13] photolysis of BrCl accounted for 40% of the total Cl and ClO radical production within the troposphere. By comparison, photolysis of $ClNO_2$ and Cl_2 accounted for only 8 and 4% respectively, with the reaction between HCl and OH responsible for 45%. Despite the simulated importance of BrCl as a reservoir species, field measurements are sparse. Whilst measurements of the species have been made in polar regions, in which concentrations are typically in the low 10s of pptv,[49, 83] the species has not been observed in coastal or open ocean marine air despite detection limits < 2 pptv.[84, 85]

HOCl and $ClONO_2$ are by-products of the reaction of Cl radicals with O_3 to form chlorine monoxide (ClO) as depicted in reaction 1.1, which in turn can react with HO_2 and NO_2 (reactions 1.46 and 1.47 respectively).[62] Both species can be photolysed to liberate a chlorine radical, however, their rate of formation in polluted regions is limited by the availability of ClO where reaction with NO is the dominant sink – a reaction which itself produces a Cl radical (reaction 1.48).[62]

$$ClO + HO_2 \rightarrow HOCl + O_2 \quad \text{(Reaction 1.46)}$$

$$ClO + NO_2 + M \rightarrow ClONO_2 + M \quad \text{(Reaction 1.47)}$$

$$ClO + NO \rightarrow Cl + NO_2 \quad \text{(Reaction 1.48)}$$

Several additional sinks of ClO are known to exist. Reaction with OH represents one such minor pathway, and is known to proceed via two different routes as represented by reaction 1.49 and 1.50:[86, 87]

$$ClO + OH \rightarrow Cl + HO_2 \quad \text{(Reaction 1.49)}$$

$$\rightarrow HCl + O_2 \quad \text{(Reaction 1.50)}$$

Reaction with bromine monoxide (BrO) is a further route by which ClO can be lost, resulting in the formation of BrCl (reaction 1.51), the chlorine peroxy radical (ClOO, reaction 1.52) and chlorine dioxide (OClO, reaction 1.53).[88] ClOO is known to rapidly undergo photolysis to generate a Cl radical and O_2. Similarly, OClO can also undergo photolysis, reforming ClO and O and as such can lead to the formation of O_3.

$$ClO + BrO \rightarrow BrCl + O_2 \quad \text{(Reaction 1.51)}$$

$$\rightarrow ClOO + Br \quad \text{(Reaction 1.52)}$$

$$\rightarrow OClO + Br \quad \text{(Reaction 1.53)}$$

Self-reaction is the final sink mechanism for ClO. The reaction is known to proceed via four channels; a termolecular reaction (reaction 1.54) and three bimolecular pathways (reactions 1.55-1.57).

$$ClO + ClO + M \rightarrow Cl_2O_2 + M \quad \text{(Reaction 1.54)}$$

$$ClO + ClO \rightarrow Cl_2 + O_2 \quad \text{(Reaction 1.55)}$$

$$\rightarrow Cl + ClOO \quad \text{(Reaction 1.56)}$$

$$\rightarrow Cl + OClO \quad \text{(Reaction 1.57)}$$

In all instances the pathways ultimately generate a Cl atom as chlorine peroxide (Cl_2O_2), generated in reaction 1.55, also readily undergoes photolysis to generate ClOO and a Cl atom.

A summary of the chemical sources and sinks of tropospheric Cl atoms that have been described in this section is given in Figure 1.4.

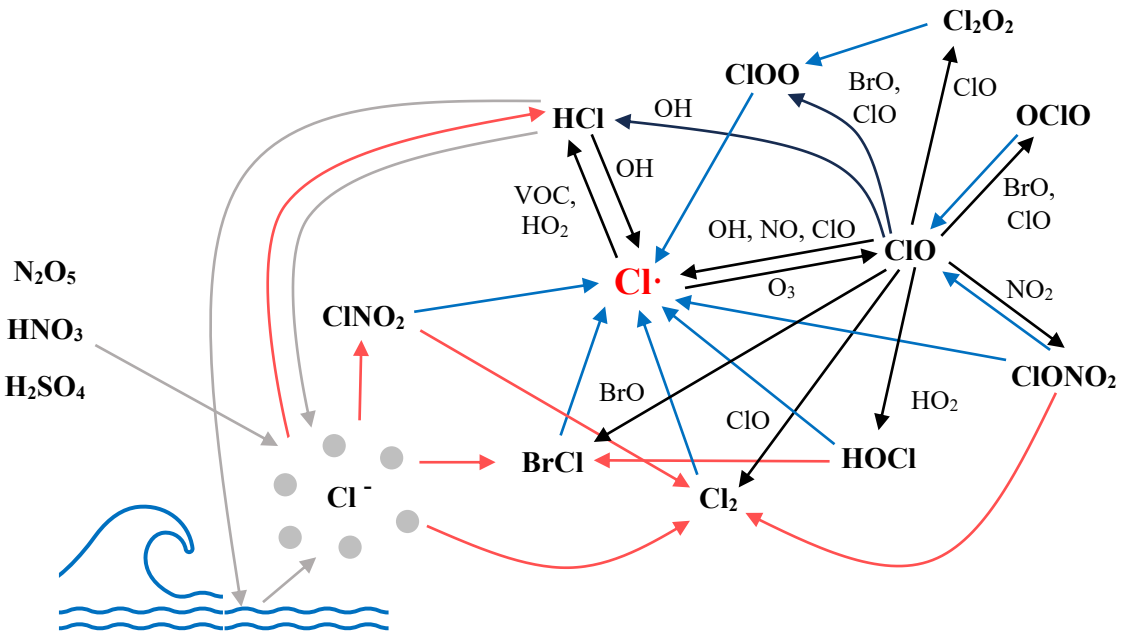

Figure 1.4. Summary of the chemical sources and sinks of tropospheric Cl atoms. Red arrows represent heterogeneous reactions resulting in the formation of chlorine reservoir species. Additional heterogeneous reactions of importance are denoted by grey arrows. Black arrows are used to represent chemical reactions whilst photolysis is shown by blue lines.

1.3.2 Direct Emissions

In addition to chemical sources of Cl_y, both natural and anthropogenic emission sources are also known to exist. With respect to the former, HCl is known to be emitted following volcanic eruptions.[42, 89] By comparison, primary anthropogenic emissions of HCl, pCl^-, Cl_2 and HOCl have been reported from coal combustion,[46, 90, 91] waste incineration,[92, 93] industrial processes such as lime and brick production,[90, 94] and biomass burning.[95, 96] Hypochlorite (OCl^-) bleach solutions, commonly used for domestic and industrial cleaning purposes, is an additional source of chlorinated gases. Whilst measurement of organic species such as carbon tetrachloride (CCl_4) and chloroform ($CHCl_3$) have been reported after the application of the product in indoor environments,[97-101] HOCl, Cl_2, $ClNO_2$ have also been measured.[102, 103] In a study conducted by Mattila *et al.*[102], peak concentrations of up to 370, 130, 34 ppbv were observed respectively – several orders of magnitude greater than that reported in outdoor environments. Whilst measurements of HCl were not recorded during the study, it was estimated that the application of bleach could lead to an enhancement of its concentration by 1-2 ppbv under background levels of NO, and up to 15-20 ppbv under periods of elevated NO. Such concentrations are, however, in large excess to direct measurements by Dawe *et al.* who observed enhancements of ~ 0.1 ppbv.[104] Whilst indoor air chemistry is not the primary focus of this thesis, the observation of these species within such environments further highlights the need to further our understanding of Cl chemistry.

1.3.3 Measurement of Cl_y

A summary of the global annual mean vertical distributions of the inorganic Cl_y constituents discussed in this chapter, as modelled in GEOS-Chem, is provided in Figure 1.5. Traditionally the measurement of such species within the troposphere was achieved by sampling ambient air through an alkaline-impregnated filter fitted downstream of a particulate filter, or alternatively through the use of an alkaline coated denuder, with the resulting extract analysed through ion chromatography.[42] Recent advancements in observational techniques have, however, enabled online measurements to be possible. Chemical ionisation mass spectrometry (CIMS) is an example of such a technique which has been routinely deployed to measure a variety of different reservoir species including HCl, $ClNO_2$, HOCl and Cl_2.[53, 61, 66, 105] Owing to the well-defined and spectrally isolated adsorption features of HCl,[106] measurements of ambient HCl have also been reported using infrared adsorption spectroscopy, through techniques such as cavity ring down spectroscopy (CRDS) and tunable infrared laser direct absorption spectroscopy (TILDAS). [55, 107-109] Conversion of the remaining components of Cl_y into HCl would enable the total Cl atom reservoir to be measured by these spectroscopic techniques. Such an approach has recently been developed by Furlani *et al*. to measure the total gaseous Cl concentration (TCl_g).[110] The technique is dependent on the complete thermolysis of TCl_g , which is achieved by passing ambient air through a heated platinum mesh, resulting in the release of Cl atoms which react with a propane standard (mixed with ambient air prior to heating) to

generate HCl. One limitation of this approach, however, is that organic Cl containing species such as methyl chloride (CH_3Cl) and dichloromethane (CH_2Cl_2) also undergo thermolysis within the setup. Whilst such species are the dominant fraction of TCl_g, they are more stable to degradation within the troposphere than inorganic sources as previously discussed, with the lifetimes of CH_3Cl and CH_2Cl_2 simulated to be 573 and 109 days respectively. Consequently, an alternative approach to generating HCl is required which would enable only the inorganic fraction to be considered in order to calculate the total Cl atom reservoir through steady state calculations.

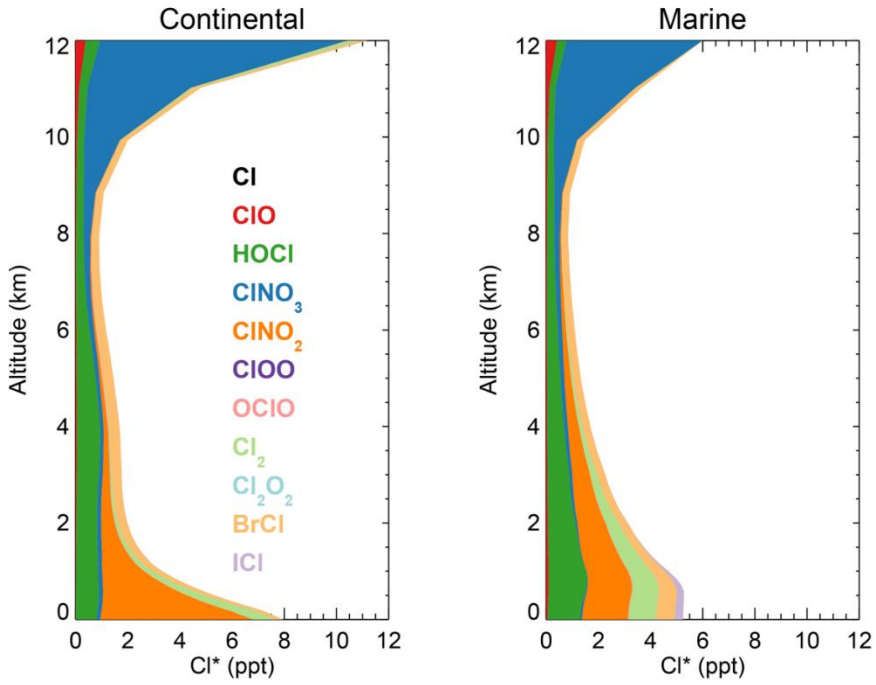

Figure 1.5. Global annual mean vertical distributions of inorganic Cl_y constituents simulated in GEOS-Chem for continental and marine air. Taken from Wang *et al.*[13]

1.4 Total Loss Rate Measurement Techniques

As reported by Goldstein and Galbally,[111] there has been an estimated 10^4 – 10^5 different organic species that have been measured in the atmosphere, with such a range potentially just a small fraction of the number species that are actually present. Consequently, deriving the total Cl loss rate from concentrations of VOCs measured in the field is unlikely to be sufficient, as has been found in several studies investigating OH in which 10-50% of the measured reactivity has been unaccounted for when only considering the measured species.[112-115] Direct measurement of the total ambient Cl reactivity in the field is therefore vital if we are to test our understanding of the associated loss mechanisms and accurately calculate local Cl atom concentrations. Whilst no such technique has been developed to achieve this specifically for investigating Cl, several different techniques have been utilised for

the direct measurement of the total OH reactivity that could be modified to enable such analysis. A discussion of such techniques is provided herein.

1.4.1 Flow Tube Reactivity Measurements

The first method developed to measure the total OH reactivity was the Total OH Loss rate Method (TOHLM).[116] This approach utilises the discharge-flow technique,[117-119] with OH generated within a narrow moveable tube that is injected into the centre of a larger flow tube, through which ambient air is passed. Upon mixing, OH and the trace gases present in the ambient air react, with the resulting mixture sampled through a inlet situated at the end of the flow tube and the concentration of OH measured. Alterations in the reaction time can then made by adjusting the position of the injector relative to the detection chamber. By measuring the concentration of OH at different reaction times, an OH decay profile can then be obtained of the form:

$$[OH]_t = [OH]_0 \, exp^{-k_{OH}t} \qquad \text{(Equation 1.2)}$$

where:

- $[OH]_0$ and $[OH]_t$ are the concentrations of OH at the start of the reaction and time t
- k_{OH} is the pseudo 1st order rate constant for the loss of OH

Assuming that the reaction between OH and the reactive species present in the ambient air sample fulfils the pseudo first-order requirement (that the concentration of the reactive species is in large excess of OH and does not change significantly within the reaction chamber), a plot of ln(OH signal) against time should yield a straight line with a gradient equivalent to k_{OH}. It should be noted, however, that due to physical losses of OH within the reactor (e.g. wall loses), the value of k_{OH} obtained is the sum of both the chemical and physical losses of OH ($k_{OH} = k'_{OH} + k'_{phys}$). Consequently, the value of k'_{phys} must be well established in order to determine the true loss rate of OH.

Since the development of the TOHLM, several similar instruments have been developed.[120-122] In all instances, the measurement of OH is achieved using Laser-Induced Fluorescence-Fluorescence Assay by Gas Expansion (LIF-FAGE). In such an approach, OH is excited by laser light from the ground state to an electronically excited state, from which the deactivation to the ground state is achieved following fluorescence and collisional quenching.[123] The resulting fluorescent photon at 308 nm that is emitted during the process is then detected, with the number of photons proportional to the concentration of OH within the detection chamber.[123] The detection chamber is held at low pressure in order to reduce the collisional quenching of the excited OH radicals, allowing for the fluorescence lifetime to be extended in order for temporal discrimination of the laser pulse and the subsequent OH fluorescence to be achieved.[123]

It should be noted that this approach is not without its limitations. As the formation of OH within the instruments is typically achieved through the photolysis of water vapour (reaction 1.58), HO_2 is also formed as a secondary product as described by reaction 1.59:

$$H_2O + h\nu \rightarrow OH + H \qquad \text{(Reaction 1.58)}$$

$$H + O_2 + M \rightarrow HO_2 + M \qquad \text{(Reaction 1.59)}$$

Recycling of OH within the flow tube can therefore occur prior to detection following the reaction of HO_2 with any NO present in the ambient air sample (> ~1 ppbV) as outline in reaction 1.22. This recycling process reduces the observed decay rate in OH and therefore can interfere with the calculated value of k_{OH}.[124] Consequently, in order to correct for this interference, the concentration of NO must be simultaneously measured during the operation of the instrument. A further limitation of the flow tube technique is the need for both OH and the ambient air mixture to be well mixed prior to measurement. In order to achieve this, the air flow at the outlet of the moveable injector is typically made turbulent, which can result in further physical losses of OH to the reactor walls that would need to be quantified – with the uncertainty on this measurement reducing the limit of detection (LOD) of the instrument.[116] A final disadvantage of the technique is its poor time resolution owing to the need to adjust the reactor position. During these periods, the OH reactivity could exhibit significant variability which can result in the obtainment of erroneous k_{OH} values.

1.4.2 Laser Flash Photolysis

Another method which utilises LIF to measure the total OH reactivity is the pump probe method. First developed by Calpini *et al.*,[125] ambient air is sampled into a reaction cell within which OH is generated via the photolysis of ambient O_3 (λ = 266 nm) by a pump laser beam as described by reactions 1.9 and 1.10. As with the flow tube reactivity measurements, the OH concentration decreases after the irradiation of the pump laser beam as a result of its reactions with the trace species present in the air sample. Time-resolved LIF measurements are then conducted on the resulting mixture within a detection chamber by pulsing a probe laser at 308 nm, enabling the decay profile of OH to be obtained. There are number of advantages of using this technique over the flow tube method, and since the work of Calpini *et al.* several similar instruments have been developed.[126-128] The first advantage is the use of ambient O_3 photolysis as a source of OH radicals as it does not form any HO_2 like the photolysis of H_2O, and as such the NO interference on the measured k_{OH} is minimised. The production of OH radicals by this approach also ensures that their concentration is uniform throughout the reaction cell, removing the issue of poor mixing that could arise in the flow tube method. A laminar flow through the reaction cell can therefore be utilised, reducing losses of OH to the walls of the reactor, leading to reduced uncertainty in the value of k'_{phys} and potentially lower LODs. The approach also offers improved time-resolution when compared to the flow tube technique

as the OH measurements are made in "real-time" through the use of time-resolved OH decay measurements.[128]

1.4.3 Comparative Reactivity

An alternative method was published by Sinha *et al*. at the Max Planck Institute for Chemistry in 2008 which enables the total OH reactivity to be determined without directly measuring the concentration of OH radicals.[129] The comparative reactivity method (CRM) is similar in its underlying principles to that of relative rate measurements. The method employs a reference compound (X), for which its rate coefficient with reaction towards OH is well established, and its natural abundance within the atmosphere negligible, to indirectly measure the OH reactivity with ambient air. The compound is first introduced into a glass reactor in a flow of zero air and its concentration monitored with a suitable detector upon its exit. OH radicals are then introduced through a side arm in the glass reactor following the photolysis of water vapour, whereupon they react with the compound X resulting in a depletion in its concentration that is measured by the chosen detector. Once the concentration has stabilised, the zero air flow is switched for ambient air. As a result of the trace species that are subsequently introduced into the reactor which compete with compound X for the finite amount of OH radicals, the concentration of compound X increases. Using the concentrations of compound X exiting the reactor at each stage, the OH reactivity of the ambient air sample can be derived:

$$R_{ambient} = \frac{(\boldsymbol{C3}-\boldsymbol{C2})}{(\boldsymbol{C1}-\boldsymbol{C3})} \times k_X \boldsymbol{C1} \qquad \text{(Equation 1.3)}$$

where:

- $R_{ambient}$ is the total OH reactivity with the ambient air sample
- k_X is the rate coefficient for the reaction of compound X with OH
- ***C1*** is the concentration of compound X measured exiting the reactor in zero air
- ***C2*** is the concentration of compound X in zero air after the addition of OH
- ***C3*** is the concentration of compound X after the addition of both OH and ambient air

A key assumption of the CRM technique is that the system is under pseudo-first order conditions. Consequently, the concentration of compound X introduced into the reactor must be in large excess to that of OH. In the instrument developed by Sinha *et al*., pyrrole was used as reference compound X with proton transfer reaction mass spectrometry (PTR-MS) chosen as the detector. A number of different studies have used comparable setups,[113, 130-133] with some using gas chromatography-mass spectrometry (GC-MS) as a detector instead of PTR-MS.[134, 135] The utilisation of such techniques which are routinely deployed during field investigations is an advantage of the CRM technique over the flow tube and flash photolysis approaches which would require the use of an expensive FAGE setup. A further advantage of the CRM over the aforementioned alternatives is that the physical losses

of OH within the system do not need to be known, assuming that they are constant in zero and ambient air, and therefore do not need to be frequently calculated. The LOD of the technique is instead determined by the detection system.

There are, however, several disadvantages of the CRM technique. Like the flow tube method, as OH is generated via the photolysis of water vapour, the measured reactivity rate is susceptible to interference from any NO introduced into the system. To overcome this issue, the concentration of NO would need to be simultaneously measured so that the corresponding ***C3*** concentrations can be corrected as described by Michoud *et al*.[136] An alternative approach has more recently been proposed by Wang *et al*., referred to as the improved CRM (ICRM), in which NO is introduced alongside water vapour into the side arm of the glass reactor within which the OH radicals are generated.[132] The concentration of NO introduced is in excess of the concentration of HO_2 generated during the photolysis of water vapour, ensuring that no further OH recycling occurs when the system is switched from zero air to ambient air. A further issue with this approach is its sensitivity to changes in humidity between ***C2*** and ***C3***, with increased humidity at either stage resulting in an increase in the concentration of OH radicals produced. Changes in humidity can also impact the concentration of the H_3O^+ reagent ions used in PTR-MS, with a larger degree of clustering ($H_3O(H_2O)_n^+$) observed at higher humidity. The formation of such clusters can impact the sensitivity of PTR-MS towards VOCs with different rate coefficients for reaction with H_3O^+ and the cluster ions, resulting in changes in the concentration of the reference compound X.[137, 138] Consequently, efforts need to be made to ensure that the humidity of the zero air introduced into the system is comparable to ambient by monitoring the m/z 37:19 ratio at each stage. In instances in which this is not possible, a further correction factor would be required.[136] Additional correction factors may also need to be applied to account for photolytic losses of the reference compound, and other photolabile trace species present within the ambient air sample as well. In the original design developed by Sinha *et al.*, this could account for up to 25% of the observed depletion in pyrrole.[129] The CRM instrument developed by Mines Douai (MD-CRM), however, has managed to reduce this interference down to 5% through the re-positioning of the UV mercury lamp used to generate the OH radicals.[133]

Intercomparison between the MD-CRM and the pump probe method have previously been conducted by Hansen *et al*. at the University of Lille campus, a site heavily influenced by anthropogenic NO_x and VOC emissions.[133] Initial measurements were conducted using synthetic VOC mixtures, one consisting of NMHCs and another containing oxygenated VOCs (OVOC), from which the CRM instrument was found to underestimate the OH reactivity by 39 and 53% respectively. By comparison, the pump probe method underestimated the reactivity of the NMHC mixture by 1% whilst tests of the OVOC mixture were inconclusive owing to limited measurements. During sampling of ambient air, the CRM instrument was found to underestimate the OH reactivity by 22% on average when compared to the LIF measurements. The source of the large discrepancies between the two techniques

was attributed to the photolytic losses of VOCs in the CRM instrument, which was later rectified by adjusting the position of the mercury lamp as previously discussed. No evidence was found to suggest any NO-dependent bias in the MD-CRM measurement after the application of a correction factor to account for interferences arising from the increased concentrations of OH within the system. A further intercomparison study was later conducted at the outdoor atmospheric simulation chamber SAPHIR by Fuchs *et al.*[139] Following the modifications to the MD-CRM instrument, good agreement was observed with the pump-probe instrument deployed during the campaign when measuring urban air mixtures containing anthropogenic hydrocarbons and NO_x. Poorer agreement was observed, however, upon the addition of low-volatility terpenoid compounds in which rates were up to a factor of five lower than those obtained by the pump-probe method. Whilst additional OH recycling owing to the chemistry of these compounds was not ruled out, losses of the OH reactants to the walls of the inlet line were proposed as a source of this increased discrepancy owing to the increased residence time and differing inlet material of the CRM instrument.

1.5 Thesis Objectives

It is clear that if we are to thoroughly assess the importance of Cl atoms in tropospheric oxidation chemistry, further constraints on the mechanisms controlling Cl chemistry are required. In particular, greater observational constraints of the Cl budget are required. As such, the overall aim of this thesis is to investigate the mechanisms by which Cl atoms and HCl are lost within the troposphere through a combination of instrument development, laboratory experiments and atmospheric models. The methods used during these investigations are described in detail in chapter 2.

Chapter 3 investigates the feasibility of the OH reactivity instruments described in section 1.5 for the measurement of the total Cl reactivity. The performance of the chosen method will first be assessed using zero-dimensional box models to determine whether it can accurately calculate ambient Cl reactivity and identify any potential sources of interference. Several potential mechanisms and precursors for the formation of Cl radicals within the proposed instrument will also be examined.

Chapter 4 focuses on the characterisation of the proposed total Cl reactivity instrument through the measurement of increasingly more complex VOC mixtures. The interferences identified in chapter 3 will be examined through a combination of both laboratory and box model simulations to identify potential mitigating measures which could be adopted to minimise the impact on the calculated rate. The suitability of the instrument for the measurement of unknown rate coefficients will also be explored, which would be provide an additional application of the instrument when not deployed in the field. Modifications to the reactor design used in this study will also be proposed.

Chapter 5 investigates the partitioning of HCl/pCl^- during summer and winter field campaigns conducted at an urban background site in the UK. The measurements will be used to assess the

performance of a thermodynamic partitioning model, with the observations compared to previous studies within the literature.

Chapter 6 summarises the findings of chapters 3-5 and provides a discussion as to the future work required to constrain the radical loss processes.

Chapter 2

Experimental

Throughout this thesis a range of different experimental techniques have been utilised, both in the development of a total Cl loss rate instrument, and the investigation of chloride partitioning. Chemical models have also been used to examine both laboratory and field measurements in these respective areas. This chapters serves to provide a general overview of the underlying principles of the main techniques that have been used. Specific details of their mode of operation is provided in the relevant chapters.

2.1 Proton Transfer Reaction Mass Spectrometry

As the name suggests, PTR-MS operates under the basis of chemical ionisation, specifically through proton transfer, with the technique routinely used for direct, real time analysis of trace gas species present in ambient air.[140] In this work, the technique was used as a detector during the initial development stages of the total Cl loss rate instrument. PTR-MS was favoured over GC-MS for this application owing to the improved acquisition rate of the former, with modern commercial units capable of response times less than 100 ms.

In general, the process by which PTR-MS functions can be broken down into three stages, with a simplified schematic of a typical unit provided in Figure 2.1. In the initial stage, humified air is introduced into an ion source from which the reagent hydronium ions (H_3O^+) are generated via electron impact reactions as outlined in reactions 2.1 and 2.2.

$$H_2O + e^- \rightarrow H_2O^+ + 2e^- \qquad \text{(Reaction 2.1)}$$

$$H_2O^+ + H_2O \rightarrow H_3O^+ + OH \qquad \text{(Reaction 2.2)}$$

The purity of the generated H_3O^+ ions exiting the ion source is typically ~ 99.5%, with nitrosonium (NO^+) and dioxygenyl (O_2^+) the only significant impurity ions regularly observed.[141] Consequently, there is no need for a quadrupole system to pre-select the reagent ion. As such, the H_3O^+ ions are directly injected into a drift tube whereupon they are mixed with the sample flow and undergo a proton transfer reaction with species (M) that have a higher proton affinity than water (691 kJ/mol) as depicted in reaction 2.3.[142]

$$H_3O^+ + M \rightarrow MH^+ + H_2O \qquad \text{(Reaction 2.3)}$$

As the main constituents of air have proton affinities lower than water, they do not undergo proton transfer and therefore do not unnecessarily deplete the reagent ion count. Fragmentation of the resulting product ion (MH^+) is generally minimal owing to the low amount of excess energy that is produced during the proton transfer reaction. After formation, the product ions are guided towards the detection system by an electric field (E/N), the strength of which can be controlled by the user through adjustments in the pressure, temperature and potential difference across the drift tube. In

general, higher E/N values result in an increased velocity of ions through the drift tube regions leading to reduced response times. Such conditions also reduce the rate of formation of water cluster products, the formation of which is depicted in reaction 2.4. It should be noted, however, that higher E/N values also increase the level of product ion fragmentation within the system. As such a balance must be struck between fragmentation and response time when choosing the operating conditions of the instrument.

$$H_3O^+ + M \rightarrow MH.H_2O^+ \qquad \text{(Reaction 2.4)}$$

With respect to the detection of the product ions, traditionally PTR-MS instruments were fitted with quadrupole mass analysers and secondary electron multipliers (SEM), as is the case for the instrument used in this work. Upon leaving the drift tube, a series of ion lenses are used to guide the product ions towards the quadrupole mass filter. A turbopump is connected to the ion lens region in order to achieve a reduction in pressure between the drift tube and quadrupole regions of the instrument. This decrease in pressure is necessary in order to stop further reactions between the reagent ions and sample, whilst also minimising ion-neutral collisions which would otherwise reduce the transmission efficiency within the detection region. The instrument can either be operated in full mass scan or selection ion monitoring (SIM) mode, with the latter used in this work. In this setting only ions of select mass-to-charge ratios (m/z) are allowed to pass through the quadrupole, with filtration achieved by combining both high and low pass filters. These filters are created by the alteration of the radio frequency (RF) potential or RF frequency and the DC potential of the quadrupole respectively. Once the ion are through the quadrupole, they are then fired into a SEM which amplifies the signal from the product ions such that a measurable current is generated. Mixing ratios for the detected species are then automatically calculated within the operating software provided by the instrument manufacturer (Ionicon, Austria) via equation 2.1:

$$[M]_{ppb} = \frac{I(MH^+)}{I(H_3O^+)} \frac{T(H_3O^+)}{T(MH^+)} \frac{1}{kt} \frac{10^9}{N} \qquad \text{(Equation 2.1)}$$

where:

- $I(x)$ is the signal intensity (measured in ion counts per second)
- $T(x)$ is the transmission of ions
- k is the rate of reaction for the proton transfer between H_3O^+ and M
- t is the reaction time
- N is the number density in the drift tube

The number density can, in turn, be calculated using equation 2.2:

$$N = \frac{N_A}{V_m} \frac{p_d T_0}{p_0 T_d} \qquad \text{(Equation 2.2)}$$

where:

- N_A is Avogadro's number (6.022×10^{23} mol^{-1})
- V_m is the molar gas volume at standard temperature and pressure (22414 cm^{-3} mol^{-1})
- p_d is the drift tube pressure
- p_0 is atmospheric pressure (1013.25 hPa)
- T_0 is 273.15K
- T_d is the temperature of the drift tube

It should be noted that in more recent variants of the PTR-MS instrument, time-of-flight (ToF) mass analysers and ion traps have been used as alternative detection systems, with the former offering improved mass resolution and mass range when compared to its quadrupole counterpart.

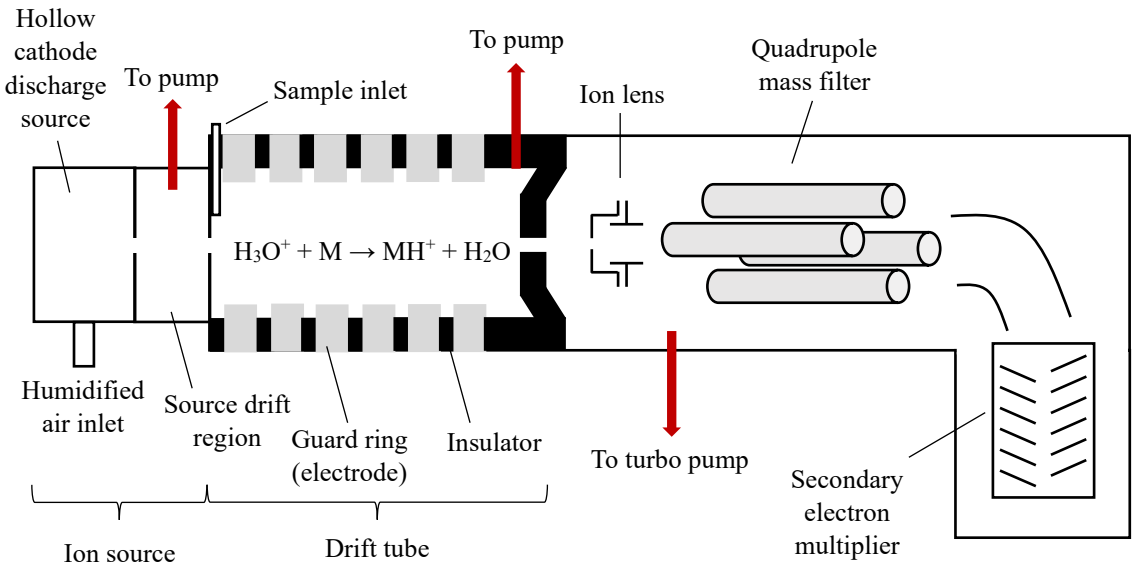

Figure 2.1. Simplified schematic of a PTR-MS equipped with a quadrupole mass filter.

2.2 Selected-Ion Flow Tube Mass Spectrometry

A Voice200 selected-ion flow tube mass spectrometer (SIFT-MS) (Syft Technologies, New Zealand) was also used during the later developmental stages of the total Cl reactivity instrument discussed in chapters 3 and 4. A simplified schematic of this instrument is provided in Figure 2.2. In summary, the instrument is composed of a novel ion source region in which H_3O^+, NO^+ and O_2^+ ions are generated from an air/water mixture via a microwave discharge. Upon their formation, the ions are extracted into an upstream (relative to the sample inlet and flow tube) chamber. A series of electrostatic lenses directs the regent ions towards a quadrupole mass filter which can rapidly (< 1 ms) switch between the available reagent ions to effectively enable a single measurement to simultaneously utilise all three reagent ions. Ions not rejected by the mass filter are then injected into fast-flowing inert carrier gas through a Venturi-type orifice. As with PTR-MS, the reagent ions are mixed with the sample within the flow tube region. The various reagent ions react differently with the sample gas molecules resulting in the formation of differing association and fragmentation patterns. The proton transfer process of H_3O^+ operates under the same basis as described earlier for PTR-MS. By comparison, the reactions of NO^+ with organic molecules are much more varied. These can be summarised as charge transfer processes (reaction 2.5), hydride ion transfer (reaction 2.6), hydroxide ion transfer (reaction 2.7), alkoxide ion transfer (reaction 2.8) and ion molecule association (reaction 2.9), although typically an organic species will only react with NO^+ via one of these routes.[143]

$$NO^+ + M \rightarrow M^+ + NO \qquad \text{(Reaction 2.5)}$$

$$NO^+ + MH \rightarrow M^+ + HNO \qquad \text{(Reaction 2.6)}$$

$$NO^+ + MOH \rightarrow M^+ + HNO_2 \qquad \text{(Reaction 2.7)}$$

$$NO^+ + MOR \rightarrow M^+ + RNO_2 \qquad \text{(Reaction 2.8)}$$

$$NO^+ + M \rightarrow NO^+M \qquad \text{(Reaction 2.9)}$$

As the ionisation energy of O_2 is greater than most organic molecules, their reaction with O_2^+ proceeds either via non-dissociative charge transfer (reaction 2.10) or through dissociative charge transfer resulting in the formation of fragment ions.

$$O_2^+ + M \rightarrow M^+ + O_2 \qquad \text{(Reaction 2.10)}$$

Product ions, and remaining precursor reagent ions, are sampled through a small pinhole orifice located downstream of the flow tube into a differentially-pumped quadrupole mass filter. As with the PTR-MS described above, the quadrupole was operated in SIM mode in this work, with the filtered ions detected using an electron multiplier and pulse counter. Concentrations were calculated in real

time based on the precursor ion to product ion ratio, and the known reaction rate between the two, using equation 2.3:

$$[M] = \gamma \times \frac{[M^+]}{[R^+]\, t\, r} \qquad \text{(Equation 2.3)}$$

where:

- γ is the instrument calibration factor
- $[M^+]$ is the product ion concentration
- $[R^+]$ is the reagent ion concentration
- t is the reaction time
- k is the rate coefficient for reaction between the reagent ion and M

It should be noted that whilst the generation of multiple reagent ions can be useful with respect to obtaining structural information of a sample gas molecule, the efficiency with which these are generated is poorer than that of H_3O^+ in PTR-MS, resulting in elevated limits of detection (LOD).

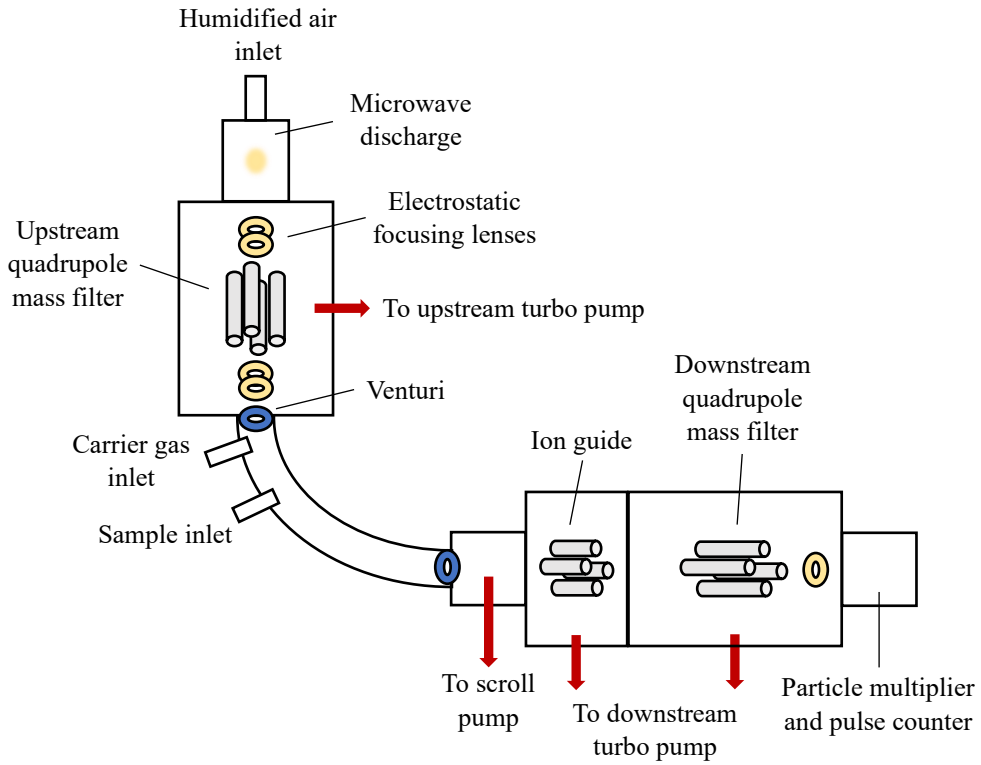

Figure 2.2. Simplified representation of the Voice200 SIFT-MS used in this work.

2.3 HCl Tunable Infrared Laser Direct Absorption Spectroscopy

HCl measurements used in chapter 5 of this thesis were obtained using a HCl-TILDAS instrument (Aerodyne Research Inc, Billerica, MA, United States) by Dr John Halfacre of the University of York. As previously discussed in section 1.3.3, the underlying principle of the TILDAS technique is infrared absorption spectroscopy, with a simplified schematic of the instrument provided in Figure 1.3. To generate the necessary infrared radiation, the TILDAS is fitted with an inter-band cascade laser. To transform the broad output from the laser into a narrow beam, the output is first collected by an objective and subsequently focused through a flip-in pinhole which is only in position during the laser alignment process. After focusing, the beam in the reimaged into a multi-pass, astigmatic Herriott cell, with the output directed to a thermoelectrically cooled detector. By using a multi-pass absorption cell, the effective pathlength within the TILDAS is 204 m. Such a pathlength is necessary owing to the low ambient concentrations of HCl, and thus the need for high detection sensitivity.

In order to determine the concentration of HCl within the sampled air flow, the infrared radiation is used to probe the strong absorption line at 2925.89645 cm^{-1} corresponding to the 1-0 rovibrational band of the molecule.[106, 144] To achieve this, the instrument software (TDLWintel) scans over a spectral window of 2925.80 to 2926.75 cm^{-1} which is found via the strong absorption bands belonging to other spectrally close absorbers such as water and CH_4. Line widths and strengths for the measured species are based upon the HITRAN 2016 database.[145] For each measurement, the instrument software produces a spectral fit based on these HITRAN parameters, as well as the pressure and temperature within the system to account for any pressure broadening and changes in the rovibrational state population respectively. The HCl mixing ratio can then be determined by the instrument software using the Beer-Lamber Law (equation 2.4):

$$I(\upsilon) = I_0(\upsilon) \exp\left[-\left(l\, N_0(P,T)\, M\, S(\upsilon,P,T)\right)\right] \qquad \text{(Equation 2.4)}$$

where:

- I is the transmitted light intensity as a function of laser frequency
- I_0 is the intensity of the light output as a function of laser frequency
- l is the absorption path length
- N_0 is the molecular number density as a function of pressure and temperature
- M is the mixing ratio of HCl
- S is the line strength as a function of frequency, pressure and temperature

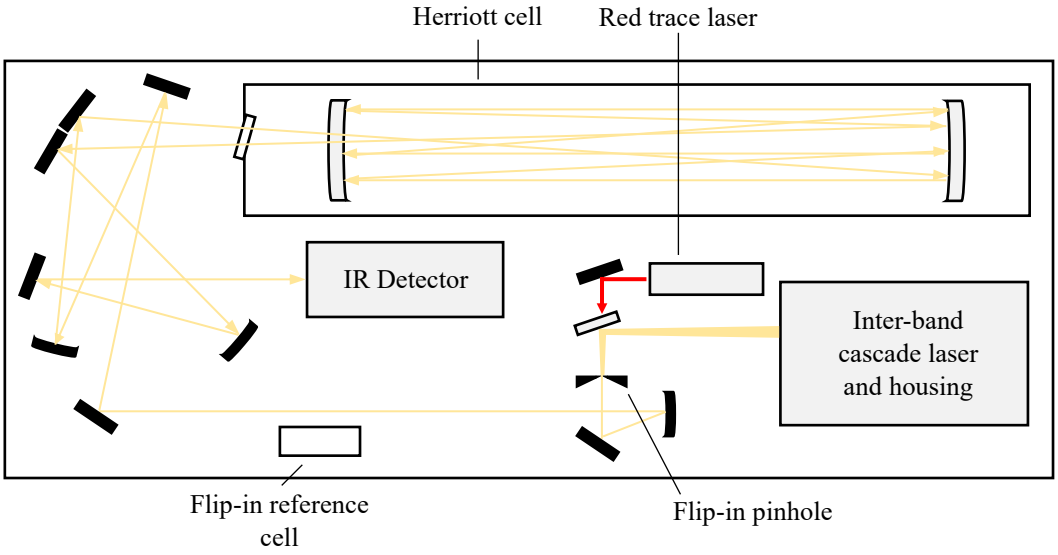

Figure 2.3. Simplified representation of the HCl-TILDAS instrument.

2.4 ISORROPIA II

The thermodynamic equilibrium model ISORROPIA II, developed by Fountoukis and Nenes for the investigation of the $K^+ – Ca^{2+} – Mg^{2+} – NH_4^+ – Na^+ – SO_4^{2-} – NO_3^- – Cl^- – H_2O$ aerosol system,[146] was used to explore the gas-particle partitioning of chloride in chapter 5. The model can be operated in two different modes, denoted as "forward" and "reverse" mode. With respect to the former, the user supplies the total (gas and particulate) concentrations of the aforementioned species, along with RH and temperature, which the model subsequently partitions into the gas and particulate phase under the assumption of thermodynamic equilibrium within the system. By contrast, in reverse mode, the same calculations are conducted although only the particulate concentration of the investigated species is supplied. To achieve this, the model must first identify the major species that are potentially present within the system and thereby the equilibrium reactions of interest. In this work, the model was initiated without crustal species (Ca^{2+}, K^+, Mg^{2+}). As a result, identification of species of interest was achieved through the calculation of the following two ratios:

$$R_{SO_4} = \frac{[Na^+] + [NH_4^+]}{[SO_4^{2-}]} \qquad \text{(Equation 2.5)}$$

$$R_{Na} = \frac{[Na^+]}{[SO_4^{2-}]} \qquad \text{(Equation 2.6)}$$

where:

- [X] denotes the concentration of an aerosol precursor X (mol m^{-3} of air)
- R_{SO_4} is the SO_4^{2-} ratio
- R_{Na} is the Na ratio

The values of R_{SO_4} and R_{Na} are used by ISORROPIA in order to classify the type of aerosol system which is being modelled. In instances in which $R_{SO_4} < 1$, the system is defined as being SO_4^{2-} rich, with some of this SO_4^{2-} existing in the form of free H_2SO_4. Whilst the system is still classified as being SO_4^{2-} rich when $1 \leq R_{SO_4} < 2$, there is enough NH_3 and Na present to partially neutralise the SO_4^{2-} which prevents the formation of H_2SO_4 within the model. Once $R_{SO_4} \geq 2$, there is sufficient NH_3 and Na present to fully neutralise the SO_4^{2-} leading to the system being classified as SO_4^{2-} poor. Such systems are then further classified as being Na rich or poor. The former arises when $R_{Na} \geq 2$ and indicates that there is sufficient Na to fully neutralise the SO_4^{2-}. In such instances excess NH_3 and Na can react with the other gaseous species within the system (HCl and HNO_3) to form salts, whilst no $(NH_4)_2SO_4$ is predicted. By contrast, the system is classified as Na poor when $R_{Na} < 2$, indicating that both NH_3 and Na are required to neutralise the SO_4^{2-}. It therefore follows that only excess NH_3 is available to react with the other gasses within the system. Table 2.1 summarises the possible species for each regime.

Table 2.1. Summary of the four aerosol types and the associated possible species predicted by ISORROPIA II when initialised without crustal species.[147]

SO_4^{2-} ratio	Na ratio	Aerosol type	Solid species	Aqueous Ions	Gases
$R_{SO_4} < 1$	Any value	SO_4^{2-} rich (free HNO_3)	$NaHSO_4$, NH_4HSO_4	Na^+, NH_4^+, H^+, HSO_4^-, SO_4^{2-}, NO_3^-, Cl^-	HNO_3, HCl, H_2O
$1 \leq R_{SO_4} < 2$	Any value	SO_4^{2-} rich	$NaHSO_4$, NH_4HSO_4, Na_2SO_4, $(NH_4)_2SO_4$, $(NH_4)_3H(SO_4)_2$	Na^+, NH_4^+, H^+, HSO_4^-, SO_4^{2-}, NO_3^-, Cl^-	HNO_3, HCl, H_2O
$R_{SO_4} \geq 2$	$R_{Na} < 2$	SO_4^{2-} poor Na poor	Na_2SO_4, $(NH_4)_2SO_4$, NH_4NO_3, NH_4Cl	Na^+, NH_4^+, H^+, HSO_4^-, SO_4^{2-}, NO_3^-, Cl^-	HNO_3, HCl, NH_3, H_2O
$R_{SO_4} \geq 2$	$R_{Na} \geq 2$	SO_4^{2-} poor Na rich	Na_2SO_4, $NaNO_3$, NaCl, NH_4NO_3, NH_4Cl	Na^+, NH_4^+, H^+, HSO_4^-, SO_4^{2-}, NO_3^-, Cl^-	HNO_3, HCl, NH_3, H_2O

Below the mutual deliquescence relative humidity (MDRH) of an aerosol system, the point it which all salts are simultaneously saturated, the particulate phase can be considered a solid. In instances in which the RH over a wet particle is decreasing, it is, however, possible for the wet aerosol to not undergo crystallisation below the MDRH. In such an instance, the aerosol can be considered to exist in a metastable state in which it consists of an aqueous supersaturated solution. Both scenarios can

be simulated by the user by initiating the model in either “stable” or “metastable” mode, providing an additional constraint on the potential species within the system.

Once the species of relevance have been identified, the model then calculates the relevant equilibrium reaction constants as expressed by equation 2.7:

$$K(T) = K_0 \exp\left[-\frac{\Delta H^0(T_0)}{RT_0}\left(\frac{T_0}{T} - 1\right) - \frac{\Delta c_p^0}{R}\left(1 + ln\left(\frac{T_0}{T}\right) - \frac{T_0}{T}\right)\right] \qquad \text{(Equation 2.7)}$$

where:

- K is the equilibrium constant
- T is the temperature of the system
- T_0 is the reference temperature (typically 298.15 K)
- K_0 is the equilibrium constant at T_0
- $\Delta H^0(T_0)$ is the standard enthalpy change at T_0
- Δc_p^0 is the change of heat capacity at T_0
- R is the ideal gas constant

By combining the resulting equilibrium reaction constants with the calculated activity coefficients and water activity (equivalent to ambient RH), and maintaining electroneutrality and mass conservation within the system, the equilibrium concentrations of the investigated species in the gas, solid and liquid phase are obtained.

Chapter 3

Development of a Cl-CRM Instrument

3.1 Introduction

3.1.1 Importance of Measuring Cl Loss Rates

To fully understand tropospheric Cl chemistry an understanding of Cl-atom sinks, and thus loss rates, is required alongside an understanding of its sources; with the accuracy of atmospheric chemistry models dependent on how well these two terms and their associated reaction mechanisms can be represented. In comparison to OH, of which global mean concentrations are estimated to be 0.7 – 1.5 × 10^6 molecules cm^{-3},[22] estimations of Cl-atom concentrations span over two orders of magnitude (10^2 – 10^4 atoms cm^{-3})[23-27] making it difficult to assess its importance as a tropospheric oxidant. In part, such a large degree of uncertainty in this concentration arises from the large spatial variability in the concentration of reservoir species, with Cl-atom concentrations highest in polluted coastal environments owing to elevated levels of SSA, NO_x and acidic gases. By contrast, O_3 concentrations, whilst still displaying some spatial variability, is typically more abundant than chlorine reservoir species leading to a narrower range in the global mean OH concentration. A further factor which contributes to the increased uncertainty in the concentration of Cl-atoms is a lack of field observations, as there is currently no observational technique that will enable direct measurement of the low levels of Cl-atoms within the troposphere to be recorded. As a result of the short atmospheric lifetime of the radical however, the concentration of Cl-atoms can be considered to exist within steady state, as previously described in chapter 1, such that:

$$\frac{d[Cl]}{dt} = \Sigma P_{Cl} - k'_{Cl}[Cl] = 0 \qquad \text{(Equation 1.1)}$$

where:

- ΣP_{Cl} is the total rate of Cl-atom production,
- k'_{Cl} is the total loss rate of Cl-atoms,
- [Cl] is the concentration of Cl at steady-state.

Therefore the simultaneous deployment of instruments capable of measuring both Cl sources and sinks would provide a means by which atomic Cl concentrations can be determined within the field, providing a significant improvement on our estimation of localised concentrations and overcoming the need for a direct measurement technique.

In addition to the above, the measurement of Cl loss rates also offers insight into the widely reported difference between the measured and expected OH reactivity that has been published within the literature.[113, 148-153] Typically this 'missing' reactivity has been made up to account for 40-50% of the measured OH loss rate, with Figure 3.1 outlining the typical contributing factors to OH reactivity as obtained by Dolgorouky *et al* in Paris.[113] The source of this missing reactivity is uncertain, with some studies suggesting it is the result of missing emissions of temperature dependent biogenic volatile organic compounds (BVOCs) and others suggesting it is through reaction with oxidation products of

known VOCs, with the uncertainty reduced when modelled oxidation products are considered. Due to the differing reactivities of OH and Cl with different classes of VOC, for example the increased reactivity of Cl towards alkanes,[36] the simultaneous deployment of an OH and Cl reactivity instrument would allow the missing reactivities of both radicals to be compared. Such an intercomparison would therefore provide a useful constraint to diagnose the type of compound(s) that are not currently being accounted for.

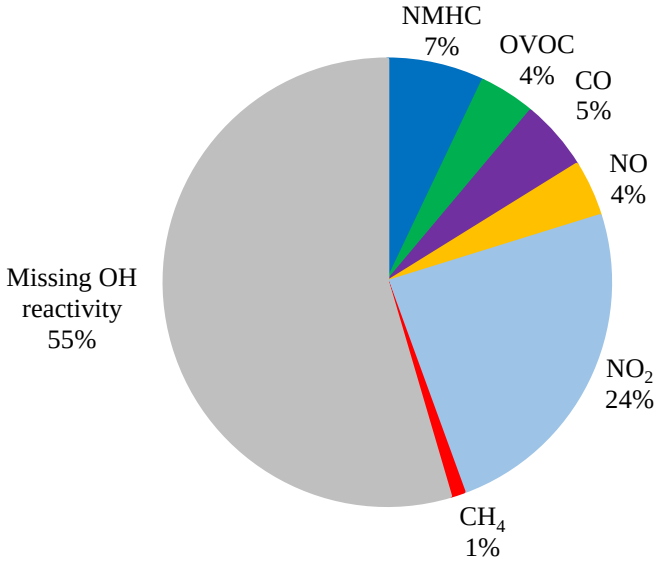

Figure 3.1. Contribution of the 'missing' reactivity fraction on the total measured OH reactivity during the 2010 MEGAPOLI winter campaign, Paris.[113]

3.1.2 Comparative Reactivity Measurements

Whilst the direct measurement of sink species is possible using existing techniques, the measurement of radical loss rates to calculate the total Cl-atom sink is more challenging. As discussed in chapter 1 however, methods have previously been developed to measure the total OH reactivity and generally fall into one of two categories:

- The concentration of OH is measured at different time intervals following reaction with trace species present in ambient air using a suitable detection method such as LIF.[149, 150] From the resulting exponential decay in the concentration of OH, a reactivity rate can be calculated.

- The concentration of a reference VOC, a compound introduced into the system which is not naturally abundant, is monitored following its reaction with OH. By modulating between ambient and zero air flows through the system, an ambient OH reactivity rate can be calculated.[113, 129, 151, 152]

Whilst the use of resonance fluorescence to monitor the decay of Cl is possible, such a technique would require high levels of Cl-atoms to be generated and would therefore either require a highly

efficient method for generating Cl, or high concentrations of the precursor species from which it is formed. Furthermore, such an approach would be difficult to conduct in air owing to both O_2 and H_2O absorbing vacuum ultraviolet (VUV) light within the range required to excite Cl-atoms (133-138 nm).[154] These factors, coupled with the difficulties in making the resonance fluorescence lamp associated with the measurements, mean that the use of the CRM technique is preferred. It should be noted, however, that this approach is not without its own disadvantages. One such issue, as discussed in chapter 1, is the potential for interference from secondary radical species that may react with the reference compound or with Cl itself. To ascertain just how significant such secondary chemistry may be on the calculated reactivity rate, the development of box models to simulate the proposed Cl-CRM instrument would be required. Another disadvantage of the technique is the difficulty to conduct such measurements under kinetically-controlled pseudo-first order conditions, in which the concentration of the monitored VOC is in large excess of the Cl-atoms. Deviation from such conditions has been reported to result in significant systematic error at low reactivity, resulting in non-linear responses.[129] Using low concentrations of Cl would, however, make it difficult to measure a depletion in the reference compound. By contrast, using higher concentrations of Cl would require elevated concentrations of the reference VOC to be used which may pose detection issues in itself. As such, box model simulations will also be required in order to identify the ideal [reference VOC] : [Cl] ratio for use in this work and any necessary correction factors which may need to be applied to the measured reactivity rate.

3.1.3 Chapter Objectives

Adopting a similar approach to the work conducted by Sinha *et al.*, the work presented in this chapter outlines the development stages of a Cl-CRM instrument for the measurement of the total Cl loss rate.[129] Previous work conducted by Boothroyd *et al.* had led to the development of a radiofrequency plasma Cl-atom source which utilised Cl_2 as precursor species.[155] It was found, however, that this method of generating Cl-atoms also resulted in the formation of additional radicals such as OH, O and NO from impurities present in Cl_2 cylinders. As discussed earlier, such radicals have the potential to interfere with the calculated reactivity rate, either by directly reacting with the reference VOC, or by out-competing Cl for reaction with species present in ambient air. It therefore follows that such a source of Cl-atoms would not be suitable for use in the proposed Cl-CRM instrument. Consequently, this chapter will explore the suitability of several different Cl-atom sources that could be used instead. Once a suitable precursor has been identified, characterisation of the resulting CRM instrument will then be achieved by comparing measured reactivity rates of a single VOC species against rates derived from the literature rate coefficients.

3.2 Methods

3.2.1 Comparative Reactivity Measurements

As has briefly been discussed earlier in this chapter and in chapter 1, the CRM technique is similar in principle to a relative rate experiment. Reactivity measurements are deduced based upon observed changes in the concentration of a reference VOC, herein referred to as compound X, as opposed to the concentration of the radical species of interest. As such, no optical techniques (e.g. LIF) are required to directly measure the concentration of Cl. The process of a rate measurement through this technique can be broken down into three stages which are outlined in Figure 3.2. Initially, compound X is introduced into a reactor in a flow of zero air, with the concentration of the species monitored from the outgoing airflow. Once this initial concentration is well established, Cl-atoms are then generated and introduced into the reactor, leading to an observed depletion in the concentration of X following the reaction of the two species. Assuming that no other radical species are generated during this process, the change in concentration of X should be equivalent to the concentration of Cl-atoms within the reactor. In the final stage, the zero air flow through the reactor is switched to ambient air. Such a switch introduces new trace species into the reactor which can compete with X for reaction with the limited Cl-atoms, leading to an increase in the concentration of X.

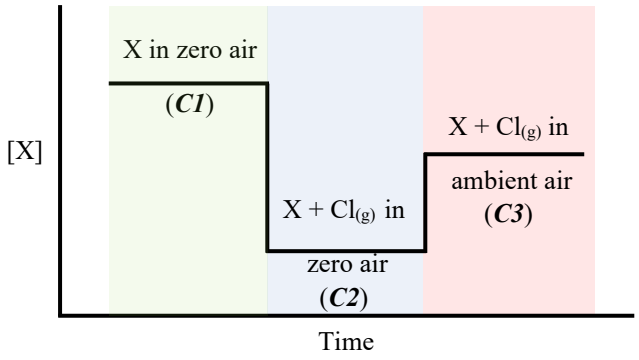

Figure 3.2. Schematic representation of the concept of rate measurement process of the CRM technique where X denotes a reference VOC.

By monitoring the changes in the concentration of compound X at each stage of the measurement process, an expression can be derived for the total reactivity of Cl with the trace gases present in the ambient air sample ($R_{ambient}$). A derivation of how this calculation can be achieved is given below. In the subsequent equations, ***C1*** denotes the initial concentration of compound X, ***C2*** represents the concentration of X upon reaction with $Cl_{(g)}$ in zero air, and ***C3*** represents the concentration of X following reaction with $Cl_{(g)}$ in ambient air.

During the measurement, there are two competing Cl initiated reactions to consider:

$$Cl_{(g)} + X_{(g)} \rightarrow \text{products} \qquad \text{(Reaction 3.1)}$$

$$Cl_{(g)} + \text{ambient} \rightarrow \text{products} \qquad \text{(Reaction 3.2)}$$

From these reactions the following rate expression can be drawn:

$$-\delta[Cl_{(g)}]/dt = k_X [Cl_{(g)}] [X] + R_{ambient} [Cl_{(g)}] \quad \text{(Equation 3.2)}$$

where:

- k_X represents the rate coefficient for the reaction of $Cl_{(g)}$ with X,
- $R_{ambient}$ is the sum of all k_{VOC} [VOC] terms for the ambient air sample.

Assuming that [X] >> $[Cl_{(g)}]$, the reactions can be treated as pseudo first-order. As a result the rate coefficients for the reaction of $Cl_{(g)}$ with X is given as $R_X = k_X [X]$.

If all of the $Cl_{(g)}$ is consumed via reaction with X and the trace species present in the air sample, the change in concentration of X (***C1*** – ***C3***) can be approximated as:

$$(\boldsymbol{C1} - \boldsymbol{C3}) = \frac{R_X}{R_X + R_{ambient}} \times [Cl_{(g)}] \qquad \text{(Equation 3.3)}$$

As change in concentration of X from the ***C1*** to ***C2*** stage is equivalent to the concentration of Cl-atoms generated within the system, ***C1*** – ***C2*** can be used in place of $[Cl_{(g)}]$. Substitution of this yields equation 3.4, from which equation 3.5 can be obtained following rearrangement:

$$(C1 - C3) = \frac{R_X (C1 - C2)}{R_X + R_{ambient}} \qquad \text{(Equation 3.4)}$$

$$R_{ambient} = \left\{\frac{(\boldsymbol{C1} - \boldsymbol{C2})}{(\boldsymbol{C1} - \boldsymbol{C3})} - 1\right\} \times R_X \qquad \text{(Equation 3.5)}$$

Since ***C1*** is the initial concentration of X, this is equivalent to equation 1.3 which will be used herein to derive the measured reactivity rates.

$$R_{ambient} = \frac{(\boldsymbol{C3} - \boldsymbol{C2})}{(\boldsymbol{C1} - \boldsymbol{C3})} \times k_X \boldsymbol{C1} \qquad \text{(Equation 1.3)}$$

3.2.2 Box Model Simulations

Zero-dimensional box models were used to simulate the chemical reactions occurring within the Cl-CRM reactor. Model development was conducted using the AtChem2 modelling toolkit.[156] Cl-atom initiated oxidation mechanisms of $C_{1\text{-}14}$ alkanes were taken from the Master Chemical Mechanism (MCM, v3.3.1).[157, 158] The MCM contains the near-explicit degradation of 143 primary emitted VOCs in the troposphere, resulting in 17,500 reactions and 6,900 species. Rate coefficients used within the mechanism are obtained, where possible, through available experimental measurements.[159, 160] In instances where such kinetic data is unavailable, rate coefficients are estimated using structural activity relationships.[161]

For other functionalities of interest, primary reactions were obtained from a variety of sources which were combined, where possible, with the breakdown chemistry of secondary products as described by the MCM. Several inorganic reactions identified as being of potential importance within the Cl-CRM setup were also incorporated within the models and are given in Table 3.1. All model simulations within this chapter were initialised with a defined concentration of Cl-atoms to mimic radical production prior to the introduction of the reference VOC and sample. Simulations were conducted over a period of 1 second to ensure complete consumption of the Cl-atoms, and to incorporate potential residence within sample lines prior to detection. Models were initialised with the 'roof' closed so as to eliminate any photolytic processes, and a temperature and pressure of 298.15 K and 1013.25 mbar respectively.

Table 3.1. Summary of the inorganic reactions involving atomic Cl and additional reactions considered to be of importance included in the chemical mechanism.

Reaction	k / cm^3 molecules^{-1} s^{-1}	Source
$Cl + O_3 \rightarrow ClO + O_2$	$2.8 \times 10^{-11} \times \exp(-250/T)$	57
$Cl + HO_2 \rightarrow HCl + O_2$	3.5×10^{-11}	57
$Cl + HO_2 \rightarrow ClO + OH$	$7.5 \times 10^{-11} \times \exp(-620/T)$	57
$Cl + H_2O_2 \rightarrow HCl + HO_2$	$1.1 \times 10^{-11} \times \exp(-980/T)$	57
$Cl + NO_3 \rightarrow ClO + NO_2$	2.4×10^{-11}	57
$Cl + ClONO_2 \rightarrow Cl_2 + NO_3$	$1.1 \times 10^{-11} \times \exp(-980/T)$	57

3.2.3 Proton Transfer Reaction Mass Spectrometry

PTR-MS (Ionicon, Austria) was initially utilised for monitoring the reference VOC concentration during the early design stages of the Cl-CRM reactor. A description of the underlying principles of the technique has already been provided in section 2.1 and will therefore not be discussed here. The instrument used in this work consists of a quadrupole mass filter (Pfeiffer Vacuum QMA 400) connected to a secondary electron multiplier (Pfeiffer Vacuum QMA 400), which in turn is coupled to an ion count pre-amplifier (Pfeiffer Vacuum SEM-217) for the detection of reagent and product

ions within the system. Drift tube conditions were maintained at a temperature of 70 °C and a voltage of 590 V throughout the measurement period. A constant 5.5 standard cubic centimetres per minute (sccm) flow of water vapour, controlled by a mass flow controller (MFC), was passed into the ion source to generate the H_3O^+ reagent ions. Such a flow rate was used in order to minimise the formation of $H_3O^+(H_2O)_n$ clusters, which were monitored over the course of the experiments and kept below 1% of the H_3O^+ level. At the start of each measurement, the system was initially left to stabilise for 20 minutes under ambient air. The molecular ion of the reference VOC, $[M+H]^+$, was monitored over the course of the experiment. Product ions were not considered as part of this work.

3.2.4 Selected-Ion Flow Tube Mass Spectrometry

A Voice200 SIFT-MS instrument (Syft Technologies, New Zealand) was used in place of PTR-MS for the measurement of the reference VOC during the later developmental and characterisation stages of the Cl-CRM instrument. A detailed description of the underlying principles of the technique has already been provided in section 2.2. With respect to the operating conditions used in this work, the microwave discharge was held at a pressure of 440 mTorr and a 40 mW current. The flow tube was operated at a temperature of 120 °C, a pressure of 460 mTorr and a voltage of 25 V. All measurements were conducted using a N_2 carrier gas flow. Calibration of the instrument was achieved using a 1 parts per million volume (ppmv) 14-component VOC gas standard (National Physical Laboratory, United Kingdom). These components include: methanol, ethanol, acetonitrile, acetone, isoprene, butanone, 2-butanone, benzene, toluene, m-xylene, 1,2,4-trimethylbenzene, 1,3-butadiene, n-octane, n-nonane, n-decane and n-dodecane.

3.3 Modelling of the Cl-CRM Instrument Conditions

3.3.1 Identification of a Suitable Reference VOC

As outlined by Sinha *et* al.,[129] there are several criteria which a VOC must meet in order to be suitable for use as reference compound in a CRM study. First, it should not be present at detectable levels within ambient air so as to avoid complications during analysis. Secondly, the VOC should have the physical and chemical properties required for easy and accurate detection, in this case by either PTR-MS or SIFT-MS. A well-established rate coefficient for reaction with chlorine is also required. If possible, a preference for reactivity with chlorine over other oxidants, such as OH, would also be favourable so as to avoid interference from any by-products of Cl-atom formation or additional secondary chemistry which may occur within the experimental setup.

In the OH-CRM instrument developed by Sinha *et al.*,[129] pyrrole was used as a reference compound due to its low natural abundance and well known OH-reactivity. An additional benefit of the use of pyrrole is the inclusion of a nitrogen atom within its structure, resulting in an even mass of 68 upon protonation with PTR-MS. As most organic species present in ambient air generate molecular ions with odd masses when protonated, the likelihood of measuring ions isobaric to pyrrole during field

measurements is reduced. The use of pyrrole within this work, however, is not possible as a rate coefficient for its reaction with Cl has not been published in the literature. By extension, there are a limited number of reactivity rate measurements which have been conducted for other nitrogen-containing VOCs. As such, a review of the literature was required in order to identify a suitable candidate for application in the Cl-CRM setup. One group of compounds investigated were deuterated VOCs, with their mass offset when compared to their non-deuterated counterparts reducing the likelihood of measuring an isobaric compound when in the field. OVOCs were also considered during the short-listing process as kinetic studies of their reactivity with Cl is more commonly conducted. Table 3.2 summarises the compounds which were shortlisted based on the above criteria.

Table 3.2. k_{Cl} and k_{OH} (298 K) of potential reference compounds in CRM experiments.

Compound	k_{Cl} / cm^3 molecules^{-1} s^{-1}	k_{OH} / cm^3 molecules^{-1} s^{-1}	$\frac{k_{Cl}}{k_{OH}}$	Reference
Ethanol-1, 1-d$_2$ CH_3CD_2OH	5.35×10^{-11}	1.62×10^{-12}	33	162, 163
2-methylpropane-2-d$_1$ $(CH_3)_3CD$	1.12×10^{-10}	1.37×10^{-12}	82	164, 165
Methanol-d$_3$ CD_3OH	3.80×10^{-11}	4.50×10^{-13}	84	166, 167
Ethanol-OD CH_3CH_2OD	1.13×10^{-10}	3.32×10^{-12}	34	163, 168
Diethyl ether $(C_2H_5)_2O$	2.57×10^{-10}	1.32×10^{-11}	19	169, 170

To determine which of the shortlisted reference compounds would be most suitable, box simulations were conducted in AtChem to determine how accurately the CRM technique could calculate the rate of reactivity when utilising each VOC as the reference compound. C_3H_8 was used within the simulations as a source of Cl reactivity ($k_{Cl} = 1.4 \times 10^{-10}$ cm^3 molecules^{-1} s^{-1}),[15] with its concentration adjusted between runs to give a reactivity range of 50 – 500 s^{-1} (n = 10). Whilst such a range encompasses the expected atmospheric range within polluted environments,[36] the upper limit far exceeds previously reported reactivities and has been chosen to test the upper limits of the CRM technique. Each measurement was repeated at elevated reference VOC concentrations to identify the ideal reference : Cl ratio for use in the experimental setup. Primary chemistry was only considered within the model due to the high uncertainty in the kinetics associated with the subsequent breakdown of secondary products. Furthermore, due to the high reactivity of Cl with C_3H_8 and the reference VOC, it is likely that these primary reactions represent the dominant fate of Cl within the system. As such, it is expected that the absence of secondary chemistry within the model runs is unlikely to have

a significant impact on the calculated reactivity rates under experimental conditions. The resulting model derived reactivity rates were plot against the rates derived from literature rate coefficients, with linear regression analysis conducted to determine the performance of each reference compound. An example of such a plot is given in Figure 3.3 for diethyl ether ($(C_2H_5)_2O$), with a summary of the fitting parameters obtained for all of the investigated reference compounds provided in Table 3.3.

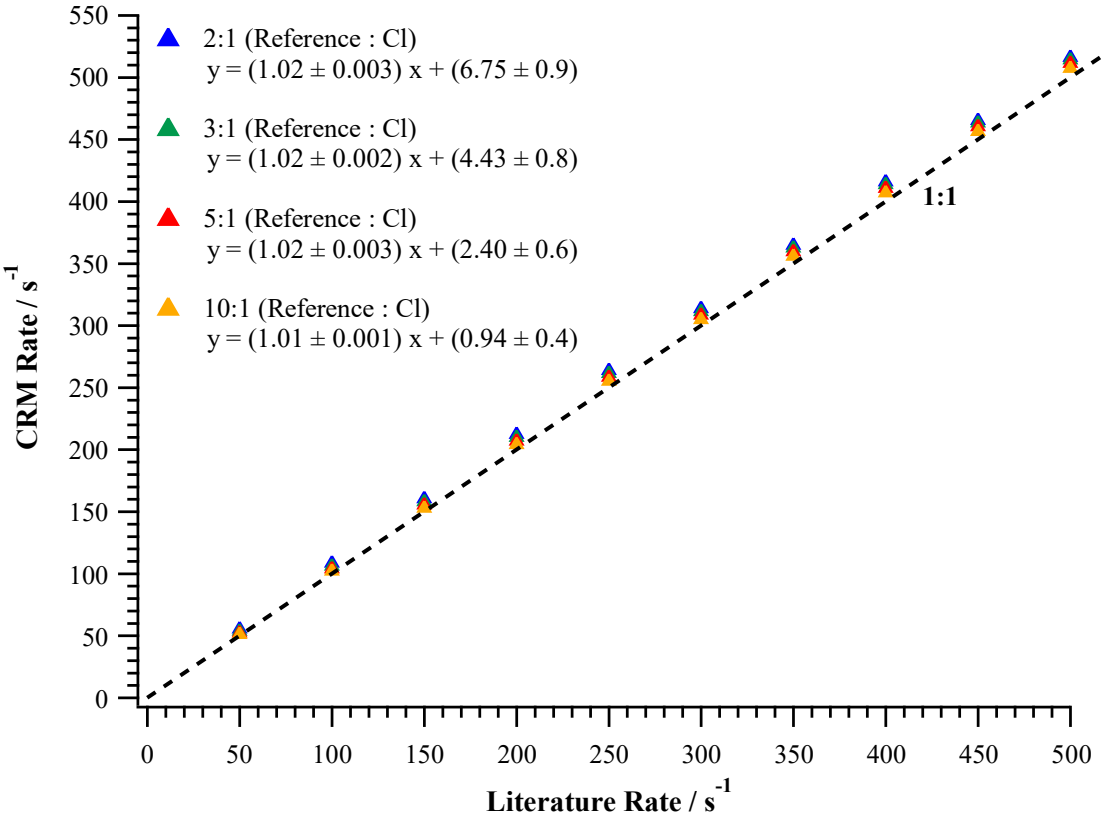

Figure 3.3. Performance of the CRM technique to calculate C_3H_8 reactivity using $(C_2H_5)_2O$ as the reference VOC under various [reference VOC] : [Cl] ratios. Values in the y-axis denote model derived CRM reactivity rates whilst the x-axis represents the calculate rate from literate rate coefficients. The dashed line represents unity between the two variables. conditions.

Table 3.3. Fitting parameters obtained between R_{true} and R_{CRM} based on AtChem simulations of the proposed reference VOCs use in CRM experiments to measure C_3H_8 reactivity. Fitting is of the form y = mx + c.

Compound	X : Cl	m	c
CH_3CD_2OH	2:1	0.990	-10.9
	3:1	0.987	-9.0
	5:1	0.984	-6.6
	10:1	0.982	-3.8
$(CH_3)_3CD$	2:1	0.995	-2.5
	3:1	0.994	-1.9
	5:1	0.994	-1.2
	10:1	0.995	-0.5
CD_3OH	2:1	0.990	-14.3
	3:1	0.987	-12.2
	5:1	0.983	-9.49
	10:1	0.979	-5.93
CH_3CH_2OD	2:1	0.995	-2.4
	3:1	0.994	-1.8
	5:1	0.994	-1.1
	10:1	0.995	-0.5
$(C_2H_5)_2O$	2:1	1.022	+6.7
	3:1	1.022	+4.4
	5:1	1.019	+2.4
	10:1	1.014	+0.9

From the AtChem simulations it is clear that operating the system under pseudo first-order conditions has a significant impact on the accuracy of the CRM rate. This is represented by a reduction in the offset of the y-axis intercepts of the linear fits from the origin as the reference : $Cl_{(g)}$ ratio is increased. Interestingly however, there is no scenario in which a y-axis intercept of 0 is obtained – an intercept that would be expected as there should be no change in the ***C2***/***C3*** concentrations when no additional sources of reactivity are added to the system. This observation occurs despite all of the Cl-atoms generated in the system being consumed in both the ***C2*** and ***C3*** stages. As such, this artefact does not arise as a result of the model being run for an insufficient amount of time. Furthermore, as wall losses are not considered within the simulations they cannot explain the observed discrepancies. Similarly, as the model is initialised with fixed concentration of all three species, issues surrounding mixing are also an unlikely source. It is interesting to note, however, that the use of $(C_2H_5)_2O$ as the reference VOC leads to an overestimation of the C_3H_8 reactivity within the system, as represented by a gradient greater than 1 for the corresponding linear fit. By contrast, all of the other reference VOCs

underestimate this reactivity – indicating that the rate coefficient of the reference VOC relative to the sample may also be important in determining the accuracy of the CRM technique.

3.3.2 Exploring the Literature – CRM Rate Offset

To further explore the modelled discrepancy between the literature derived rate and that obtained using the CRM technique, additional AtChem simulations were conducted utilising $(C_2H_5)_2O$ as the reference VOC. Each model run was initialised with 35 ppbv of $Cl_{(g)}$ (representative of the mixing ratio required to yield a depletion in the reference compound from which discernible changes between the ***C2*** and ***C3*** stage could be measured for a range of reactivities), with the concentration of $(C_2H_5)_2O$ scaled to assess the importance of the [reference VOC] : [Cl] ratio on the magnitude of the discrepancy. Simulations were initially conducted using C_3H_8 as a gas standard and then repeated with isoprene (C_5H_8) to explore the relationship between the sample and reference VOC rate coefficients on the nature of the discrepancy. The results of these simulations are presented in Figure 3.4(a). Whilst it is clear that deviation from pseudo first-order conditions plays a part in the observed offset, it is interesting to note that even under a regime in which the concentration of the reference VOC is two orders of magnitude greater than that of $Cl_{(g)}$, a discrepancy between the two rates is still observed. As such it is clear that non-pseudo first-order conditions are not the sole contributor to this artefact. It is also interesting to note that the CRM technique leads to an overestimation of the rate for C_3H_8, yet underestimates the rate of reaction for C_5H_8 despite both VOCs being initialised with concentrations that yield comparable reactivities (343.47 and 312.43 s^{-1}). Such an observation would suggest that in instances in which the rate coefficient of the sample gas is greater than that of the reference VOC, as is the case with C_5H_8 in these models ($k_{Cl} = 4.07 \times 10^{-10}$ cm^3 $molecules^{-1}$ s^{-1}), the CRM technique underestimates the reactivity rate, whilst the inverse is true when the rate coefficient is lower. This is consistent with the observations reported in Table 3.3 in which all of the potential reference VOCs (other than $(C_2H_5)_2O$) had rate coefficients lower than that of C_3H_8 and resulted in an underestimation of the rate when applying the CRM calculation, as reflected by gradients lower than 1. To probe whether this was an artefact specific to the CRM technique or to relative rate measurements as a whole, the results obtained from the C_3H_8 simulations were then analysed using the relative rate formula:

$$\ln\frac{[\text{Sample}]_t}{[\text{Sample}]_{t=0}} = \frac{k_a}{k_b}\ln\frac{[\text{Reference}]_t}{[\text{Reference}]_{t=0}} \qquad \text{(Equation 3.6)}$$

Where:

- $[Sample]_{t=0}$ and $[Sample]_t$ are the concentrations of the sample at the start and end of the measurement
- $[Reference]_{t=0}$ and $[Reference]_t$ are the concentrations of the reference VOC at the start and end of the measurement

- k_a and k_b are the rate coefficients for the reaction of the sample and the reference VOC with Cl respectively

As depicted in Figure 3.4(b), the rate obtained using equation 3.6 was in good agreement with that obtained from the literature rate coefficients across the range of [reference VOC] : [Cl] ratios investigated, indicating that this discrepancy must arise from one of the assumptions of the CRM calculation.

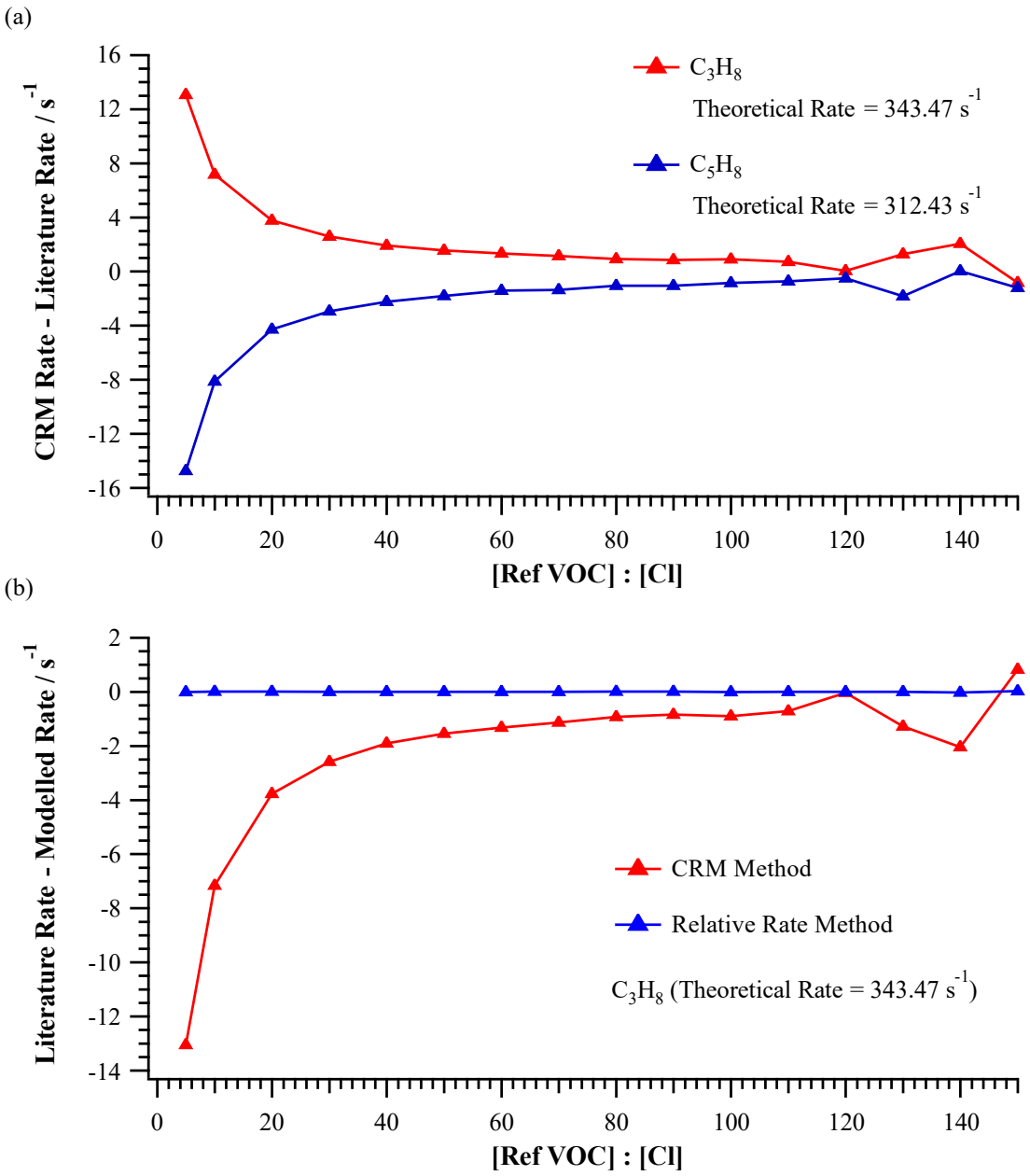

Figure 3.4. (a) Discrepancy between the CRM and literature derived rates for the reaction of Cl with C_3H_8 and C_5H_8 using $(C_2H_5)_2O$ as a reference VOC. (b) Comparison of the performance of the CRM to the relative rate technique in calculating the reactivity rate for C_3H_8.

To explore if this discrepancy arises solely from the difference in rate coefficients of the sample and the reference VOC, or if it is due to the difference in reaction rates, several simulations were conducted in which both species were set to react with $Cl_{(g)}$ at equal rates. In each simulation, the rate coefficient for the reaction of the sample VOC was adjusted to investigate the impact of k_{sample} : $k_{reference}$ on the CRM derived rate, with the concentration of the sample adjusted to ensure the theoretical rate of reaction was consistent between runs. Each model run was again initialised with 35 ppbv of $Cl_{(g)}$ and 175 ppbv of $(C_2H_5)_2O$ to yield a reference VOC : Cl ratio of 5:1. As can be seen in Figure 3.5, the discrepancy between the CRM derived rate and the literature rate follows a strong linear relationship. In instances in which the rate coefficient of the sample was lower than that of $(C_2H_5)_2O$, an overestimation of the rate was obtained – as observed during the simulations with C_3H_8. Interestingly, in the instance in which both species had the same rate coefficient, there was no discrepancy observed between the literature and the CRM rate. Such an observation indicates that the rate of change in the concentration of the two species plays a key role in determining the magnitude of difference between the theoretical and CRM derived rates.

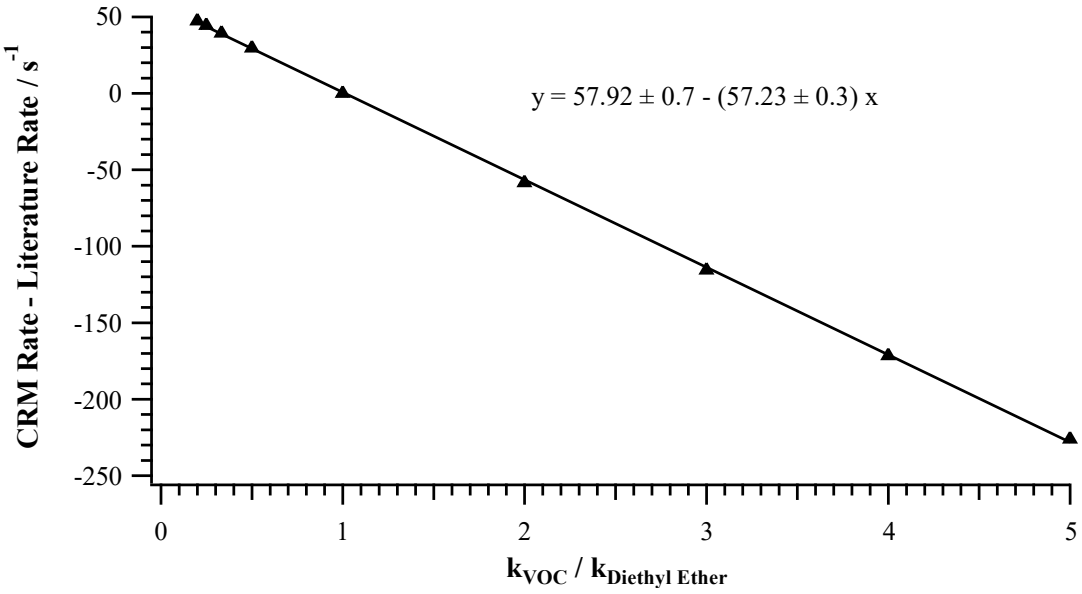

Figure 3.5. Discrepancy between the CRM and literature derived rates as a function of the ratio of the sample and $(C_2H_5)_2O$ rate coefficients of reaction with Cl.

To probe this further, the concentration of both the reference VOC and the sample of interest were kept constant over the course of subsequent model simulations. In order to determine the corresponding ***C3*** concentration, the concentration of a tracer compound (added to the mechanism as a product of the reaction between $(C_2H_5)_2O$ and Cl) was subtracted from the concentration of $(C_2H_5)_2O$. Under these conditions, the CRM calculated rate was found to be in agreement with the literature within the precision error of the model output. Consequently, it can be deduced that the change in concentration of both the reference VOC and the sample over the measurement period is

the source of the observed discrepancy. For example, in instances in which the sample has a lower rate coefficient than the reference VOC, the concentration of the reference compound initially decreases at a greater rate. Overtime, this results in the rate of reaction of Cl with the reference compound decreasing. Consequently, the difference in reactivity between the reference VOC and the sample decreases, resulting in in a larger proportion of the Cl-atoms reacting with the sample then at the start of the reaction. This ultimately results in a ***C3*** concentration which is larger than expected, leading to the overestimation of the reaction rate within the system as has been observed above. By contrast, the inverse is true in instances in which the rate coefficient of the sample is greater than the reference VOC. Such an artefact is not observed in conventional relative rate experiments as the concentration of both the reference and sample are required to derive the reactivity rate. It therefore follows that a correction factor would be required both to account for this artefact and the operation of the CRM instrument under non-pseudo first-order conditions.

Based on this modelled discrepancy, both CH_3CD_2OH and CD_3OH were disregarded as potential reference compounds from the shortlisted candidates giving in Table 3.3 owing to their low rate coefficient of reaction with Cl, and therefore increased likelihood for larger correction factors to be required if they were used in the CRM setup. $(CH_3)_3CD$ was also ruled out due to limited commercial availability, with CH_3CH_2OD favoured over $(C_2H_5)_2O$ as a result of its higher ratio of k_{Cl} : k_{OH}. Unfortunately, attempts to detect CH_3CH_2OD via PTR-MS, and later SIFT-MS, proved unsuccessful. As a result, $(C_2H_5)_2O$ was used as the reference compound in this study.

3.3.3 Modelling of Different Atmospheric Regimes

To probe the suitability of the CRM technique for measuring the Cl-reactivity with ambient air, AtChem simulations were conducted using recorded VOC concentrations at the Cape Verde Atmospheric Observatory site and London during the ClearfLo campaign conducted between 22 July and 18 August 2012.[171, 172] The sites were chosen as part of this investigation as they represent two different atmospheric regimes; Cape Verde represents a clean air environment situated within the MBL, whilst London represents a polluted mainland environment. A breakdown of the constraints used for each environment is given in Table 3.4.

Table 3.4. Summary of the VOC concentrations and associated rate coefficients used during the simulation of the CRM technique in London during the 2012 ClearfLo campaign and Cape Verde. *The rate coefficient used for C_5H_8 is an average of reported values of the R and S enantiomers.

Species	Clearflo – Mean Concentration SW flow / ppbv	Clearflo – Mean Concentration E flow / ppbv	Cape Verde – Mean Concentration (Noon) / ppbv	Rate Constant / cm^3 $molecule^{-1}$ s^{-1} (298 K)	Ref.
Methanol	2.4	5.2	0.749	5.50×10^{-11}	15
Ethanol	2.4	5.7	-	1.00×10^{-10}	15
Propanol	0.3	0.64	-	1.60×10^{-10}	15
Butanol	0.6	0.84	-	2.20×10^{-10}	15
Methane	1853	1903.2	1821	1.00×10^{-13}	15
Ethane	3.1	6.8	0.845	5.80×10^{-11}	MCM
Propane	1.2	2.7	0.05	1.40×10^{-10}	MCM
i-Butane	0.5	1.1	0.0022	1.43×10^{-10}	MCM
n-Butane	1	2.2	0.0039	2.06×10^{-10}	MCM
i-Pentane	0.5	1.2	-	2.20×10^{-10}	MCM
n-Pentane	0.2	0.6	-	2.80×10^{-10}	MCM
n-Hexane	0.3	0.7	-	3.40×10^{-10}	MCM
n-Heptane	0.2	0.4	-	3.90×10^{-10}	MCM
n-Octane	0.1	0.3	-	4.60×10^{-10}	MCM
2-Methyl pentane	0.2	0.3	-	2.90×10^{-10}	MCM
n-Nonane	0.2	0.4	-	4.80×10^{-10}	MCM
n-Decane	0.2	0.4	-	5.55×10^{-10}	MCM
Undecane	0.3	0.7	-	6.17×10^{-10}	MCM
Dodecane	0.6	1.3	-	6.74×10^{-10}	MCM
Dichloromethane	0.03	0.06	-	3.40×10^{-10}	15
Acetylene	0.3	0.5	0.119	4.97×10^{-11}	173
Ethene	0.5	0.9	0.021	1.00×10^{-10}	15
Propene	0.2	0.3	0.022	2.70×10^{-10}	15
Trans-but-2-ene	0.02	0.03	-	3.31×10^{-10}	174
But-1-ene	0.05	0.08	-	3.00×10^{-10}	175
Isobutylene	0.04	0.07	-	3.40×10^{-10}	174
Cis-but-2-ene	0.01	0.02	-	3.76×10^{-10}	174
Pent-1-ene	0.02	0.04	-	3.97×10^{-10}	174
Trichloroethene	0.01	0.02	-	8.70×10^{-11}	176
Benzene	0.12	0.2	-	1.30×10^{-15}	177
Toluene	0.36	0.7	-	5.90×10^{-11}	177

Table 3.4. (continued).

Species	Clearflo – Mean Concentration SW flow / ppbv	Clearflo – Mean Concentration E flow / ppbv	Cape Verde – Mean Concentration / ppbv	Rate Constant / cm^3 $molecule^{-1}$ s^{-1} (298 K)	Ref.
Ethylbenzene	0.06	0.1	-	9.10×10^{-11}	173
1,3-Dimethylbenzene	0.04	0.08	-	1.40×10^{-10}	177
1,4-Dimethylbenzene	0.04	0.08	-	1.50×10^{-10}	177
1,2-Dimethylbenzene	0.05	0.11	-	1.50×10^{-10}	177
1,2,3-Trimethylbezene	0.01	0.01	-	3.60×10^{-10}	173
1,3,5-Trimethylbezene	0.01	0.01	-	3.10×10^{-10}	173
1,2,4-Trimethylbezene	0.02	0.03	-	3.60×10^{-10}	173
Phenylethene	0.02	0.05	-	3.60×10^{-10}	177
Propylbenzene	0.03	0.09	-	7.50×10^{-11}	173
3-Ethyltoluene	0.01	0.02	-	1.40×10^{-10}	173
4-Ethyltoluene	0.01	0.02	-	2.20×10^{-10}	173
2-Ethyltoluene	0.01	0.01	-	1.10×10^{-10}	173
Benzaldehyde	0.01	0.01	-	7.66×10^{-11}	173
α-Pinene*	0.12	0.2	-	4.70×10^{-10}	178
Limonene	0.04	0.07	-	6.40×10^{-10}	178
Formaldehyde	6.7	13.8	0.328	7.20×10^{-11}	15
Acetaldehyde	3.3	6.6	0.826	8.00×10^{-11}	15
Acetone	2	3.4	0.487	2.10×10^{-12}	15
Methacrolein	0.02	0.03	-	2.20×10^{-10}	179
Methyl vinyl ketone	0.02	0.04	-	2.10×10^{-10}	179
2-Methylpropanol	0.04	0.06	-	1.51×10^{-10}	173
Acetic acid	0.04	0.06	-	2.65×10^{-14}	15
Butanone	0.05	0.08	-	4.00×10^{-11}	15
n-Butanal	0.01	0.02	-	1.44×10^{-10}	173
2-Pentanone	0.02	0.04	-	1.17×10^{-10}	173
n-Pentanal	0.02	0.03	-	1.72×10^{-10}	173
4-Methyl-2-pentanone	0.04	0.07	-	3.40×10^{-10}	173
Hexan-2-one	0.03	0.05	-	2.18×10^{-10}	173
Cyclohexanone	0.01	0.02	-	1.30×10^{-10}	173
1,3-Butadiene	0.01	0.02	-	3.20×10^{-10}	180
Isoprene	0.1	0.2	0.01	4.07×10^{-10}	179

As with the simulations conducted in section 3.3.2, the models were initialised with 35 ppbv of $Cl_{(g)}$ and 175 ppbv of $(C_2H_5)_2O$ to yield a reference VOC : Cl ratio of 5 : 1 – representative of the proposed CRM operating conditions for this work. In order to derive a correction factor to account for the aforementioned systematic interferences, initial simulations were conducted in which only primary reactions between the measured VOCs and Cl were considered. The reaction of Cl with O_3 (for which average concentrations of 37.9 and 24.2 ppbv were reported in the E and SW airflows during the ClearfLo campaign and 35 ppbv in Cape Verde) was also included in these initial simulations to account for a further sink mechanism of tropospheric Cl-atoms. To ascertain the potential importance of secondary chemistry within the reactor, in particular the formation of OH as a result of the reaction between O_3 and HO_2 (reaction 3.3), full breakdown mechanisms of the VOCs, including their reactions with OH, and the inorganic reactions listed in Table 3.1 were subsequently incorporated into the model where possible. Simulations were finally repeated using measured NO concentrations for each site since its reactions with HO_2, as described by reaction 1.22, presents a potential additional source of OH within the reactor.

$$HO_2 + O_3 \rightarrow OH + 2\,O_2 \qquad \text{(Reaction 3.3)}$$

A summary of the CRM rates calculated for the two locations is given in Table 3.5.

Table 3.5. CRM derived Cl reactivity rates at the Cape Verde Atmospheric Observatory and North Kensington, London during the 2012 ClearfLo campaign. 1° and 2° denote the inclusion of primary and secondary chemistry within the model respectively.

Location	Conditions	CRM Rate / s^{-1}	Literature Derived Rate / s^{-1}
ClearfLo, London	1° Only	104.67	100.69
(SW flow)	2° (no NO)	104.69	100.69
	2° (NO included)	103.35	100.69
ClearfLo, London	1° Only	205.57	202.89
(E flow)	2° (no NO)	205.55	202.89
	2° (NO included)	200.49	202.89
Cape Verde	1° Only	21.41	20.16
	2° (no NO)	20.75	20.16
	2° (NO included)	20.68	20.16

In comparison to the literature derived rates, the proposed operating conditions of the CRM instrument, and the use of $(C_2H_5)_2O$ as a reference VOC, were simulated to result in a ~ 3 and 6% overestimation of the Cl reactivity rate at the Cape Verde and ClearfLo sites respectively. Consequently, it is proposed that unless detailed VOC measurements are made during the field deployment of the CRM instrument which would enable the systematic error to be identified through

similar box model simulations, a standard correction factor of 4.5% should be applied to the measured reactivity rate to account for these measurement artefacts. In the absence of NO, as hypothesised in section 3.3.1, the addition of secondary chemistry within the model had little impact on the calculated rate, with the additional losses of $(C_2H_5)_2O$ to OH accounting for a maximum 3% decrease in the rate over both environments. The simulations have, however, identified NO as potential sources of interference as has been reported for OH-CRM instruments. For ClearfLo, a consistent decrease in the calculated rate was observed upon initialising each model with NO (5.5 and 2.5 ppbv for the E and SW flow measurements) indicating that the reaction between NO and HO_2 can act as a dominant source of OH radicals within the setup. Furthermore, as reported max noontime concentrations of NO far exceeded the mean concentrations used in these model simulations (33.4 and 11.9 ppbv for the E and SW flow measurements), it is clear that larger interferences are likely during the deployment of the instrument in polluted environments. By contrast, owing to the low reported NO concentrations (2.3 pptv), the interference in the calculated rate for Cape Verde was minor. As such, it is clear that without implementation of methods to mitigate the formation of OH within the system, or the application of a correction factor to account for the formation of OH, the instrument would only be suitable for deployment in low NO_x environments such as marine environments and remote forests.

3.4 Development of a Suitable Cl-atom Source

3.4.1 Thermolysis of Cl_2

Initial development work on the Cl-CRM instrument focused on the thermal dissociation of Cl_2 as a source of Cl-atoms, an approach previously reported by Stevens *et al.* [181] Unfortunately, a detailed description of the experimental setup used in the study was not provided. Consequently, a heated filament was designed following a similar approach to that undertaken by Toohey *et al.* for the thermolysis of Br_2.[182] The resulting experimental setup is given in Figure 3.6. Briefly, a known flow rate of 0.6% Cl_2 in argon was passed through a 2 mm i.d quartz tube containing coiled platinum wire (approximately 20 cm in length with a diameter of 0.008 cm when uncoiled). Acting as a catalyst, the Pt wire provides a surface upon which dissociative adsorption of Cl_2 could occur. Temperatures between 580 – 1100K have previously been reported to yield a mixture of Cl_2 molecules and Cl-atoms through this method, the exact ratio dependent upon the surface structure of the catalyst used.[183, 184] As this was unknown for the Pt wire used in this work, a temperature of 800 °C was utilised, sufficient to achieve a "dull red glow" as observed by Toohey *et al.* in their studies.[182] Heating was achieved by passing an electrical current, equivalent to ~ 4.5 amp, through the Pt wire. After passing over the Pt wire, the resulting mixture of Cl-atoms and Cl_2 was directed into a glass reactor and mixed with $(C_2H_5)_2O$ and zero air / the sample of interest. Changes in the concentration of $(C_2H_5)_2O$ over the course of a measurement were monitored using PTR-MS, with transitions between the ***C1*** and ***C2***/***C3*** state achieved by cycling the heated filament. To ensure that the rate

coefficient used in the CRM calculation for the reaction between $(C_2H_5)_2O$ and Cl was valid, and that the reaction rates calculated for the sample of interest were representative of tropospheric conditions, the glass reactor was held at ambient pressure and temperature.

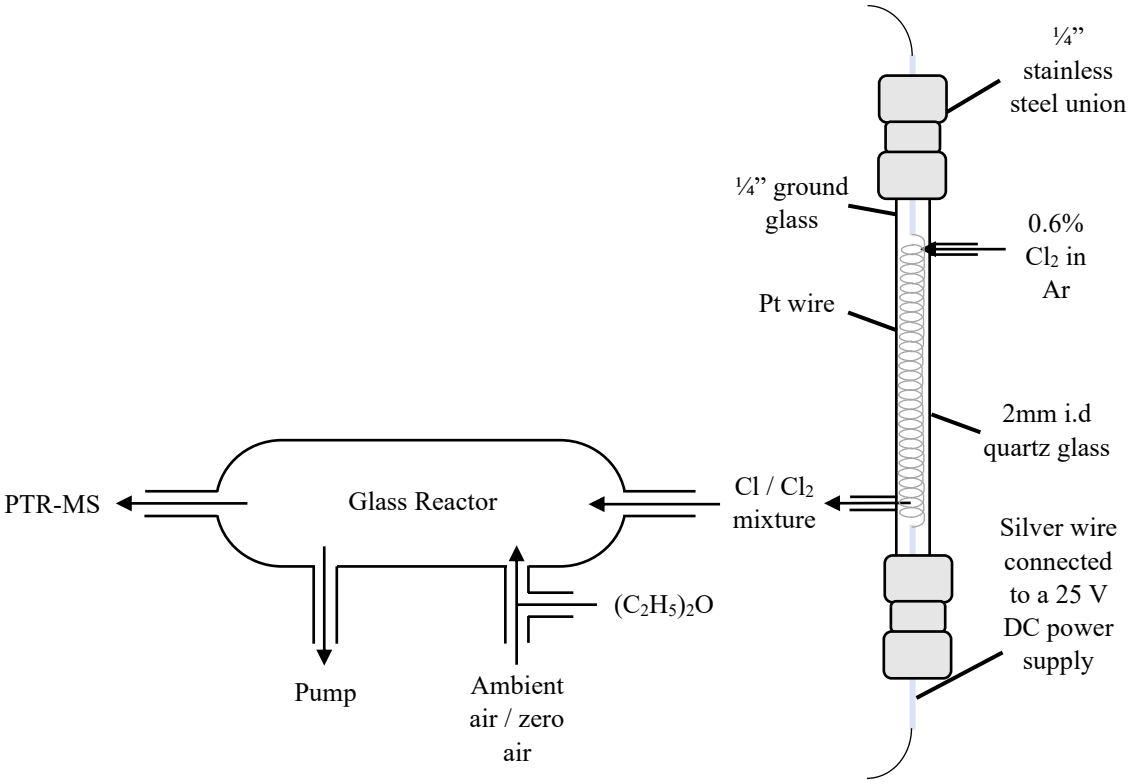

Figure 3.6. Schematic representation of the reactor used for the thermal dissociation of Cl_2.

Unfortunately, no depletion in the $(C_2H_5)_2O$ signal was observed with this setup. Elevated temperatures of the Pt wire were also investigated but proved to be equally unsuccessful. As thermolysis has been proven to be a viable source of Cl-atoms within the literature, one potential reason for the lack of depletion in this work is the recombination of the Cl-atoms prior to introduction into the glass reactor. The kinetics of radical recombination has been extensively reported for chlorine and is summarised below.[185-187] Upon the collision of two Cl-atoms, Cl_2 is initially generated in an energetically excited state as shown in reaction 3.4.

$$Cl + Cl \rightarrow Cl_2^* \qquad k_a \qquad \text{(Reaction 3.4)}$$

After formation, the energetically excited Cl_2^* can either dissociate (reaction 3.5) or transfer its excess energy through collision with another inert molecule, M (reaction 3.6).

$$Cl_2^* \rightarrow Cl + Cl \qquad k_a' \qquad \text{(Reaction 3.5)}$$

$$Cl_2^* (+ M) \rightarrow Cl_2 + M \qquad k_b \qquad \text{(Reaction 3.6)}$$

By applying the steady-state approximation to the formation of Cl_2^*, the rate of formation for the ground state Cl_2 can be expressed as follows:

$$d\frac{d[Cl_2]}{dt} = \frac{k_a\, k_b\, [M]}{k'_a + k_b\, [M]}\,[Cl]^2 \qquad \text{(Equation 3.7)}$$

Under high pressure conditions, as [M] → ∞, collisions between molecules become more frequent resulting in k_b[M] > > k_a'. As such, under these conditions, the reaction follows second-order kinetics and can be expressed as follows:

$$\frac{d[Cl_2]}{dt} = k_a[Cl]^2 \qquad \text{(Equation 3.8)}$$

Under low pressure conditions, as [M] → 0, the inverse is true with the dissociation of Cl_2^* dominating resulting in the following expression:

$$\frac{d[Cl_2]}{dt} = \frac{k_a\, k_b\, [M]}{k'_a}[Cl]^2 \qquad \text{(Equation 3.9)}$$

The rate coefficient of reaction under any pressure can then be calculated using the Lindemann – Hinshelwood equation:[188]

$$k_r = \frac{k_0\, k_\infty}{k_0 + k_\infty} \qquad \text{(Equation 3.10)}$$

Where:

- k_∞ is the high pressure rate limit (k_∞ = k_a)
- k_0 is the low pressure limit ($k_0 = \frac{k_a\, k_b\, [M]}{k'_a}$)

From the high pressure limit, k_∞, the rate coefficient for the recombination of Cl-atoms begins to decrease owing to the reduced third body concentration [M], resulting in a "falloff curve" when k_r is plot against pressure. From measurements reported by Hippler and Troe,[189] it can be inferred that the rate of Cl-atom recombination increases linearly with pressure up to ~ 5 atm. As the experimental setups of Toohey *et al*. and Stevens *et al*. were operated at reduced pressures (1.0 – 3.0 torr and 1.4 – 1.6 torr respectively), the rate of recombination in this work would be at least a factor of 250 greater. It should be noted, however, that neither reported recombination as a loss of Cl-atoms and, as such, it is not possible to conclude whether such an issue would be present in this work.

An alternative reason for the lack of depletion in the reference VOC is the loss of the Cl-atoms to the walls of the heated filament and the glass reactor. To minimise such losses, the moveable injectors used by Toohey *et al*. and Stevens *et al*. were coated with phosphoric acid. Such conditioning of the reactor walls was not carried out in this work, and as such, it is likely that radical losses through this pathway were greater than in the aforementioned studies. Furthermore, as the outlet of the heated

filament is perpendicular to the flow over the Pt wire, it is also anticipated that radical wall loses would have been further enhanced as the generated Cl-atoms transitioned through to the glass reactor.

3.4.2 Photolysis of $(COCl)_2$

3.4.2.1 Reactor Design

Following the unsuccessful attempts to thermally dissociate Cl_2, attention shifted towards alternative sources of Cl-atoms. A review of the literature highlighted that the photolysis of chlorine precursors and the use of a microwave discharge are the two most common methods used to achieve this. Owing to the aforementioned complications experienced in the work by Boothroyd *et al.* however,[155] photolysis was chosen as the most suitable alternative. Various precursors have been used in the literature including Cl_2,[174, 190, 191] trichloroacetyl chloride (CCl_3COCl),[178, 192, 193] oxalyl chloride ($(COCl)_2$)[194-197] and thionyl chloride ($SOCl_2$).[178] As the photolysis of oxalyl chloride (λ = 254 nm) would form two relatively inert CO molecules that could react with any OH radicals present within the system, in addition to two Cl-atoms, it was considered the most suitable precursor of the shortlisted candidates.

Figure 3.7 shows a schematic outline of the PTFE reactor developed to conduct these experiments, with inlets labelled as A, B and C. Due to difficulties in storing $(COCl)_2$ within stainless steel and Silco canisters, delivery of the precursor into the reactor via inlet A was achieved by flushing the headspace of a PFA midget impinger (SKC Inc, United States) containing a solution of 98% $(COCl)_2$ (Sigma Aldrich, United States) with 25 sccm of N_2. Both the $(COCl)_2$ and N_2 carrier gas were kept at a temperature of -5 °C in order to minimise volatilisation, with gravimetric analysis used to determine the amount of gaseous $(COCl)_2$ being introduced into the system. Within the reactor, formation of Cl-atoms was achieved using a 6" pen ray Hg lamp (Analytik Jena, Germany) seated perpendicular to inlet A. Both the reference VOC and the sample of interest were introduced into the reactor downstream through inlet C. The distance of the inlet from the Hg lamp was kept to a minimum in order to minimise the residence time of the Cl-atoms within the reactor prior to reaction and therefore reduce radical losses through recombination. To minimise potential photolytic losses of VOCs present in the sampled air, the reactor was designed in a 'L' shape so that inlet C was offset from the lamp. To compensate for this, and to minimise wall losses of the Cl-atoms, a flow of N_2 was introduced into the reactor via inlet B, directing the air flow towards the sample inlet. Over the course of a measurement, the flow of the N_2 carrier gas was varied to maintain a total flow rate of 500 sccm within the system. All gas carrier lines were plumbed with ¼" PFA tubing (Swagelok, United States), with MFCs (Alicat Scientific, United States) used to ensure that the relevant gas flow rates were constant throughout the measurement period. The outflow from the reactor was connected to a SIFT-MS to monitor changes in the concentration of $(C_2H_5)_2O$.

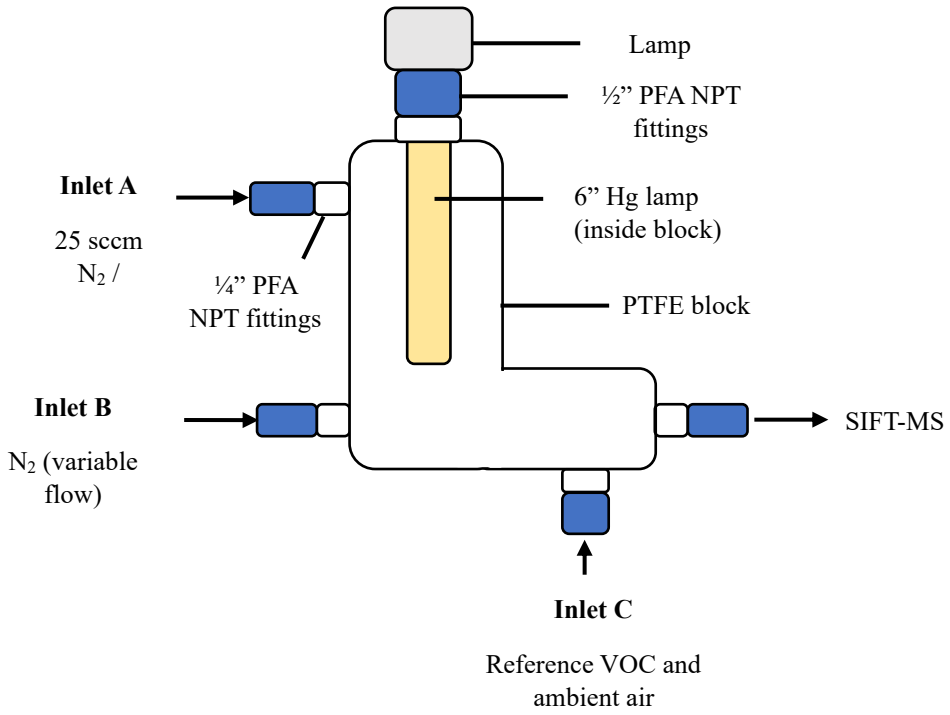

Figure 3.7. Schematic representation of the PFA reactor used for the photolysis of $(COCl)_2$.

Methyl iodide (CH_3I), a species readily photolysed by UV radiation (λ_{max} = 257.7 nm, $\sigma = 1.12 \times 10^{-18}$ cm^2 $molecule^{-1}$ at 298 K) at wavelengths emitted by the Hg lamp, was used to test the effectiveness of the reactor design in minimising losses of photolabile VOCs at the sample inlet (inlet C). To ensure that a depletion in the VOC could be measured, CH_3I was initially introduced into the reactor through inlet A whereupon a ~ 50 ppbv depletion was observed when the Hg lamp was switched on, as depicted in Figure 3.8(a). Upon confirmation of this, the VOC was then introduced into the reactor through inlet C, with N_2 carrier gas flows introduced through inlets A and B to mimic typical experimental conditions. As can be seen in Figure 3.8(b), no depletion in methyl iodide was observed suggesting that photolytic losses at the sample inlet were negligible if present. As trace VOC species present in ambient air samples are unlikely to absorb as strongly as CH_3I at the wavelengths emitted by the Hg lamp, it can be inferred that losses of photolabile VOCs during sampling would be negligible with the design.

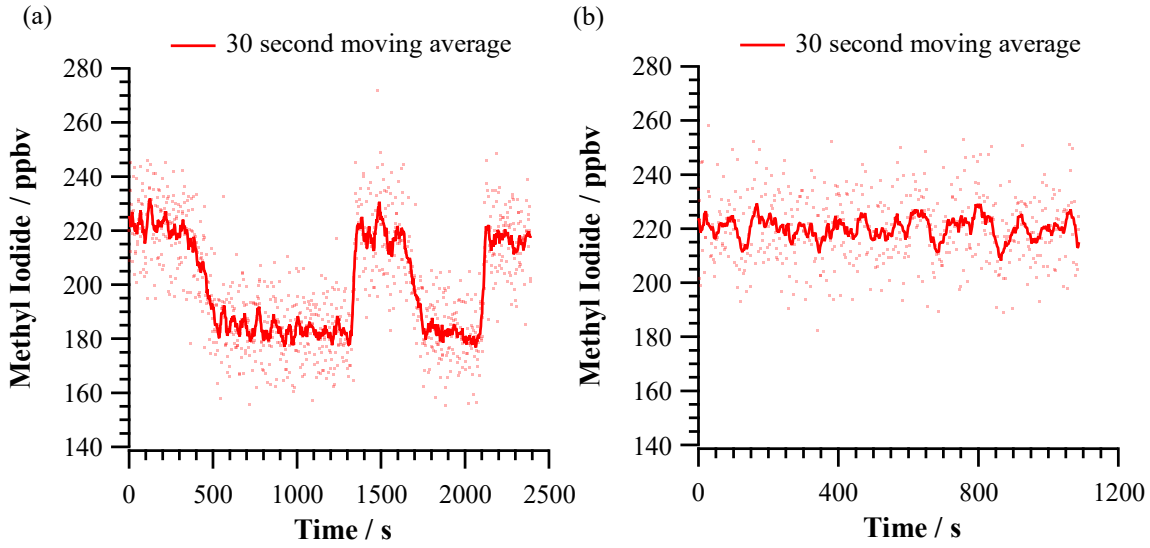

Figure 3.8. (a) Depletion of CH_3I due to photolysis. (b) Measured CH_3I concentration when introduced through the PTFE reactor inlet with the lamp on and off.

3.4.2.2 Instrument Characterisation

Several tests were conducted to assess the suitability of the PTFE reactor, both as a source of Cl-atoms as well as for measuring Cl reactivity rates. A breakdown of these tests is given below.

Photolysis of Diethyl Ether

Although unlikely based upon the CH_3I measurements, initial experiments were focused on calculating any depletion owing to the photolysis of $(C_2H_5)_2O$ (λ_{max} = 188.5 nm)[198] by the Hg lamp so as to determine whether a correction factor would need to be applied to the ***C2*** and ***C3*** concentrations prior to use in the CRM calculation. To achieve this, a constant flow of the reference VOC was introduced into the reactor through inlet A and allowed to pass over the Hg lamp. No deviation from the baseline concentration was observed when the lamp was switched on, indicating that photolytic losses can be disregarded as a potential source of depletion within the setup.

Formation of Cl-atoms and Photolytic Efficiency

Having ruled out photolytic losses, $(C_2H_5)_2O$ was introduced into the reactor via inlet C to determine whether the setup could successfully generate Cl-atoms through the photolysis of $(COCl)_2$ which are sufficiently long-lived that a depletion in the reference VOC could be observed via SIFT-MS. As can be seen in Figure 3.9(a), depletion of $(C_2H_5)_2O$ was observed when the lamp was switched on, indicating that Cl-atoms had been formed and were reacting with the reference VOC. In order for the CRM calculations to be valid however, all of Cl-atoms produced within the setup have to be consumed during the measurement. As such, the concentration of $(C_2H_5)_2O$ was gradually increased over the course of the measurement in Figure 3.9(a) until the level of depletion eventually plateaued.

From these measurements it was deduced that ~20 ppbv of Cl-atoms were available for reaction with the reference VOC and sample of interest upon reaching inlet C. To probe the repeatability of this depletion, a constant flow of $(C_2H_5)_2O$ was introduced into the reactor with the lamp switched on and off. As can be seen in Figure 3.9(b), whilst the concentration of $(C_2H_5)_2O$ gradually decreased over the course of the measurement, the absolute change in the concentration upon turning on the Hg lamp was found to be constant, indicating that the light source would provide a consistent level of Cl-atoms over the course of a measurement.

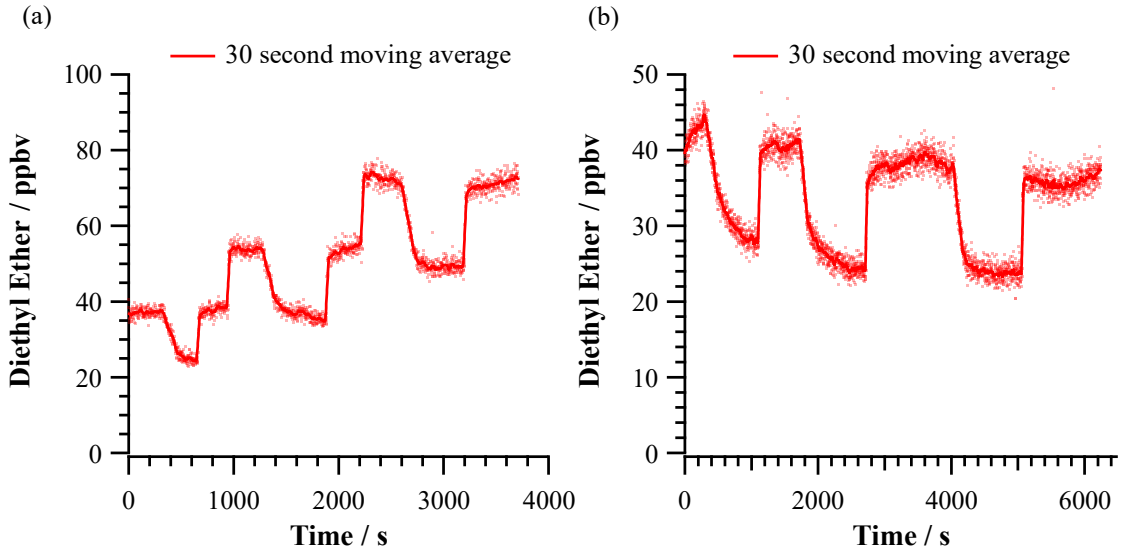

Figure 3.9. (a) Quantification of [Cl] present at the sample inlet of the Cl-CRM reactor through the depletion of $(C_2H_5)_2O$. (b) Reproducibility of the observed depletion.

To evaluate what photolytic efficiency this 20 ppbv depletion would represent, and to gain an appreciation for the radical losses within the system, the flows of $(C_2H_5)_2O$ and $(COCl)_2$ were mixed together and introduced to the reactor through inlet A. By combining the flows and allowing the reference VOC to react at the source of Cl production, the probability of Cl recombination and wall loss processes can be minimised. As can be seen in Figure 3.10(a), depletion levels of up to ~ 90 ppb were observed in $(C_2H_5)_2O$ upon this modification to the setup which, based upon the depletion levels observed at inlet C, would yield a 78% loss of Cl-atoms through recombination and wall losses within the reactor. With respect to the efficiency of the Hg lamp, gravimetric analysis was performed on the $(COCl)_2$ source to yield an emission rate of 1 ± 0.2 mg min^{-1} as shown in Figure 3.10(b). Based on an N_2 flow rate of 25 sccm, a mass flow rate of 40 g m^{-3} and a molar flow rate of 0.3 mol m^{-3} can be calculated. From the stoichiometric coefficients for the photolytic breakdown of $(COCl)_2$, a maximum Cl molar flow of 0.6 mol m^{-3} would be achieved if photolysis was 100% efficient. Assuming standard temperature and pressure (and therefore 0.0409 mol L^{-1} air), such a mass flow rate would equate to a mixing ratio 15 ppm. As such a photolytic efficiency of 6×10^{-4} % can be

calculated which, when combined with wall and recombination losses, yields an overall efficiency of 0.01 %.

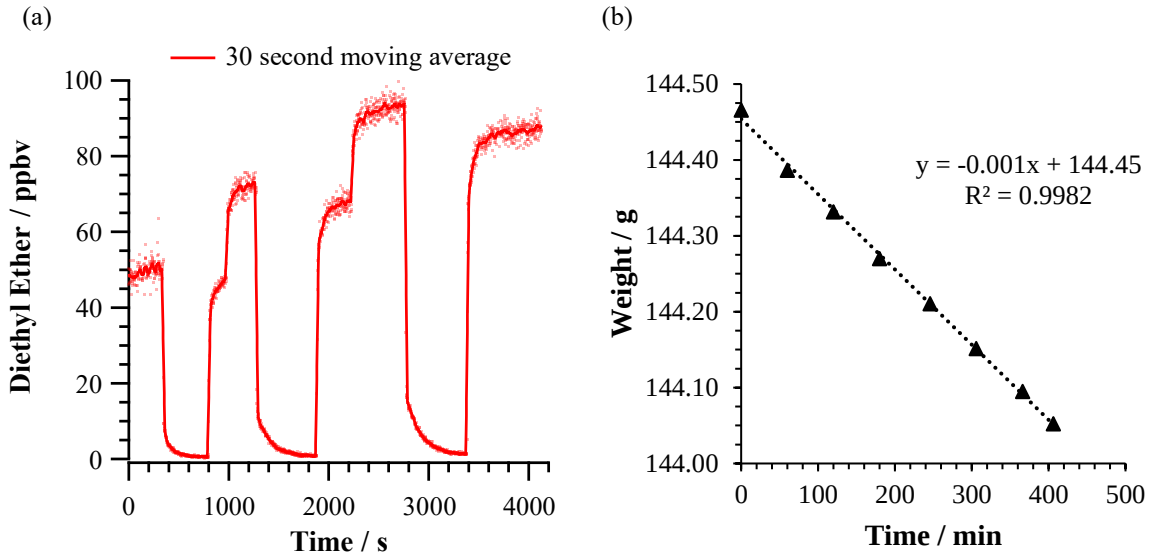

Figure 3.10. (a) Quantification of [Cl] formed by the photolysis of $(COCl)_2$ through the depletion of $(C_2H_5)_2O$. (b) Gravimetric analysis of the $(COCl)_2$ source.

3.4.2.3 Limitations of $(COCl)_2$ as a Precursor

Whilst the use of $(COCl)_2$ was found to be a viable source of Cl-atoms, its use as a precursor in a CRM setup was not feasible due to practical limitations identified during the aforementioned tests and preliminary rate measurement experiments. As $(COCl)_2$ reacts with water to form HCl and a mixture of CO and CO_2, as described by reaction 3.7, it was found to be highly sensitive to any moisture present within the setup.

$$(COCl)_2 + H_2O \rightarrow 2\ HCl + CO_2 + CO \qquad \text{(Reaction 3.7)}$$

Due to the high concentrations $(COCl)_2$ being introduced into the reactor as a result of the low photolytic efficiency, the formation of HCl proved to be a significant issue due to its highly corrosive properties, with the backflow of $(COCl)_2$ into MFCs leading to damage to their exposed valves and pressure gauges and ultimately their inability to control flows. As these observations were made during the use of $(COCl)_2$ under laboratory conditions in which dry N_2 was used a carrier gas, it is likely that these issues would be worsened when sampling humid air during field campaigns.

3.4.3 Photolysis of Cl_2

3.4.3.1 Reactor Design

Due to the aforementioned issues with the use of $(COCl)_2$ in the CRM setup, the decision was taken to switch to the photolysis of Cl_2 as a precursor of Cl-atoms instead. As both precursors have different absorption cross sections, a change in light source was required leading to the development of a new quartz reactor as depicted in Figure 3.11. The length and volume of the reactor are approximately 20 cm and 83 cm^3 respectively, with the total flow rate through the system maintained at 500 sccm over the course of a measurement to yield a residence time of 10 seconds. Photolysis of Cl_2 (λ_{max} = 330 nm) is achieved using an EQ-77 laser driven light source (Energetiq, United States), a broad-band lamp which radiates at wavelengths from 190 nm through the visible region of the spectrum, and will herein be referred to as the LDLS. Known flow rates of Cl_2 in Ar, gas phase $(C_2H_5)_2O$ and the sample of interest are mixed together prior to introduction into the reactor, with N_2 (later replaced with zero air for reasons discussed further in this chapter) used as a carrier gas to maintain the total flow through the system at each stage of the CRM experiment. All gas lines are plumbed with ¼" PFA tubing (Swagelok, United States), with MFCs (Alicat Scientific, United States) used to ensure that the relevant gas flow rates are constant throughout a measurement. Changes in the concentration of $(C_2H_5)_2O$ and Cl_2 are monitored using SIFT-MS using the NO^+ and O_2^+ reagent ions respectively.

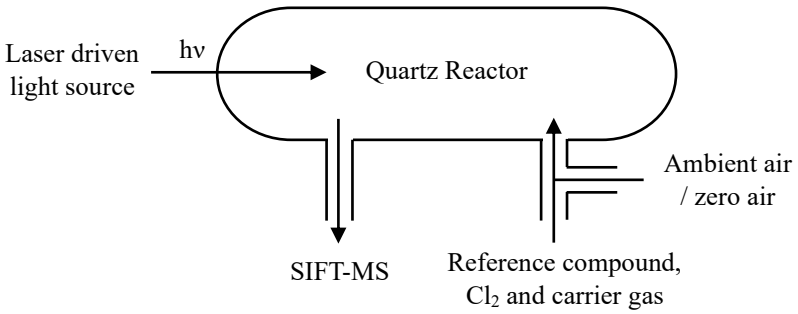

Figure 3.11. Schematic representation of the quartz reactor used for the photolysis of Cl_2.

3.4.3.2 Lamp Flux Measurements

During initial tests to determine whether the LDLS would be a suitable light source for the photolysis of Cl_2, $(C_2H_5)_2O$ was introduced into the outflow from the quartz reactor. Such a design was preferential in order to minimise any potential photolytic losses within the system, in particular during field measurements in which photolabile VOCs may be present within the ambient air sample. Unfortunately no change in the concentration of $(C_2H_5)_2O$ was observed in this configuration upon switching on the light source, indicating that Cl-atoms were either recombining or being lost to surfaces prior to reaction with the VOC. Consequently the decision was taken to add the reference compound, and thus the sample of interest, into the quartz reactor alongside Cl_2 as discussed above. An appreciation of the radiation flux of the LDLS is therefore vital in order to determine the rate at

which some species may be lost through photolysis within the setup. In general, the rate coefficient, *j*, for a photolytic reaction is described by the wavelength-integrated product expressed in equation 3.12:

$$j = \int_{\lambda min}^{\lambda max} F(\lambda)\ \sigma(\lambda, T)\ \Phi(\lambda, T)\ d\lambda \qquad \text{(Equation 3.12)}$$

Where:

- F is the photon flux
- σ is the absorption cross section of the photolysed species
- Φ is the quantum yield of photodissociation

Whilst absorption cross sections and quantum yields for species of interest can be obtained from the literature, the photon flux of the LDLS at each wavelength is unknown. Spectral power measurements of the light source were, however, provided by the manufacturer. As such, if the photolysis rate coefficient of a species can be calculated within the system independent of any knowledge of the photon flux, a correction factor (y) can be applied to equation 3.12 that would enable the use of the spectral power measurements (P) in place of the photon flux:

$$j = \int_{\lambda min}^{\lambda max} P(\lambda)\ \sigma(\lambda, T)\ \Phi(\lambda, T)\ d\lambda \times y \qquad \text{(Equation 3.13)}$$

To achieve this, NO_2 actinometric experiments were conducted to calculate a value of j_{NO2}, the photolysis of which at wavelengths below ~ 420 nm and in the presence of air can be described by the following three reactions (disregarding any side reactions which may also occur):[199, 200]

$NO_2 + h\nu \rightarrow NO + O$ $\quad j_{NO2}$ (Reaction 3.23)

$O + O_2 + M \rightarrow O_3 + M$ $\quad k_b$ (Reaction 3.24)

$NO + O_3 \rightarrow NO_2 + O_2$ $\quad k_c$ (Reaction 3.25)

Consequently, by passing NO_2 through the quartz reactor and allowing the system to reach dynamic equilibrium after switching on the LDLS, j_{NO2} can be calculated using the equilibrium concentrations of NO, NO_2 and O_3, and a rate coefficient for k_c of 1.90×10^{-14} cm^3 $molecule^{-1}$ s^{-1} at 298K via equation 3.14:

$$j_{NO_2} = k_c \frac{[O_3][NO]}{[NO_2]} \qquad \text{(Equation 3.14)}$$

In order to allow the system to establish equilibrium, the flow rate through the reactor during these measurements was reduced to 5 sccm leading to a residence time of ~ 17 minutes. Concentrations of NO and NO_2 over the course of the experiments were monitored using a T200UP chemiluminescent analyser (Teledyne Technologies, United States) whilst O_3 concentrations were monitored using a T265 chemiluminescent analyser (Teledyne Technologies, United States). Whilst a depletion in the

concentration of NO_2 and a corresponding increase in the concentration of NO were observed upon switching on the light source, no change in the concentration of O_3 from the background levels was measured suggesting potential losses within the system. The concentration of O_3 was therefore assumed to be equivalent to the change in concentration of NO over the measurement period, leading to an upper estimate of j_{NO2} of 0.084 s^{-1}.

Calculations of j_{NO2} were also conducted by measuring the conversion of NO_2 into NO at varied residence times within the quartz reactor and fitting the resulting plot of conversion factors against time to the form of equation 3.15 as proposed by Kley and McFarland:[201]

$$CF = \left[\frac{j_{NO_2}t}{j_{NO_2}t+k[Ox]t}\right]\left[1-\exp\left(-j_{NO_2}t-k[Ox]t\right)\right] \qquad \text{(Equation 3.15)}$$

Where:

- CF is the effective conversion factor between NO_2 and NO
- t is the residence time in the quartz reactor
- k[Ox] is the rate coefficient and the concentration of any oxidising species which can react with NO to reform NO_2

In total, measurements were recorded at 11 different residence times from which a j_{NO2} value of 0.025 s^{-1} was obtained as illustrated in Figure 3.12. It should be noted, however, that the measurement of the conversion factors are typically conducted on a much shorter timescale than that used in this study, and as such the j_{NO2} value calculated likely represents a lower estimate

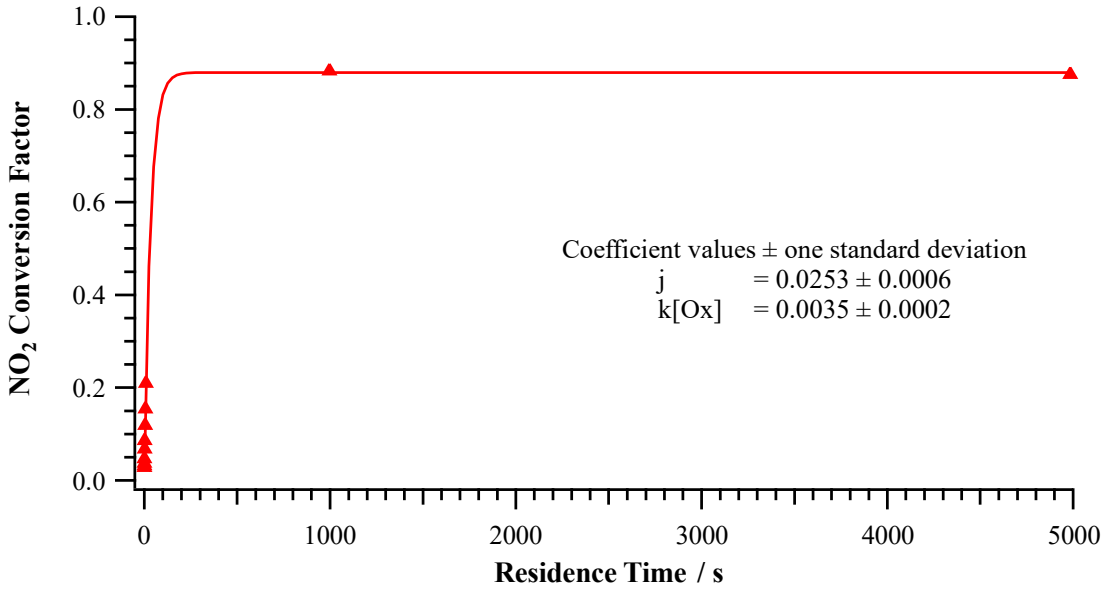

Figure 3.12. NO_2 conversion factor for the LDLS in zero air as a function of reactor residence time.

In comparison to the two experimentally derived photolysis rates, a j_{NO2} value of 1.16×10^{-16} s^{-1} was obtained when considering the lamp spectral power measurements within the wavelength range of the NO_2 absorption cross section and quantum yield reported by IUPAC.[202] From this, correction factors of 7.28×10^{14} and 2.18×10^{14} were calculated based on the j_{NO2} values obtained from equations 3.14 and 3.15 respectively to account for the use of spectral power as opposed to flux in the calculation of j. Assuming a quantum yield of 1, and using the absorption cross section of Cl_2 reported by IUPAC in equation 3.13, j_{Cl2} is estimated to be in the range of 0.0089 – 0.030 s^{-1} within the system upon application of the aforementioned correction factors.

3.4.3.3 Instrument Characterisation

Diethyl ether photolysis

No deviation from the baseline concentration of the VOC was observed when the LDLS was switched on. As such, photolytic losses can be disregarded as a potential source of interference in the CRM calculation.

Photolytic efficiency

One advantage of using SIFT-MS as a detector is the ability to directly monitor the concentration of Cl_2 over the course of a measurement using the O_2^+ reagent ions, something not possible using PTR-MS due to Cl_2 having a lower proton affinity than water. As a result, the efficiency of the LDLS for Cl_2 photolysis was assessed by monitoring its depletion in the presence of $(C_2H_5)_2O$ as the light source was switched on/off. Over the course of the measurement, the concentration of $(C_2H_5)_2O$ was gradually increased to ensure that all of the generated Cl-atoms were being consumed. As can be seen in Figure 3.13 the level of depletion remained constant over the course of these incremental changes, with an efficiency of (10.4 ± 1)% calculated.

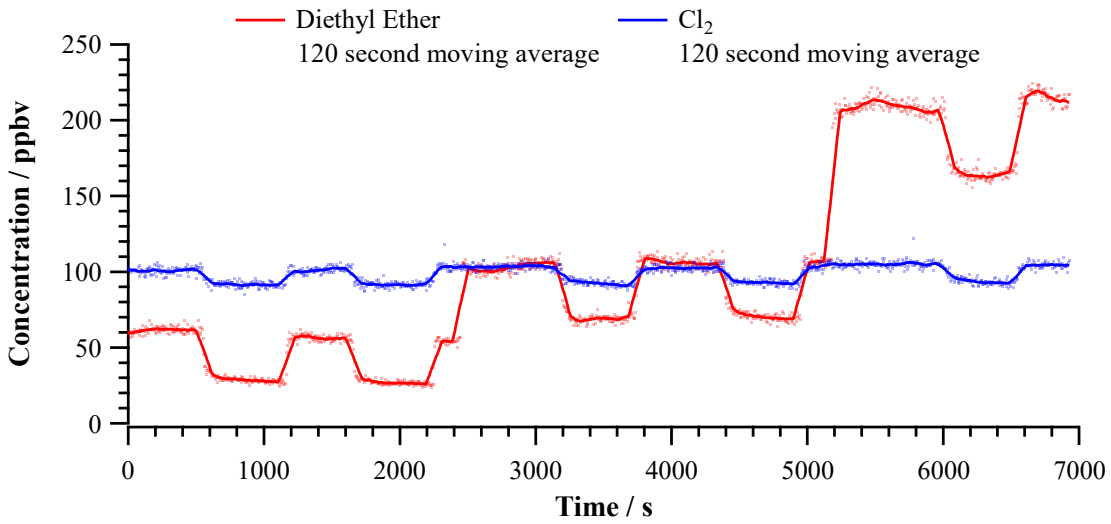

Figure 3.13. Quantification of [Cl] formed by the photolysis of Cl_2 and subsequent reaction with $(C_2H_5)_2O$.

Measurement of isoprene reactivity

Having ruled out photolytic loses of the reference VOC, tests were performed to ascertain whether the Cl-CRM concept could reliably quantify reactivity rates based on known rate coefficients. C_5H_8 was chosen as the source of additional reactivity for these preliminary tests for a number of reasons. The ability to measure C_5H_8 using SIFT-MS was one of these factors, allowing for changes in its concentration and that of $(C_2H_5)_2O$ to be monitored over the course of an experiment. As a result, the sum of depletion of both species could be calculated and then compared to that observed in $(C_2H_5)_2O$ during the C1-C2 stage in order to ensure that no additional radicals were being formed within the reactor that could act as an interference. Furthermore, the ability to measure C_5H_8 with the SIFT enables tests to be conducted to ensure that it would not be photolysed by the LDLS. No change in concentration was observed during the tests and as such C_5H_8 is a suitable VOC to test the CRM concept in the current reactor configuration. The final benefit of using C_5H_8 in these preliminary tests is that its reaction with Cl has been well studied with a recommended value published by JPL of $7.60 \times 10^{-11} \times \exp(500/T)$ cm^3 $molecule^{-1}$ s^{-1}, allowing for the rate of reactivity being introduced into the reactor to be calculated.[179] It is, however, noted that the values used by JPL to determine their recommended rate coefficient show a large degree of variability, with some suggesting rate coefficients nearly 20% faster than the recommended value at 298 K.[203-205] Such variability would therefore impose a greater degree of uncertainty surrounding the reactivity being introduced into the system.

Figure 3.14 shows an example plot of a typical Cl-CRM experiment. As reflected by the drop in concentration of $(C_2H_5)_2O$ between ***C1*** and ***C2***, reaction with $Cl_{(g)}$ occurs when the LDLS is turned on. The level of depletion observed in $(C_2H_5)_2O$ then decreases upon the addition of C_5H_8 owing to the competing reaction for $Cl_{(g)}$, as reflected by the simultaneous decrease in the concentration of C_5H_8.

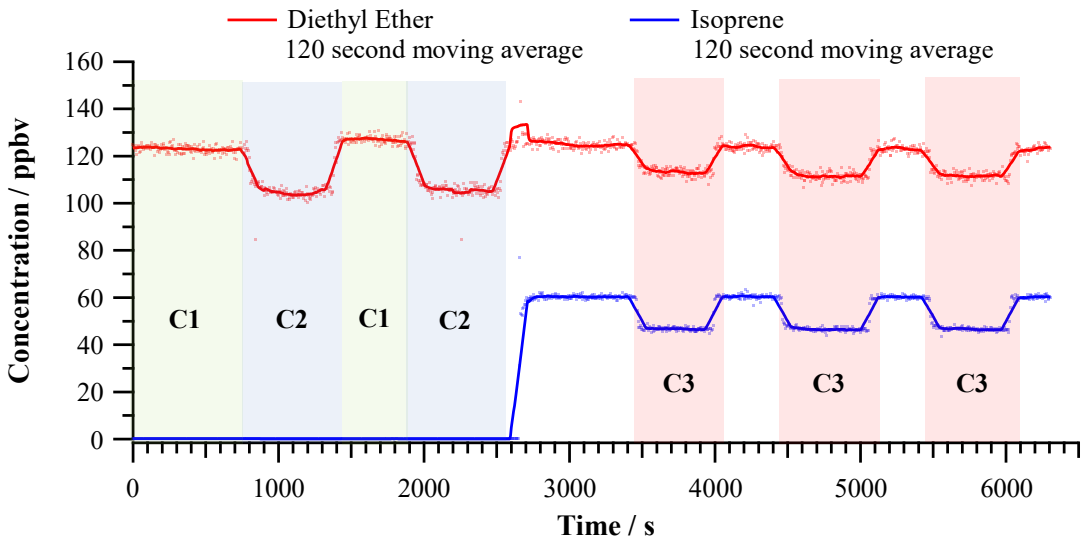

Figure 3.14. Representative Cl-CRM experiment using $(C_2H_5)_2O$ as a reference gas to measure the reaction of C_5H_8 with Cl.

By adjusting the concentration of C_5H_8 introduced into the reactor, the operating range of the Cl-CRM instrument could be probed. Figure 3.15 shows the reactivity measured by the CRM setup (vertical axis) plot against the reactivity introduced into the system by addition of C_5H_8 (horizontal axis). The horizontal error bars represent the total uncertainty in the reactivity introduced into the system, which includes the uncertainty in the concentration of C_5H_8, uncertainty in the rate constant and fluctuations in the flow rate. With respect to the former, as the C_5H_8 measurements were uncalibrated, the error comprises of the uncertainty in the rate coefficient for the reaction of C_5H_8 with the NO^+ reagent ions of the SIFT-MS (20%) and the error associated with the transmission curve (10%). As JPL do not quote an uncertainty with their recommended rate coefficient for the reaction of C_5H_8 with Cl, this is assumed to be 20% upon considering the range of rate coefficients that were used to derive the recommended value at 298K as discussed above. Applying the root square propagation of errors for these uncertainties, and including an uncertainty of 0.6% for the flow rate, an overall error of 30% was obtained for the sampled reactivity. A similar procedure was conducted to determine the uncertainty in the measured Cl reactivity, reflected in the vertical error bars. This includes the uncertainty in the rate coefficient for the reaction of $(C_2H_5)_2O$ with Cl (16.8%), uncertainty in the concentration of $(C_2H_5)_2O$ introduced into the reactor (as this was uncalibrated, these errors are the same as that for the concentration of C_5H_8), SIFT-MS precision errors (7.5%) and flow fluctuations of the MFCs (0.6%), yielding a total measurement error of 28.96% which is rounded to 30% herein.

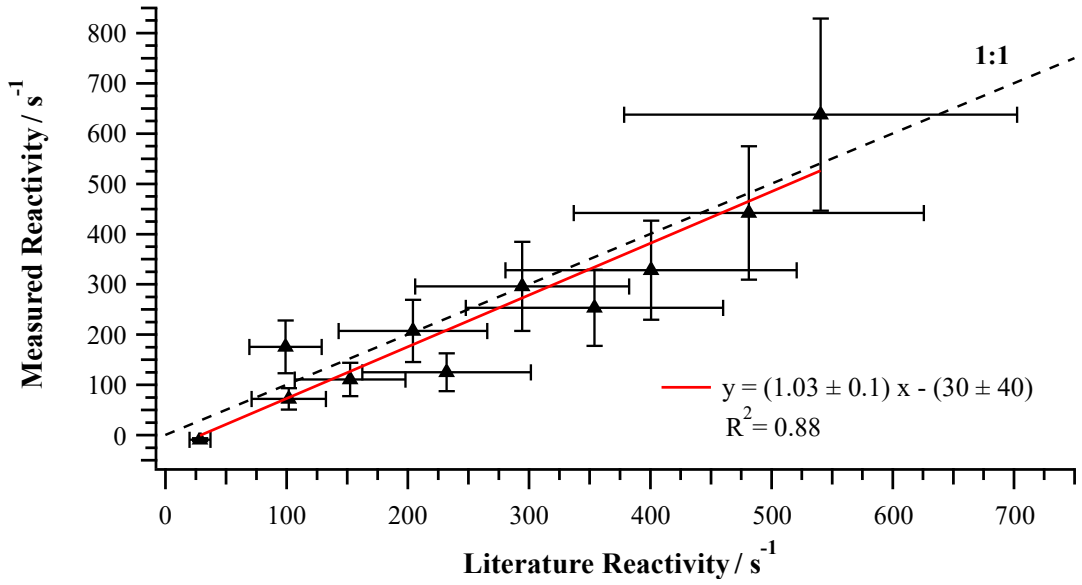

Figure 3.15. CRM validation using C_5H_8 as a source of reactivity under the initial reactor conditions.

Whilst a good agreement was found between the CRM and JPL derived rates, as reflected by a gradient of 1.03 being obtained following linear regression analysis, an R^2 value of 0.88 highlighted significant variability in the measurements across the investigated reactivity range. In an attempt to minimise this variability, several changes were made to the experimental setup, the results of which are summarised in Table 3.6. Initial modifications to the design involved the shortening of the sampling inlet line to the SIFT-MS in order to minimise any potential surface losses that may be occurring to the walls of the PFA tubing. The carrier gas was also switched from oxygen-free N_2 to zero air during these modifications in order for the experiments to more closely mimic the conditions of the reactor during operation in the field, in which O_2 would be present in the sampled air. Upon these changes the reactivity rate was observed to drop from 150 s^{-1} to 70 s^{-1}, both of which lower than the literature derived rate of 202 s^{-1} based on the concentration of C_5H_8 introduced into the reactor. Large variability in the measurements also continued to be observed despite the modifications made. It was hypothesised that this variability may arise from the photolytic formation of additional radical species within the reactor due to the high energy photons emitted from the LDLS. This hypothesis is supported by comparing the depletion levels at each stage of the CRM, with the combined depletion of C_5H_8 and $(C_2H_5)_2O$ during the ***C3*** stage being on average 2.5 ppbv greater than the observed C1-C2 depletion in $(C_2H_5)_2O$ when using N_2 as a carrier gas. The observed discrepancy was even more profound upon the use of zero air, with the difference in depletion levels increasing to 12.4 ppbv, potentially arising from the formation of O radicals following the photolysis of O_2 within the setup. To mitigate for this, the LDLS was fitted with a 280 nm longpass filter (Newport, United States, part number: 20CGA-280) to remove the high energy photons not required for Cl_2 photolysis at $\lambda < 280$ nm. Rate measurements were repeated using both N_2 and zero air carrier

gasses to assess the impact of the removal of these high energy photons. In both instances the variability in the repeat measurements was reduced whilst the calculated rate increased in comparison to that obtained during the unfiltered experiments. It is interesting to note that use of zero air as a carrier gas resulted in an 18% increase in the measured rate when compared to that obtained with N_2, and the JPL derived rate, indicating that the ***C3*** concentration of $(C_2H_5)_2O$ was higher than expected and thus suggesting a potential sink of Cl-atoms within the zero air cylinder.

Table 3.6. Impact of carrier choice and filtration of the light source on calculate CRM rates for the reaction of C_5H_8 with $Cl_{(g)}$. Literature rate calculated to be 202 s^{-1}. Measurements were repeated 3 times with the average (± one standard deviation) reported.

Carrier Gas	Light Source Status	CRM rate / s^{-1}
Nitrogen	Unfiltered	151 ± 40
Nitrogen	Filtered	182 ± 10
Zero air	Unfiltered	70 ± 40
Zero air	Filtered	214 ± 10

Following the modifications to the experimental setup, the operating range of the CRM instrument was re-examined with the results depicted in Figure 3.16. In comparison to the original measurements, a stronger linear response was observed in the measured reactivity as reflected by an increase in R^2 of the linear regression fit from 0.87 to 0.99. An increase in the gradient was also observed, indicating a slight overestimation of the reactivity introduced into the system by 8%. To explore this further, orthogonal distance regression (ODR) was conducted to determine whether consideration of the error in the x-axis (the reactivity introduced into the system) would have any impact on the linear fit. As can be seen from the blue line in Figure 3.15, both regression methods yielded comparable fits, with ODR suggesting a slight increase in the overestimation to 9%. Such overestimations cannot be attributed to the operation of the instrument under non-pseudo first-order conditions, with AtChem simulations identifying an expected underestimation of the rate by 4% instead, as shown in Figure 3.17. It should be noted, however, that both linear fits are within the 30% uncertainty of the measurement as previously discussed.

From the measurements, an averaged detection limit of the instrument could also be obtained. The LOD was determined by calculating standard deviations of the ***C2*** $(C_2H_5)_2O$ concentration (σ_{C2}) for each measurement and calculating an associated Cl reactivity arising from the measurement noise through equation 3.16:

$$LOD = \frac{((\boldsymbol{C2}+3\sigma_{\boldsymbol{C2}})-\boldsymbol{C2})}{(\boldsymbol{C1}-(\boldsymbol{C2}+3\sigma_{\boldsymbol{C2}}))} \times k_{Diethyl\ Ether}\ \boldsymbol{C1} \qquad \text{(Equation 3.16)}$$

From this, an LOD of 12 s^{-1} was calculated, indicating the instrument in its current configuration would lack the sensitivity to be deployed in its current configuration in clean air environments such as that experienced in Cape Verde. It is also interesting to note, however, that both fits in Figure 3.15 yield non-zero y-axis intercepts exceeding this LOD values (-34 and -36 for linear regression and ODR respectively). As can be seen in Figure 3.16, whilst a non-zero y-axis intercept is also obtained from the AtChem simulations, this is substantially lower than that obtained from the experimental measurements indicating that the operation of the system under non-pseudo first-order conditions is not solely responsible for this systematic error. One potential reason for the negative intercept is an underestimation of the rate of reaction at low reactivity. This is reflected in the measured reactivity rates falling below the 1:1 literature : measured reactivity rate line in Figure 3.16 at rates below 220 s^{-1}. As an underestimation of the reactivity rate would indicate a larger than expected depletion of diethyl ether in the ***C3*** stage, such an observation may indicate that additional radical sources were generated within the system. Such radical formation and subsequent interference would, however, still be anticipated when introducing higher reactivity into the system and thus seems unlikely. An alternatively possibility is an overestimation of the concentration of isoprene available to react with Cl within the system, consequently leading to an overestimation of the literature reactivity used in Figure 3.16. Whilst the concentration of isoprene was monitored during the experiments, the SIFT had not been calibrated with a standard containing the compound leading to increased uncertainty in the measured concentration.

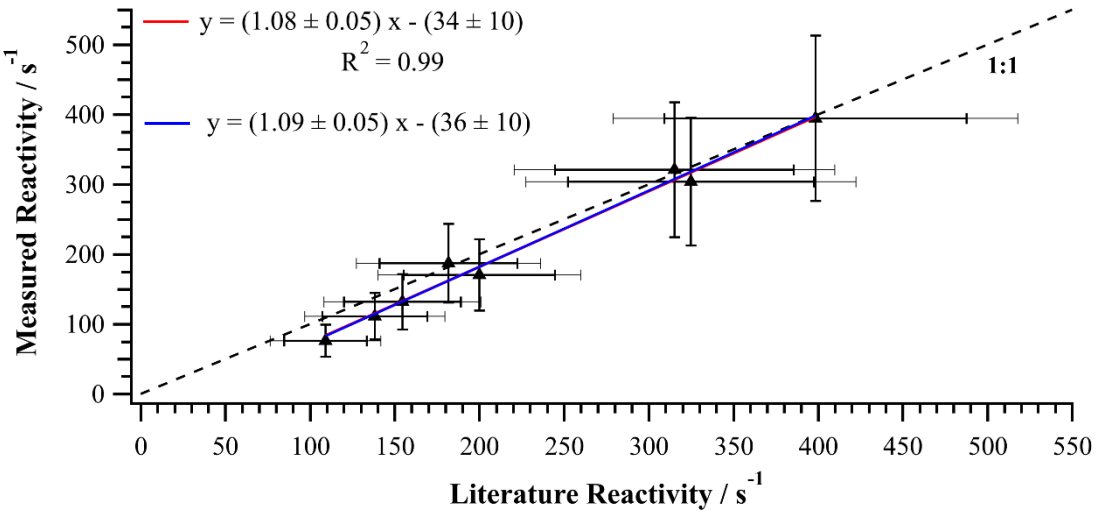

Figure 3.16. CRM validation using C_5H_8 as a source of reactivity post-reactor modifications. Error bars represent the total calculated uncertainty with the fainter error bars including the uncertainty in the literature rate coefficient. Red and blue lines represent the fits obtained via linear regression and orthogonal distance analysis respectively.

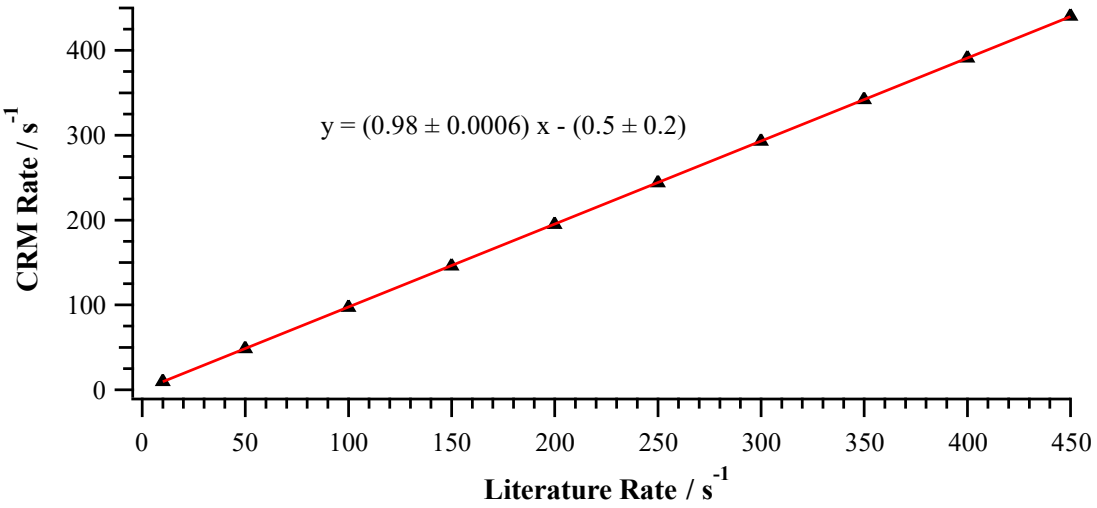

Figure 3.17. AtChem derived CRM rates for the measurement of isoprene reactivity.

3.5 Conclusions

The feasibility of the CRM concept for the measurement of chlorine reactivity has been explored in this chapter. Box model simulations conducted in AtChem have identified that while the method would be appropriate for such an application, as reported previously in the literature, the accuracy of the technique is sensitive to the operating conditions with significant errors introduced upon operating the system under non-pseudo first-order conditions. A previously unreported sensitivity to the rate coefficient of the reference compound was also identified during the aforementioned simulations, with the technique found to overestimate the reactivity when measuring samples with rate coefficients lower than that of the reference compound whilst conversely underestimating those with higher rate coefficients. As a result, $(C_2H_5)_2O$ was identified as the most suitable candidate for use as a reference compound in this study, with a [Reference VOC] : [Cl] ratio of 5 : 1 proposed to strike a balance between instrument sensitivity and the need for pseudo first-order conditions.

Several approaches to the formation of Cl-atoms under atmospheric pressure were investigated, with the photolysis of Cl_2 via a broad spectrum lamp identified as the most suitable for application in this study. Owing to the ability to monitor the concentration of Cl_2 in real-time, SIFT-MS was also identified as the most suitable detection method for use during the development of the CRM setup.

Validation of the CRM concept was probed through standard additions of isoprene within a reactivity range of approximately 100 – 400 s^{-1}. The technique was found to reproduce rates to within (8 ± 5)% of those obtained using the recommended rate coefficient of JPL,[179] well within the approximate 30% total uncertainty of the measurement. Further validation of the method is required through the addition of increasingly more complex gas mixtures to better mimic the measurement of an ambient air sample. Exploration of the impact of NO on the measured reactivity is also suggested, with box model simulations indicating interference arising from the formation of OH within the system.

Chapter 4

Application of the Cl-CRM Instrument

4.1 Introduction

4.1.1 Chapter Objectives

In the previous chapter a clean source of Cl-atoms for the CRM technique was identified through the photolysis of Cl_2 using a broad-spectrum lamp. Tests using C_5H_8 as a gas standard identified that the rates obtained using the technique were in good agreement with those derived from the literature rate coefficient. This chapter will continue to build upon these comparisons by measuring the reactivity of increasingly more complex gas mixtures that begin to mimic an ambient air sample in order to ascertain whether the instrument would be suitable for field deployment. Should good agreement with the literature continue to be found, the technique will also be utilised to measure the rate coefficient of a VOC for which no existing measurements have been published; providing another potential application of the instrument when not deployed in the field.

4.2 Characterisation Against Literature Rates

4.2.1 Methane / Propane Mixture

Continuing the validation of the CRM technique, the reactivity of a CH_4 and C_3H_8 mixture with chlorine was measured and compared to the literature. Such a mixture was chosen owing to the well-established rate coefficients of reaction with Cl for these species (1.0×10^{-13} and 1.4×10^{-10} cm^3 $molecule^{-1}$ s^{-1} at 298 K for CH_4 and C_3H_8 respectively)[15] allowing for reduced uncertainty in the reactivity being introduced into the reactor when compared to C_5H_8. It should be noted however that one limitation of these species is that neither can be detected using SIFT-MS since short chain hydrocarbons do not react with the NO^+ or H_3O^+ reagent ions.[206] Measurement of CH_4 using the O_2^+ reagent ion is possible, however the reaction is slow and therefore can only be used to quantify concentrations in excess of 1000 ppmv and thus would not be suitable in this study.[207] Consequently, quantification of the cylinder concentrations used in this study was achieved using GC-MS, with the subsequent concentrations of both species introduced into the reactor calculated based upon the dilution flow rates used. Figure 4.1 shows the resulting measured vs literature reactivity rate plot from these experiments for which four different species concentrations were used and measurements repeated three times. As with the C_5H_8 experiments reported in section 3.4.3, the CRM rates were found to be in good agreement with those derived from the literature, with linear regression analysis suggesting an overestimation of the rate by 6%, and little variability over the measured reactivity range as reflected by the R^2 value of 0.97. Upon considering the uncertainty in the reactivity introduced into the system (~22%) through ODR, the calculated overestimation increased to 8%. Whilst both of these overestimations are greater than that which can be attributed to the operation of the CRM setup under non-pseudo first-order conditions (simulated to lead to a 3% overestimation), it should be noted that both of these values, including the uncertainty in the linear fits, are within the combined uncertainty in the measured reactivity (~30%) as previously calculated in section 3.4.3. As

such, any improvements in the CRM's ability to reproduce literature rates would first require a reduction in the uncertainty of each measurement. Similarly, whilst both linear and ODR analyses yield non-zero y-axis intercepts, both are also within the uncertainty of the fit.

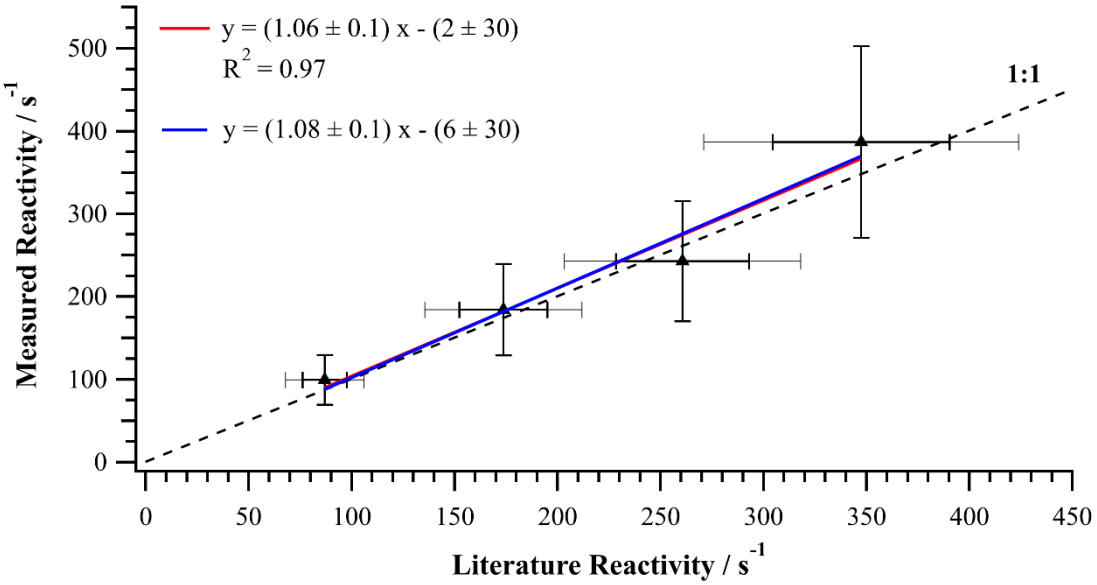

Figure 4.1. Calibration plot of the CRM instrument using a CH_4 / C_3H_8 mixture. Error bars in the y-axis represent the total measurement uncertainty (30% as discussed in section 3.4.3). Error bars in the y-axis represent the uncertainty of the reactivity introduced into the system (8.8% uncertainty in the concentrations of both species measured by the GC-MS, 0.6% uncertainty in the MFC flow rate) with the fainter error bars including the uncertainty in the literature rate coefficients of CH_4 and C_3H_8 (11.5% and 13.9% respectively). Red and blue lines denote the linear and ODR fits respectively.

Figure 4.2(a) shows the resulting calibration plot obtained upon merging the reactivity measurements of both C_5H_8 and the CH_4 / C_3H_8 mixture. Little variability is observed between the measurements of both systems as reflected by an R^2 value of 0.97, however larger y-axis offsets of - 22 and - 27 s^{-1} are obtained using linear and ODR analyses respectively, further highlighting the lack sensitivity of the instrument. To assess the importance of the y-axis intercept on the observed relationship between the measured and literature reactivity rates, the linear regression of the measured rates was repeated by forcing the fit through the zero point. As can be seen from the plot in Figure 4.2(b), the resulting regression analysis yields a linear fit with excellent agreement between the literature and measured rates, suggesting an underestimation of just 1% across the range of 86 – 400 s^{-1}. This apparent improvement in accountability is at the expense of significantly worsened quality of fit as reflected by a drop in R^2 to 0.82. As discussed in section 3.3.2, whilst this would not pose an issue in polluted environments such as London, the offset obtained here is greater than the expected reactivity rate within clean air environments such as Cape Verde. As such, it is suggested that a separate set of CRM

operating conditions would need to be investigated in order for deployment of the instrument within these environments to be viable.

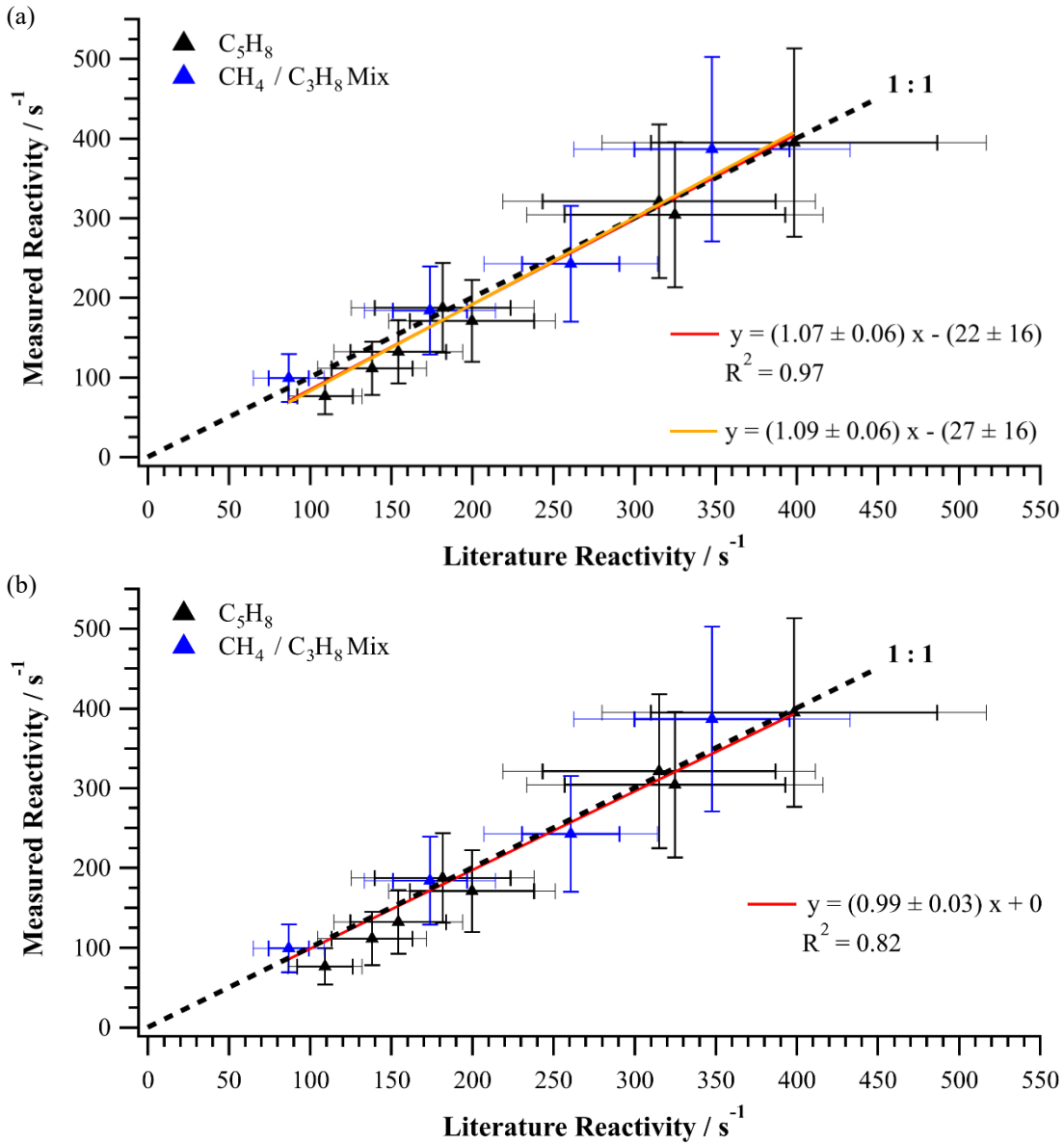

Figure 4.2. Combined CH_4 / C_3H_8 and C_5H_8 calibration plot of the CRM instrument (a) using linear regression (red) and orthogonal distance (orange) derived y-axis intercept (b) forcing through zero.

4.2.2 35-Component Mixture

Increasing the complexity of the sample further, a 35-component gas mixture consisting of alkanes, alkenes, and aromatics in nitrogen (BOC, 177664-AL-HC) was used as a final reactivity standard to validate the CRM concept. A breakdown of the components present within the gas standard, their GC validated concentrations (post dilution from the stock cylinder) and their literature rate constants is given in Table 4.1. For trans-pent-2-ene, no rate constant could be found in the literature, so it was assumed to be comparable to that of pent-1-ene (3.97×10^{-10} cm^3 $molecule^{-1}$ s^{-1}).

Table 4.1. Composition of the 35-component gas standard used, GC validated species concentrations and literature rate coefficients. * No rate coefficient for trans-pent-2-ene could be found within the literature so it has been assumed to be equal to that of pent-1ene in this study.

Component	Concentration ± σ / ppbv	k / cm^3 molecule^{-1} s^{-1} (298 K)	Source
n-Decane	86.2 ± 1	5.55×10^{-10}	MCM
1,2,3-trimethyl benzene	100.2 ± 1	3.60×10^{-10}	173
1,2,4-trimethyl benzene	91.3 ± 1	3.60×10^{-10}	173
1,3,5-trimethyl benzene	90.0 ± 0.8	3.10×10^{-10}	173
n-Nonane	109.4 ± 1	4.80×10^{-10}	MCM
o-Xylene	87.5 ± 0.6	1.50×10^{-10}	177
m-Xylene	86.6 ± 0.8	1.70×10^{-10}	173
p-Xylene	85.4 ± 1	2.60×10^{-10}	173
Ethyl benzene	83.7 ± 0.7	9.10×10^{-11}	173
n-Octane	93.0 ± 0.6	4.60×10^{-10}	MCM
Toluene	93.0 ± 0.6	5.90×10^{-11}	177
Benzene	100.7 ± 0.3	1.30×10^{-15}	177
n-Heptane	88.1 ± 0.4	3.90×10^{-10}	MCM
2,2,4-trimethyl pentane	93.0 ± 0.1	2.26×10^{-10}	208
2-Methyl pentane	86.9 ± 0.1	2.90×10^{-10}	MCM
n-Hexane	92.6 ± 0.2	3.40×10^{-10}	MCM
Trans-pent-2-ene	92.3 ± 0.3	3.97×10^{-10} *	174
Cyclopentane	92.8 ± 0.2	2.31×10^{-10}	209
Isoprene	80.2 ± 0.2	4.07×10^{-10}	179
n-Pentane	98.0 ± 0.2	2.80×10^{-10}	MCM
i-Pentane	126.8 ± 0.1	2.20×10^{-10}	MCM
Pent-1-ene	92.9 ± 0.2	3.97×10^{-10}	174
Cis-but-2-ene	100.1 ± 0.2	3.76×10^{-10}	174
1,3-butadiene	94.9 ± 0.2	3.20×10^{-10}	180
But-1-ene	95.1 ± 0.2	3.00×10^{-10}	175
Trans-but-2-ene	97.1 ± 0.2	3.31×10^{-10}	174
Acetylene	69.7 ± 0.2	4.97×10^{-11}	173
Isobutylene	88.4 ± 0.2	3.40×10^{-10}	174
i-Butane	101.9 ± 0.1	1.43×10^{-10}	MCM
n-Butane	98.0 ± 0.1	2.06×10^{-10}	MCM
Propane	95.2 ± 0.1	1.40×10^{-10}	MCM
Propylene	94.9 ± 0.2	2.70×10^{-10}	15
Ethane	96.4 ± 0.4	5.80×10^{-11}	MCM
Ethylene	96.6 ± 0.2	1.00×10^{-10}	15

The gas standard was introduced into the reactor at five different mixing ratios to yield reactivities within the 86 – 400 s^{-1} range already investigated. Each measurement was repeated three times with the average reactivity taken. An average relative standard deviation of 7.5% was calculated across the reactivity ranges investigated, highlighting reasonable reproducibility in the measurement. As can be seen from the resulting calibration plot given in Figure 4.3, in comparison to the previous calibrations, a greater discrepancy between the literature and measured rates was observed, with linear regression analysis identifying a 33% overestimation and ODR identifying a 37% overestimation. Similarly, both linear fits resulted in a significantly increased offset from zero in the y-axis intercept. It is proposed that these changes arise from the increased uncertainty in the reactivity introduced into the system (143%), particularly due to the addition of VOCs within the gas standard for which no known rate coefficient for their reaction with Cl has been reported. Using the root square propagation of uncertainty, and assuming an uncertainty of 20% in the rate coefficients used in the MCM, a total uncertainty of ~ 146% is calculated for the reactivity within the system. Therefore, for clarity, only errors in both the cylinder concentration (3.5%) and the flow rate (0.6%) are accounted for in the x-axis error bars in Figure 4.3.

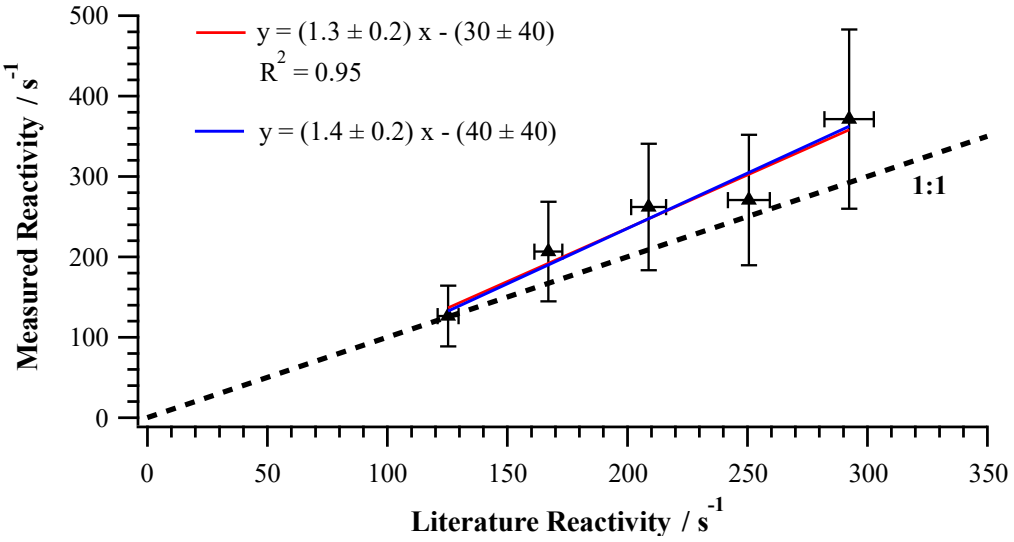

Figure 4.3. Calibration plot of the CRM instrument using a 35-component mixture. Error bars in the y-axis represent the total measured uncertainty (30% as discussed in section 3.4.3). Error bars in the y-axis represent the uncertainty in the reactivity introduced into the system (3.5% uncertainty in the cylinder concentration measured by the GC-MS, 0.6% uncertainty in the MFC flow rate) with the uncertainty in the literature rate coefficients of the constituents of the gas mixture (143%) omitted for clarity. Red and blue lines denote the linear and ODR fits respectively.

The final calibration plot for the CRM instrument based on all three standard measurements is given in Figure 4.4(a). Overall, the measurements show good agreement with the literature when viewed as a collective, as reflected by the gradient of 1.08, with a strong degree of linearity across the measured range (R^2 = 0.91), although it is noted that this degree of linearity is weaker upon the

addition of the 35-component mixture. Such performance compares well with the OH-CRM instrument developed by Sinha *et al*. and the more recent ICRM by Wang *et al*. in which gradients of 1.08 and 0.72 were obtained respectively, even when considering a gradient of 1.14 as obtained by ODR analysis.[129, 132] Forcing the linear fit through the zero point was observed to improve the relationship between the measured and literature rates as reflected by a drop in the gradient to 1.04. As previously observed in Figure 4.2(b) however, the quality of the fit was slightly poorer upon this change as reflected in the drop of R^2 to 0.84 (compared to 0.99 for both OH-CRM instruments). In comparison to the aforementioned OH-CRM instruments, the lack of sensitivity of the Cl-CRM instrument developed in this work is substantially greater (y-axis intercept of -12 for the Cl-CRM compared to -3.4 and -2.1 s^{-1} respectively for the OH-CRMs). It is therefore clear that any dilution factor of the sampled air should be kept to a minimum to increase the range of environments in which the Cl-CRM instrument could be deployed. As discussed in section 3.4.3 following the characterisation of the instrument through addition of C_5H_8, the negative intercept obtained in Figure 4.4 would suggest an underestimation of the reactivity rate at low reactivity. Underestimating the VOC concentrations introduced into the system and the formation secondary radicals within this region could potentially explain this observation, however, both would be expected to have similar, if not larger, impacts as the reactivity introduced into the system is increased. Due to the wide reactivity range that has been explored in this work, it is possible that the operating conditions used were not optimal for measuring low reactivities leading to the observed lack of sensitivity. Further work would therefore be required to investigate whether the use of a less reactive VOC would yield improved performance under such conditions. It should be noted, however, that calibration of both OH-CRM instruments was conducted using the more sensitive PTR-MS technique as opposed to the SIFT-MS technique used in this study. Should sensitivity continue to be a problem for the deployment of the Cl-CRM instrument, switching to a detector such as a PTR-ToF-MS would be recommended. It is also recommended that the chosen detector is calibrated with a diethyl ether (or alternative reference VOC) standard in the future in order to reduce the uncertainty in the measured reactivity.

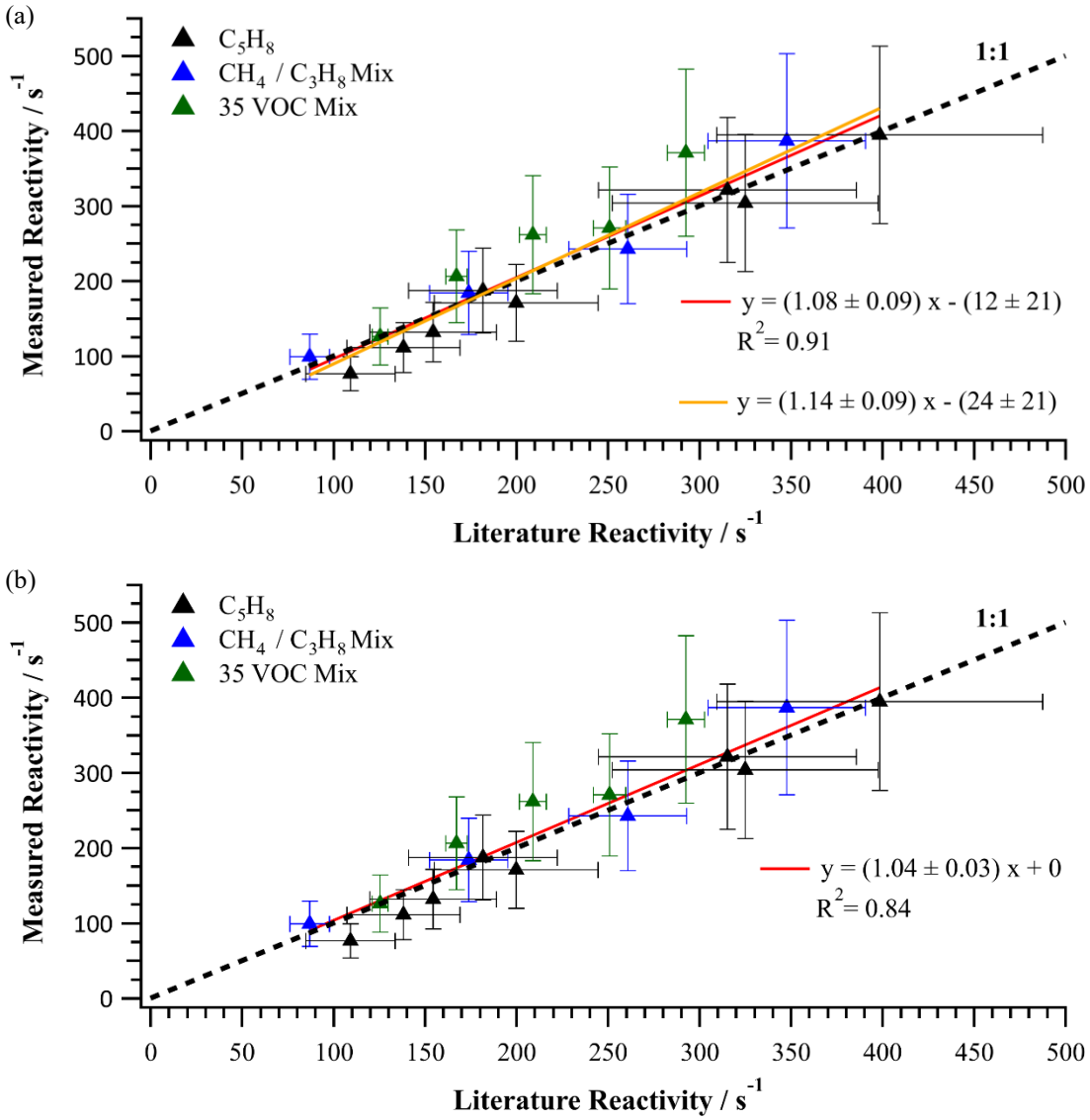

Figure 4.4. Final calibration plot of the CRM instrument (a) using linear regression (red) and orthogonal distance (orange) derived y-axis intercept (b) forcing through zero. Uncertainty in the sample rate coefficients have been omitted for clarity.

4.3 Measurement of Unknown Reactivity Rates

Having deduced that the CRM technique can reliably recreate literature reactivity rates under laboratory conditions, and developed a calibration curve within the range of 86 – 400 s^{-1}, tests were conducted to determine how well the technique would be suited for measuring unknown rate coefficients. Typically such measurements are achieved using either absolute techniques, such as discharge flow and flash photolysis, or relative rate techniques.[210] As discussed in section 3.3.2 of this thesis, the CRM and relative rate technique are closely related with both approaches utilising a reference compound to ascertain the reactivity of the sample of interest. The key difference with the relative rate technique, however, is that the concentrations of both the sample and the reference compound are monitored over the course of the experiment. Assuming that the sole loss process of both compounds is through reaction with Cl, the reactions of interest during a relative rate experiment can be summarised as follows (additional loss terms such as those with reactor walls can also be included if well understood but are not included in this description for simplicity):

$$\text{Sample} + \text{Cl} \rightarrow \text{Products} \qquad k_a \qquad \text{(Reaction 4.1)}$$

$$\text{Reference} + \text{Cl} \rightarrow \text{Products} \qquad k_b \qquad \text{(Reaction 4.2)}$$

From these reactions the following rate expressions can be derived:

$$d\ln[\text{Sample}]/dt = -k_a[\text{Cl}] \qquad \text{(Equation 4.1)}$$

$$d\ln[\text{Reference}]/dt = -k_b[\text{Cl}] \qquad \text{(Equation 4.2)}$$

Integration of the above yields:

$$\ln[\text{Sample}]_t = -k_a \int_{t=0}^{t} [\text{Cl}]dt + \ln[\text{Sample}]_{t=0} \qquad \text{(Equation 4.3)}$$

$$\ln[\text{Reference}]_t = -k_b \int_{t=0}^{t} [\text{Cl}]dt + \ln[\text{Reference}]_{t=0} \qquad \text{(Equation 4.4)}$$

Following rearrangement, we obtain:

$$\ln\frac{[\text{Sample}]_t}{[\text{Sample}]_{t=0}} = -k_a \int_{t=0}^{t} [\text{Cl}]dt \qquad \text{(Equation 4.5)}$$

$$\ln\frac{[\text{Reference}]_t}{[\text{Reference}]_{t=0}} = -k_b \int_{t=0}^{t} [\text{Cl}]dt \qquad \text{(Equation 4.6)}$$

As such, it follows that:

$$\ln\frac{[\text{Sample}]_t}{[\text{Sample}]_{t=0}} = \frac{k_a}{k_b} \ln\frac{[\text{Reference}]_t}{[\text{Reference}]_{t=0}} \qquad \text{(Equation 4.7)}$$

Therefore, a plot of the logarithmic depletions of the sample against the logarithmic depletion of the reference compound should yield a straight line passing through, or close to, the origin with a gradient

k_a / k_b. As the rate coefficient for the reaction between Cl and the reference compound, k_b, is known, multiplication of the gradient by k_b would yield the rate coefficient of the sample.

As the CRM technique does not monitor the change in concentration of the sample, the rate coefficient must instead be inferred from the measured reaction rates calculated at various sample concentrations based on the depletion of $(C_2H_5)_2O$. As unity between the literature and measured reaction rates was not achieved during the calibration of the CRM instrument, the rates must be corrected by applying the calibration term obtained in Figure 4.4. A plot of the resulting corrected rates against the concentration of the sample introduced into the reactor should yield a straight line with a gradient equivalent to the rate coefficient for the reaction with Cl.

Tests for this application of the CRM concept were conducted using 3,3-dimethyl-2-butanone (pinacolone, $C_6H_{12}O$), a compound identified as a potential "green" solvent to replace the use of hazardous, volatile, non-polar solvents such as toluene.[211] The classification of compounds as "green" solvents arises from their ability to be derived from renewable sources, low-toxicity and good solvation properties. Their atmospheric breakdown and subsequent impact on air quality are, however, often not considered.[211] An understanding therefore of the Cl loss term would provide a constraint against which their atmospheric breakdown could be determined.

CRM calculations were conducted at five different concentrations of $C_6H_{12}O$, with each measurement repeated three times and the average taken. As shown in Figure 4.5, least squares fitting of the corrected rates plot against the concentration of $C_6H_{12}O$ introduced into the system yields a rate constant of $(5.5 \pm 0.4) \times 10^{-11}$ cm^3 molecule^{-1} s^{-1} at approximately 298 K and 14.78 psi pressure. By comparison, without application of the aforementioned correction factor, a rate coefficient of $(5.9 \pm 0.5) \times 10^{-11}$ cm^3 molecule^{-1} s^{-1} was obtained. To gain an appreciation as to the feasibility of the proposed rate coefficient, comparisons were drawn to existing measurements for butanone for which a rate coefficient of 3.6×10^{-11} cm^3 molecule^{-1} s^{-1} has been reported by IUPAC.[15] Due to the structural similarities of both species, it would be expected that their rates of reaction with Cl would be comparable. This is reflected in their reactions with OH, for which rate coefficients of 1.1×10^{-11} and $(1.2 \pm 0.2) \times 10^{-11}$ cm^3 molecule^{-1} s^{-1} have been reported for butanone and $C_6H_{12}O$ respectively.[15, 212] Assuming the rate coefficients for reaction with Cl have a comparable difference, a theoretical rate coefficient of $(3.9 \pm 0.6) \times 10^{-11}$ cm^3 molecule^{-1} s^{-1} can be derived for $C_6H_{12}O$. Whilst such a rate coefficient falls outside of the uncertainty of the linear fit used to derive the experimental rate coefficient in this study, it is important to note that this is still within the uncertainty of the measured rate (30 %) as previously discussed. Consequently, should the CRM setup be used to derive further Cl rate coefficients, a reduction in this uncertainty is vital.

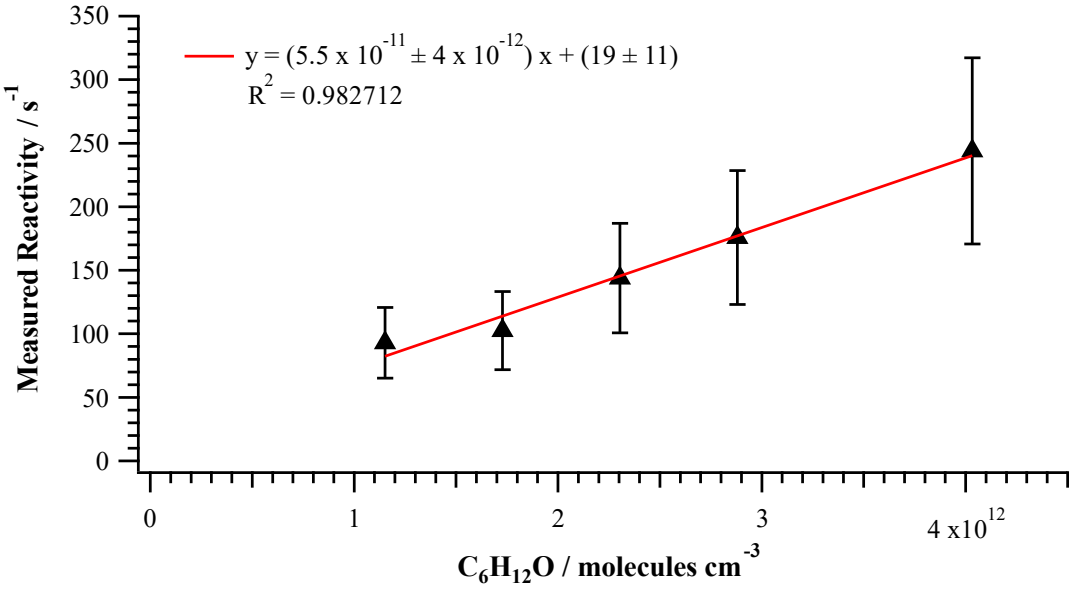

Figure 4.5. CRM plot for the reaction of $C_6H_{12}O$ with Cl at approximately 298 K and 14.78 psi pressure.

The attainment of a non-zero y-axis intercept of 19 s^{-1} in the linear fit used to derive the rate coefficient is also interesting to note. In part, this offset can be attributed to the application of the correction factor to the measured rates, however a y-axis intercept of 9 s^{-1} is still obtained if the uncorrected values were used in Figure 4.5 instead. As the intercept is positive, it can be inferred that the depletion of $(C_2H_5)_2O$ during the ***C3*** stage is smaller than expected when the added reactivity is low, potentially indicating a reduction in the amount of Cl-atoms available for reaction when compared to the ***C2*** stage. Such an observation is, however, in contrast to the negative y-axis intercepts that were obtained during the calibration of the instrument. Such an intercept could therefore potentially indicate the formation of additional radical species such as OH within the setup. To probe this further, model simulations of the $C_6H_{12}O$ CRM experiments were conducted in AtChem, with the mechanism for the reaction of $C_6H_{12}O$ and OH (and associated secondary reactions) extracted from the MCM. Simulations were also conducted for C_5H_8 to examine whether contrasting y-axis intercepts would be anticipated, with a detailed description of the mechanism used during these simulations provided later in this chapter (section 4.4.2.2). Model runs were conducted over a period of 11 seconds to replicate the experimental conditions; 10 seconds to account for the residence time within the reactor (during which the photolysis of Cl_2 was "switched on"), and an additional 1 second to account for the sample line connection to the SIFT-MS. To obtain a ***C1*** – ***C2*** depletion comparable to that observed during the CRM experiments, a value of 0.0348 s^{-1} was used for *j*Cl2, greater than the 0.0296 s^{-1} that was derived from the NO_2 actinometric experiments discussed in section 3.4.3. This discrepancy between the calculated and observed likely originates from wall losses of the radicals, a process which is expected to be of less significance in the CRM experiments

as both the VOC and Cl_2 are introduced into the reactor together thus enabling the Cl-atoms to react upon formation.

As can be seen from Figure 4.6(a), whilst a positive y-axis intercept is obtained from the modelled CRM experiments of $C_6H_{12}O$, the magnitude of the offset is substantially smaller than that observed for both the corrected and uncorrected experimentally derived rates. It should be noted, however, that the y-axis intercept for the uncorrected rate is below the LOD, and as such the discrepancy is likely the result of instrument noise. By comparison, however, whilst the simulated C_5H_8 rates yield a negative y-axis intercept as shown in Figure 4.6(b), the discrepancy between the model and experimentally derived intercepts exceeds the LOD. Based on the ***C1*** and ***C2*** concentrations used in the simulations, the 31.54 s^{-1} difference would account for an additional 0.94 ppbv depletion in $(C_2H_5)_2O$, potentially indicating an under-representation of the formation of OH within the model. Further laboratory experiments would be required to confirm this, potentially through the addition of an OH scavenging species such as CO and C_6H_6 – concepts which will be re-visited later.

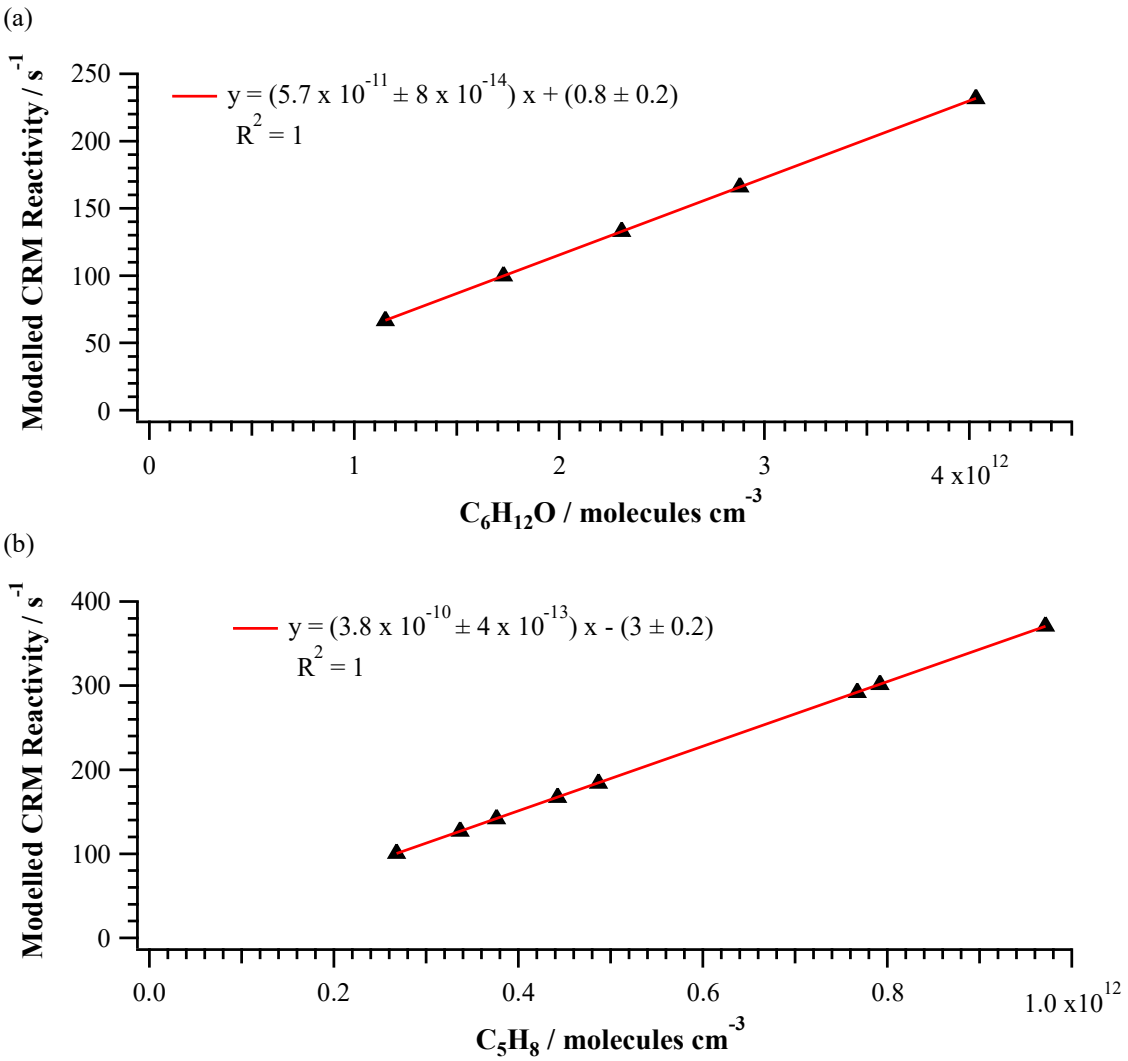

Figure 4.6. Modelled CRM experiments for the reaction between (a) $C_6H_{12}O$, (b) C_5H_8 and Cl.

4.4 Impact of NO on Reactivity Measurements

4.4.1 Experimental Measurements

In order to compare the reactivity rates obtained from the Cl-CRM instrument against the literature, the experiments reported earlier in this chapter were conducted in zero air. However, as the instrument is ultimately designed to measure Cl reactivity with ambient air, the impact of NO on the calculated reactivity rates should also be considered. As discussed in section 1.2, NO will react with HO_2 produced during the oxidation of hydrocarbons to form OH. This can interfere with the calculated reactivity rate if the OH radicals subsequently react with the reference VOC, resulting in a lower than expected ***C3*** concentration thereby reducing the calculated reactivity rate as identified in section 3.3.3 of this thesis. To probe how significant this secondary chemistry would be, reactivity measurements of the 35-component mixture were repeated with the inclusion of 4.6 and 15.0 ppbv of NO, concentrations comparable to the mean and maximum observations from the 2010 Clearflo campaign at the North Kensington, London site (5.5 and 11.9 ppbv based on an easterly flow).[171] When conducting these experiments, the total flowrate in the setup was kept consistent with those used in previous experiments (500 sccm) with the zero air carrier gas flow reduced to accommodate the required flow rate of NO. As with the previous experiments discussed, measurements were repeated three times with the average rate taken. It was observed that the inclusion of NO into the system had a profound effect on the calculated rate, with a previously measured rate of (210 ± 20) s^{-1} dropping to (64 ± 20) and (27 ± 30) s^{-1} in the presence of 4.6 and 15.0 ppbv of NO respectively. It is therefore clear that the current experimental setup would not be suitable for measuring ambient air reactivity unless in low NO_x conditions (< 10 pptv) such as those experienced in remote marine environments and rainforests. It is acknowledged, however, that within these environments the lack of sensitivity of the instrument may prove to be an issue instead.

4.4.2 AtChem Simulations

4.4.2.1 Methane / Propane Mixture

In order to investigate the impact of NO on the system, and the reproducibility of the experimental measurements, a set of idealised model simulations of the aforementioned experiments were carried out in AtChem. To minimise the complexity and uncertainty in the secondary chemistry involved, initial model runs were conducted investigating the CH_4 / C_3H_8 system discussed in section 4.2.1. Primary reactions (VOC + Cl) were at first only considered to establish a baseline against which the impact of secondary chemistry could be compared. The model was initialised with CH_4 and C_3H_8 concentrations of 2.48×10^{12} molecules cm^{-3} which, based upon the literature rate coefficients, should yield a rate of 344 s^{-1}. Under these conditions, however, a rate of 347 s^{-1} was calculated using the CRM technique. As discussed in section 3.3.2, this discrepancy arises from a combination of the non-

pseudo first-order conditions that have been used in the experiment and the varying rate of reactivity of the sample and reference VOC with Cl over the course of a measurement.

The impact of the increasing concentrations of NO on the CRM rate upon the addition of secondary chemistry, extracted from the MCM, is presented in Figure 4.7.[157] Interestingly, it is initially observed that under low NO concentrations (≤ 2 ppbv) the model rate is greater than that calculated when considering only primary reactions. Such an increase in rate can only arise following an increase in the ***C3*** concentration, indicating that either the amount of Cl-atoms available to react with $(C_2H_5)_2O$ has been reduced or that the concentration of CH_4 and C_3H_8 within the system has been reduced through reaction with another radical such as OH. To probe the source of this reduction, analysis was conducted on the loss rates of Cl. Whilst losses to $(C_2H_5)_2O$, CH_4 and C_3H_8 dominate, it is observed that losses to HCHO, and to a lesser extent HO_2, are also present. These contributions increase as the concentration of NO within the system increases as shown in Figure 4.8(a); a result of the elevated levels of HCHO and HO_2 following the oxidation of $(C_2H_5)_2O$ and C_3H_8 (and to a lesser extent CH_4). Removal of the aforementioned Cl sinks from the mechanism brings the calculated rate within these region below the primary rate, following the trend observed at the higher NO concentrations as shown in Figure 4.8(b).

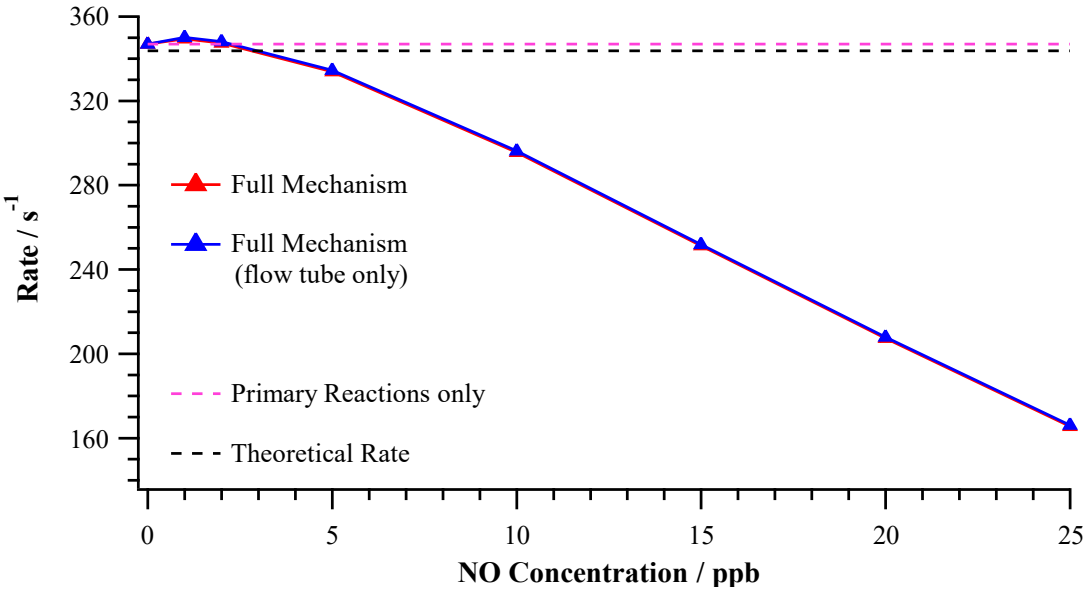

Figure 4.7. CRM calculations derived for the CH_4 / C_3H_8 mixture considering the full mechanism and primary reactions only.

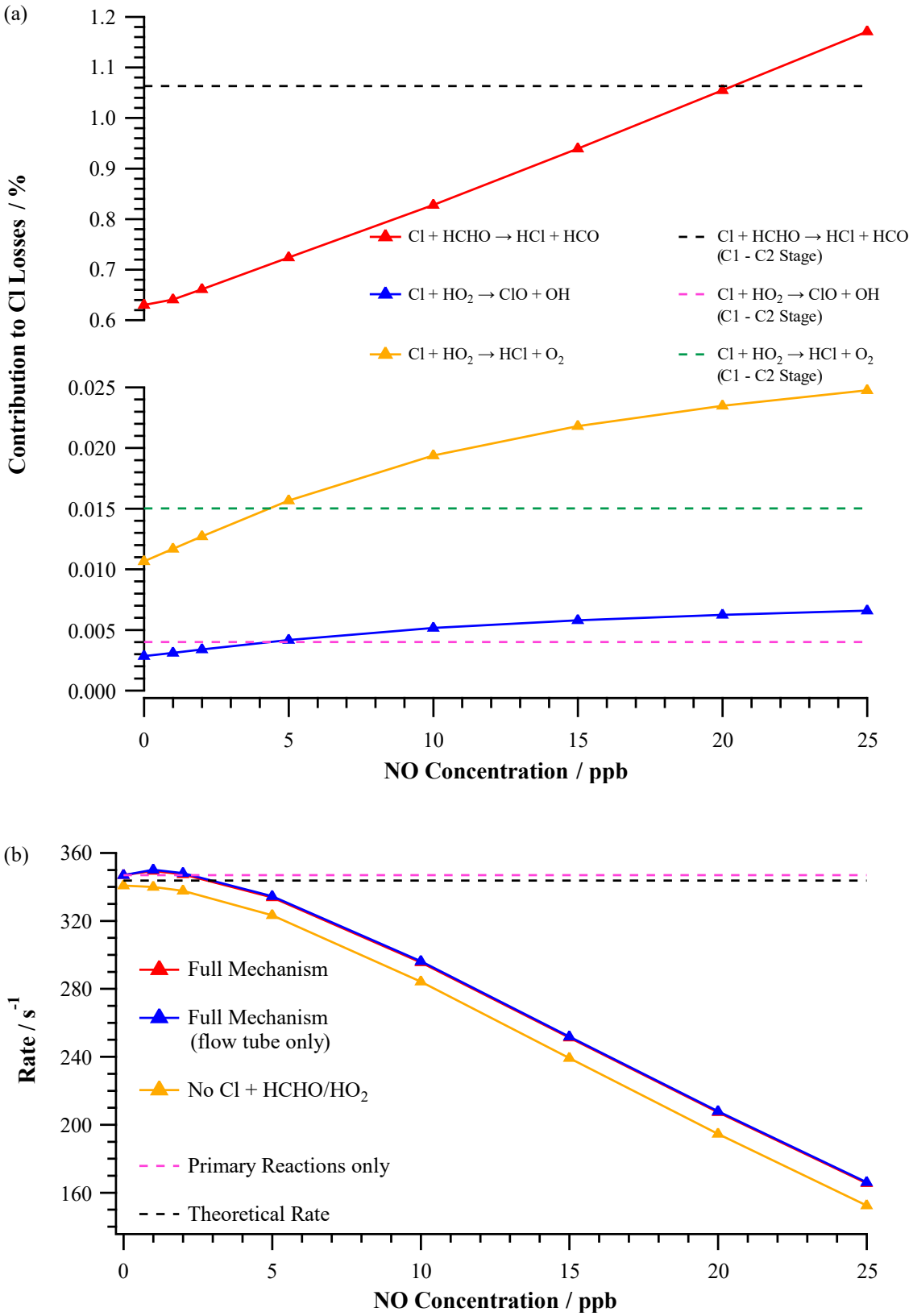

Figure 4.8. (a) Breakdown of the Cl losses observed with the full mechanism for the CH_4 / C_3H_8 mixture within AtChem. (b) Impact on calculated rate upon the removal of the HO_2 and HCHO sink reactions from the model.

As expected based on the increased HCHO and HO_2 production from the oxidation of $(C_2H_5)_2O$, the observed decrease in the CRM rate at higher NO concentrations is the result of increasing formation of OH and subsequent reaction with the reference VOC as summarised in Figure 4.9(a). Analysing the production rates of OH, the dominant source in the absence of NO is the reaction between Cl and HO_2 - responsible for 96% of the total OH production. Upon initialising the model with 1 ppbv of NO, however, this contribution drops to just 6%, with the reaction between NO and HO_2 subsequently accounting for 94% of the OH production within the system. The removal of the reaction between $(C_2H_5)_2O$ and OH brings the resulting calculated rates into much better agreement with the primary rate as shown in Figure 4.9(b), with the slight offset at higher concentrations of NO attributed to the loss of CH_4 and C_3H_8 through reaction with OH instead.

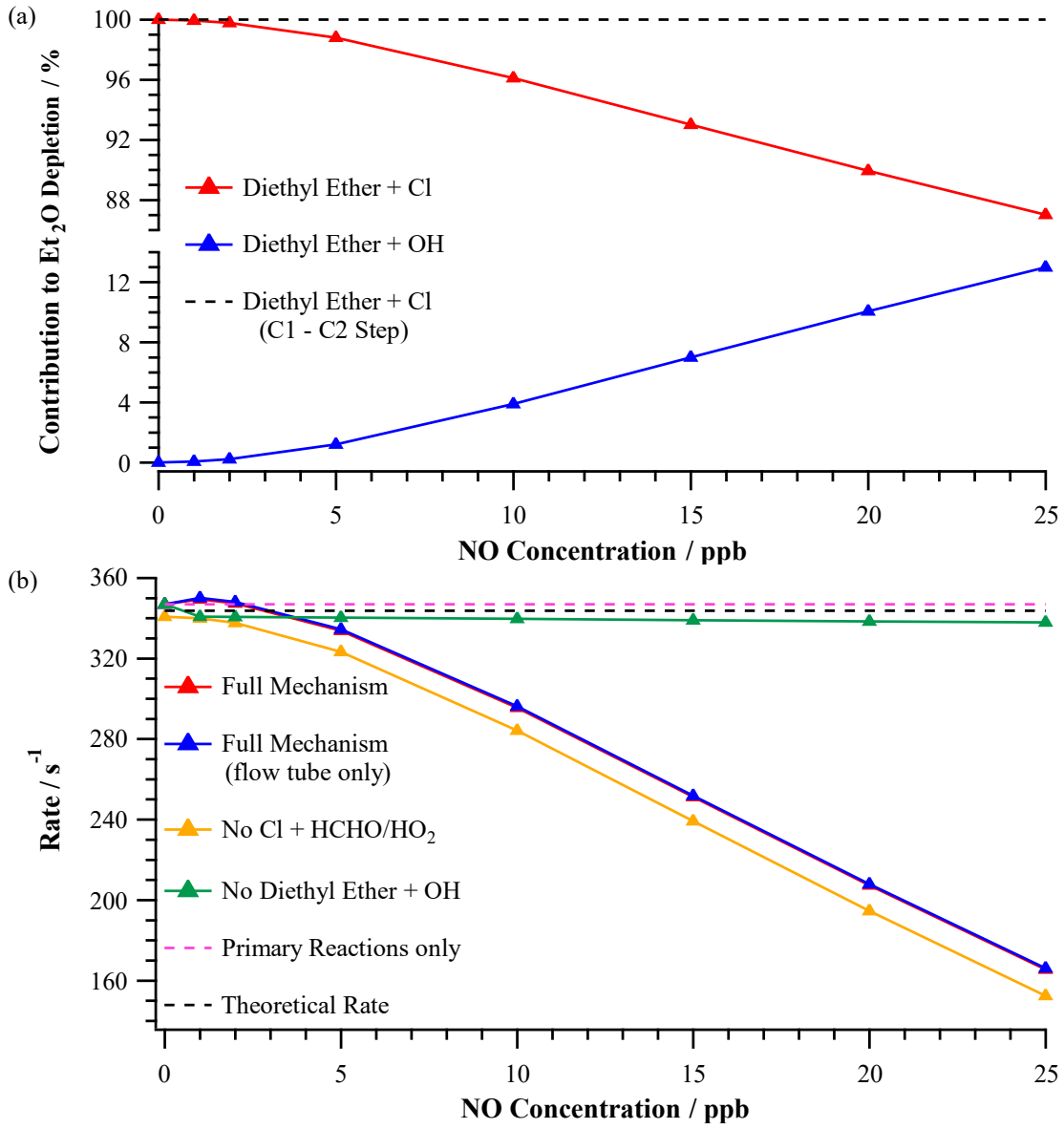

Figure 4.9. (a) Breakdown of the $(C_2H_5)_2O$ losses observed with the full mechanism for the CH_4 / C_3H_8 mixture. (b) Impact on calculated rate upon the removal of the OH + $(C_2H_5)_2O$ reaction from the model.

4.4.2.2 Isoprene

Having developed a model which re-created the conditions of the CRM reactor for the CH_4 / C_3H_8 mixture, the impact of NO on measuring the reactivity of C_5H_8 was analysed. As the chemistry of C_5H_8 with Cl is not included in the MCM, additional reactions were added based upon the mechanism proposed by Wennberg et al. as presented in Figure 4.10.[213] Briefly, C_5H_8 predominantly reacts with Cl via an addition mechanism with theoretical studies conducted at 300 K determining branching ratios for this pathway of 0.40:0.02:0.08:0.50 at the 1:2:3:4 positions respectively.[214] Experimental measurements have also identified the abstraction of a methyl hydrogen to yield HCl and an allylic radical, with NASA JPL recommending a branching fraction of 0.15 at 298 K for this pathway; an average of the values obtained from the aforementioned experimental measurements.[179, 203, 204, 215-217] Combining both these pathways, and by assuming that the addition of Cl to the inner carbon atoms of the double bonds is negligible, Wennberg *et al.* recommend branching fractions of 0.15:0.38:0.47 for the abstraction : 1-addition : 4-addition pathways respectively at 298 K. The resulting radicals rapidly react with O_2 to form peroxy radicals. In the case of the addition products, whilst the fate of these peroxy radicals has been proposed by Wennberg *et al.* the rate constants for their reactions with HO_2 and NO are unknown. To account for this, the peroxy radicals are treated instead as species which already exist as part of the MCM C_5H_8 mechanism (CISOPAO2, ISOPDO2, CISOPCO2 and ISOPBO2), in which the structures only differ by having an OH functional group as opposed to a Cl atom. For the abstraction pathway, the proposed mechanism terminates at the peroxy radical and as such no subsequent reactions are considered within the model.

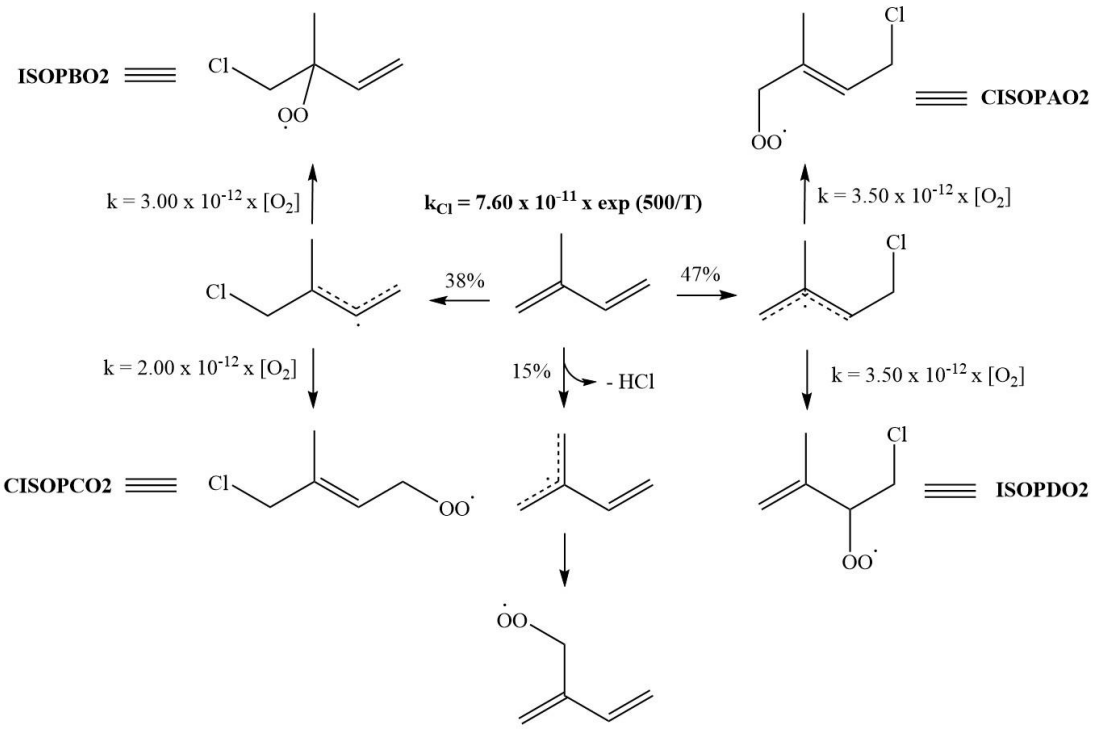

Figure 4.10. Mechanism and rate constants for the reaction between Cl and C_5H_8 used within the AtChem simulations alongside the existing MCM mechanism.

Reactions of Cl with the major first-generation products of the oxidation of C_5H_8 methyl vinyl ketone (MVK) and methacrolein (MACR) were also added to the model, with the incorporated schemes presented in Figures 4.11(a) and (b) respectively. Product yields for these reactions were estimated, and scaled to 100%, based on Kaiser *et al*. and Orlando *et al*.,[175, 218] with a rate coefficient of 2.1 × 10^{-10} and 2.2 × 10^{-10} cm^3 $molecule^{-1}$ s^{-1} for MVK and MACR respectively obtained from JPL.[179] Peroxy radicals formed following the addition of Cl are treated as their OH counterparts (highlighted in bold in Figure 4.11) in the model.

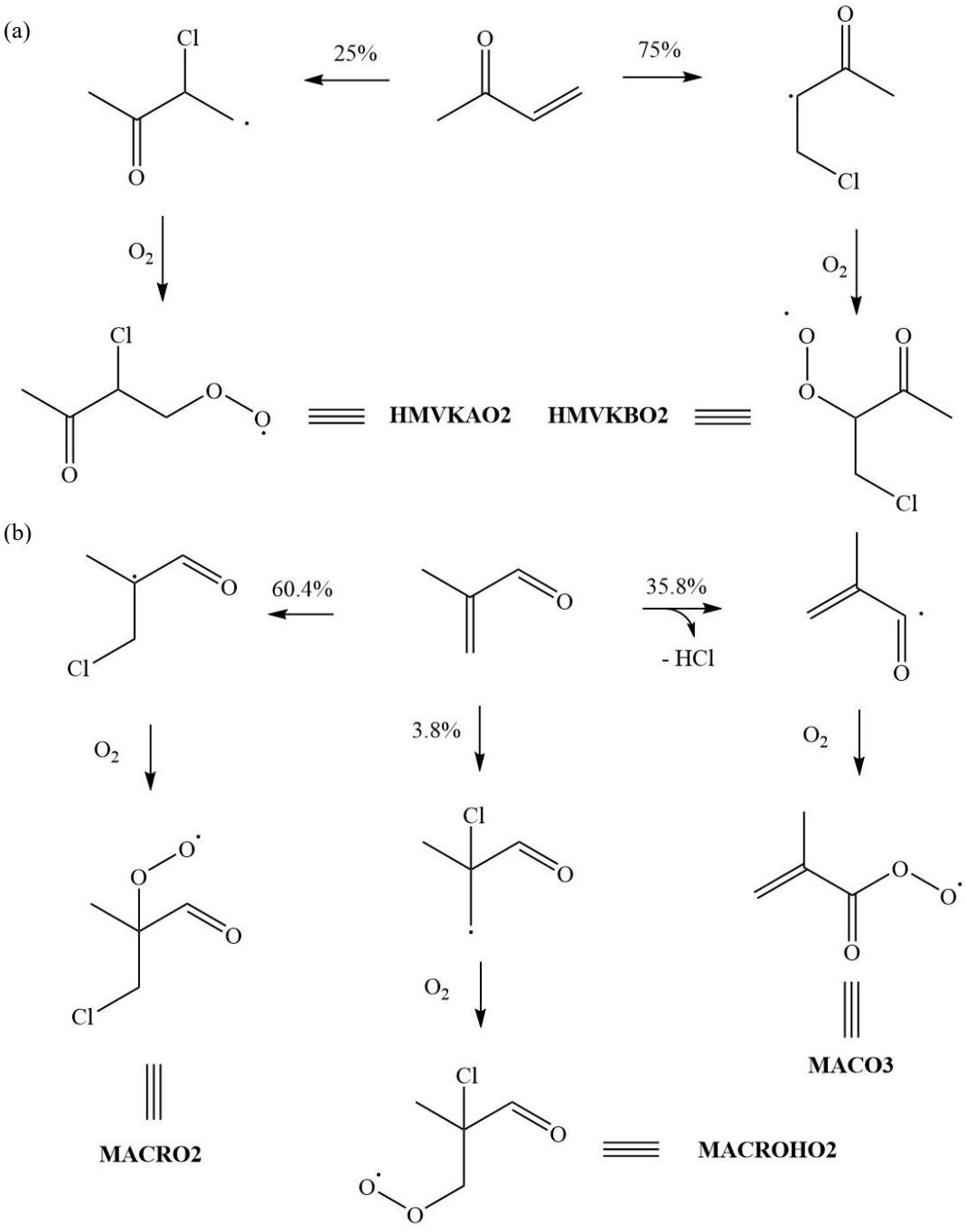

Figure 4.11. Mechanism and branching ratios for the reaction between Cl and (a) MVK, (b) MACR used within the AtChem simulations alongside the existing MCM mechanism.

The model runs were initialised with an C_5H_8 mixing ratio of 31.2 ppbv which, based upon a rate constant of 4.07×10^{-10} cm^3 $molecule^{-1}$ s^{-1}, should yield a rate of 312 s^{-1}. As was found with the CH_4 / C_3H_8 model runs however, there is an offset between the modelled CRM derived rate and the literature rate of 30 s^{-1} and as such this value will be used as the baseline against which the impact of secondary chemistry will be considered. With respect to the changes observed upon the introduction of NO into the system, the trend is comparable to that observed with the CH_4/C_3H_8 mixture as shown in Figure 4.12(a). Upon considering the full mechanism, we initially obtain a CRM rate greater than that calculated from the primary reactions, a feature arising from the loss of Cl radicals through reaction with either HO_2 or HCHO, whilst the general decrease in the calculated rate with elevated NO concentrations coincides with increased losses of $(C_2H_5)_2O$ to OH as depicted in Figure 4.12(b). Upon the removal of this reaction from the mechanism the calculated rate increases, although the trend of decreasing rate with NO is still observed due to the loss of C_5H_8 through the reaction with OH - increasing the amount of Cl available to react with $(C_2H_5)_2O$.

One notable difference between the two systems is that, upon the removal of the reaction between $(C_2H_5)_2O$ and OH, the calculated rate is initially greater than that obtained when considering only the primary reactions at NO concentrations below 10 ppbv. This difference arises from the additional Cl loss pathways through MACR and MVK; the contributions of which are shown in Figure 4.12(c). In general, the loss of Cl to both species increases as the NO concentration increases due to the additional oxidation of C_5H_8 brought about by the elevated levels of OH within the system.

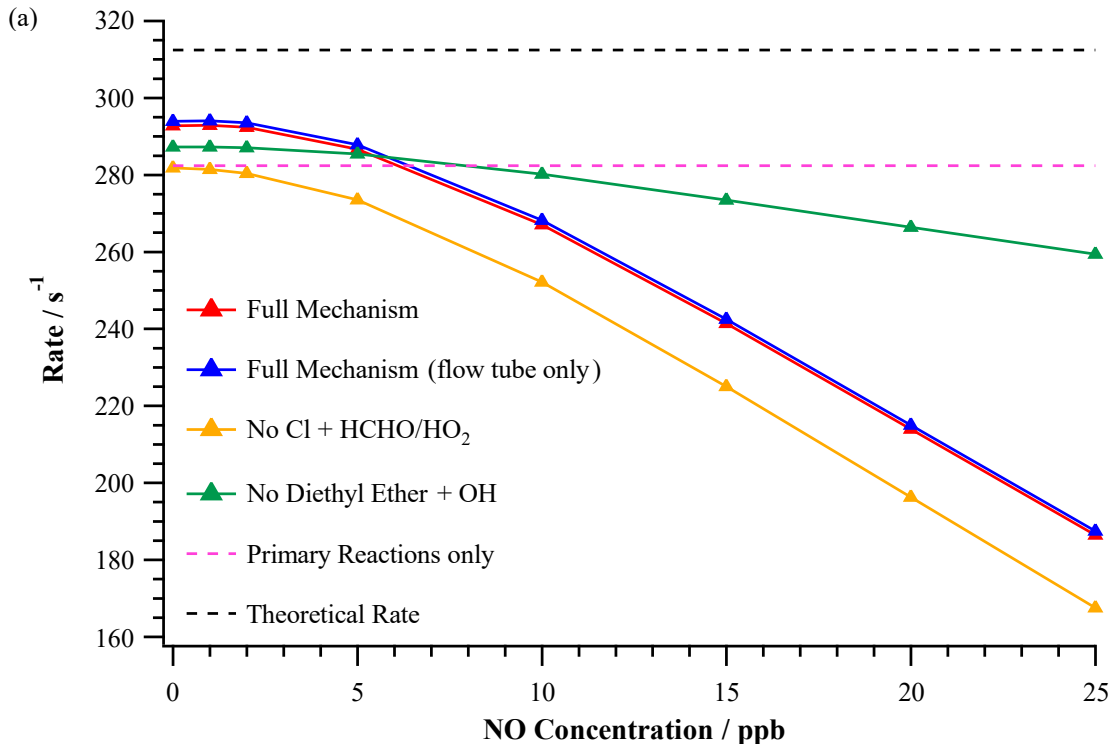

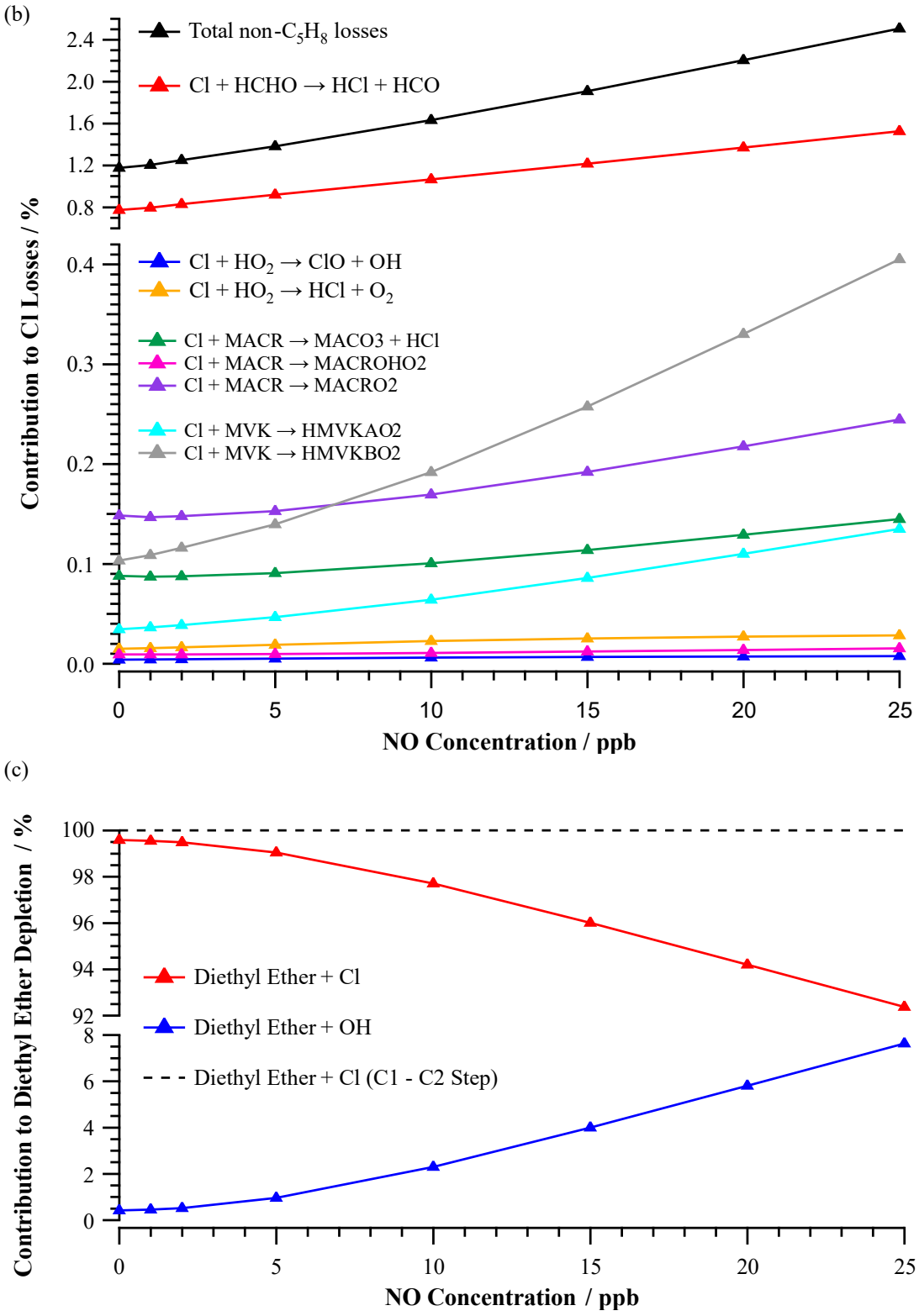

Figure 4.12. (a) CRM calculations derived from the AtChem simulations of the C_5H_8 system. Breakdown of the (b) Cl, (c) $(C_2H_5)_2O$ losses observed with the full mechanism for the C_5H_8 system.

4.4.2.3 35-Component Mixture

As the model runs of the previous systems identified that NO could have a substantial impact on the CRM rate as a result of the secondary chemistry it introduces, the 35-component mixture was modelled within AtChem to determine if a similar rate could be obtained to that calculated during the experimental measurements. The rate coefficients used within the model are given in Table 4.1 with the mechanisms of MACR and MVK outlined in the previous section incorporated in the model to account for the presence of C_5H_8 within the gas mixture. It should be noted that both cyclopentane and 2,2,4-trimethylpentane do not exist within the MCM and as such only their primary reactions are considered within the model. As with the previous two systems, it was found that there was a discrepancy between the CRM calculated rate and that obtained from the literature rate coefficients (149 and 167 s^{-1} respectively). A breakdown of the model runs as conducted for the previous two systems is given in Figure 4.13. The explanation for the trends observed upon each adjustment of the model is consistent with that of the other systems and as such will not be repeated here.

In comparison to the experimental measurements, the model calculated CRM rate in the absence of NO, 162 s^{-1}, is lower than the experimentally measured rate of 210 s^{-1}. It should be noted, however, that the rate is still within the uncertainty of the measured rate and also does not take into account the uncertainty in the rate coefficients used in the model. When considering the impact of NO on the system, however, there is a much poorer agreement between the model and the experimentally derived rates. Considering first an NO concentration of 5 ppbv, the model derived rate drops by 7.2 s^{-1} when compared to initialising the model without NO. By comparison, whilst using a lower NO concentration of 4.6 ppbv, the CRM rate dropped by 146 s^{-1} in the experimental measurements. Similarly, at 15 ppbv NO, the experimental rate dropped by 183 s^{-1} whilst a decrease of 60.1 s^{-1} was observed within the model. Whilst some discrepancy between the model and experimental measurements could be rationalised by the missing secondary chemistry of cyclopentane and 2,2,4-trimethylpentane, the magnitude of difference observed here indicates that there must be a much more significant source of OH that is not currently being considered within this analysis and as such will be explored further herein.

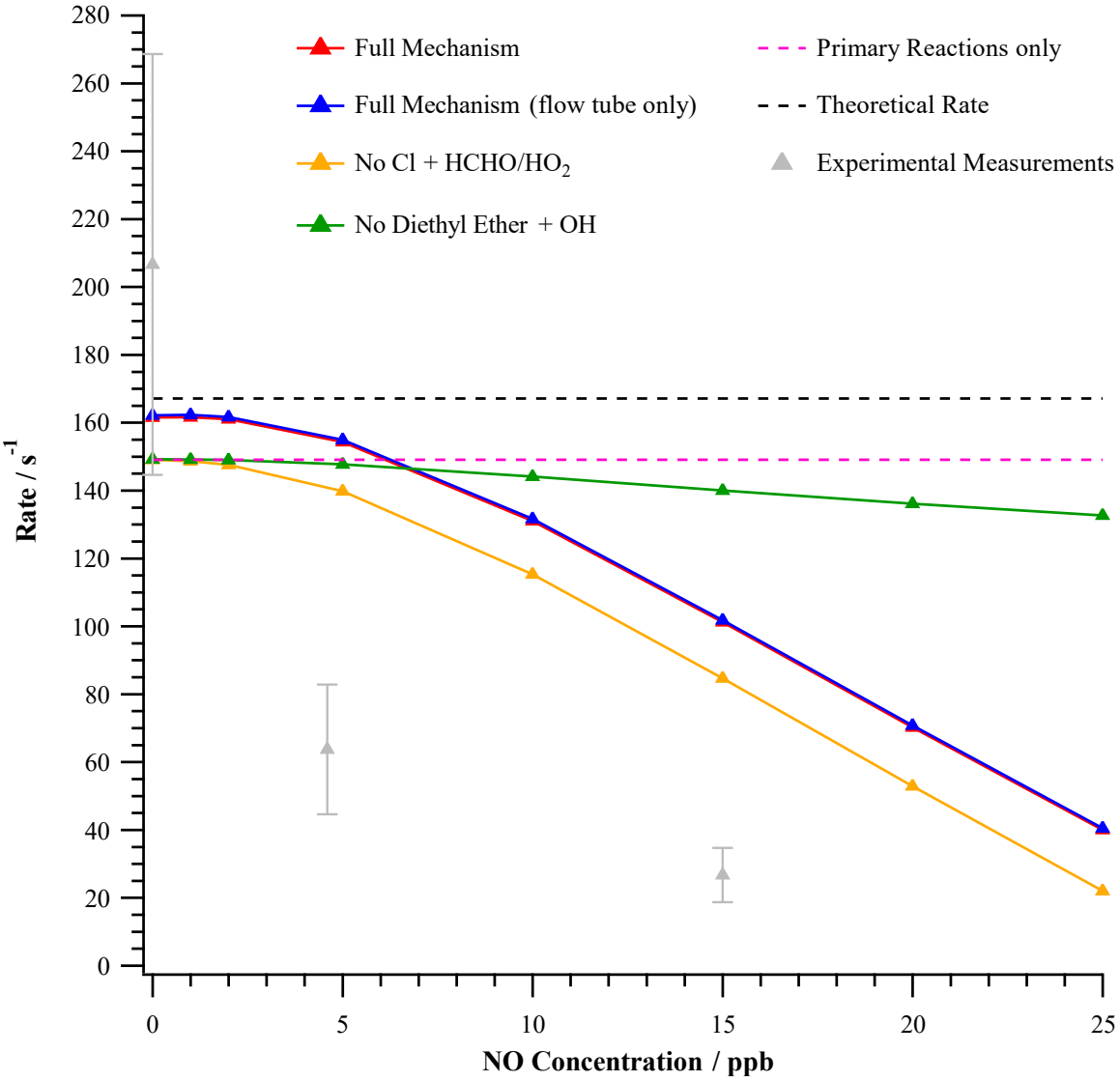

Figure 4.13. CRM calculations derived from the AtChem simulations of the 35-component system.

4.5 Impact of Photolysis on Reactivity Measurements

One factor not considered within the previous AtChem simulations was the impact of photolysis on the gas standard being analysed, a potential source of additional OH radicals which may account for the discrepancy between the model calculated rates and the experimental measurements. As discussed in section 1.2, the predominant source of OH within the troposphere stems from the photodissociation of O_3. As O_3 should not be present in any of the gas standards, nor the zero-air carrier gas, this is unlikely to be a significant contributor to OH formation within the lab experiments. It is, however, acknowledged that this may act as a source of OH when measuring ambient air, and as such will be incorporated into the model. The photolysis of HCHO, already identified as being present at appreciable levels such that it can contribute to ~ 1% of the total Cl sink within the setup, is an additional potential source of OH radicals within this work. Through one of the photolysis channels, reaction 4.2, HCO and H radicals are generated from HCHO which can rapidly react with O_2 to produce 2 HO_2 radicals. As discussed previously this can then go on to react with NO to generate OH alongside NO_2.

$$HCHO + h\nu \rightarrow H + HCO \qquad \lambda < 330\ nm \qquad \text{(Reaction 4.2)}$$

$$H + O_2 + M \rightarrow HO_2 + M \qquad \text{(Reaction 4.3)}$$

$$HCO + O_2 \rightarrow HO_2 + CO \qquad \text{(Reaction 4.4)}$$

To a lesser extent, the photodissociation of any hydrogen peroxide and other oxygenated VOCs produced within the system may also function as a source of OH. To evaluate the importance of these processes, photolysis rates were calculated alongside additional existing photochemical reactions within the MCM. Calculations were achieved in a similar fashion to that used during the lamp flux measurements in section 3.4.3, with a correction factor obtained by scaling the $j$$Cl_2$ valued used in AtChem to the lamp power output supplied by the manufacturer. A summary of the reactions added to the model, the calculated photolysis rates, and sources of the absorption cross sections and quantum yields used during these calculations is given in Table 4.2.

Table 4.2. Summary of the photolytic reactions, their literature absorption cross sections and quantum yields, incorporated within the AtChem models and the calculated rates used in this study. †A quantum yield of 1 is assumed over the modelled wavelength based on the work of Peeters *et al*.[219]

Reaction	MCM Designation	Calculated j value / s^{-1}	Absorption Cross Section	Quantum Yield
$O_3 \rightarrow O(^1D) + O_2$	1	1.60×10^{-2}	220	202
$O_3 \rightarrow O(^3P) + O_2$	2	2.95×10^{-3}	220	202
$H_2O_2 \rightarrow 2OH$	3	6.07×10^{-4}	202	202
$NO_2 \rightarrow NO + O(^3P)$	4	9.93×10^{-2}	202	202
$HCHO \rightarrow H + HCO$	11	1.57×10^{-3}	15	15
$HCHO \rightarrow H_2 + CO$	12	1.07×10^{-3}	15	15
$CH_3CHO \rightarrow CH_3 + HCO$	13	1.05×10^{-3}	15	15
$C_2H_5CHO \rightarrow C_2H_5 + HCO$	14	2.49×10^{-3}	15	15
$C_3H_7CHO \rightarrow n\text{-}C_3H_7 + HCO$	15	7.88×10^{-4}	15	15
$C_3H_7CHO \rightarrow C_2H_4 + CH_3CHO$	16	3.75×10^{-4}	15	15
$(CH_3)_2CHCHO \rightarrow n\text{-}C_4H_9 + HCO$	17	2.83×10^{-3}	221	222
C_4H_6O (MACR) $\rightarrow CH_2{=}CCH_3 + HCO$	18	1.63×10^{-5}	15	15
C_4H_6O (MACR) $\rightarrow CH_2{=}C(CH_3)CO + H$	19	1.63×10^{-5}	15	15
$C_5H_8O_3 \rightarrow CH_3C(CHO){=}CHCH_2O + OH$	20	8.36×10^{-3}	223	†
$CH_3COCH_3 \rightarrow CH_3CO + CH_3$	21	4.42×10^{-4}	224	225
$CH_3CH_2COCH_3$ (MEK)$\rightarrow CH_3CO + C_2H_5$	22	3.43×10^{-4}	221	226
$CH_3COCHCH_2$ (MVK) $\rightarrow CH_3CHCH_2 + CO$	23	8.78×10^{-5}	223	223
$CH_3COCHCH_2$ (MVK) $\rightarrow CH_3CO + C_2H_3$	24	8.78×10^{-5}	223	223
$C_2H_2O_2$ (GLYOX) $\rightarrow 2\ CO + H_2$	31	4.74×10^{-4}	227	228
$C_2H_2O_2$ (GLYOX) $\rightarrow HCHO + CO$	32	1.25×10^{-3}	227	228
$C_2H_2O_2$ (GLYOX) $\rightarrow 2HCO$	33	1.49×10^{-3}	227	228
$C_3H_4O_2$ (MGLYOX) $\rightarrow CH_3CO + HCO$	34	2.02×10^{-3}	229	230
$C_4H_6O_2$ (BIACET) $\rightarrow 2\ CH_3CO$	35	1.99×10^{-3}	231	232
$CH_3OOH \rightarrow CH_3CO + OH$	41	2.33×10^{-4}	15	15

4.5.1 Methane / Propane Mixture

Repeating the AtChem modelling of the CH_4 / C_3H_8 mixture with the photolysis reactions included, a significant increase is observed in the loss of $(C_2H_5)_2O$ through reaction with OH as shown in Figure 4.14(a). This is reflected in the calculated reactivity rate, given in Figure 4.14(b), in which the addition of these reactions results in a decrease in the calculated rate by as much as 53 s^{-1} at an NO concentration of 25 ppbv. Analysing the production rates for OH within the model runs, the

photodissociation of H_2O_2 is simulated to contribute 2% of the OH generated within the system in the absence of NO. Upon introducing NO into system, production of OH via this pathway is negligible. Instead, the reaction between HO_2 and NO continues to be the dominant source of OH within the setup, accounting for 81% of its production in the presence of 1 ppbv of NO and up to 98% at 25 ppbv. With regards to the sources of this increase in HO_2, the photodissociation of HCHO is fairly minor, accounting for only 2% at 25 ppbv of NO. Removal of this pathway from the mechanism results in an increase of just 2 s^{-1} in the CRM rate. Instead, the dominant sources of HO_2 within these model runs are $C_2H_5OCH_3O$ (ETOMEO, 52%), CH_3O (15%), i-C_3H_7O (15%) and n-C_3H_7O (12%). As all of these species were present in the system in the original AtChem simulations, it is clear that their concentrations must be increased via the photolysis of precursor species.

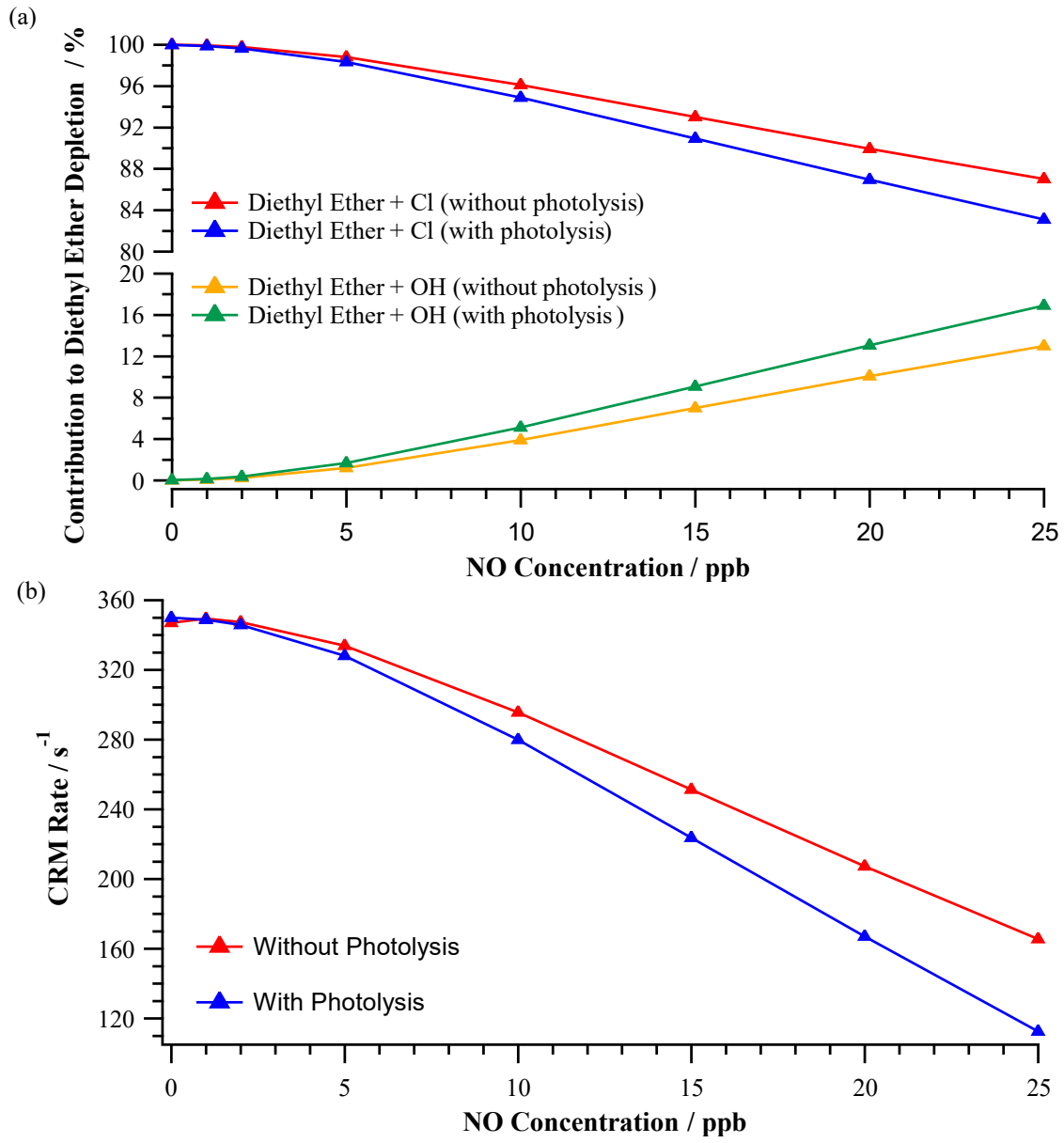

Figure 4.14. (a) Breakdown of the $(C_2H_5)_2O$ losses observed in the CH_4 / C_3H_8 system with/without photolysis within the AtChem simulations. (b) Corresponding CRM calculations.

4.5.2 Isoprene

As with the CH_4 / C_3H_8 mixture, the addition of photolysis into the C_5H_8 mechanism has a significant impact on the level of contribution OH has on the loss of $(C_2H_5)_2O$ as depicted in Figure 4.15(a), with the resulting CRM rates given in Figure 4.15(b). Again, the reaction between NO and HO_2 is the dominant source of OH within the system, accounting for 93% at 25 ppbv NO, with 2% of this being derived from the photolysis of HCHO. The photolysis of MVK provides a negligible contribution (< 0.1%) to the formation of HO_2 despite both photodissociation pathways of MVK yielding H and HCO radicals like HCHO. This, however, can be justified upon comparing the rates at which both species are photolysed, with HCHO undergoing photodissociation at approximately 2 orders of magnitude greater than MVK.

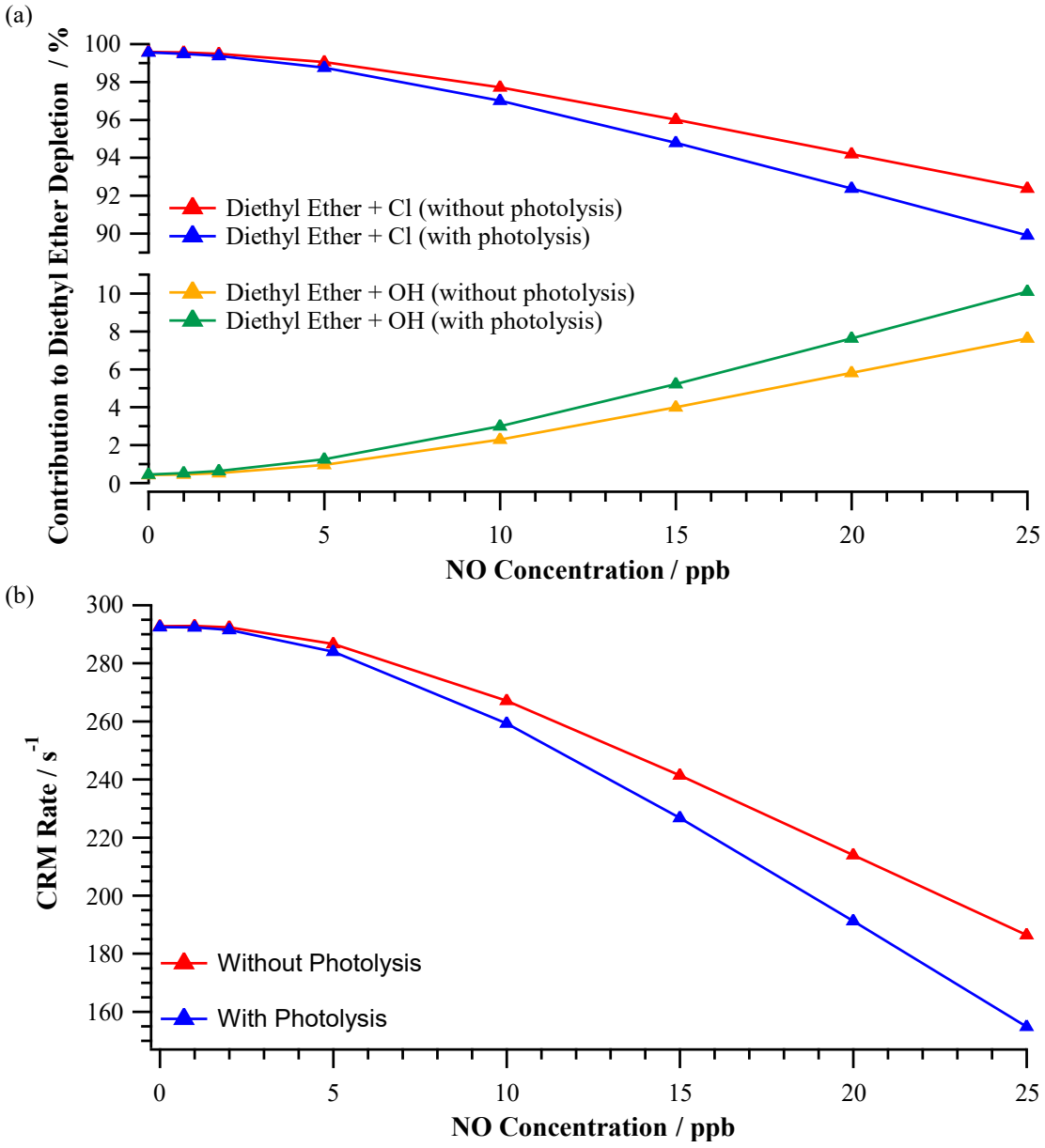

Figure 4.15. (a) Breakdown of the $(C_2H_5)_2O$ losses observed in the C_5H_8 system with/without photolysis within the AtChem simulations. (b) Corresponding CRM calculations.

4.5.3 35-Component Mixture

Whilst consideration of photolytic processes results in an increase in the fractional loss of $(C_2H_5)_2O$ to OH and a subsequent reduction in the modelled reactivity rate for the 35-component mixture, as depicted in Figures 4.16(a) and (b) respectively, a significant discrepancy is still observed between the modelled and experimental reactivity measurements. For example, whilst the CRM rate was simulated to drop from 101 s^{-1} to 84 s^{-1} at 15 ppbv NO, such a rate is still approximately a factor of 3 greater than the experimentally derived rate of 27 s^{-1}. Similarly, the rate simulated following the addition of 5 ppbv NO (151 s^{-1}), is 87 s^{-1} faster than the experimentally derived rate obtained at a lower NO concentration of 4.6 ppbv. Both discrepancies are in excess of the 30% uncertainty in the measured rate, potentially indicating that there is an additional source of OH which is not being considered within the simulations. By considering the ***C1*** and ***C2*** concentrations used in the simulations, the difference in rates would suggest an additional 2.5 and 1.7 ppbv of OH that is unaccounted for within the model simulations following the addition of 4.6 and 15 ppbv NO respectively.

To gain confidence that the chemistry within the model is representative of the experimental conditions, it is therefore recommended that additional rate measurements are conducted at various NO concentrations within the range that has been studied here. Furthermore, as it has been established that the introduction of NO into the CH_4 / C_3H_8 mixture would have a significant impact on the calculated rate, it is recommended that these experiments are initially conducted for that system since the secondary chemistry associated with both species is simpler and better understood than that of the 35-component mixture. Unfortunately owing to a lack of access to the SIFT-MS, these studies could not be conducted as part of this thesis.

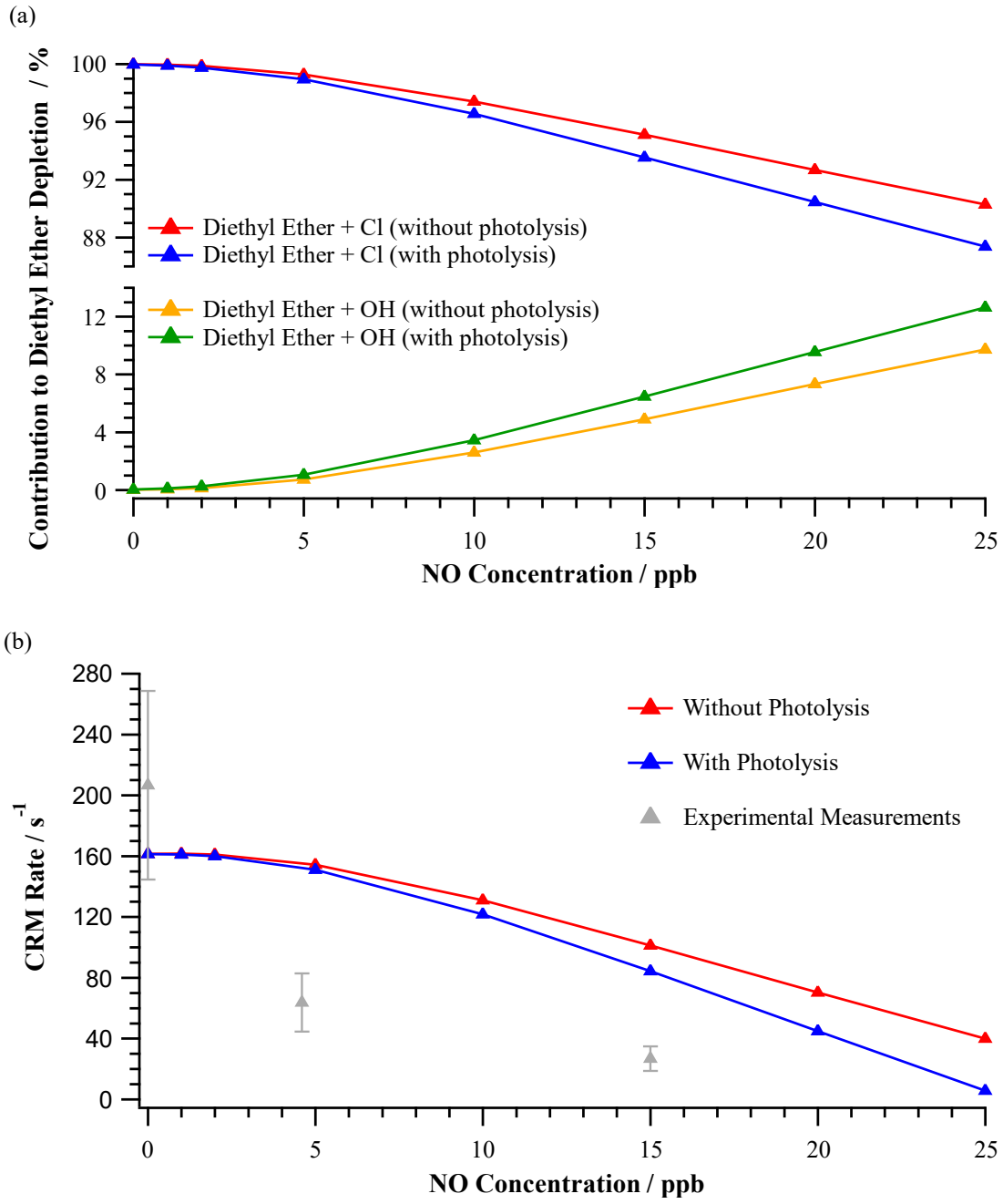

Figure 4.16. (a) CRM calculations derived from the AtChem simulations of the 35-component system upon the addition of photolytic reactions. (b) Breakdown of the $(C_2H_5)_2O$ losses observed with the full mechanism.

4.6 Secondary Chemistry Mitigation

As it is clear both from the AtChem simulations and the experimental observations that the developed Cl-CRM instrument is not suitable for measuring ambient air in environments with significant levels of NO_x due to the NO interference, attention shifted to identifying a potential route by which this secondary chemistry could be mitigated. One clear route in which this could be achieved is through introducing the reference VOC and sample downstream of the photolysis of Cl_2, however as attempts to achieve this with the CRM reactor used in this work were found to be unsuccessful, this would require the re-designing of the reactor and potentially a new photolysis source. As such this section investigates the options available to achieve this utilising the existing setup, although alternative reactor designs will be explored in section 4.7.2 later in this chapter. In general, three different avenues were explored; the use of an OH scavenger that could be introduced into the system to react with any OH formed over the course of the measurement, an adjustment of the residence time within the reactor to minimise the length of time available for secondary chemistry to occur, and a correction factor to account for the NO artifact. A detailed discussion of these is presented in the following sub-sections.

4.6.1 OH Scavenger

In order to prevent the addition of another Cl loss mechanism within the CRM setup, any scavenger species used would either need to react solely, or at least preferentially, with OH. Beyond its lack of reactivity with Cl, the use of CO for this application would be desirable as it is not detectable through SIFT-MS and as such would not consume reagent ions which would otherwise reduce sensitivity. Furthermore, the chemistry between CO and OH is well established as summarised by the following reactions:

$CO + OH \rightarrow H + CO_2$	k_3	(Reaction 4.5)
$H + O_2 + M \rightarrow HO_2 + M$	k_4	(Reaction 1.12)
$CO + OH + M \rightarrow HOCO + M$	k_5	(Reaction 4.6)
$HOCO + O_2 \rightarrow HO_2 + CO_2$	k_6	(Reaction 4.7)

As HOCO rapidly reacts to form HO_2 and CO_2 in the presence of excess O_2, both reaction pathways would ultimately yield the same products within the CRM reactor.[233] As such, the rate constant 2.4×10^{-13} cm^3 $molecule^{-1}$ s^{-1} can be used to represent k_3 alone.[15] Since these reactions are well understood, it follows that any additional secondary chemistry which may arise from its addition, in particular following the formation of HO_2, can be quantified within the AtChem models with a high degree of confidence. The key drawback however with the use of CO is its associated health and safety risks owing to its odourless, tasteless, and colourless properties. This would require the operator or building within which the setup is housed to have a CO alarm to ensure that the operator is not unknowingly exposed to a potential leak. Should CO be found to be unfeasible, a potential

alternative is benzene (C_6H_6). Whilst reactions between Cl and C_6H_6 have been reported, the reaction proceeds at a rate approximately three orders of magnitude slower than analogous reaction with OH (1.2×10^{-12} and 1.3×10^{-15} cm^3 $molecule^{-1}$ s^{-1} for OH and Cl respectively).[177, 234] Careful consideration of the concentration of C_6H_6 used would be required so as to not significantly deplete the NO^+ reagent used to monitor the concentration of $(C_2H_5)_2O$ as the species is measurable with SIFT-MS. As C_6H_6 reacts with OH five times faster than CO, however, it would be expected that lower concentrations would be required. If the required concentration is low enough, the ability to monitor the concentration of C_6H_6 would enable changes in the concentration of OH to be observed in real-time.

To determine what concentrations of C_6H_6 and CO would be required to supress the impact of OH on the calculated rates, AtChem simulations were conducted for the CH_4 / C_3H_8 system. A concentration of 2.48×10^{12} molecules cm^{-3} was used in each model, as in sections 4.4 and 4.5, with the models also initialised with 25 ppbv of NO and the previously discussed photolytic reactions to represent the most extreme secondary chemistry impacts. The corresponding rates calculated from each iteration of the model are given in Figures 4.17(a) and (b) for CO and C_6H_6 respectively. For both species it was found that the necessary concentrations to quench any OH formed would be too high for use within the CRM setup for this to be a feasible approach. In the case of C_6H_6 this is due to the significant depletion of reagent ions that would arise at a concentration of 10 ppmv - impacting the instrument's sensitivity towards the depletion of $(C_2H_5)_2O$. It should also be noted that at this level 5.2% of the $(C_2H_5)_2O$ depletion still arises from its reaction to OH, as reflected by the calculated rate being 60.8 s^{-1} lower than the theoretical rate. As such, higher concentrations of C_6H_6 would still be required which would further compound this issue. With respect to CO, at a concentration of 1000 ppmv, the OH contribution towards the loss of $(C_2H_5)_2O$ drops to 0.5%, resulting in a calculated CRM rate of 352 s^{-1}.Whilst this is an excess of the theoretical 344 s^{-1} rate, the overestimation can be attributed to the previously discussed losses of Cl to HCHO and HO_2. It should also be noted that the reaction between CO and OH to generate HO_2 contributes to the Cl sink, as reflected by the loss of Cl to HO_2 increasing from 0.05% in the absence of CO to 0.8% at 1000 ppmv CO. Considering this, whilst the use of 450 ppmv of CO is simulated to result in a 1.08% loss of $(C_2H_5)_2O$ through reaction with OH, the modelled reactivity rate (343.5 s^{-1}) is within 0.1% of the theoretical rate, indicating that lower concentrations of CO could be utilised. Such concentrations are still likely to pose serious health and safety risks and therefore the use of an aforementioned CO detector and operation of the instrument in a well-ventilated environment would be necessary for this approach to be valid. Combining the use of CO with another measure to minimise the production of OH would enable lower concentrations to be used and therefore further minimise the H&S risks.

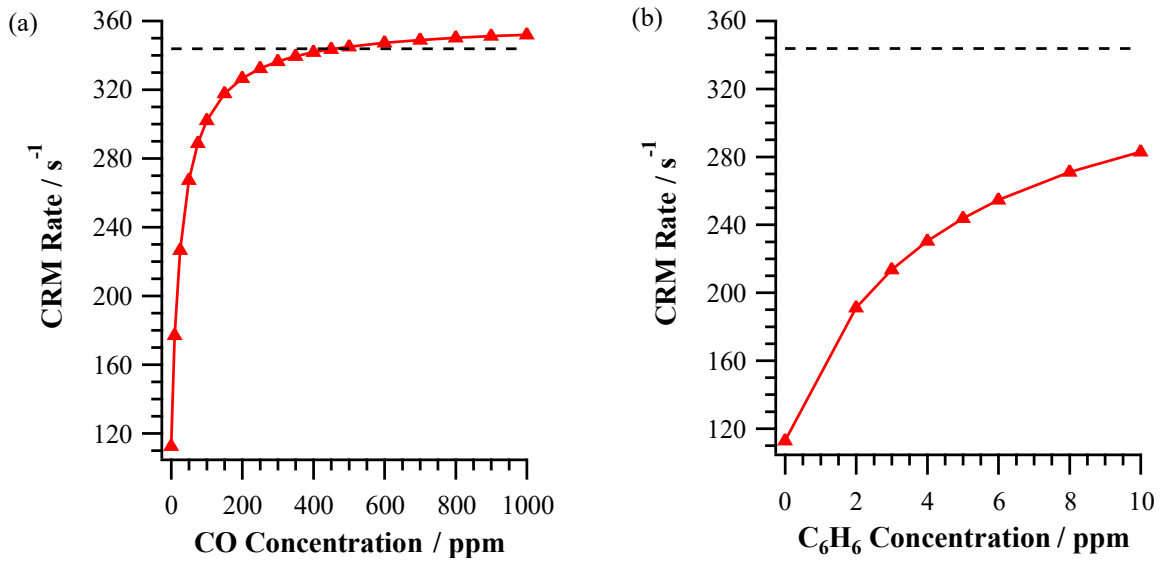

Figure 4.17. Simulated impact on the calculated CRM rate upon the addition of (a) CO, (b) C_6H_6 to the CH_4 / C_3H_8 system. Dashed line represents the theoretical rate of reaction.

4.6.2 Adjusting Residence Time

Reducing the time available for NO to react with any HO_2 generated within the reactor can either be achieved by increasing the total flow rate through the system or by reducing the volume of the glass reactor. Such changes would however also reduce the time available for Cl_2 to be photolysed, leading to the need for higher concentrations to be introduced into the reactor to generate the same level of Cl radicals – a potential issue if Cl_2 itself reacts with any VOCs present within the air sample. To identify what residence time would be required to achieve this, analysis of the CH_4 / C_3H_8 system was repeated using photolysis durations of 2, 3 and 5 seconds, with the results compared to the original 10 second model runs. Each model run included an additional second in which photolysis was switched 'off' to account for the residence time within the sample line before connecting to the SIFT-MS. To identify the necessary concentration of Cl_2 required at each residence time, the models were first initialised considering only $(C_2H_5)_2O$ and Cl_2, as to represent the ***C1-C2*** stage of the CRM method, and iterated until a 35 ppbv depletion in $(C_2H_5)_2O$ was obtained. It was found that these changes would require the concentration to be increased from 60 ppbv to 111, 178 and 263 ppbv if photolysis durations of 5, 3 and 2 seconds were pursued. Upon identifying these values, CH_4, C_3H_8 and NO were added to the model using the concentrations from section 4.6.1. The calculated rate of reaction for each residence time and the contribution of Cl and OH towards the depletion of $(C_2H_5)_2O$ is summarised in Figures 4.18(a) and (b) respectively. Whilst the loss of $(C_2H_5)_2O$ to OH was found to be roughly halved upon reducing the photolysis duration to 2 seconds, this pathway still accounted for 9.7% of its total loss resulting in a calculated rate 125.3 s^{-1} lower than the literature derived rate. Disregarding the residence time within the sample line, it is clear that most of the secondary chemistry takes place within the photolysis flow tube itself as reflected by the calculated rate

differing by a maximum of 5 s^{-1} across all of the model runs. As such, reducing the residence time within the glassware on its own would not resolve the issue of secondary chemistry.

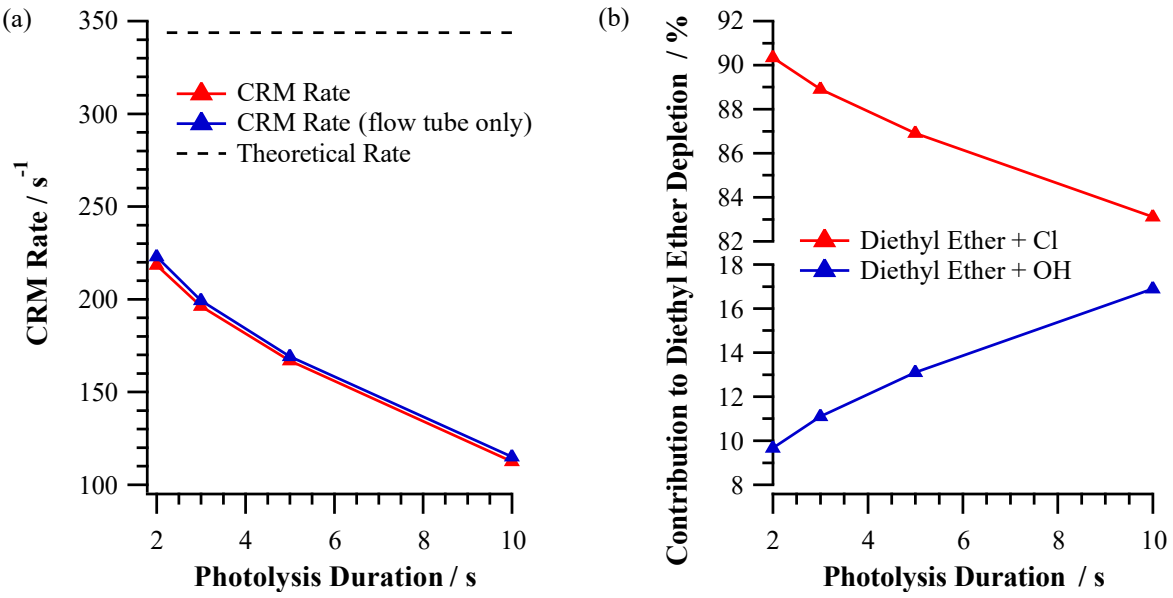

Figure 4.18. (a) Simulated impact on the calculated CRM rate upon adjusting the photolysis duration. (b) Corresponding impact on $(C_2H_5)_2O$ losses.

4.6.3 Combining Both Approaches

As neither approach was found to be suitable on their own, the reduced residence time models were iterated with increasing levels of CO to identify whether a combination of both methods would provide a viable solution to minimise the impact of the OH generated within the current system. The resulting calculated rates are given in Figure 4.19(a) with a breakdown of $(C_2H_5)_2O$ losses in Figure 4.19(b). By comparison to the analysis for the existing 10 second photolysis duration, reducing the residence time to either 3 or 2 seconds would result in the CO concentration required to bring the OH contribution to $(C_2H_5)_2O$ losses down to 1% being reduced by ~ 50% (from 450 ppmv to 250 and 200 ppmv respectively). At such an OH contribution, the loss of Cl to HCHO and HO_2 begins to have a larger impact on the calculated rate rather than losses of the reference compound to OH. As such, further addition of CO is considered unnecessary, with concentrations as low as 150 and 100 ppmv yielding reactivities within 0.3 and 2.6% of the theoretical rate respectively when combined with a 2 second residence time. It therefore follows that if a reactor redesign to enable the addition of the reference VOC and sample downstream of the Cl_2 photolysis is found to be unfeasible, it is recommended that the existing glass flow tube used within this work is replaced by a new cell with a 2 second residence time. To gain confidence in the model, it is then recommended that a series of lab experiments are conducted in which the reactivity of the CH_4 / C_3H_8 mixture is measured with 25 ppbv NO and increasing concentrations of CO up to 250 ppmv to ensure that the calculated rates are in agreement with those obtained within the model. If this is found to be the case, and if the rates

calculated with and without NO for the C_5H_8 and the 35-component mixture are comparable, then the instrument is likely in a position where it would be suitable to measure ambient reactivity with the caveat that any species within the sample of interest which absorbs at wavelengths > 280 nm may undergo some photolytic losses.

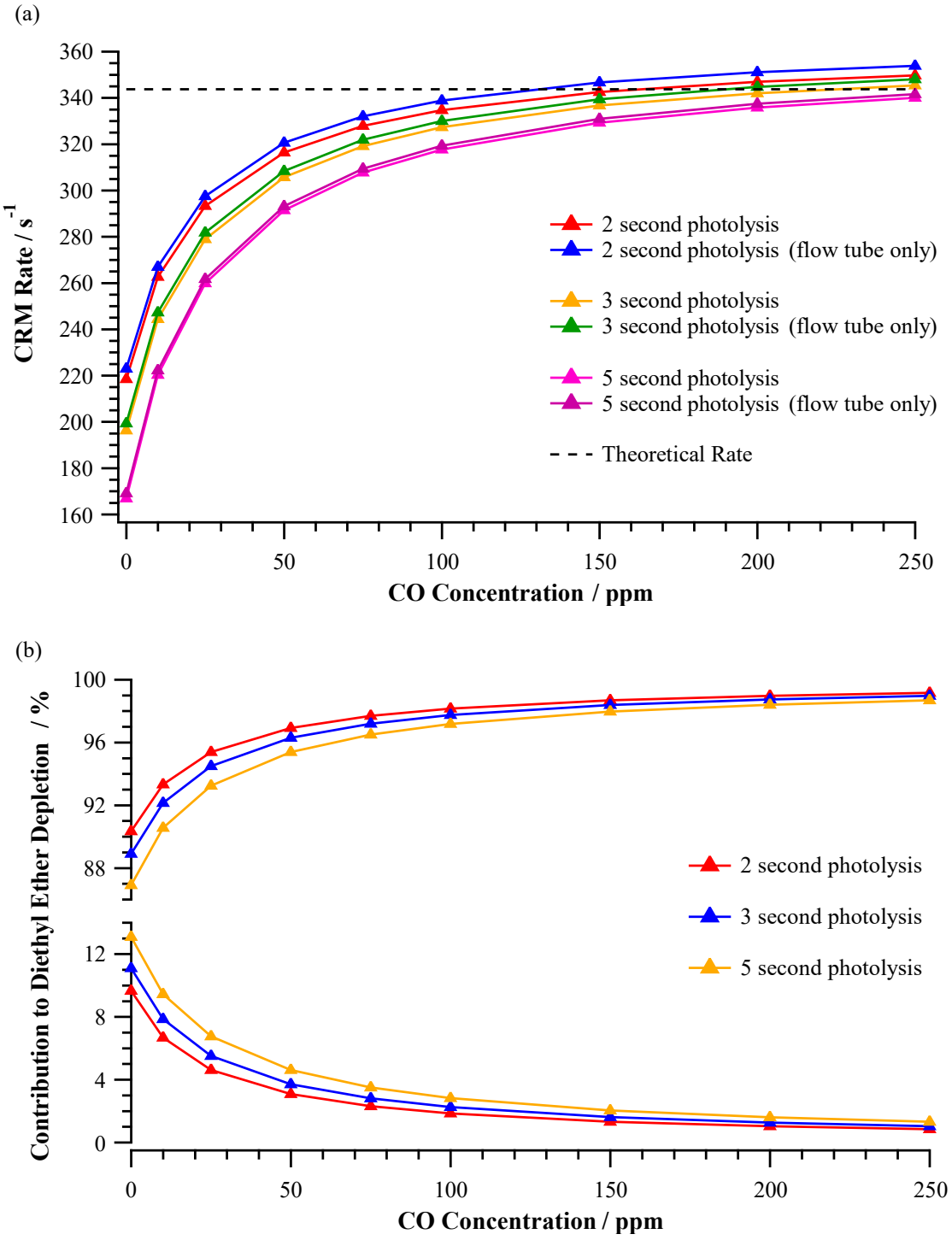

Figure 4.19. (a) Simulated impact on the calculated CRM rate upon a combined adjustment of the photolysis duration and addition of CO. (b) Corresponding impact on $(C_2H_5)_2O$ losses.

4.6.4 Correcting for the NO Artifact

To avoid the need to add CO into the system, if the CRM measurements are made alongside concurrent measurements of NO, the impact of the formation of OH from the reaction between NO + HO_2 can be corrected for. To achieve this, following a similar approach as conducted by Michoud *et al*.,[136] a plot of the variation in ***C3*** (the difference between the expected ***C3*** concentration and the modelled concentration owing to losses to OH) as a function of NO for all three systems examined in sections 4.3 and 4.4 was derived through AtChem simulations. By applying a quadratic regression function forced through the origin to the above plots, a corrected ***C3*** concentration can be obtained using equation 4.9 where a and b denote fitting parameters obtained from the quadratic regression function:

$$C_3^{Corrected} = C_3^{Measured} + (a[NO]^2 + b[NO]) \qquad \text{(Equation 4.9)}$$

The resulting quadratic fits for all three systems are presented in Figure 4.20. Owing to the discrepancy observed between the modelled and experimental impact of NO for the 35-component mixture, the use of such quadratic fits is not currently feasible. Furthermore, whilst the impact of NO on different VOC mixtures has not been investigated as part of this work, the AtChem simulations suggest that the composition of the sample has a significant impact on the required correction factor. As this would be unknown when conducting ambient measurements, the use of a general correction factor would add an additional source of uncertainly in the calculated reactivity rate. Consequently, physical methods to mitigate the impacts of secondary chemistry within the CRM setup would likely be the most suitable option for this application.

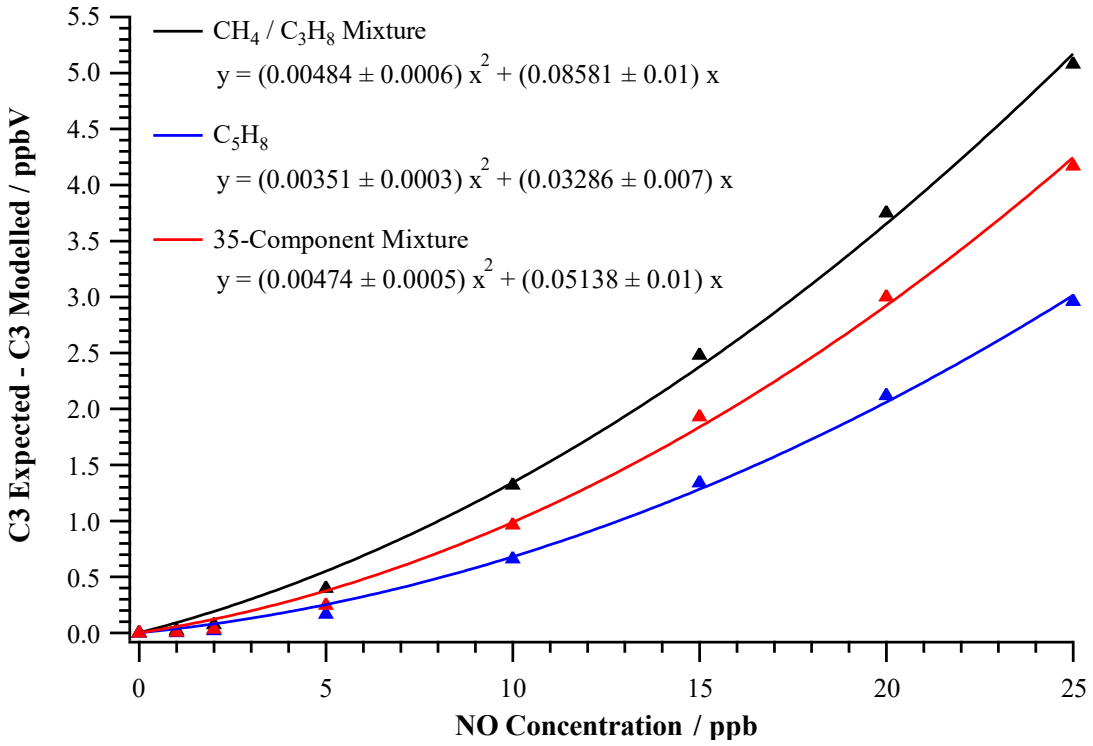

Figure 4.20. Simulated changes in the ***C3*** concentration as a function of NO for the CH_4 / C_3H_8, C_5H_8 and 35-component mixture systems.

4.7 Potential Modifications to the CRM Setup

Whilst potential mitigating conditions for the existing experimental setup have been identified, it is noted that the use of CO, even at the levels proposed in section 4.6, will still require additional health and safety measures to be put in place to prevent the user from being exposed to any potential leaks. As such, this section will look at two potential changes that could be made in an attempt to prevent the need of CO addition within the reactor, or at least reduce the concentrations required; the use of a new reference VOC with a greater difference between k_{Cl} and k_{OH} than $(C_2H_5)_2O$, and a reactor re-design which would allow for the air sample to be introduced after photolysis has occurred.

4.7.1 The Ideal Reference VOC

Based on the published rate constants (2.57×10^{-10} and 1.32×10^{-11} cm^3 $molecule^{-1}$ s^{-1}),[169, 170] $(C_2H_5)_2O$ reacts with Cl approximately 20 times faster than with OH. Increasing this differential would help to minimise the fraction of reference VOC lost to OH under comparable concentrations. To identify what ratio would be required to achieve this, and thus determine whether or not a suitable VOC exists, iterations of the CH_4 / C_3H_8 system with 25 ppbv NO were conducted using the $(C_2H_5)_2O$ mechanism as a baseline and gradually increasing the rate constant for its reaction with Cl. Photolysis was conducted over a period of 10 seconds so as to re-create the conditions of the existing reactor.

As can be seen in Figure 4.20, even when considering a VOC which reacts 500 times faster with Cl than OH, some losses to OH would still occur (estimated to account for 3.4% under these conditions) resulting in an underestimation of the reactivity by 36.5 s^{-1}. It is therefore clear that simply changing the reference VOC used within the setup would not be sufficient on its own to mitigate any secondary chemistry. Consequently, the model runs were repeated with the addition of 50 ppmv of CO, an 80% reduction of the concentration recommended for the existing system in section 4.6.3. Under these conditions, the OH contribution was significantly reduced as depicted in Figure 4.21, dropping to below 1% at k_{Cl} : k_{OH} ratios greater or equal to 170. It is noted that within this region the CRM begins to overestimate the reactivity within the system, a trend observed due to the previously discussed non-pseudo first-order conditions present within the system. With respect to potential reference compound, such a difference in reactivity with Cl and OH is often observed within alkanes however the use of such VOCs is likely to pose several issues due to the additional criteria of the CRM. As the reference compound should not be present at detectable levels within ambient air to avoid complications during analysis, the use of longer chain hydrocarbons would be required. Studies of the Cl reactivity of such species are however limited which will introduce a large degree of uncertainty within the CRM measurement with respect to the rate constants used in the calculation Typically, the k_{Cl} : k_{OH} ratio for these species is also smaller than their shorter chain counterparts (e.g. 47 and 49 for $C_{10}H_{22}$ and C_9H_{20} respectively compared to 247 and 127 for C_2H_6 and C_3H_8). An alternative approach would therefore be the use of a deuterated short chain alkane. Such a change would, however, require the use of a different detection system to monitor the reference VOC. As previously discussed, whilst it is possible to measure short chain hydrocarbons through SIFT-MS using the O_2^+ reagent ions, due to the slow charge transfer rates, this would require the reference VOC to be introduced at excessive concentrations. One potential detection system which could be used in this instance is GC-MS, however, such a change would likely be at the expense of response time if pre-concentration of the sample is required.

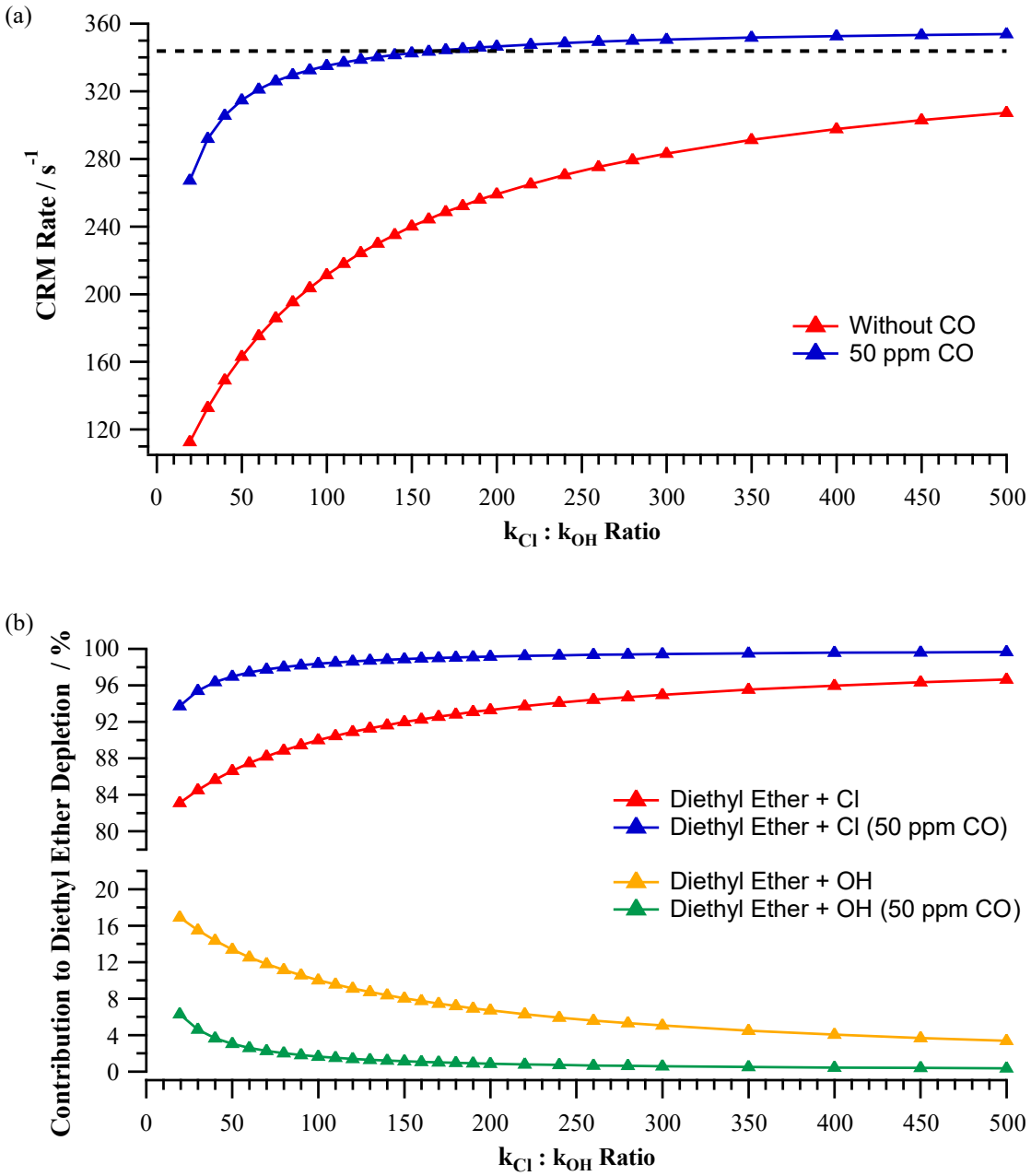

Figure 4.21. Simulated impact of adjusting the k_{Cl} : k_{OH} ratio on (a) the CRM derived rate (b) the losses of the reference VOC within the system with and without CO. The dashed line in (a) represents the literature reactivity of the CH_4 / C_3H_8 mixture used to initialise the model run.

4.7.2 Reactor Redesign

As highlighted in section 4.5, photolysis has an impact on the formation of OH within the system and consequently on the calculated reactivity rate. Furthermore, as the exact composition of the ambient air samples being measured during field deployment of the instrument would be unknown, quantifying the losses of VOCs via photolysis would also not be possible. Consequently, redesigning

the reactor such that the photolysis of Cl_2 is conducted prior to the addition of both the sample and the reference VOC is an essential next step. Two potential designs by which this could be achieved are given in Figure 4.22. The first design, Figure 4.22(a), utilises a U-bend quartz reactor, in which the carrier gas and Cl_2 are introduced together along the length in which the LDLS has been directed. The reference VOC and the sample are then introduced at the other side of the U-bend so as to minimise their exposure to the light source. Such a design would, however, be highly dependent on the Cl_2 being introduced into the reactor under a laminar flow so as to minimise losses of the generated Cl-atoms to the reactor walls. For a straight piece of tubing, the nature of the flow can be determined using the Reynolds equation:

$$\mathrm{Re} = \frac{\rho \nu L}{\mu} \qquad \text{(Equation 4.10)}$$

Where:

- Re is the Reynolds number
- ρ is the density of the gas mixture
- ν is velocity of the gas
- L is the characteristic length of the flow tube
- μ is the dynamic viscosity of a gas

If the Reynolds number obtained is less than 2000, the flow through the system can be considered laminar. As the proposed design is non-linear, however, the flow properties would not be uniform throughout the reactor. As a result, modelling of the system using computational fluid dynamic software would be required to determine what regime each point within the reactor would be under, and thus whether such a design would be feasible.

The second proposed design, Figure 4.22(b), is based upon the IU-TOHLM instrument discussed in chapter 1.5 of this thesis.[122] The reference VOC and Cl_2 are introduced through a side arm into a quartz vessel, whilst Cl_2 is introduced via a narrower moveable injector. Photolysis of Cl_2 is achieved by the 365 nm emission from a phosphor coated Hg pen lamp seated within the moveable injector. The injector itself is made from amber borosilicate glass to minimise the transmission of light into the quartz vessel – reducing losses of photolabile species in the sampled air. Such a material is also chemically inert so as to prevent any additional loss mechanism of Cl prior to their reaction with the sample or reference VOC. The benefit of using a moveable injector, at the very least when characterising the instrument, is that the residence time for reaction can be controlled and therefore the impact of secondary chemistry. As with the first design, ensuring that there is laminar flow through the system will be critical in order to minimise wall loses.

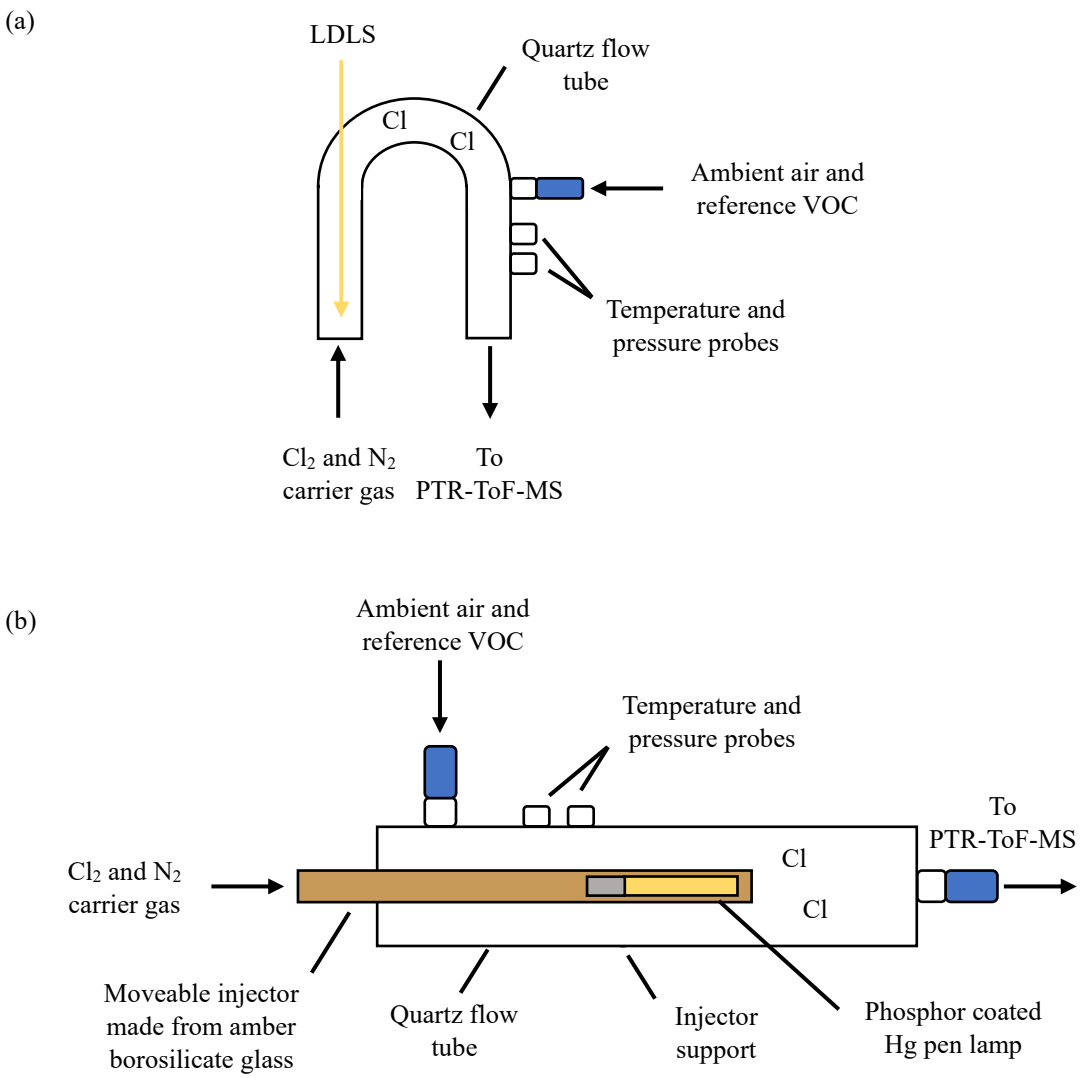

Figure 4.22. Proposed reactor designs to minimise photolytic losses of VOCs during the CRM experiment.

4.8 Conclusions

The work presented in this chapter has outlined the calibration of the Cl-CRM instrument for which good agreement with the literature has been observed and a working range of 12 – 400 s^{-1} identified. As discussed in the concluding remarks of chapter 3, such a working range would result in the instrument being unsuitable for deployment within clean environments. It is suggested that a change in the detection system used in this method, from SIFT-MS to PTR-ToF-MS providing lower levels of detection, may provide a resolution to this issue. An increase in the sensitivity would also enable the use of lower Cl atom concentrations, allowing for the system to be operated under conditions more closely resembling that of pseudo first-order.

At present, owing to the formation of OH radicals upon the sampling of NO, the instrument is also unsuitable for deployment in NO_x polluted environments. Interestingly, whilst a reduction in the CRM rate was obtained using box model simulations, significant variation between the measured and modelled rates was obtained with the difference between the two suggesting up to 2.5 ppbv of OH which was unaccounted for. Mitigation techniques using the existing setup have been identified through the aforementioned simulations, with a reduction in the residence time and addition of 250 ppmv of CO found to minimise the impact of this secondary chemistry interference. Switching to an alternative reference VOC with a greater k_{Cl} : k_{OH} than $(C_2H_5)_2O$ is an alternative option, however this would still require the addition of CO and is likely to require the use of GC-MS as a detection system which may result in increased response times due to the need for sample pre-concentration. In all instances however, owing to the discrepancy between the modelled and observed impact of OH, further experimental measurements under such conditions are recommended in order to gain confidence in the model.

A combination of the improved sensitivity and the implementation of measures to reduce the formation of OH would also increase the viability of using the CRM technique to measure unknown rate coefficients. Two designs have also been suggested which are proposed to enable the addition of both the reference VOC and the sample of interest after the photolysis of Cl_2. Such a re-design of the reactor is an important next step in minimising photolytic interferences and further improving the suitability of the instrument for field deployment and expanding the range of VOCs for which rate coefficients could be derived when the instrument is not in the field.

Chapter 5

Gas-Particle Partitioning of Chlorine in Central Manchester

5.1 Introduction

Within the troposphere, HCl and pCl^- are known to exist in equilibrium. As discussed in section 1.3, partitioning between the two states is dependent upon a number of factors including RH, liquid water content, particle pH and solute activity (α) - parameters which are in turn influenced by meteorological conditions such as ambient pressure and temperature as well as the atmospheric composition.[53] As the formation of photolabile reservoir species such as Cl_2, $ClNO_2$ and BrCl are dependent upon the level of chloride available to react in the particulate phase, an understanding of the partitioning between the two states is therefore vital if we are to improve our constraint on the Cl-atom budget and assess its importance as a tropospheric oxidant. Unfortunately, however, simultaneous measurements of pCl^- and HCl, alongside the necessary supporting aerosol and gas phase composition measurements required for such analysis, are limited. The lack of these observational constraints in a range of different environments limits our ability to thoroughly investigate our understanding of this partitioning chemistry. In the few studies in which this has been investigated, thermodynamic models have been reported to capture the observed partitioning behaviour with varying degrees of success. A brief summary of these studies follows.

5.1.1 Summary of Previous Studies

Exploring the $NH_4^+ – Na^+ – SO_4^{2-} – NO_3^- – Cl^- – H_2O$ system, the thermodynamic models ISORROPIA,[147] SCAPE2,[235] GEFMN and EQSAM2 were reported to underestimate pCl^-, and subsequently overestimate HCl, at RHs < 90% in a study conducted by Trebs *et al*.[236-238] A similar RH dependence has also been reported by Dasgupta *et* al. for the AIM thermodynamic model.[239, 240] It should be noted, however, that agreement between the modelled and measured concentrations of both species was obtained by Trebs *et al*. upon initialisation of the models with crustal species (Ca^{2+}, Mg^{2+}, K^+) – either explicitly or as Na^+ equivalents. Despite including these crustal species, overestimation of the measured HCl concentrations has also been reported by Sudheer *et al*. whilst using the ISORROPIA II thermodynamic model.[241] Interestingly, unlike the previous two studies, no correlation between the model-measurement agreement and RH was observed. Haskins *et al*. have also reported poor agreement between the modelled and measured HCl/pCl^- concentrations whilst using the ISORROPIA II model.[53] In contrast to the previous studies, however, the model was found to underestimate the concentration of HCl by 5% whilst overestimating pCl^- by a consistent factor of 2. One reason proposed for this discrepancy was the absence of NaCl from the measured PM_1 fraction, with the modelled concentration brought into agreement with the observed once this additional source of pCl^- had been accounted for. An alternative reason proposed was thermodynamic inconsistencies within the model. Specifically, Haskins *et al*. suggest a reduction in the temperature dependence of the HCl effective equilibrium constant used within ISORROPIA II.

In contrast, however, good agreement between the thermodynamically modelled and observed HCl/pCl^- phase partitioning has been obtained in other studies. For example, in a study conducted by Guo *et al*. using ISORROPIA II, the model was found to capture the concentration of both species to within 5%, biasing partitioning into the gas phase. Good agreement was also observed by Tao *et al*.,[54] although interestingly such a level of agreement could not be obtained for the PM_1 size fraction, with the model only able to capture the partitioning of the $PM_{2.5}$ fraction once crustal species were included, similar to that reported by Trebs *et al*.

5.1.2 Chapter Objectives

With such an uncertainty in the performance of thermodynamic models with respect to their ability to capture the partitioning behaviour of the chloride system, it is clear that further ambient measurements are required to scrutinise such models and understand the conditions under which discrepancies arise. The work presented in this chapter will analyse the partitioning behaviour of HCl and pCl^- observed during the Integrated Research Observation System for Clean Air (OSCA) campaign. The results will then be used to assess the performance of the ISORROPIA II thermodynamic model, providing a further constraint to probe our understanding of the partitioning chemistry for an urban background site.

5.2 Methodology

5.2.1 Site Description

Measurements during the OSCA campaign were made at the Manchester Air Quality Supersite (MAQS) between 10 June – 22 July 2021 and 5 February – 20 February 2022. The site is located at the Firs Environmental Research Station on the University of Manchester's Fallowfield Campus (53.444° N, 2.214° W) approximately 3 miles south of Manchester city centre. Air masses sampled at the site are consequently believed to be strongly influenced by the surrounding urban environment.

5.2.2 HCl – TILDAS

Measurements of HCl during both campaigns were obtained using a HCl-TILDAS instrument (Aerodyne Research Inc, Billerica, MA, United States) by Dr John Halfacre of the University of York. Details of the underlying principles of this method have been provided in section 2.3. The instrument was housed within an air-conditioned shipping container and held at 25 °C over the measurement period. Air masses were sampled through a custom-built inertial inlet situated above the container roof, ~3 m above ground level. As described by Halfacre *et al*., [109] the inertial inlet is designed to remove large particulate matter (> 300 nm diameter) from the sampled air so that the absorption and scattering of light by particulate is reduced within the system. To minimise wall loses of HCl during the sampling process, a small flow of perfluorobutanesulfonic acid (PFBS) vapour is introduced into the system in order to passivate the surfaces between the inertial inlet and the Herriott cell. Despite

these measures, 5.8% of the sampled HCl was calculated to be lost to the inlet surface, quantified through regular additions of a HCl permeation standard. Using integration times of 30 seconds, a limit of detection of 6 pptv was calculated.

5.2.3 ISORROPIA II – Thermodynamic Equilibrium Partitioning Model

The thermodynamic equilibrium model ISORROPIA II, used to investigate $K^+ – Ca^{2+} – Mg^{2+} – NH_4^+ – Na^+ – SO_4^{2-} – NO_3^- – Cl^- – H_2O$ aerosol systems, was employed to test our understanding of the partitioning of chloride between the gas and particulate phase during both campaigns and compare to the observed concentrations. Calculations were performed in "forward mode", in which the total (gas + aerosol) concentrations of NH_3, HCl, HNO_3, and particulate concentrations of SO_4^{2-}, are provided alongside ambient temperatures and relative humidities. A detailed description of how partitioning is calculated within the model has been described earlier in this thesis in section 2.4. Briefly however, the model solves a series of equilibrium equations based on the aforementioned conditions, incorporating water activity equations, activity coefficient calculations, electroneutrality, and mass conservation to determine the gas and aerosol concentrations at thermodynamic equilibrium. In all model calculations, the aerosol is assumed to be in a metastable state, in which salts do not precipitate if saturation is exceeded, owing to the high relative humidities experienced during both campaigns.

5.2.4 Supporting Gas and Particulate Measurements

A variety of techniques were employed to collect the supporting gas and particulate species concentrations required to investigate the thermodynamic partitioning of the chloride system using ISORROPIA II. Mass concentrations of non-refractory, submicron particulate SO_4^{2-}, NO_3^-, NH_4^+ and Cl^- were obtained using an Aerosol Chemical Speciation Monitor (ACSM, Aerodyne Research Inc, Billerica, MA, United States).[242] In the context of ACSM, the term non-refractory refers to particulate material which can be vaporised at 600 °C. Consequently, the technique is unable to measure refractory species such as NaCl, $NaNO_3$ and Na_2SO_4. 1 Hz NH_3 measurements were obtained using a Los Gatos research ammonia analyser instrument (Enviro Technology Services Ltd, United Kingdom).[243] HNO_3 concentrations used in this work were obtained through the subtraction of observed NO_x concentrations from NO_y. Both NO_y and NO concentrations were collected using a 42*i*-Y chemiluminescent NO_y analyser (Thermo Fischer Scientific, United States) at 20 second intervals.[244] NO_2 concentrations were recorded at 10 second intervals using a API T500U cavity attenuated phase shift instrument (Teledyne API, United States).[245] To assess the feasibility of the measurement of HNO_3 through this method, comparisons were drawn to HNO_3 measurements recorded prior to the start of the OSCA campaign by a CIMS instrument using I^- primary ions. The results of this intercomparison are discussed in section 5.3.2.4. Air samples for all of the aforementioned instruments (excluding CIMS) were collected 7m above the ground. For modelling in ISORROPIA II, all species concentrations were averaged over a period of 1 hour.

Particle size distribution measurements were obtained using a TSI 3082 scanning mobility particle sizer (SMPS, TSI Inc, United States), covering the diameter range 15 – 660 nm.[246] $PM_{2.5}$ and PM_{10} particulate measurements were obtained using an XACT® 625i instrument (Acoem, France).[247] The fine mode particulate measurements acquired by the ACSM was used in favour of the XACT measurements owing to the coarse mode chloride being dominated by non-volatile sea salt [personal communication, Dr James Allan, University of Manchester]. As with the previous instruments, air samples for the XACT and SMPS instruments were taken 7m from the ground,

5.3 Results and Discussion

5.3.1 Intercomparison of Seasonal Observations

Hourly averaged pCl^- and HCl concentrations measured during the summer and winter OSCA campaigns are depicted in Figures 5.1(a) and (b) respectively. Strong seasonal variability in the partitioning behaviour was observed, with the gas phase accounting for an average 66% of the total (PM_1 pCl^- + HCl) chloride fraction throughout the measurement period. Mixing ratios of HCl during this period ranged from 0 – 237.9 pptv (0 – 0.355 μg m^{-3}), with a median concentration of 36.9 pptv (0.055 μg m^{-3}). For pCl^-, a median concentration of 0.023 μg m^{-3} was obtained within a range of 0 – 0.366 μg m^{-3}. By comparison, pCl^- concentrations during the winter campaign were on average a factor of 18 times greater (median value of 0.385 μg m^{-3}), ranging between 0.009 – 1.500 μg m^{-3}. HCl concentrations over the same period were found to be lower than those obtained in the summer by a factor of approximately 2.5, ranging from 0 to 52.6 pptv (0 – 0.078 μg m^{-3}) with a median concentration of 8.9 pptv (0.013 μg m^{-3}). As a result, the particulate phase was responsible for an average of 94% of the total measured chloride budget in the winter.

Whilst source appointment studies were not conducted as part of this work, such a substantial increase in the concentration of pCl^- during the winter could, in part, be attributed to an increase in localised sources such as residential wood and coal burning. As can be seen from the XACT measurements depicted in Figure 5.2, significant quantities of chloride were also observed in both the $PM_{2.5}$ and PM_{10} size fractions during the winter OSCA campaign. Whilst no Na measurements were recorded by the XACT instrument, previous work in Manchester has shown that the course mode pCl^- in the area is dominated by sea salt [personal communication, Dr James Allan, University of Manchester] as previously discussed. Consequently, the increased concentrations observed in the winter could also be attributed to increased sea salt transport as a result of stronger winds experienced over the measurement period, although it is likely this is a minor source when compared to the aforementioned localised sources.

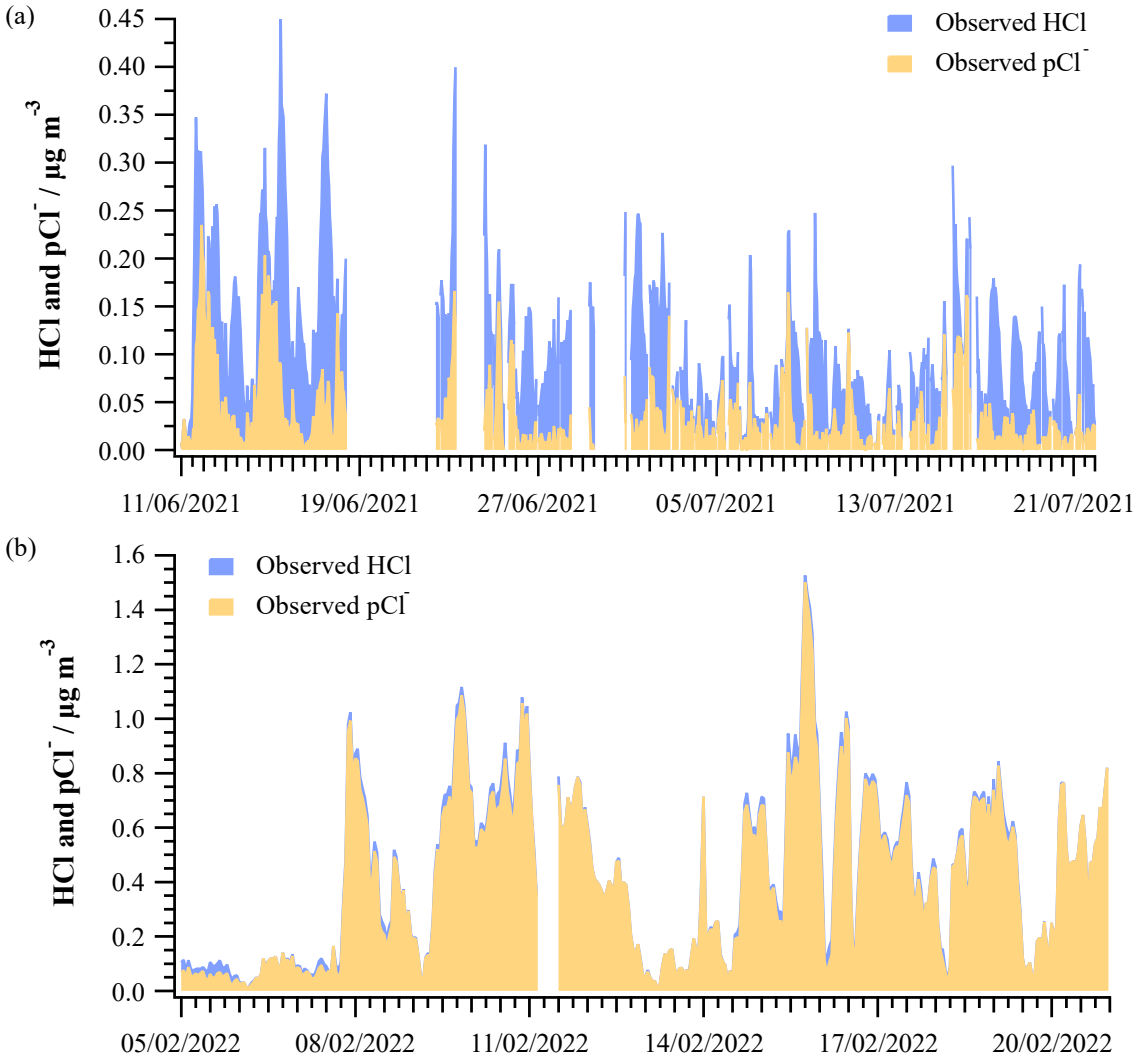

Figure 5.1. Measured concentrations of HCl and ACSM PM_1 pCl^- during the (a) summer and (b) winter OSCA campaigns.

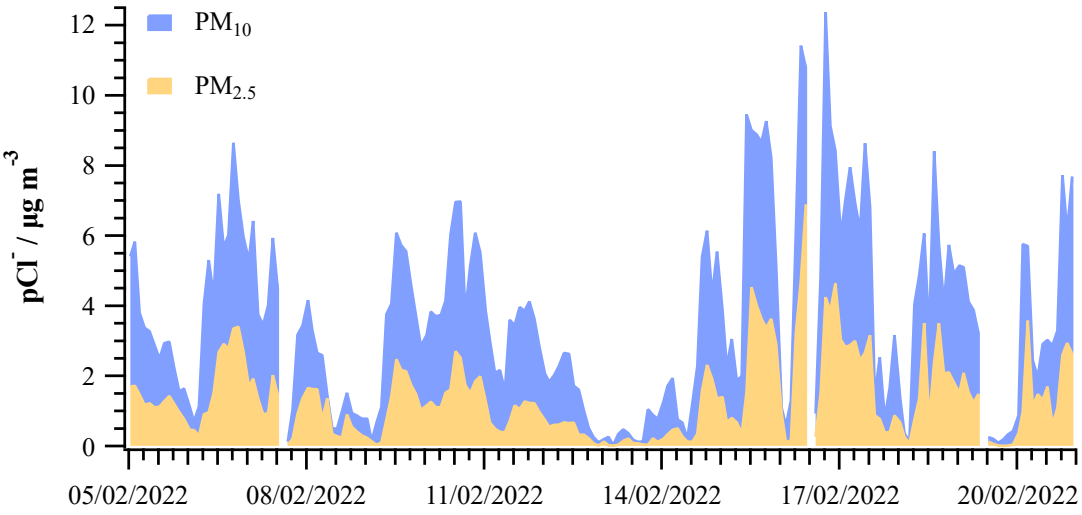

Figure 5.2. XACT measurements of $PM_{2.5}$ and PM_{10} particulate chloride recorded during the winter OSCA campaign.

Using the observations depicted in Figure 5.1, averaged hourly diurnal cycles of HCl and pCl^- for both campaigns were derived. As can be seen in Figures 5.3, both species exhibited strong diurnal cycles during the summer, with minimum HCl concentrations in the range of 15 – 20 pptv (0.022 – 0.030 µg m^{-3}) observed between the hours of 22:00 – 04:00, before gradually increasing and reaching a maximum median concentration of 76.5 pptv (0.114 µg m^{-3}) at 12:00. Conversely, pCl^- concentrations were observed to be at their lowest (~ 0.011 µg m^{-3}) around 13:00, whilst higher concentrations were observed at night – reaching a maximum of 0.037 µg m^{-3} at 04:00.

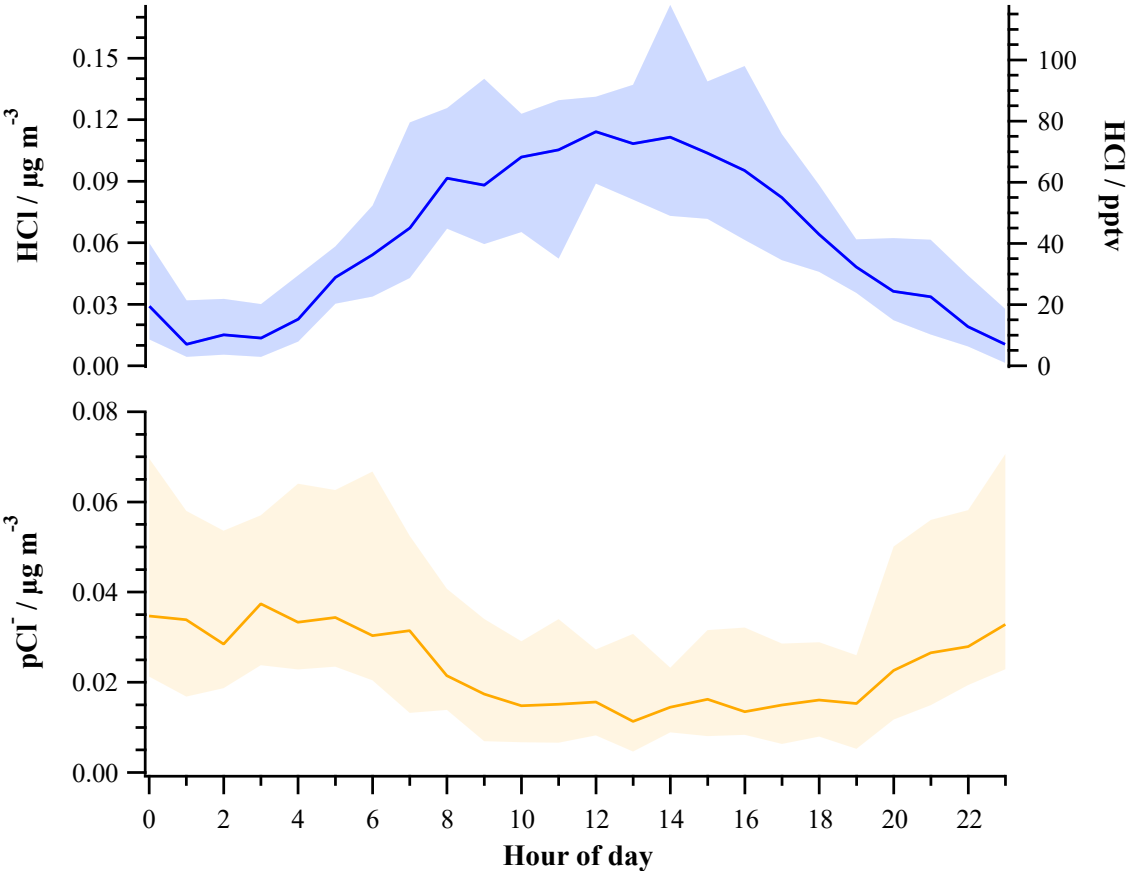

Figure 5.3. Average hourly diurnal cycle of HCl (top) and PM_1 pCl^- (bottom) during the summer OSCA campaign. Solid line represents the median species concentration. Shaded region represents the 25th and 75th

By comparison, observations from the winter campaign showed no clear sign of diel patterns in the concentrations of both HCl and pCl^-. With respect to the former, whilst elevated concentrations of 16 – 17.2 pptv (0.024 – 0.256 µg m^{-3}) were observed between the hours of 10:00 – 12:00, concentrations typically varied between 5.5 – 12 pptv (0.008 – 0.018 µg m^{-3}) throughout the day as depicted in Figure 5.4. For pCl^-, a gradual increase can be seen between 16:00 to 24:00, potentially arising from local biomass burning.

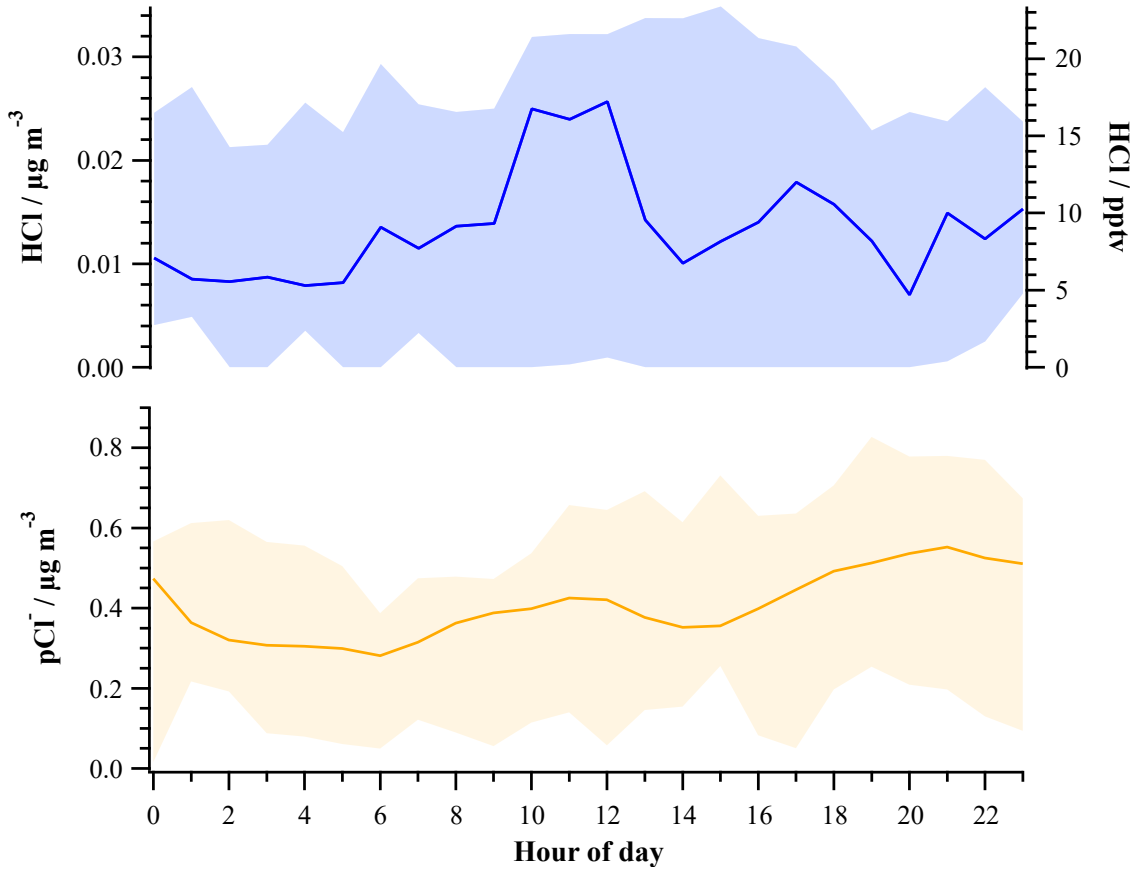

Figure 5.4. Average hourly diurnal cycle of HCl (top) and PM_1 pCl^- (bottom) during the winter OSCA campaign. Solid line represents the median species concentration. Shaded region represents the 25th and 75th percentile values.

5.3.2 Observed and Modelled Partitioning Intercomparison

5.3.2.1 Model Assumptions

A key assumption of the ISORROPIA II thermodynamic model is that all aerosol particles are internally mixed, implying that particles of the same size have the same composition.[147] Consequently only submicron measurements of the particulate phase have been used in the simulations, as internal mixing of super-micron particles is less likely to occur. As the ACSM does not have the capability to measure particle size, such information was extracted from the SMPS measurements to aid in the interpretation of the particulate distributions in the two campaigns. Plots of the resulting average particle number density and surface area for the summer and winter campaigns are given in Figure 5.5. It should be noted that the SMPS data used for the winter campaign were obtained in the week prior and after the measurements of HCl as concurrent measurements were unavailable. From the SMPS measurements it is clear that the particulate measured in both campaigns comfortably falls within this category. Whilst only 61 and 63% of the summer and winter PM_1 fractions would be detectable by the ACSM instrument, as a result of the

instrument only measuring particles with diameters between 40 nm - 1µm, it should be noted that this is unlikely to be a significant issue owing to the measured fractions accounting for 95 and 96% of the total surface area for each campaign.

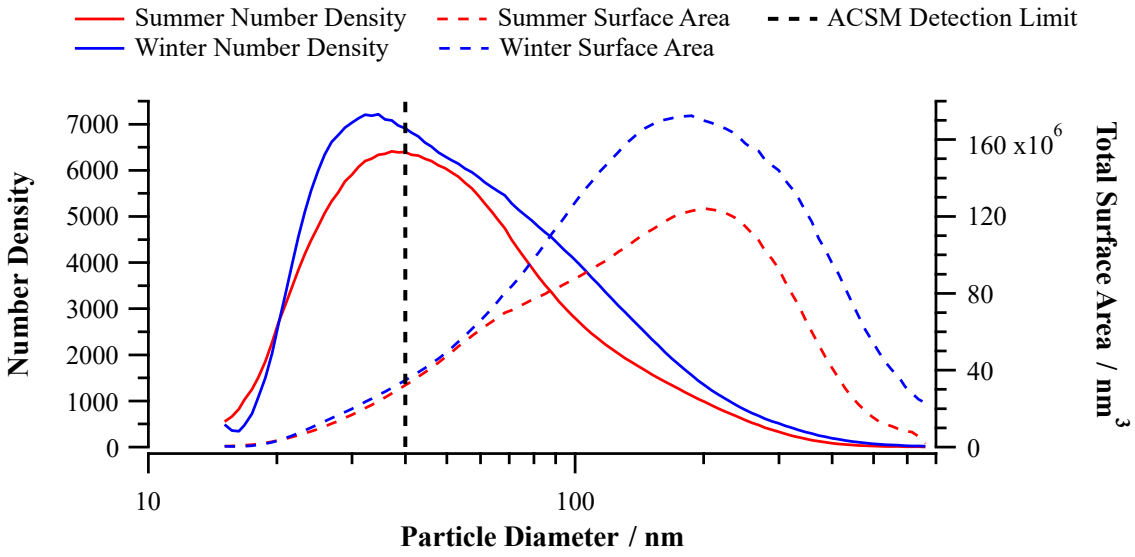

Figure 5.5. Average aerosol number size distribution recorded during the summer (red) and winter (blue) OSCA campaigns with corresponding aerosol surface area. The black dashed line represents the minimum sample size detectable by the ACSM (40 nm).

The second assumption made during the ISORROPIA II simulations is that the aerosol exists in a metastable state, which as discussed in section 5.2.4, inhibits the formation of solid precipitates. Mean RHs of (72.2 ± 15) and (82.9 ± 9)% alongside minimum values of 37.4 and 64.0% were experienced during the summer and winter campaigns respectively. As previous reports have indicated deliquescence in some particles at RHs as low as 20%, it is likely that this is a valid assumption for the datasets used in this study.[146, 248]

5.3.2.2 Base ISORROPIA II Simulations - Summer

Intercomparisons of the measured and modelled species concentrations obtained from the base ISORROPIA II simulations for the summer OSCA campaign are provided in Figure 5.6. The model was found to capture the observed NH_3 – NH_4^+ partitioning well, with a 4% underestimation of the gas phase and a corresponding 15% overestimation of the particulate phase concentrations identified through regression analysis. By comparison, however, whilst good agreement between the TILDAS and model derived HCl concentrations was obtained, as reflected by a gradient of 1.11, the model was found to underestimate the concentration of pCl^- by an average factor of 2. As can be seen in Figure 5.6(b), the partitioning behaviour of the chloride system predicted by the model appears to follow two distinct patterns, with a cluster of points observed along the 1:1 model : predicted relationship line and another along the x-axis - indicating that ISORROPIA is forcing all of the

measured chloride into the gas phase. Such behaviour is also observed in the nitrate system, resulting in the NO_3^- concentrations being underpredicted by 40% on average when compared to the concentrations recorded by the ACSM. For both systems this behaviour is found to correlate with RH, with reasonable agreement between the measured and modelled HCl and pCl^- concentrations obtained during periods in which the RH is in excess of 80%. Such a relationship can be rationalised upon considering the impact of RH on particle pH. As the RH increases, the liquid water content of the particle also increases, resulting in a decrease in the concentration of pCl^- as a result of dilution. Assuming that the chloride system is under thermodynamic equilibrium, partitioning between the gas and particulate phase can be described by Henry's Law:

$$[H^+] \times [Cl^-] = k'_H + c_g(HCl) \qquad \text{(Equation 5.1)}$$

where:

- $[H^+]$ and $[Cl^-]$ are the aqueous concentrations of H^+ and Cl^- respectively
- k'_H is the Henry's law constant of HCl multiplied by the equilibrium constant for the dissociation of HCl
- $c_g(HCl)$ is the gas phase concentration of HCl

Assuming both k'_H and $c_g(HCl)$ do not change significantly, in order for the two terms in equation 5.1 to remain equivalent as RH increases, $[H^+]$ has to increase to compensate for the lower $[Cl^-]$. This increase in acidity is achieved through the uptake of HCl from the gas-phase.[249] As discussed in section 5.1, similar observations have been reported by Trebs *et al*.,[238] in which no particulate phase nitrate or chloride were predicted at relative humidities below 90% prior to the inclusion of organic acids and crustal species (Ca^{2+}, K^+, Mg^{2+}) when using the SCAPE2 equilibrium model. Interestingly, the discrepancy between the modelled and measured HCl concentrations exhibited no temperature relationship. This suggests that the temperature dependence of the effective equilibrium constant of HCl used within the model is not a source of issue in this study, in contrast to the conclusions of Haskins *et al*.[53]

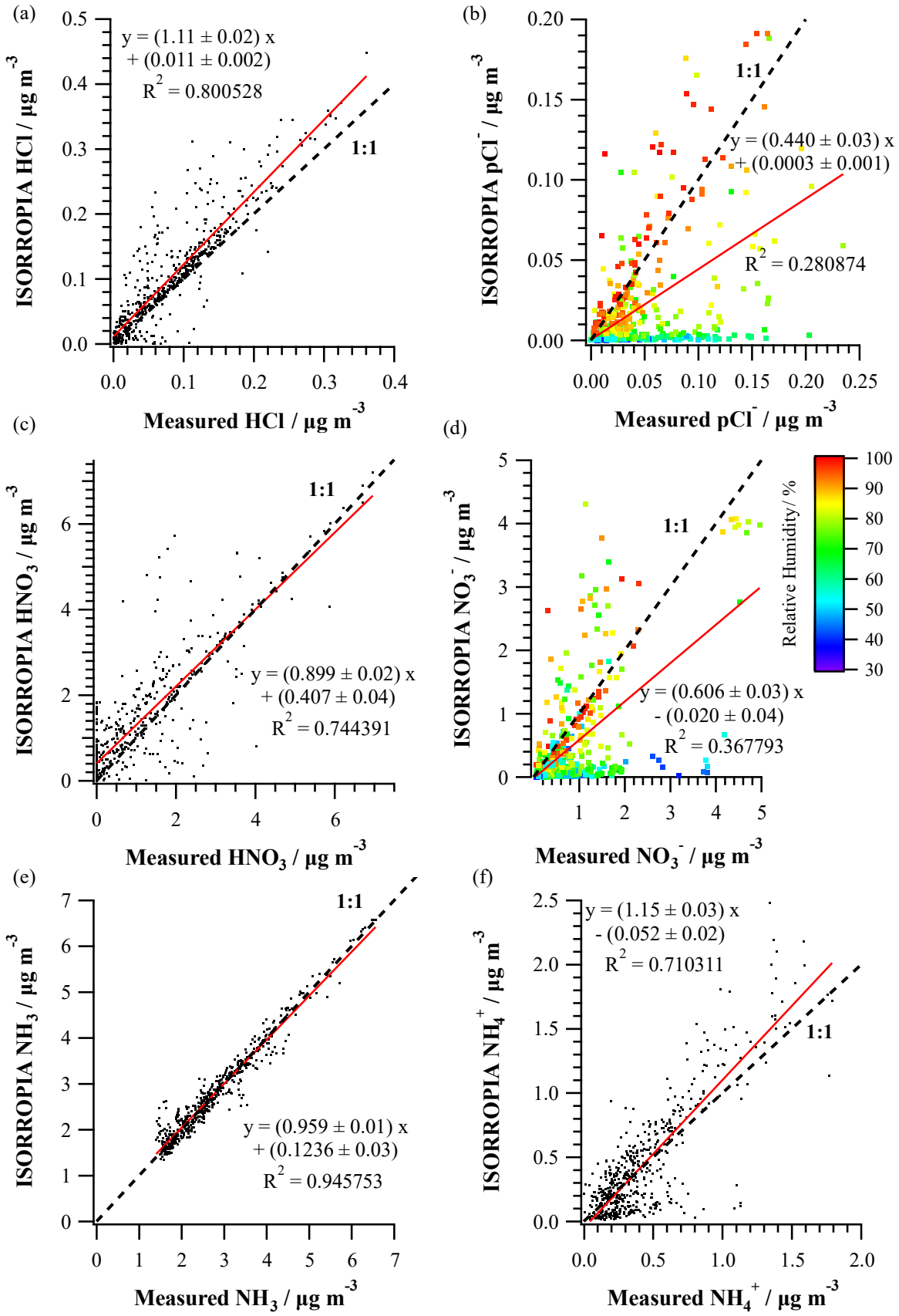

Figure 5.6. Intercomparison of the ISORROPIA II predicted (a) HCl, (b) pCl^-, (c) HNO_3, (d) NO_3^-, (e) NH_3, (f) NH_4^+ concentrations obtained from the Base simulations with the summer campaign measurements.

Despite the underestimation of the particulate phase, as can be seen from Figures 5.7, ISORROPIA II captures the diurnal profiles of HCl and pCl^- well, with elevated concentrations in the gas phase observed during the day and the particulate phase dominating during the night. From these profiles, it is clear that the overestimation in the concentration of HCl occurs throughout the day as with the underestimation of the particulate phase. It is also clear that the clustering of points observed around the x-axis in Figure 5.6(b) arises from ISORROPIA forcing the daytime total chloride measurements into the gas phase. These observations correlate with the measured diurnal variation in the relative humidity during the campaign, in which lows of 58.6% were observed at 13:00 and highs of 89.1% recorded at 01:00.

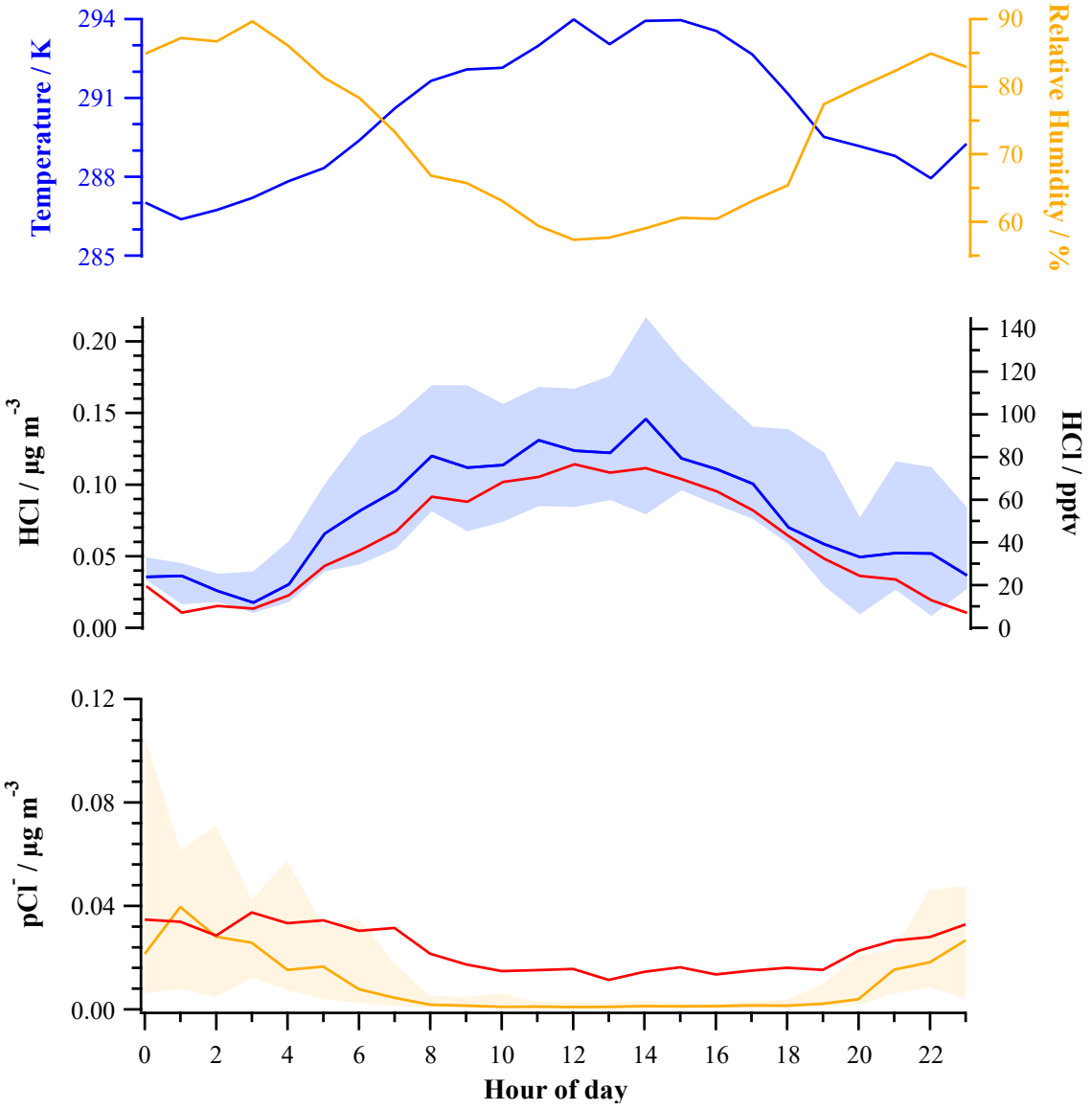

Figure 5.7. Average hourly diurnal cycle of RH and temperature (top), modelled HCl (middle) and modelled pCl^- (bottom) during the summer OSCA campaign. Solid line represents the median species concentration. Shaded region represents the 25th and 75th percentile values. Red line denotes the median measured concentration.

5.3.2.3 Base ISORROPIA II Simulations - Winter

Intercomparisons of the measured and ISORROPIA II derived species concentrations for the winter OSCA campaign are provided in Figure 5.8. As with the summer dataset, ISORROPIA captures the concentration of NH_3 reasonably well, with an average overestimation of 7.7% calculated. Interestingly however, the model performed substantially poorer at predicting the concentration of NH_4^+ resulting in an average underestimation of 37%. This perceived bias in predictions is the opposite to that observed in the summer dataset in which the particulate phase was overestimated by 15% as previously discussed. Substantially poorer agreement was also obtained for the chloride system, with modelled HCl concentrations on average a factor of 7.7 greater than that observed during the campaign whilst pCl^- concentrations were approximately a third of their measured values. Interestingly, ISORROPIA was found to positively bias partitioning into the particulate phase for the NO_3^- system, in contrast to the predictions observed for the aforementioned species, leading to the gas phase being underestimated by a factor of 4 and the particulate phase being overestimated by 24%. It should be noted, however, that this is likely an artefact of using the NO_y measurement to determine HNO_3 concentrations in this study, and this is explored in more detail in the next section. In comparison to the summer, HNO_3 concentrations would be expected to be lower in the winter due to the importance of the photolytic production of OH on its formation.[250] As such, a smaller NO_z fraction would make the method more susceptible to noise in both the NO_x and NO_y measurements. This is reflected by 58% of the HNO_3 concentrations calculated for the winter campaign being less than zero when using this approach. Consequently, the simulated concentration of HNO_3 will not be discussed in detail for the winter dataset.

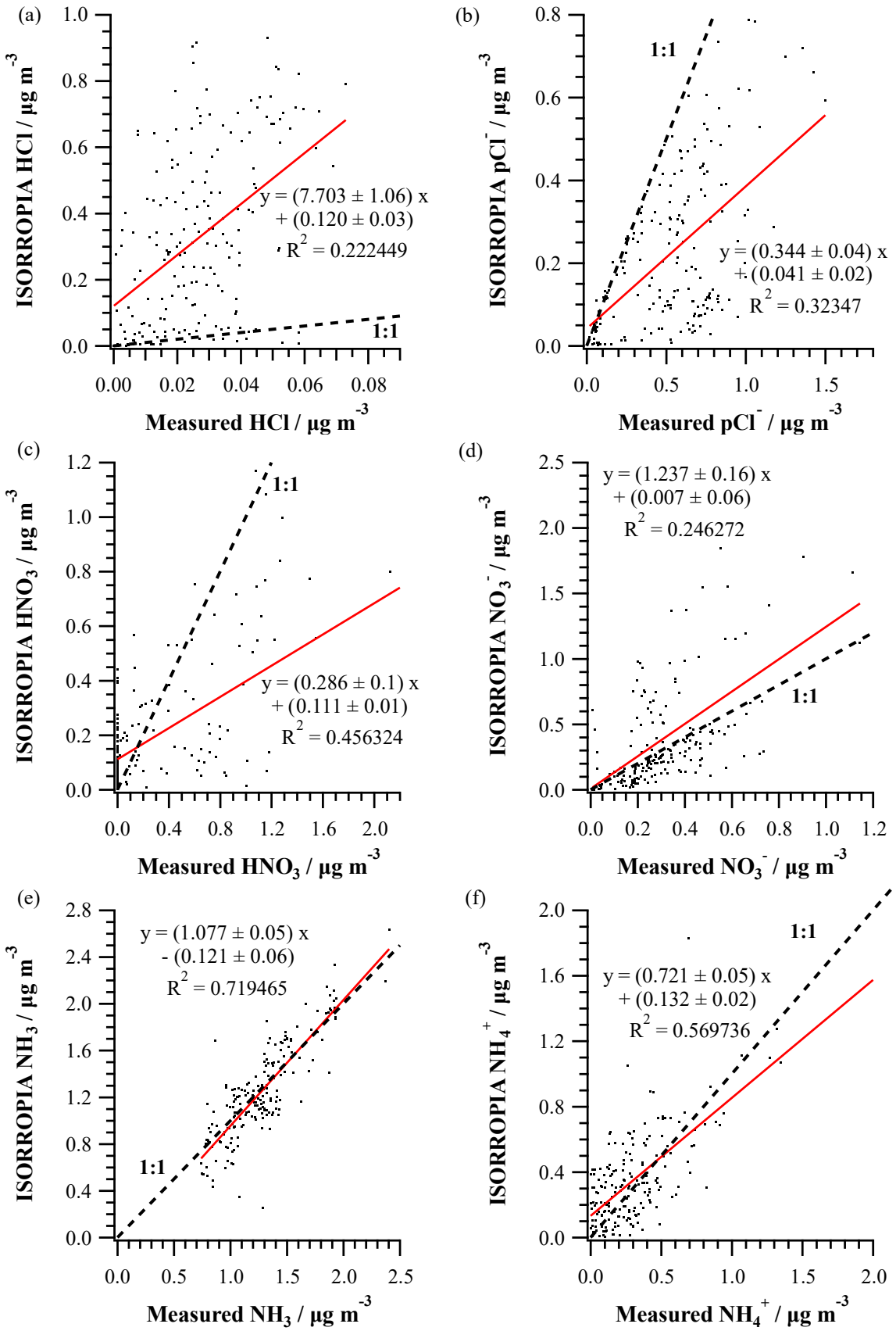

Figure 5.8. Intercomparison of the ISORROPIA predicted (a) HCl, (b) pCl^-, (c) HNO_3, (d) NO_3^-, (e) NH_3, (f) NH_4^+ concentrations obtained from the Base simulations with the winter campaign measurements.

As observed in the measurements, no discernible diurnal patterns for either HCl or pCl^- was obtained from the hourly averaged modelled concentrations as shown in Figures 5.9. Interestingly, the model still predicted elevated concentrations of HCl between the hours of 10:00 – 12:00.

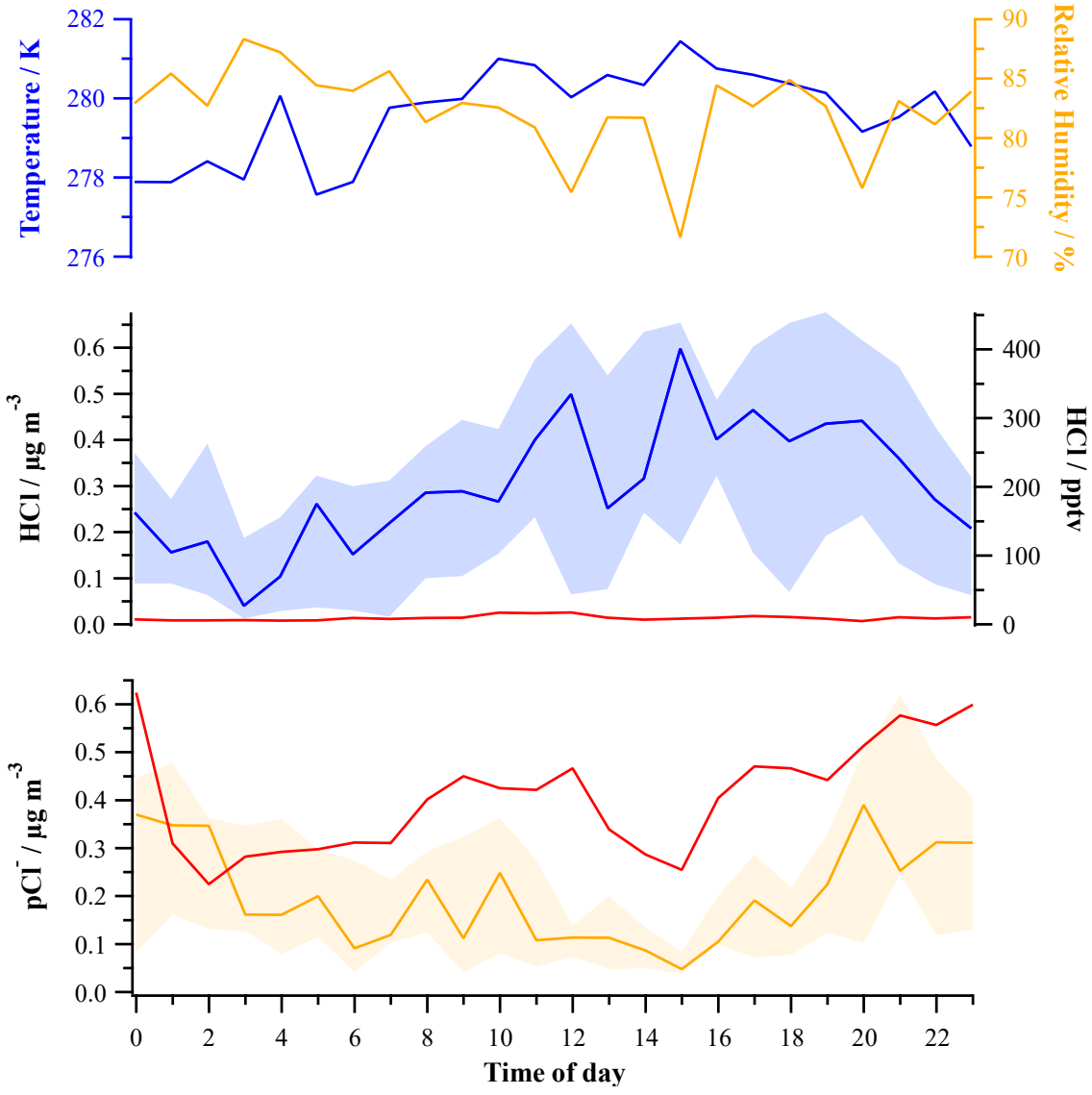

Figure 5.9. Average hourly diurnal cycle of RH and temperature (top), modelled HCl (middle) and modelled pCl^- (bottom) during the winter OSCA campaign. Solid line represents the median species concentration. Shaded region represents the 25th and 75th percentile values. Red line denotes the median measured concentration.

Whilst it is clear that ISORROPIA II performed notably poorer at capturing the observed chloride partitioning during the winter, overestimation of the gas phase contribution was observed for both seasons. The sections herein will therefore explore potential reasons as to why such discrepancies between the modelled and measured species concentrations may arise.

5.3.2.4 Sensitivity to HNO_3

Whilst the issue of using NO_y measurements to derive the concentration of HNO_3 has already been discussed with respect to the winter campaign, the assumption that HNO_3 is the only component of the NO_z fraction likely results in an overestimation of the true concentrations experienced during the summer campaign as well. This is clear when comparing the CIMS measurements of HNO_3 obtained in the 5 days prior to the start of the campaign to those derived from the NOy measurement. As can be seen in Figure 5.10, variable levels of agreement between the two sets of measurements was observed. Such variation likely arises due to fluctuating concentrations of species such as organic nitrates, peroxyacyl nitrates (PANs) or HONO that would also contribute to the NO_z measurement. Unfortunately, at the time of writing this thesis, concurrent CIMS and TILDAS measurements were not available to examine what impact the overestimation of HNO_3 may have on the partitioning of the chloride system. As an approximation, however, simulations of the summer campaign were repeated using HNO_3 concentrations reduced by a factor of 1.25 - the average discrepancy observed between the CIMS and NO_y measurements. From the resulting intercomparison of the simulated and measured concentrations of HCl and pCl^- shown in Figure 5.11, the partitioning of the chloride system appears sensitive to HNO_3, at least within the uncertainty of the NO_y measurement, although the application of the correction factor increases the discrepancy between the modelled and measured concentrations of both species by further increasing partitioning into the gas phase. Consequently, it is unlikely that error in the HNO_3 measurements is solely responsible for the observed discrepencies. It should be noted that this does not, however, include the potential for acid displacement of HCl from the course mode sea salt by HNO_3, which is not considered in this analysis.

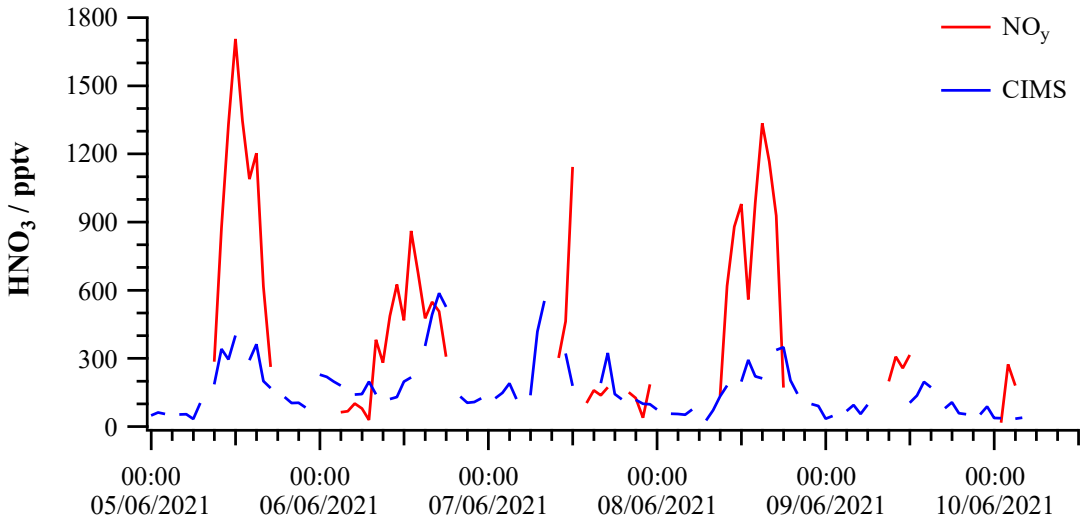

Figure 5.10. Intercomparison of the NO_y derived HNO_3 concentrations (red line) and the CIMS HNO_3 in the 5 days prior to the summer OSCA campaign.

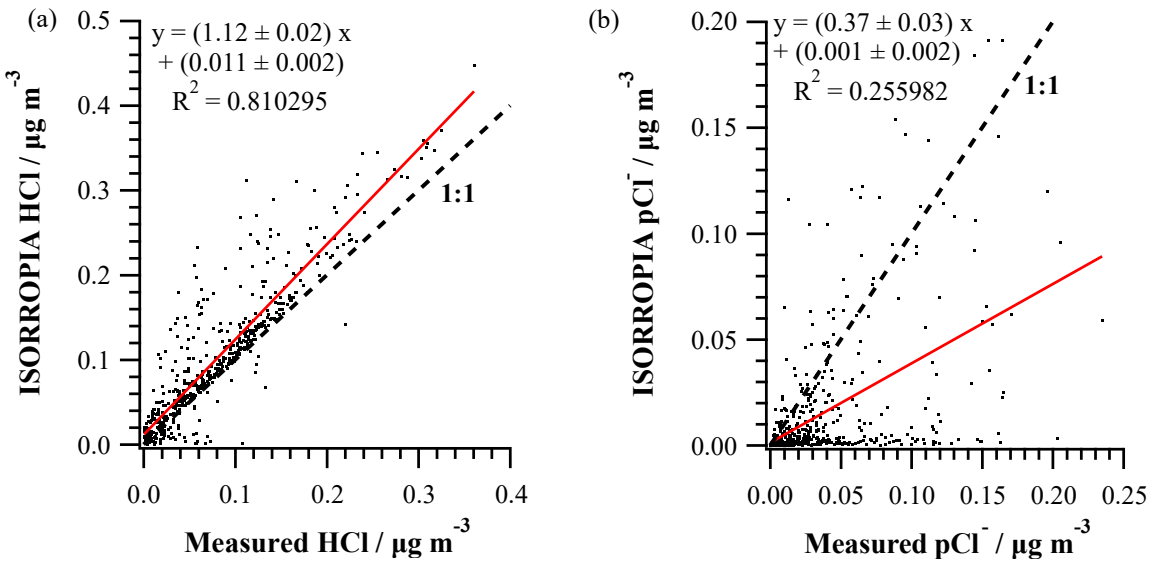

Figure 5.11. Intercomparison of the ISORROPIA predicted (a) HCl, (b) pCl^- concentrations with the summer campaign measurements upon reduction in the concentration of HNO_3 by a factor of 1.25.

5.3.2.5 Charge Balance of the Aerosol Species

A key limitation of both datasets used in this study is the lack of concurrent metal ion and organic acid measurements that may be present in the fine mode. Whilst organic acids are not considered in ISORROPIA II, their absence, and that of the metal ions in the simulations, could result in the underestimation of both chloride and nitrate in the particulate phase as their concentrations, along with that of sulphate, would be limited by the predicted concentration of NH_4^+ in order for electroneutrality to be maintained within the aerosol. To determine the feasibility of this hypothesis, the electrical charge balance of the measured aerosol components for both OSCA campaigns were investigated. As can be seen from Figure 5.12(a), the measurements obtained from the ACSM during the summer campaign yield an average anion/cation ratio of 1.10 (whilst ISORROPIA maintains a ratio of 1), suggesting that there is insufficient NH_4^+ present to neutralise both HCl and HNO_3. Such observations are consistent with the predicted concentrations obtained from ISORROPIA as previously discussed, in which both pCl^- and NO_3^- were underestimated despite the model also overestimating the concentration of NH_4^+. By contrast, however, regression analysis of the particulate concentrations recorded during the winter campaign yields an anion/cation ratio of 0.64. It is clear from Figure 5.12(b) however, that such a gradient is the result of extreme instances of charge imbalance observed during periods of low NH_4^+ concentrations, as reflected by a y-axis intercept of 0.016 µmol m^{-3} in the corresponding linear fit. To overcome this issue, the difference in concentration between the measured anionic species and NH_4^+ for each measurement period was calculated and

introduced as a colour gradient in the plots of the predicted versus measured concentrations of HCl and pCl^-. From the resulting Figures 5.13(a) and (b), it can be seen that ISORROPIA generally captures the measured concentration of both species well during periods in which either the charge imbalance was negligible or NH_4^+ was in excess. Increasing bias towards partitioning into the gas phase is observed as the excess of anions within the system increases. Similar trends are also observed in the summer dataset, as shown in Figures 5.13(c) and (d), although it is interesting to note that there are instances in which the model is in good agreement with the measured concentration of pCl^- despite the anionic concentrations being in large excess of NH_4^+ (> 0.1 μmol m^{-3}). Such periods are found to correlate with high RH, further highlighting the previously discussed potential sensitivity of ISORROPIA II to the variable when the model is initialised without any crustal species.

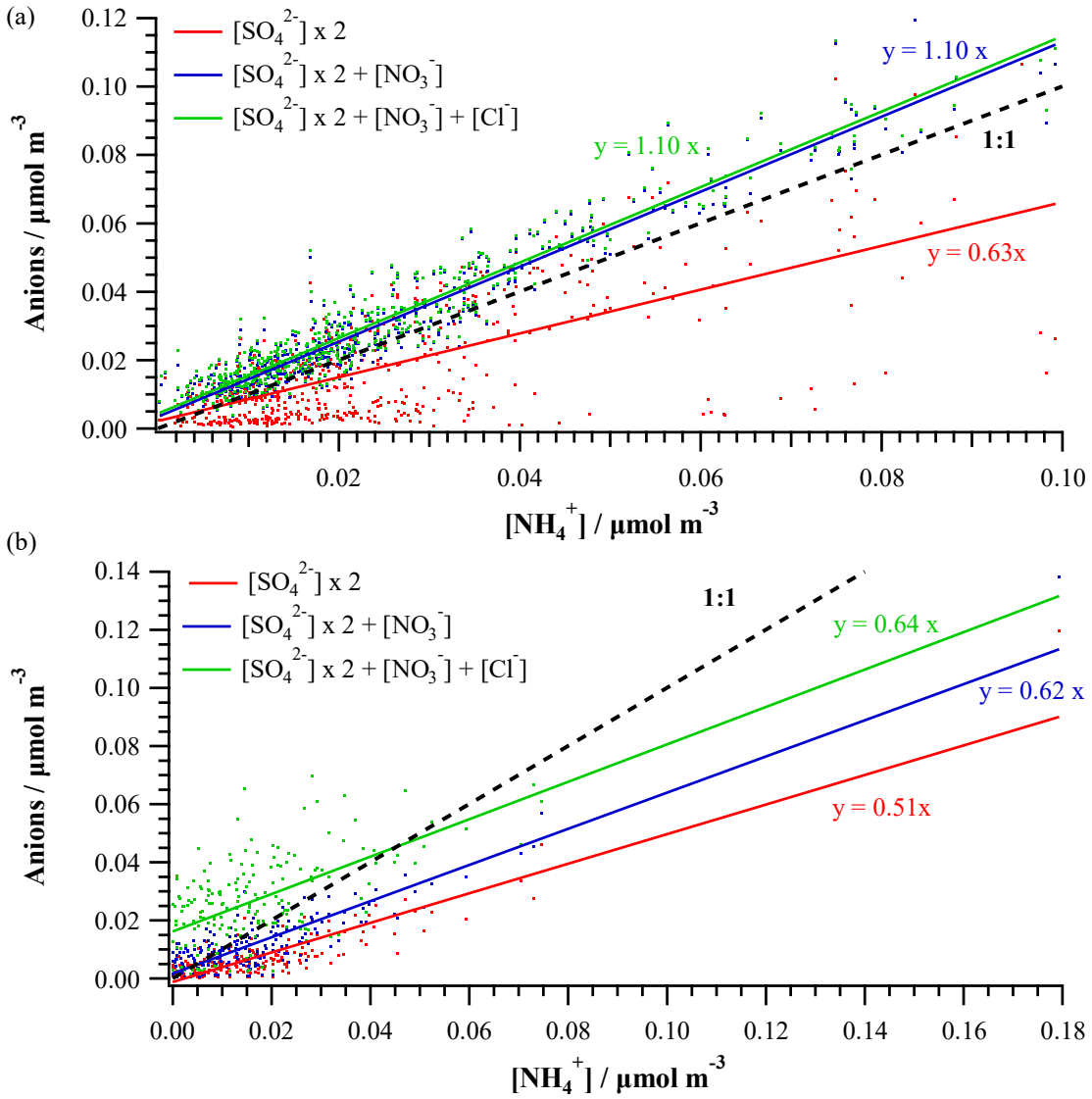

Figure 5.12. Calculated charge balance of the aerosol system over the course of the (a) summer, (b) winter OSCA campaign. Coloured lines represent the anion/cation ratio for sulfate (red), sulfate + nitrate (blue) and sulfate + nitrate + chloride (green). The black dashed line represents a 1:1 relationship.

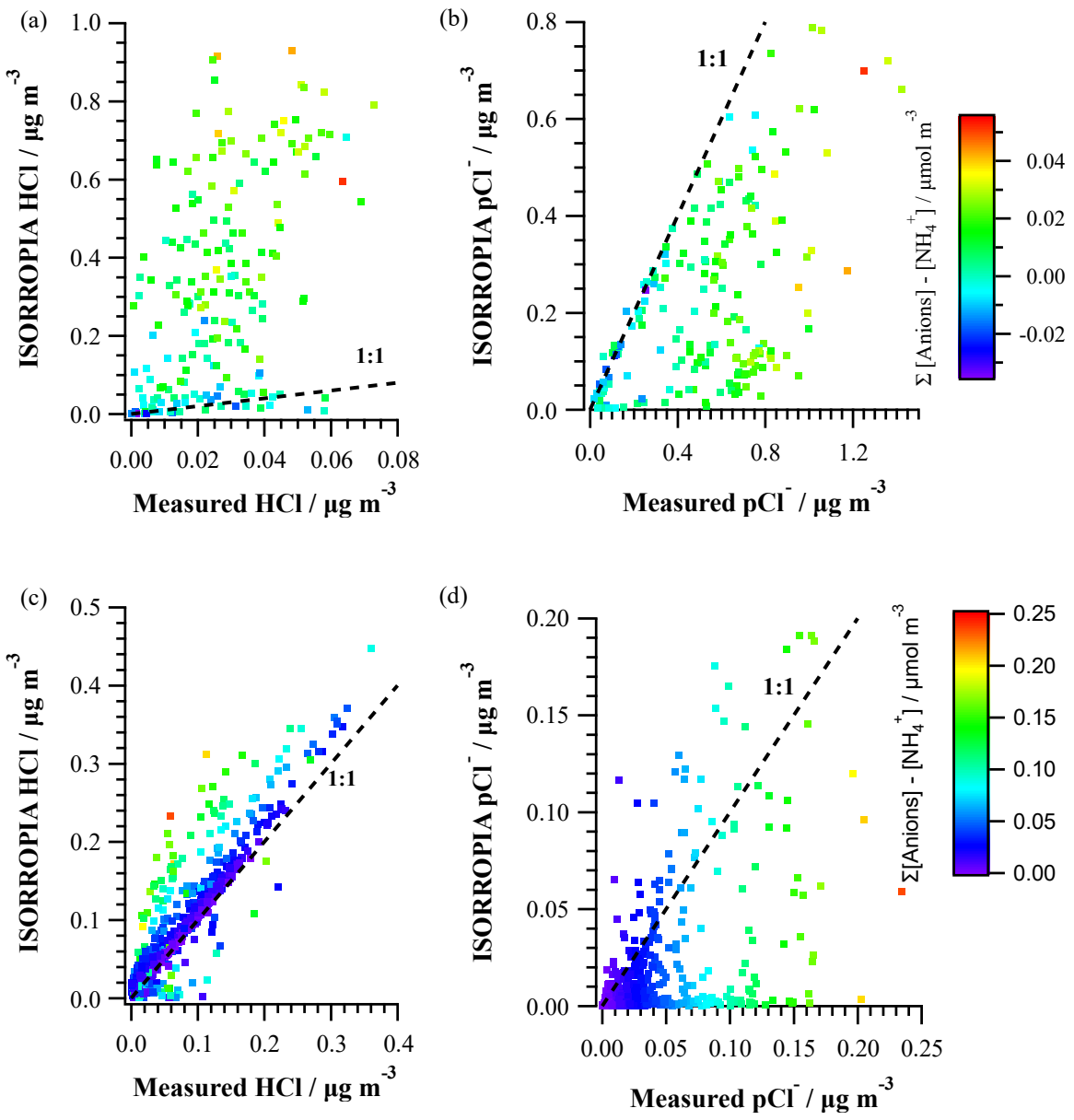

Figure 5.13. Intercomparison of the ISORROPIA predicted and modelled concentrations of (a) HCl, (b) pCl^- during the winter OSCA campaign, coloured by the measured difference in total anion (SO_4^{2-}, NO_3^- and Cl^-) and NH_4^+ concentration. Plots repeated for the predicted and modelled concentrations of (c) HCl, (d) pCl^- during the summer campaign.

In order to identify whether correcting the charge imbalance for both seasons would bring the modelled HCl and pCl^- concentrations into agreement with their observed values, iterated model simulations were conducted in which Na was used as a source of additional cations. From these simulations, two cationic concentrations could be identified; the first representing the required cation concentration at which a minimum difference between the modelled and measured HCl concentrations could be obtained, the second identifying the minimum cation concentration required to bring the modelled HCl to within 5% of the measured – the reported uncertainty of the TILDAS.[109]

Initial tests of the iterative method were conducted on the summer dataset, with the concentration of Na gradually increased for each datapoint by intervals of 0.01 μg m^{-3} to a maximum of 5.75 μg m^{-3} (0.25 μmol m^{-3}) to reflect the measured charge imbalances throughout the season. As can be seen from Figure 5.14, as by the nature of the model runs, improved agreement with the measured HCl concentrations are observed in both instance as reflected by gradients of 1 and 1.04 being obtained from both iterative approaches, down from 1.11 in the base simulations. A slight improvement in the predicted NH_3 concentration is also observed, implying the displacement of NH_4^+ into the gas phase following the addition of Na. It should be noted, however, that there are still periods in which the model is unable to reproduce the measured HCl concentrations since they were originally underpredicted in the base simulations. Again, these periods typically coincide with high RH (> 90%) in which ISORROPIA is observed to bias partitioning into the particulate phase. To gain insight into whether the metal ion concentrations identified in the iterated simulations would be typical of an urban background environment such as the Fallowfield campus, comparisons were drawn to measured metal ion concentrations in the $PM_{1.0 - 0.3}$ size range at the North Kensington sampling site during the 2012 ClearfLo campaign.[251] Mean concentrations of 135.9, 48.2, 65.9 and 31.9 ng m^{-3} of Na^+, K^+, Ca^{2+} and Mg^{2+} were observed respectively, yielding a total non $NH4^+$ cation concentration of 0.013 μmol m^{-3}. By comparison, a mean concentration of (0.022 ± 0.02) and (0.018 ± 0.02) μmol m^{-3} of Na^+ was required to achieve the minimum and five percent discrepancy between the modelled and measured HCl concentrations, suggesting that the proposed missing cation source is a possible explanation for the discrepancy which was observed.

Similar tests were also conducted on the winter dataset, however, owing to the lower charge imbalance observed during this campaign when compared to the summer, both the incremental change and maximum Na concentrations added to each datapoint were reduced to 0.001 μg m^{-3} and 1 μg m^{-3} (0.043 μmol m^{-3}) respectively. The results of the simulation are given in Figure 5.15. Whilst it is clear that the addition of Na results in a significant improvement in the ability of the model to capture the observed HCl/pCl^- partitioning behaviour, unity between the modelled and precited HCl concentrations is not achieved due to the aforementioned RH bias. Average Na concentrations required to achieve the minimum and five percent discrepancies in HCl were (1.1 ± 1) and (1.0 ± 1) × 10^{-2} μmol m^{-3} respectively. Such a cation concentration is approximately a factor of 4 greater than that observed at the North Kensington site in the winter portion of the ClearfLo campaign, in which the mean Na^+, K^+, Ca^{2+} and Mg^{2+} observations of 28.6, 12.2, 9.7 and 7.1 ng m^{-3} yield a cation concentration of 2.6 × 10^{-3} μmol m^{-3}.[252] Consequently, whilst the lack of metal ions within the simulation may play some part in the discrepancy between the modelled and measured HCl concentrations, it is unlikely to be the only factor. It is also interesting to note that in comparison to the model's ability to capture the measured NH_3 concentrations during the summer campaign, the predicted concentrations in the winter show a larger degree of variability, as reflected by an R^2 value

of 0.64 compared to 0.94 in the summer, further highlighting that other factors may be influencing the model's inability to capture the partitioning behaviour of the winter campaign.

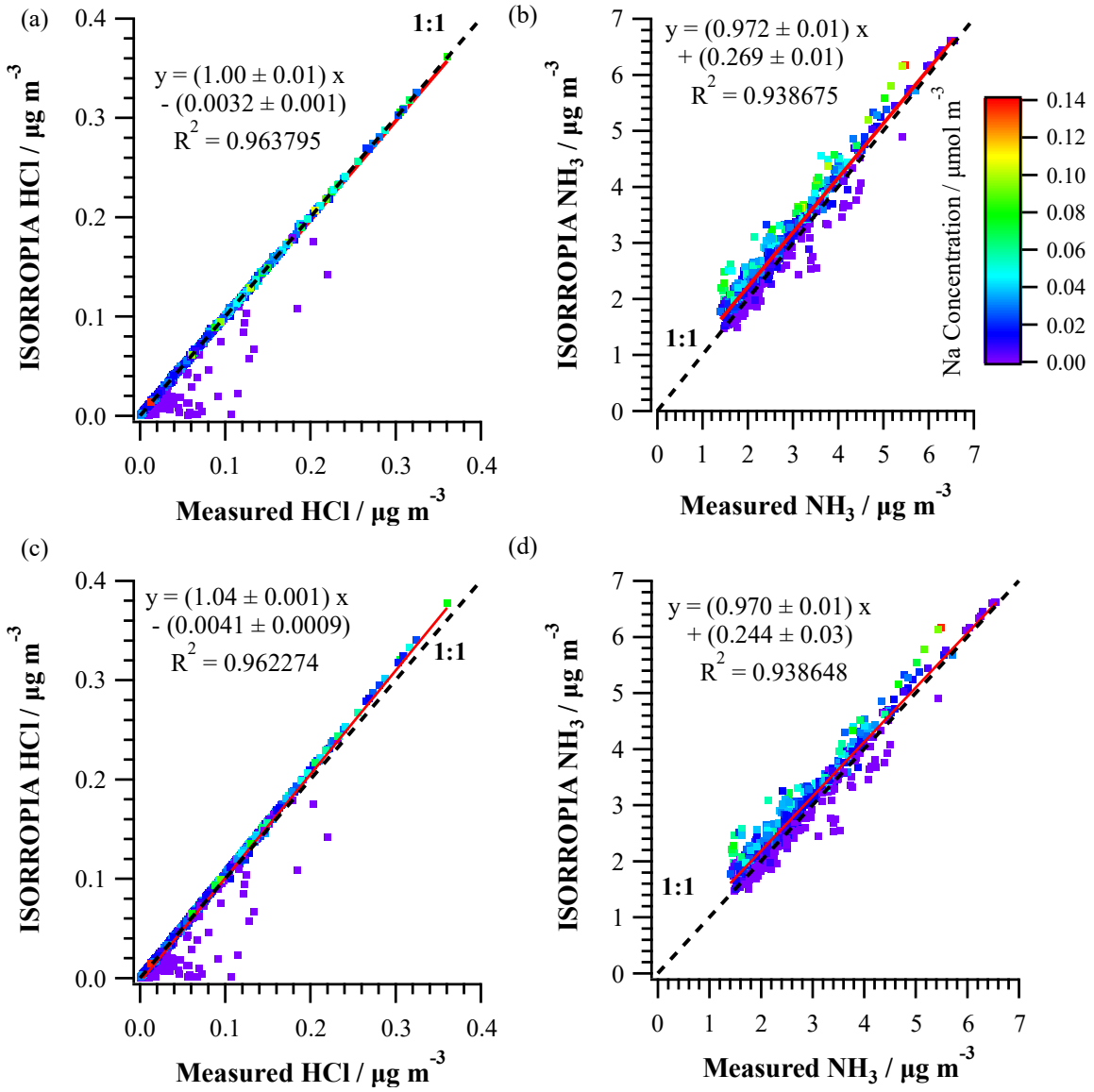

Figure 5.14. Discrepancy between the measured and ISORROPIA derived concentrations of HCl and $NH3_3$ for the summer campaign after running the Na iterated simulations to (a)/(c) achieve a minimum discrepancy in the concentration of HCl, (b)/(d) bring the discrepancy to within, or as close to, 5% of the measured HCl concentration.

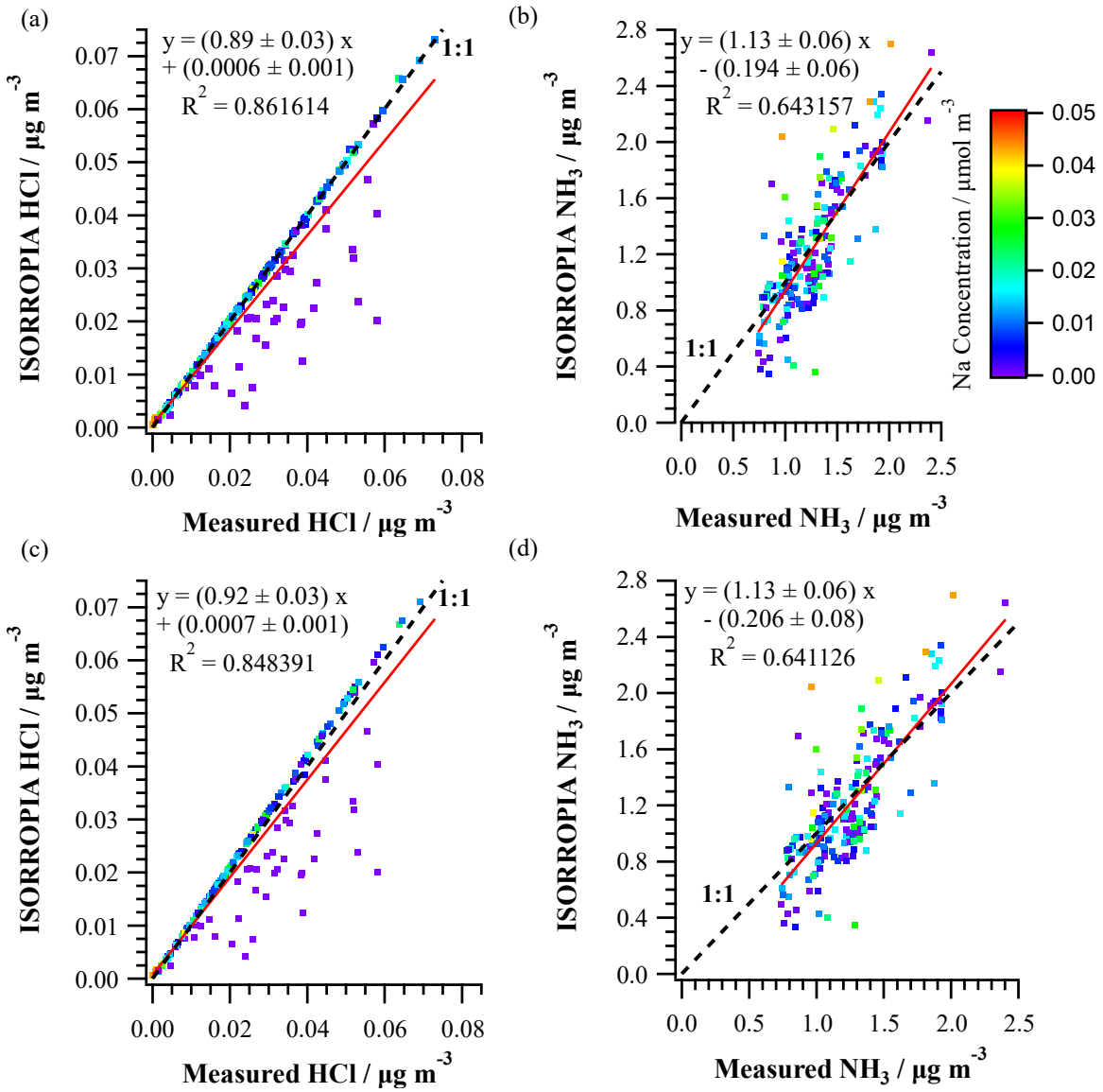

Figure 5.15. Discrepancy between the measured and ISORROPIA derived concentrations of HCl and $NH3_3$ for the winter campaign after running the Na iterated simulations to (a)/(c) achieve a minimum discrepancy in the concentration of HCl, (b)/(d) bring the discrepancy to within, or as close to, 5% of the measured HCl concentration.

5.3.2.6 Alternative sources of HCl

A key assumption which has been made throughout this study when considering the source of the discrepancy between ISORROPIA II and the observational data is that the air masses measured during both campaigns were well mixed and had sufficient time prior to sampling to establish equilibria. Consequently, the HCl measured during the campaign is assumed to be derived from thermodynamic partitioning out of the submicron particulate. Whilst this would appear to be a fair assumption during the summer campaign owing to the model's ability to capture the observed diel variability of HCl, it is possible that the discrepancy obtained with the winter dataset arises from HCl being produced from non-equilibrium processes which are not considered within the model. Interestingly, $ClNO_2$ was observed during the winter campaign, with Figure 5.16 showing the median hourly concentration of the species over the course of the measurement period and corresponding concentration of chloride. It would therefore be expected that an increase in the concentration of HCl would be observed in the morning following the photolysis of $ClNO_2$. From Figure 5.16, between the hours of 05:00 – 12:00, an average decrease of ~ 0.1 μg m^{-3} was recorded in the concentration of $ClNO_2$. This would correspond to ~ 0.044 μg m^{-3} of Cl atoms being released which subsequently react to form HCl. During this window, a ~ 0.15 μg m^{-3} increase in the concentration of HCl was observed and, as such, cannot be fully attributed to the photolysis of $ClNO_2$.

As previously discussed, significant quantities of chloride were observed in both the $PM_{2.5}$ and PM_{10} size fractions during the winter campaign. As such, equilibria between HCl and the larger $PM_{2.5}$ size fraction cannot be ruled out. Similarly, acid displacement of aged sea salt present within the coarse mode by either HNO_3 or H_2SO_4 is another potential source of HCl which would not have been accounted for in the ISORROPIA simulations of this study. Owing to the HNO_3 measurements during this period being within the noise of the NO_y instrument, it is however unknown whether sufficient amounts of either HNO_3 or H_2SO_4 would have been present to generate the concentrations of HCl observed by the TILDAS.

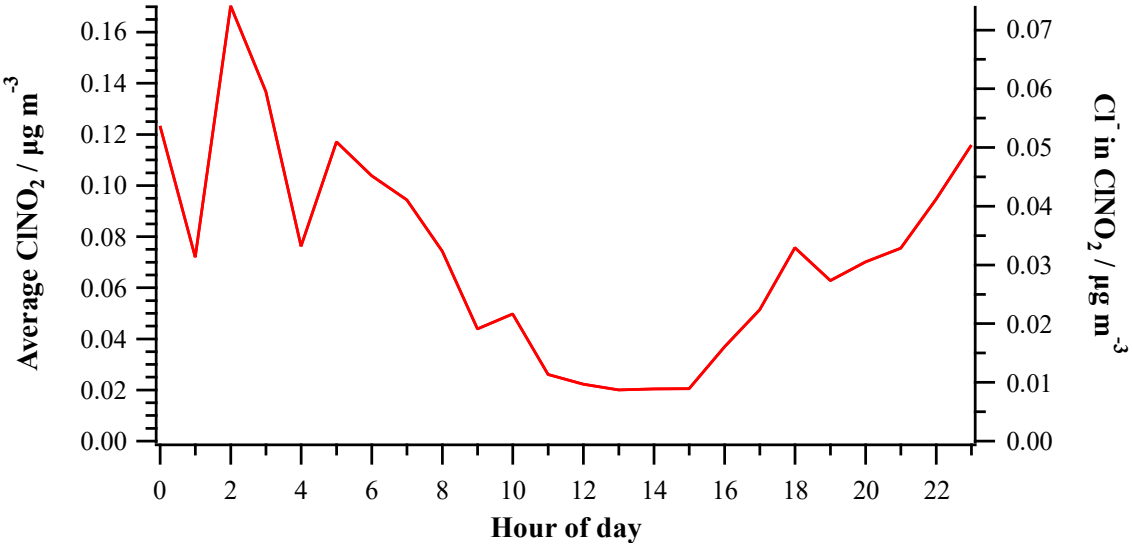

Figure 5.16. Hourly average $ClNO_2$ concentrations observed during the winter OSCA campaign.

5.4 Conclusions

The partitioning behaviour of HCl/pCl^- at an urban background site has been investigated using datasets collected during the OSCA field campaign with strong seasonal variability observed. Mixing ratios of HCl ranged from 0 – 237.9 pptv with a median concentration of 36.9 pptv during the summer, displaying a clear diurnal cycle over the course of the measurements period in which HCl levels were observed to be at their highest at midday. By contrast, no such diel variability was observed during the winter portion of the campaign in which a median concentration of 8.9 pptv was observed with a maximum of 52.6 pptv.

Thermodynamic equilibrium modelling of the inorganic ionic constituents of the PM_1 fraction and the associated precursor gases using ISORROPIA II was found to yield mixed results. Whilst the model was capable of reproducing the observed diel variability in HCl when initialised with the species concentrations recorded during the summer, the model was found to overestimate the concentration by 11%, and subsequently underestimate the concentration of pCl^- by a factor of 2. It is proposed, however, that this discrepancy arises due to lack of observational constraints used within the base model simulations as metal ion constituents within the submicron particulate were not recorded during either campaign - resulting in a charge imbalance in the particulate constituents used to initialise the model. Improved agreement was observed upon the addition of Na to correct for the charge imbalance, with the cationic concentration required to achieve this comparable to those observed at similar urban background sites. It is interesting to note that in the absence of crustal species, the partitioning of chloride within ISORROPIA appears to be highly sensitive to RH, with the model observed to bias partitioning into the gas phase at high RHs (> 90%)

By comparison the model performed notably poorer under the conditions experienced during the winter campaign with the base model found to overestimate the concentration of HCl by a factor of 7.7 and underestimate pCl^- by a factor of 3. Whilst iterating the model with Na to account for the aforementioned charge imbalances brought the modelled HCl concentrations into agreement with the observed, the cationic concentration required to achieve this was a factor of 4 larger than that measured at comparable sites. A larger degree of variability was also observed in the model's ability to capture the concentration of NH_3 recorded during the campaign. Further investigation is therefore required to better constrain the partitioning chemistry under these conditions. The measurement of the metal ion constituents, using techniques such as particle into liquid sampler – ion chromatography (PILS-IC) or ambient ion monitor – ion chromatography (AIM-IC), is also vital to constrain this partitioning chemistry, as highlighted by the sensitivity of thermodynamic partitioning model's to their absence in this study.

Chapter 6

Summary and Future Work

6.1 Overview

Whilst Cl-atoms have been identified to play a role in a number of tropospheric processes, their importance is poorly understood when compared to other oxidants such as OH. This uncertainty is the result of limited observational constraints on the Cl-atom budget, preventing the rigorous testing of the representation of Cl chemistry within global models. As direct measurement of Cl-atoms is not possible with existing observational techniques, estimations of local concentrations must be inferred through the assumption of steady state. As a result, measurement of their sources and sinks is required. The work presented in this thesis set out to explore two factors of importance in this area; the partitioning of chloride between the gas and particulate phase, and the measurement of the total Cl-atom loss rate.

6.2 Development of a Total Cl Ross Rate Instrument (Cl-CRM)

Whilst there a range of techniques that would enable the concentrations of sink species to be measured directly, from which an approximation of the Cl-atom sink could be obtained, this work presents the first development of an instrument capable of measuring the total Cl loss rate. The development of such an instrument is advantageous as it has the potential, with modifications discussed later, to directly test our understanding of reaction pathways associated with the loss of Cl whilst also providing a useful constraint on the source of missing OH reactivity that has been widely reported. Owing to the challenges faced when using resonance fluorescence to monitor the concentration of Cl-atoms, in particular when mixed with ambient air, the development of a CRM instrument was favoured over the alternative flow tube and pump probe methods which have previously been developed for the measurement of the total OH loss rate.

To assess the feasibility of the technique for this application, idealised box model simulations were conducted to simulate the deployment of the proposed instrument in Cape Verde and London, locations representative of a clean MBL and a polluted inland environment. When considering only primary reactions, overestimations of the theoretical rate by 4.7 and 6.5% were obtained respectively. In part, these errors arise from the initialisation of the model under non-pseudo first-order conditions owing to the practical difficulties that such kinetically-controlled conditions would introduce. A previously unreported systematic error arising from differences between the rate coefficients of the sample and the reference VOC has also identified as a source of the aforementioned discrepancies. Consequently, calibration of the CRM instrument is necessary in order to correct for these interferences. Upon the consideration of secondary chemistry during the measurement period, secondary radical production has been identified as an additional source of interference. This is a particular issue upon the addition of NO into the system due the formation of OH following the reaction of NO with HO_2 generated during the measurement period. It therefore follows that methods

to either minimise or correct for this interference would be required for the deployment of a Cl-CRM instrument in a high NO_x environment.

Calibration of the Cl-CRM instrument developed in this work was achieved using several single and mixed hydrocarbon standards. On average, the rates derived from these studies were found to be within (8 ± 9)% of those derived from literature rate coefficients, with a working range of 12 – 400 s^{-1} and a total measurement uncertainty of 30% identified. Whilst such a working range would be suitable for the measurement of Cl reactivity within a polluted environment, the LOD of the instrument is close to the calculated rate for Cape Verde. Consequently, a more sensitive method of detection than the SIFT-MS used in this work, for example PTR-ToF-MS, would be required if the Cl-CRM instrument were to be deployed in a similarly remote environment. Unfortunately, owing to a lack of availability of the SIFT-MS, thorough analysis of the impact of NO within the setup could not be conducted. In the limited studies that were conducted however, the observed interference exceeded that simulated in the aforementioned box model simulations, with decreases in the reactivity rate of 140 and 180 s^{-1} measured upon the addition of 4.6 and 15 ppbv of NO respectively. This increased interference can, in part, be attributed to longer residence times within the reactor than those used in the box model simulations to assess the feasibility of the technique. Furthermore, as the reference VOC and sample are exposed to the light source used to photolyse Cl_2 in the setup, additional direct and indirect photolytic sources of OH and HO_2 are present which further enhances this interference. Interestingly, when simulating the experimental conditions of the Cl-CRM instrument, the model is still unable to replicate the observed depletion in the reference VOC, with the difference in predicted concentrations suggesting an additional 1.7 – 2.5 ppbv of OH which is unaccounted for. Discrepancies between modelled and simulated impacts of NO have previously been reported by Michoud *et al*. for the MD-CRM instrument who suggest that the representation of pyrrole (used as a reference VOC) in the MCM, in particular the associated peroxy radicals, may not be reflective of the chemistry within their setup.[136] Similar sources of uncertainty are also likely present in this study, especially given that the NO interference experiments were conducted using a 35-component mixture for which not all species are represented in the MCM. Conducting these experiments using a simpler system for which the secondary chemistry is better understood, such as the CH_4 / C_3H_8 mixture, would be a sensible next step to investigate the NO interference further in order to minimise this uncertainty. Further suggestions for future work is provided later in this chapter.

6.3 Gas Particle Partitioning of Chlorine

An understanding of the partition of chloride between the gas and particulate phase is essential if we are to accurately represent the formation of reservoir such as $ClNO_2$, Cl_2, or BrCl that are formed from heterogeneous reactions on chloride containing particles. The work presented in chapter 5 investigated this partitioning behaviour at an urban background site in Manchester, UK as part of the

summer and winter OSCA campaigns. Strong seasonal variability was observed, with the gas phase dominating over the PM_1 chloride fraction during the summer whilst the inverse was true for the winter. Clear diurnal variability in the both the particulate and gas phase was observed during the summer, although such diurnal dependence was not apparent in the winter measurements, consistent with observations by Liakakou *et al*.[250] Both datasets were subsequently used to evaluate the performance of the thermodynamic partitioning model ISORROPIA II. Underestimations of a factor of 2 and 3 were obtained, on average, for the concentration of pCl^- for the summer and winter datasets respectively. For the summer dataset, it is suggested that the discrepancy between the modelled and observed concentrations arises from the absence of concurrent metal ion measurements, resulting in a deficiency of cations used to initialise the model. The modelled concentrations of HCl were brought into agreement through iteration of the model with Na^+ to account for this missing source of cations, with the required concentration comparable to the non NH_4^+ cation concentration reported by Crilley *et al*. at a comparable urban background site in North Kensington, London.[251] By comparison, the concentration of Na^+ required to bring the winter HCl concentrations into agreement was approximately a factor of 4 greater than the observed cation concentrations at the North Kensington site during the same season.[252] As such, the absence of metal ions from the constraining measurements is unlikely to be the source of discrepancy between the observed and modelled partitioning behaviour. It is therefore clear that the partitioning of chloride within the winter is an area which should be further investigated, provided additional observational constraints are available. With respect to previous reports by Haskins *et al*. that the temperature dependence of the HCl effective equilibrium constant used in the model is too large,[53] the modelled/observed discrepancy in the simulations of the summer dataset displayed no temperature relationship.

6.4 Future Work

The ultimate aim of the Cl-CRM instrument is the measurement of the total Cl loss rate in ambient air, with the simultaneous deployment of the instrument alongside measurements of the Cl reservoir species enabling localised Cl-atom concentrations to be determined through the assumption of steady state. Unfortunately, the instrument developed in this work is not suitable for such application at present. A key reason for this is that in the current reactor design, the sample is exposed to the light source used to photolyse Cl_2. As discussed above, not only does this create additional sources of HO_2 and OH that can interfere with the rate measurement, it can also lead to losses of photolabile VOC species that may be present in an ambient air sample. It therefore follows that an essential next step is the development of a new reactor which would enable the sample and reference VOC to be introduced after the production of Cl radicals. Two alternative designs by which this could be achieved have been proposed in chapter 4. To assess their validity, however, computational fluid dynamic modelling would be required to ensure that laminar flow could be achieved in such designs in order to minimise wall losses within the system. Once a new reactor is developed, characterisation

of the instrument would need to be conducted following a similar framework to that used in this study.

Resolving the issue of NO interference is another area that would require further consideration before the instrument is suitable for field deployment. As discussed in chapter 4, switching to a different reference VOC with a larger k_{Cl} : k_{OH} ratio than diethyl ether is one route through which this could be achieved. Such an approach, however, would likely require the use of a short chain deuterated alkane as a reference VOC in order to meet such a requirement. As such species are not measurable using either SIFT-MS or PTR-MS, a change to GC-MS as a detection method would be required if such an approach was chosen – potentially leading to a reduced time resolution if sample pre-concentration is required. Addition of an OH scavenger species combined with a reduction in the residence time following mixing of the Cl-atoms and sample have also been identified as potential solution to minimise this interference. Such an approach would, however, likely require the use of CO which would introduce additional safety considerations. Development of a correction factor to account for the formation of OH within the system whilst in high NO_x environments is the final method which could be adopted. Simultaneous measurements of NO would be required for this approach to work, however, as NO_x analysers are common place during field campaigns, this is unlikely to be a source of issue.

With respect to the investigation into partitioning of the chloride system, it is clear that additional observational constraints (in particular metal ion concentrations) are required, in particular during the winter. Such information could be obtained by deploying either a particle into liquid sampler – ion chromatography (PILS-IC) or ambient ion monitor – ion chromatography (AIM-IC) instrument alongside the TILDAS for HCl measurement. Collection of this information would also enable the performance of other thermodynamic models beyond ISORROPIA, such as E-AIM, to be explored as well.

Abbreviations

$(C_2H_5)_2O$	-	Diethyl ether
$(COCl)_2$	-	Oxalyl chloride
ACSM	-	Aerosol Chemical Speciation Monitor
AIM-IC	-	Ambient ion monitor - ion chromatography
BrCl	-	Bromine chloride
BrO	-	Bromine monoxide
BVOC	-	Biogenic volatile organic compound
C_5H_8	-	Isoprene
$C_6H_{12}O$	-	3,3-dimethyl-2-butanone
CCl_3COCl	-	Trichloroacetyl chloride
CCl_4	-	Carbon tetrachloride
CFCs	-	Chlorofluorocarbons
CH_2Cl_2	-	Dichloromethane
CH_3Cl	-	Methyl chloride
$CHCl_3$	-	Chloroform
CIMS	-	Chemical ionisation mass spectrometry
$ClNO_2$	-	Nitryl chloride
ClO	-	Chlorine monoxide
$ClONO_2$	-	Chlorine nitrate
ClOO	-	Chlorine peroxy radical
ClO_x	-	Oxides of chlorine (Cl + ClO)
Cl_y	-	Reactive chlorine
CRDS	-	Cavity ring down spectroscopy
CRM	-	Comparative reactivity method
E/N	-	Electric field
GC-MS	-	Gas chromatography-mass spectrometry
H_3O^+	-	Hydronium ion
HO_2	-	Hydroperoxyl radical
HOBr	-	Hypobromous acid
HOCl	-	Hypochlorous acid
IC	-	Ion chromatography
ICRM	-	Improved comparative reactivity method
LDLS	-	Laser driven light source

LIF-FAGE - Laser-induced fluorescence-fluorescence assay by gas expansion

LOD - Limit of detection

m/z - Mass-to-charge ratio

MACR - Methacrolein

MBL - Marine boundary layer

MD-CRM - Mines Douai comparative reactivity method

MDRH - Mutual deliquescence relative humidity

MFC - Mass flow controller

MVK - Methyl vinyl ketone

N_2O_5 - Dinitrogen pentoxide

NMHC - Non-methane hydrocarbon

NO^+ - Nitrosonium ion

NO_x - Nitrogen oxides ($NO + NO_2$)

O_2^+ - Dioxygenyl ion

OCl^- - Hypochlorite

OClO - Chlorine dioxide

ODR - Orthogonal distance regression

OH - Hydroxyl radical

OVOCs - Oxygenated volatile organic compounds

PANs - Peroxyacyl nitrates

pCl^- - Particulate chloride

PILS-IC - Particle into liquid sampler - ion chromatography

PM_1 - Aerosol with an aerodynamic diameter of less than 1 µm

$PM_{2.5}$ - Aerosol with an aerodynamic diameter of less than 2.5 µm

PM_{10} - Aerosol with an aerodynamic diameter of less than 10 µm

ppbv - Parts per billion volume

ppmv - Parts per million volume

pptv - Parts per trillion volume

PSC - Polar stratospheric cloud

PTR-MS - Proton transfer reaction - mass spectrometry

RF - Radio frequency

RH - Relative humidity

RO_2 - Peroxy radical

sccm - Standard cubic centimetres per minute

SIFT-MS - Selected ion flow tube - mass spectrometry

SIM - Selection ion monitoring

SML - Sea surface microlayer

SMPS - Scanning mobility particle sizer

SOA - Secondary organic aerosol

$SOCl_2$ - Thionyl chloride

SSA - Sea spray aerosols

TCl_g - Total gaseous chlorine

TILDAS - Tunable infrared laser direct absorption spectroscopy

TOHLM - Total OH Loss rate Method

VOCs - Volatile organic compounds

VUV - Vacuum ultraviolet

Bibliography

(1) Pörtner, H.-O.; Roberts, D.; Tignor, M.; Poloczanska, E.; Mintenbeck, K.; Alegría, A.; Craig, M.; Langsdorf, S.; Löschke, S.; Möller, V.; et al. *Climate Change 2022: Impacts, Adaptation and Vulnerability Working Group II Contribution to the Sixth Assessment Report of the Intergovernmental Panel on Climate Change*; 2022. DOI: https://doi.org/10.1017/9781009325844.

(2) Stolarski, R. S.; Cicerone, R. J. Stratospheric Chlorine: a Possible Sink for Ozone. *Canadian Journal of Chemistry* **1974**, *52* (8), 1610-1615. DOI: https://doi.org/10.1139/v74-233.

(3) Molina, M. J.; Rowland, F. S. Stratospheric sink for chlorofluoromethanes: chlorine atom-catalysed destruction of ozone. *Nature* **1974**, *249* (5460), 810-812. DOI: https://doi.org/10.1038/249810a0.

(4) Tritscher, I.; Pitts, M. C.; Poole, L. R.; Alexander, S. P.; Cairo, F.; Chipperfield, M. P.; Grooß, J.-U.; Höpfner, M.; Lambert, A.; Luo, B.; et al. Polar Stratospheric Clouds: Satellite Observations, Processes, and Role in Ozone Depletion. *Reviews of Geophysics* **2021**, *59* (2), e2020RG000702. DOI: https://doi.org/10.1029/2020RG000702.

(5) Farman, J. C.; Gardiner, B. G.; Shanklin, J. D. Large losses of total ozone in Antarctica reveal seasonal ClOx/NOx interaction. *Nature* **1985**, *315* (6016), 207-210. DOI: https://doi.org/10.1038/315207a0.

(6) Crutzen, P. J.; Arnold, F. Nitric acid cloud formation in the cold Antarctic stratosphere: a major cause for the springtime 'ozone hole'. *Nature* **1986**, *324* (6098), 651-655. DOI: https://doi.org/10.1038/324651a0.

(7) Molina, L. T.; Molina, M. J. Production of chlorine oxide (Cl_2O_2) from the self-reaction of the chlorine oxide (ClO) radical. *The Journal of Physical Chemistry* **1987**, *91* (2), 433-436. DOI: https://doi.org/10.1021/j100286a035.

(8) Simpson, W. R.; Brown, S. S.; Saiz-Lopez, A.; Thornton, J. A.; von Glasow, R. Tropospheric Halogen Chemistry: Sources, Cycling, and Impacts. *Chemical Reviews* **2015**, *115* (10), 4035-4062. DOI: https://doi.org/10.1021/cr5006638.

(9) Saiz-Lopez, A.; von Glasow, R. Reactive halogen chemistry in the troposphere. *Chemical Society Reviews* **2012**, *41* (19), 6448-6472, 10.1039/C2CS35208G. DOI: https://doi.org/10.1039/C2CS35208G.

(10) Lary, D. J. Halogens and the chemistry of the free troposphere. *Atmos. Chem. Phys.* **2005**, *5* (1), 227-237. DOI: https://doi.org/10.5194/acp-5-227-2005.

(11) Sander, S.; Finlayson-Pitts, B.; Friedl, R.; Golden, D.; Huie, R.; Keller-Rudek, H.; Kolb, C.; Kurylo, M.; Molina, M.; Moortgat, G.; et al. Chemical Kinetics and Photochemical Data for Use in Atmospheric Studies. Evaluation No. 15 (JPL Publication 06-2). **2006**.

(12) Sherwen, T.; Schmidt, J. A.; Evans, M. J.; Carpenter, L. J.; Großmann, K.; Eastham, S. D.; Jacob, D. J.; Dix, B.; Koenig, T. K.; Sinreich, R.; et al. Global impacts of tropospheric halogens (Cl, Br, I) on oxidants and composition in GEOS-Chem. *Atmos. Chem. Phys.* **2016**, *16* (18), 12239-12271. DOI: https://doi.org/10.5194/acp-16-12239-2016.

(13) Wang, X.; Jacob, D. J.; Eastham, S. D.; Sulprizio, M. P.; Zhu, L.; Chen, Q.; Alexander, B.; Sherwen, T.; Evans, M. J.; Lee, B. H.; et al. The role of chlorine in global tropospheric chemistry. *Atmos. Chem. Phys.* **2019**, *19* (6), 3981-4003. DOI: https://doi.org/10.5194/acp-19-3981-2019.

(14) Finlayson-Pitts, B. J. Chlorine atoms as a potential tropospheric oxidant in the marine boundary layer. *Research on Chemical Intermediates* **1993**, *19* (3), 235-249. DOI: https://doi.org/10.1163/156856793X00091.

(15) Atkinson, R.; Baulch, D. L.; Cox, R. A.; Crowley, J. N.; Hampson, R. F.; Hynes, R. G.; Jenkin, M. E.; Rossi, M. J.; Troe, J.; Subcommittee, I. Evaluated kinetic and photochemical data for atmospheric chemistry: Volume II - gas phase reactions of organic species. *Atmos. Chem. Phys.* **2006**, *6* (11), 3625-4055. DOI: https://doi.org/10.5194/acp-6-3625-2006.

(16) Sarwar, G.; Simon, H.; Xing, J.; Mathur, R. Importance of tropospheric $ClNO_2$ chemistry across the Northern Hemisphere. *Geophysical Research Letters* **2014**, *41* (11), 4050-4058. DOI: https://doi.org/10.1002/2014gl059962.

(17) Wang, T.; Tham, Y. J.; Xue, L.; Li, Q.; Zha, Q.; Wang, Z.; Poon, S. C. N.; Dubé, W. P.; Blake, D. R.; Louie, P. K. K.; et al. Observations of nitryl chloride and modeling its source and effect on ozone in the planetary boundary layer of southern China. *Journal of Geophysical Research: Atmospheres* **2016**, *121* (5), 2476-2489. DOI: https://doi.org/10.1002/2015jd024556.

(18) Donohoue, D. L.; Bauer, D.; Cossairt, B.; Hynes, A. J. Temperature and Pressure Dependent Rate Coefficients for the Reaction of Hg with Br and the Reaction of Br with Br: A Pulsed Laser Photolysis-Pulsed Laser Induced Fluorescence Study. *The Journal of Physical Chemistry A* **2006**, *110* (21), 6623-6632. DOI: https://doi.org/10.1021/jp054688j.

(19) Auzmendi-Murua, I.; Castillo, Á.; Bozzelli, J. W. Mercury oxidation via chlorine, bromine, and iodine under atmospheric conditions: thermochemistry and kinetics. *J Phys Chem A* **2014**, *118* (16), 2959-2975. DOI: https://doi.org/10.1021/jp412654s.

(20) Kim, M. J.; Farmer, D. K.; Bertram, T. H. A controlling role for the air–sea interface in the chemical processing of reactive nitrogen in the coastal marine boundary layer. *Proceedings of the National Academy of Sciences* **2014**, *111* (11), 3943-3948. DOI: https://doi.org/10.1073/pnas.1318694111.

(21) Finlayson-Pitts, B. J.; Ezell, M. J.; Pitts, J. N. Formation of chemically active chlorine compounds by reactions of atmospheric NaCl particles with gaseous N_2O_5 and $ClONO_2$. *Nature* **1989**, *337* (6204), 241-244. DOI: https://doi.org/10.1038/337241a0.

(22) Lawrence, M. G.; Jöckel, P.; von Kuhlmann, R. What does the global mean OH concentration tell us? *Atmos. Chem. Phys.* **2001**, *1* (1), 37-49. DOI: https://doi.org/10.5194/acp-1-37-2001.

(23) Singh, H. B.; Thakur, A. N.; Chen, Y. E.; Kanakidou, M. Tetrachloroethylene as an indicator of low Cl atom concentrations in the troposphere. *Geophysical Research Letters* **1996**, *23* (12), 1529-1532. DOI: https://doi.org/10.1029/96gl01368.

(24) Lowe, D. C.; Allan, W.; Manning, M. R.; Bromley, T.; Brailsford, G.; Ferretti, D.; Gomez, A.; Knobben, R.; Martin, R.; Mei, Z.; et al. Shipboard determinations of the distribution of ^{13}C in atmospheric methane in the Pacific. *Journal of Geophysical Research: Atmospheres* **1999**, *104* (D21), 26125-26135. DOI: https://doi.org/10.1029/1999jd900452.

(25) Platt, U.; Allan, W.; Lowe, D. Hemispheric average Cl atom concentration from $^{13}C/^{12}C$ ratios in atmospheric methane. *Atmos. Chem. Phys.* **2004**, *4* (9/10), 2393-2399. DOI: https://doi.org/10.5194/acp-4-2393-2004.

(26) Allan, W.; Lowe, D. C.; Gomez, A. J.; Struthers, H.; Brailsford, G. W. Interannual variation of ^{13}C in tropospheric methane: Implications for a possible atomic chlorine sink in the marine boundary layer. *Journal of Geophysical Research: Atmospheres* **2005**, *110* (D11). DOI: https://doi.org/10.1029/2004jd005650.

(27) Allan, W.; Struthers, H.; Lowe, D. C. Methane carbon isotope effects caused by atomic chlorine in the marine boundary layer: Global model results compared with Southern Hemisphere measurements. *Journal of Geophysical Research: Atmospheres* **2007**, *112* (D4). DOI: https://doi.org/10.1029/2006jd007369.

(28) Parrish, D. D.; Stohl, A.; Forster, C.; Atlas, E. L.; Blake, D. R.; Goldan, P. D.; Kuster, W. C.; de Gouw, J. A. Effects of mixing on evolution of hydrocarbon ratios in the troposphere. *Journal of Geophysical Research: Atmospheres* **2007**, *112* (D10). DOI: https://doi.org/10.1029/2006JD007583.

(29) Baker, A. K.; Sauvage, C.; Thorenz, U. R.; van Velthoven, P.; Oram, D. E.; Zahn, A.; Brenninkmeijer, C. A. M.; Williams, J. Evidence for strong, widespread chlorine radical chemistry associated with pollution outflow from continental Asia. *Scientific Reports* **2016**, *6* (1), 36821. DOI: https://doi.org/10.1038/srep36821.

(30) Pszenny, A. A. P.; Fischer, E. V.; Russo, R. S.; Sive, B. C.; Varner, R. K. Estimates of Cl atom concentrations and hydrocarbon kinetic reactivity in surface air at Appledore Island, Maine (USA), during International Consortium for Atmospheric Research on Transport and

Transformation/Chemistry of Halogens at the Isles of Shoals. *Journal of Geophysical Research: Atmospheres* **2007**, *112* (D10). DOI: https://doi.org/10.1029/2006JD007725.

(31) Wingenter, O. W.; Sive, B. C.; Blake, N. J.; Blake, D. R.; Rowland, F. S. Atomic chlorine concentrations derived from ethane and hydroxyl measurements over the equatorial Pacific Ocean: Implication for dimethyl sulfide and bromine monoxide. *Journal of Geophysical Research* **2005**, *110*, 1-10. DOI: https://doi.org/10.1029/2005JD005875.

(32) Wingenter, O. W.; Blake, D. R.; Blake, N. J.; Sive, B. C.; Rowland, F. S.; Atlas, E.; Flocke, F. Tropospheric hydroxyl and atomic chlorine concentrations, and mixing timescales determined from hydrocarbon and halocarbon measurements made over the Southern Ocean. *Journal of Geophysical Research: Atmospheres* **1999**, *104* (D17), 21819-21828. DOI: https://doi.org/10.1029/1999JD900203.

(33) Ariya, P.; Jobson, B. T. R.; Sander, R.; Niki, H.; Harris, G.; Hopper, J.; Anlauf, K. Measurements of C_2-C_7 hydrocarbons during the Polar Sunrise Experiment 1994: Further evidence for halogen chemistry in the troposphere. *Journal of Geophysical Research* **1998**, *1031*, 13169-13180. DOI: https://doi.org/10.1029/98JD00284.

(34) Singh, H. B.; Gregory, G. L.; Anderson, B.; Browell, E.; Sachse, G. W.; Davis, D. D.; Crawford, J.; Bradshaw, J. D.; Talbot, R.; Blake, D. R.; et al. Low ozone in the marine boundary layer of the tropical Pacific Ocean: Photochemical loss, chlorine atoms, and entrainment. *Journal of Geophysical Research: Atmospheres* **1996**, *101* (D1), 1907-1917. DOI: https://doi.org/10.1029/95JD01028.

(35) Wingenter, O. W.; Kubo, M. K.; Blake, N. J.; Smith Jr., T. W.; Blake, D. R.; Rowland, F. S. Hydrocarbon and halocarbon measurements as photochemical and dynamical indicators of atmospheric hydroxyl, atomic chlorine, and vertical mixing obtained during Lagrangian flights. *Journal of Geophysical Research: Atmospheres* **1996**, *101* (D2), 4331-4340. DOI: https://doi.org/10.1029/95JD02457.

(36) Young, C. J.; Washenfelder, R. A.; Edwards, P. M.; Parrish, D. D.; Gilman, J. B.; Kuster, W. C.; Mielke, L. H.; Osthoff, H. D.; Tsai, C.; Pikelnaya, O.; et al. Chlorine as a primary radical: evaluation of methods to understand its role in initiation of oxidative cycles. *Atmos. Chem. Phys.* **2014**, *14* (7), 3427-3440. DOI: https://doi.org/10.5194/acp-14-3427-2014.

(37) Keene, W. C.; Maben, J. R.; Pszenny, A. A. P.; Galloway, J. N. Measurement technique for inorganic chlorine gases in the marine boundary layer. *Environmental Science & Technology* **1993**, *27* (5), 866-874. DOI: https://doi.org/10.1021/es00042a008.

(38) Pszenny, A. A. P.; Moldanová, J.; Keene, W. C.; Sander, R.; Maben, J. R.; Martinez, M.; Crutzen, P. J.; Perner, D.; Prinn, R. G. Halogen cycling and aerosol pH in the Hawaiian marine boundary layer. *Atmos. Chem. Phys.* **2004**, *4* (1), 147-168. DOI: https://doi.org/10.5194/acp-4-147-2004.

(39) Keene, W. C.; Stutz, J.; Pszenny, A. A. P.; Maben, J. R.; Fischer, E. V.; Smith, A. M.; von Glasow, R.; Pechtl, S.; Sive, B. C.; Varner, R. K. Inorganic chlorine and bromine in coastal New England air during summer. *Journal of Geophysical Research: Atmospheres* **2007**, *112* (D10). DOI: https://doi.org/10.1029/2006JD007689.

(40) Young, A. H.; Keene, W. C.; Pszenny, A. A. P.; Sander, R.; Thornton, J. A.; Riedel, T. P.; Maben, J. R. Phase partitioning of soluble trace gases with size-resolved aerosols in near-surface continental air over northern Colorado, USA, during winter. *Journal of Geophysical Research: Atmospheres* **2013**, *118* (16), 9414-9427. DOI: https://doi.org/10.1002/jgrd.50655.

(41) Solomon, S. Stratospheric ozone depletion: A review of concepts and history. *Reviews of Geophysics* **1999**, *37* (3), 275-316. DOI: https://doi.org/10.1029/1999RG900008.

(42) Graedel, T. E.; Keene, W. C. Tropospheric budget of reactive chlorine. *Global Biogeochemical Cycles* **1995**, *9* (1), 47-77. DOI: https://doi.org/10.1029/94gb03103.

(43) de Leeuw, G.; Andreas, E. L.; Anguelova, M. D.; Fairall, C. W.; Lewis, E. R.; O'Dowd, C.; Schulz, M.; Schwartz, S. E. Production flux of sea spray aerosol. *Reviews of Geophysics* **2011**, *49* (2). DOI: https://doi.org/10.1029/2010RG000349.

(44) Quinn, P. K.; Collins, D. B.; Grassian, V. H.; Prather, K. A.; Bates, T. S. Chemistry and Related Properties of Freshly Emitted Sea Spray Aerosol. *Chemical Reviews* **2015**, *115* (10), 4383-4399. DOI: https://doi.org/10.1021/cr500713g.

(45) Wang, X.; Deane, G. B.; Moore, K. A.; Ryder, O. S.; Stokes, M. D.; Beall, C. M.; Collins, D. B.; Santander, M. V.; Burrows, S. M.; Sultana, C. M.; et al. The role of jet and film drops in controlling the mixing state of submicron sea spray aerosol particles. *Proc Natl Acad Sci U S A* **2017**, *114* (27), 6978-6983. DOI: https://doi.org/10.1073/pnas.1702420114.

(46) Keene, W. C.; Khalil, M. A. K.; Erickson III, D. J.; McCulloch, A.; Graedel, T. E.; Lobert, J. M.; Aucott, M. L.; Gong, S. L.; Harper, D. B.; Kleiman, G.; et al. Composite global emissions of reactive chlorine from anthropogenic and natural sources: Reactive Chlorine Emissions Inventory. *Journal of Geophysical Research: Atmospheres* **1999**, *104* (D7), 8429-8440. DOI: https://doi.org/10.1029/1998JD100084.

(47) Tegen, I.; Hollrig, P.; Chin, M.; Fung, I.; Jacob, D.; Penner, J. Contribution of different aerosol species to the global aerosol extinction optical thickness: Estimates from model results. *Journal of Geophysical Research: Atmospheres* **1997**, *102* (D20), 23895-23915. DOI: https://doi.org/10.1029/97JD01864.

(48) Zhang, B.; Shen, H.; Yun, X.; Zhong, Q.; Henderson, B. H.; Wang, X.; Shi, L.; Gunthe, S. S.; Huey, L. G.; Tao, S.; et al. Global Emissions of Hydrogen Chloride and Particulate Chloride from Continental

Sources. *Environmental Science & Technology* **2022**, *56* (7), 3894-3904. DOI: https://doi.org/10.1021/acs.est.1c05634.

(49) McNamara, S. M.; Garner, N. M.; Wang, S.; Raso, A. R. W.; Thanekar, S.; Barget, A. J.; Fuentes, J. D.; Shepson, P. B.; Pratt, K. A. Bromine Chloride in the Coastal Arctic: Diel Patterns and Production Mechanisms. *ACS Earth and Space Chemistry* **2020**, *4* (4), 620-630. DOI: https://doi.org/10.1021/acsearthspacechem.0c00021.

(50) Laskin, A.; Moffet, R. C.; Gilles, M. K.; Fast, J. D.; Zaveri, R. A.; Wang, B.; Nigge, P.; Shutthanandan, J. Tropospheric chemistry of internally mixed sea salt and organic particles: Surprising reactivity of NaCl with weak organic acids. *Journal of Geophysical Research: Atmospheres* **2012**, *117* (D15). DOI: https://doi.org/10.1029/2012JD017743.

(51) Gard, E. E.; Kleeman, M. J.; Gross, D. S.; Hughes, L. S.; Allen, J. O.; Morrical, B. D.; Fergenson, D. P.; Dienes, T.; E. Gälli, M.; Johnson, R. J.; et al. Direct Observation of Heterogeneous Chemistry in the Atmosphere. *Science* **1998**, *279* (5354), 1184-1187. DOI: https://doi.org/10.1126/science.279.5354.1184.

(52) De Haan, D. O.; Brauers, T.; Oum, K.; Stutz, J.; Nordmeyer, T.; Finlayson-Pitts, B. J. Heterogeneous chemistry in the troposphere: Experimental approaches and applications to the chemistry of sea salt particles. *International Reviews in Physical Chemistry* **1999**, *18* (3), 343-385. DOI: https://doi.org/10.1080/014423599229910.

(53) Haskins, J. D.; Jaeglé, L.; Shah, V.; Lee, B. H.; Lopez-Hilfiker, F. D.; Campuzano-Jost, P.; Schroder, J. C.; Day, D. A.; Guo, H.; Sullivan, A. P.; et al. Wintertime Gas-Particle Partitioning and Speciation of Inorganic Chlorine in the Lower Troposphere Over the Northeast United States and Coastal Ocean. *Journal of Geophysical Research: Atmospheres* **2018**, *123* (22), 12,897-812,916. DOI: https://doi.org/10.1029/2018JD028786.

(54) Tao, Y.; VandenBoer, T. C.; Veres, P. R.; Warneke, C.; de Gouw, J. A.; Weber, R. J.; Markovic, M. Z.; Zhao, Y.; Baker, K. R.; Kelly, J. T.; et al. Hydrogen Chloride (HCl) at Ground Sites During CalNex 2010 and Insight Into Its Thermodynamic Properties. *Journal of Geophysical Research: Atmospheres* **2022**, *127* (9), e2021JD036062. DOI: https://doi.org/10.1029/2021JD036062.

(55) Angelucci, A. A.; Furlani, T. C.; Wang, X.; Jacob, D. J.; VandenBoer, T. C.; Young, C. J. Understanding Sources of Atmospheric Hydrogen Chloride in Coastal Spring and Continental Winter. *ACS Earth and Space Chemistry* **2021**, *5* (9), 2507-2516. DOI: https://doi.org/10.1021/acsearthspacechem.1c00193.

(56) Crisp, T. A.; Lerner, B. M.; Williams, E. J.; Quinn, P. K.; Bates, T. S.; Bertram, T. H. Observations of gas phase hydrochloric acid in the polluted marine boundary layer. *Journal of Geophysical Research: Atmospheres* **2014**, *119* (11), 6897-6915. DOI: https://doi.org/10.1002/2013JD020992.

(57) Atkinson, R.; Baulch, D. L.; Cox, R. A.; Crowley, J. N.; Hampson, R. F.; Hynes, R. G.; Jenkin, M. E.; Rossi, M. J.; Troe, J. Evaluated kinetic and photochemical data for atmospheric chemistry: Volume III - gas phase reactions of inorganic halogens. *Atmos. Chem. Phys.* **2007**, *7* (4), 981-1191. DOI: https://doi.org/10.5194/acp-7-981-2007.

(58) Behnke, W.; George, C.; Scheer, V.; Zetzsch, C. Production and decay of $ClNO_2$ from the reaction of gaseous N_2O_5 with NaCl solution: Bulk and aerosol experiments. *Journal of Geophysical Research: Atmospheres* **1997**, *102* (D3), 3795-3804. DOI: https://doi.org/10.1029/96JD03057.

(59) Raff, J. D.; Njegic, B.; Chang, W. L.; Gordon, M. S.; Dabdub, D.; Gerber, R. B.; Finlayson-Pitts, B. J. Chlorine activation indoors and outdoors via surface-mediated reactions of nitrogen oxides with hydrogen chloride. *Proceedings of the National Academy of Sciences* **2009**, *106* (33), 13647-13654. DOI: https://doi.org/10.1073/pnas.0904195106.

(60) Ravishankara, A. R. Are chlorine atoms significant tropospheric free radicals? *Proceedings of the National Academy of Sciences* **2009**, *106* (33), 13639-13640. DOI: https://doi.org/10.1073/pnas.0907089106.

(61) Osthoff, H. D.; Roberts, J. M.; Ravishankara, A. R.; Williams, E. J.; Lerner, B. M.; Sommariva, R.; Bates, T. S.; Coffman, D.; Quinn, P. K.; Dibb, J. E.; et al. High levels of nitryl chloride in the polluted subtropical marine boundary layer. *Nature Geoscience* **2008**, *1* (5), 324-328. DOI: https://doi.org/10.1038/ngeo177.

(62) Riedel, T. P.; Bertram, T. H.; Crisp, T. A.; Williams, E. J.; Lerner, B. M.; Vlasenko, A.; Li, S.-M.; Gilman, J.; de Gouw, J.; Bon, D. M.; et al. Nitryl Chloride and Molecular Chlorine in the Coastal Marine Boundary Layer. *Environmental Science & Technology* **2012**, *46* (19), 10463-10470. DOI: https://doi.org/10.1021/es204632r.

(63) Kercher, J. P.; Riedel, T. P.; Thornton, J. A. Chlorine activation by N_2O_5: simultaneous, in situ detection of $ClNO_2$ and N_2O_5 by chemical ionization mass spectrometry. *Atmos. Meas. Tech.* **2009**, *2* (1), 193-204. DOI: https://doi.org/10.5194/amt-2-193-2009.

(64) Thornton, J. A.; Kercher, J. P.; Riedel, T. P.; Wagner, N. L.; Cozic, J.; Holloway, J. S.; Dubé, W. P.; Wolfe, G. M.; Quinn, P. K.; Middlebrook, A. M.; et al. A large atomic chlorine source inferred from mid-continental reactive nitrogen chemistry. *Nature* **2010**, *464* (7286), 271-274. DOI: https://doi.org/10.1038/nature08905.

(65) Mielke, L. H.; Furgeson, A.; Osthoff, H. D. Observation of $ClNO_2$ in a Mid-Continental Urban Environment. *Environmental Science & Technology* **2011**, *45* (20), 8889-8896. DOI: https://doi.org/10.1021/es201955u.

(66) Phillips, G. J.; Tang, M. J.; Thieser, J.; Brickwedde, B.; Schuster, G.; Bohn, B.; Lelieveld, J.; Crowley, J. N. Significant concentrations of nitryl chloride observed in rural continental Europe associated

with the influence of sea salt chloride and anthropogenic emissions. *Geophysical Research Letters* **2012**, *39* (10). DOI: https://doi.org/10.1029/2012gl051912.

(67) Mielke, L. H.; Stutz, J.; Tsai, C.; Hurlock, S. C.; Roberts, J. M.; Veres, P. R.; Froyd, K. D.; Hayes, P. L.; Cubison, M. J.; Jimenez, J. L.; et al. Heterogeneous formation of nitryl chloride and its role as a nocturnal NO_x reservoir species during CalNex-LA 2010. *Journal of Geophysical Research: Atmospheres* **2013**, *118* (18), 10,638-610,652. DOI: https://doi.org/10.1002/jgrd.50783.

(68) Mielke, L. H.; Furgeson, A.; Odame-Ankrah, C. A.; Osthoff, H. D. Ubiquity of $ClNO_2$ in the urban boundary layer of Calgary, Alberta, Canada. *Canadian Journal of Chemistry* **2016**, *94* (4), 414-423. DOI: https://doi.org/10.1139/cjc-2015-0426.

(69) Bannan, T. J.; Booth, A. M.; Bacak, A.; Muller, J. B. A.; Leather, K. E.; Le Breton, M.; Jones, B.; Young, D.; Coe, H.; Allan, J.; et al. The first UK measurements of nitryl chloride using a chemical ionization mass spectrometer in central London in the summer of 2012, and an investigation of the role of Cl atom oxidation. *Journal of Geophysical Research: Atmospheres* **2015**, *120* (11), 5638-5657. DOI: https://doi.org/10.1002/2014JD022629.

(70) Bannan, T. J.; Khan, M. A. H.; Le Breton, M.; Priestley, M.; Worrall, S. D.; Bacak, A.; Marsden, N. A.; Lowe, D.; Pitt, J.; Allen, G.; et al. A Large Source of Atomic Chlorine From $ClNO_2$ Photolysis at a U.K. Landfill Site. *Geophysical Research Letters* **2019**, *46* (14), 8508-8516. DOI: https://doi.org/10.1029/2019GL083764.

(71) Wang, X.; Wang, H.; Xue, L.; Wang, T.; Wang, L.; Gu, R.; Wang, W.; Tham, Y. J.; Wang, Z.; Yang, L.; et al. Observations of N_2O_5 and $ClNO_2$ at a polluted urban surface site in North China: High N_2O_5 uptake coefficients and low $ClNO_2$ product yields. *Atmospheric Environment* **2017**, *156*, 125-134. DOI: https://doi.org/10.1016/j.atmosenv.2017.02.035.

(72) Tham, Y. J.; Yan, C.; Xue, L.; Zha, Q.; Wang, X.; Wang, T. Presence of high nitryl chloride in Asian coastal environment and its impact on atmospheric photochemistry. *Chinese Science Bulletin* **2014**, *59* (4), 356-359. DOI: https://doi.org/10.1007/s11434-013-0063-y.

(73) Xia, M.; Peng, X.; Wang, W.; Yu, C.; Sun, P.; Li, Y.; Liu, Y.; Xu, Z.; Wang, Z.; Xu, Z.; et al. Significant production of $ClNO_2$ and possible source of Cl_2 from N_2O_5 uptake at a suburban site in eastern China. *Atmos. Chem. Phys.* **2020**, *20* (10), 6147-6158. DOI: https://doi.org/10.5194/acp-20-6147-2020.

(74) Ganske, J. A.; Berko, H. N.; Finlayson-Pitts, B. J. Absorption cross sections for gaseous $ClNO_2$ and Cl_2 at 298 K: Potential organic oxidant source in the marine troposphere. *Journal of Geophysical Research: Atmospheres* **1992**, *97* (D7), 7651-7656. DOI: https://doi.org/10.1029/92JD00414.

(75) Ghosh, B.; Papanastasiou, D. K.; Talukdar, R. K.; Roberts, J. M.; Burkholder, J. B. Nitryl Chloride ($ClNO_2$): UV/Vis Absorption Spectrum between 210 and 296 K and $O(^3P)$ Quantum Yield at 193 and

248 nm. *The Journal of Physical Chemistry A* **2012**, *116* (24), 5796-5805. DOI: https://doi.org/10.1021/jp207389y.

(76) Faxon, C. B.; Bean, J. K.; Ruiz, L. H. Inland Concentrations of Cl_2 and $ClNO_2$ in Southeast Texas Suggest Chlorine Chemistry Significantly Contributes to Atmospheric Reactivity. *Atmosphere* **2015**, *6* (10), 1487-1506. DOI: https://doi.org/10.3390/atmos6101487.

(77) Lawler, M. J.; Sander, R.; Carpenter, L. J.; Lee, J. D.; von Glasow, R.; Sommariva, R.; Saltzman, E. S. HOCl and Cl_2 observations in marine air. *Atmos. Chem. Phys.* **2011**, *11* (15), 7617-7628. DOI: https://doi.org/10.5194/acp-11-7617-2011.

(78) Knipping, E. M.; Lakin, M. J.; Foster, K. L.; Jungwirth, P.; Tobias, D. J.; Gerber, R. B.; Dabdub, D.; Finlayson-Pitts, B. J. Experiments and Simulations of Ion-Enhanced Interfacial Chemistry on Aqueous NaCl Aerosols. *Science* **2000**, *288* (5464), 301-306. DOI: https://doi.org/10.1126/science.288.5464.301.

(79) Knipping, E. M.; Dabdub, D. Modeling Cl_2 formation from aqueous NaCl particles: Evidence for interfacial reactions and importance of Cl_2 decomposition in alkaline solution. *Journal of Geophysical Research: Atmospheres* **2002**, *107* (D18), ACH 8-1-ACH 8-30. DOI: https://doi.org/10.1029/2001JD000867.

(80) Faxon, C. B.; Dhulipala, S. V.; Allen, D. T.; Hildebrandt Ruiz, L. Heterogeneous production of Cl_2 from particulate chloride: Effects of composition and relative humidity. *AIChE Journal* **2018**, *64* (8), 3151-3158. DOI: https://doi.org/10.1002/aic.16204.

(81) Haskins, J. D.; Lee, B. H.; Lopez-Hilifiker, F. D.; Peng, Q.; Jaeglé, L.; Reeves, J. M.; Schroder, J. C.; Campuzano-Jost, P.; Fibiger, D.; McDuffie, E. E.; et al. Observational Constraints on the Formation of Cl_2 From the Reactive Uptake of $ClNO_2$ on Aerosols in the Polluted Marine Boundary Layer. *Journal of Geophysical Research: Atmospheres* **2019**, *124* (15), 8851-8869. DOI: https://doi.org/10.1029/2019JD030627.

(82) Wang, S.; Pratt, K. A. Molecular Halogens Above the Arctic Snowpack: Emissions, Diurnal Variations, and Recycling Mechanisms. *Journal of Geophysical Research: Atmospheres* **2017**, *122* (21), 11,991-912,007. DOI: https://doi.org/10.1002/2017JD027175.

(83) Buys, Z.; Brough, N.; Huey, L. G.; Tanner, D. J.; von Glasow, R.; Jones, A. E. High temporal resolution Br_2, BrCl and BrO observations in coastal Antarctica. *Atmos. Chem. Phys.* **2013**, *13* (3), 1329-1343. DOI: https://doi.org/10.5194/acp-13-1329-2013.

(84) Finley, B. D.; Saltzman, E. S. Observations of Cl_2, Br_2, and I_2 in coastal marine air. *Journal of Geophysical Research: Atmospheres* **2008**, *113* (D21). DOI: https://doi.org/10.1029/2008JD010269.

(85) Lawler, M. J.; Finley, B. D.; Keene, W. C.; Pszenny, A. A. P.; Read, K. A.; von Glasow, R.; Saltzman, E. S. Pollution-enhanced reactive chlorine chemistry in the eastern tropical Atlantic boundary layer. *Geophysical Research Letters* **2009**, *36* (8). DOI: https://doi.org/10.1029/2008GL036666.

(86) Kegley-Owen, C. S.; Gilles, M. K.; Burkholder, J. B.; Ravishankara, A. R. Rate Coefficient Measurements for the Reaction OH + ClO → Products. *The Journal of Physical Chemistry A* **1999**, *103* (26), 5040-5048. DOI: https://doi.org/10.1021/jp9904320.

(87) Burrows, J. P.; Wallington, T. J.; Wayne, R. P. Kinetics of the reaction of OH with ClO. *Journal of the Chemical Society, Faraday Transactions 2: Molecular and Chemical Physics* **1984**, *80* (8), 957-971, 10.1039/F29848000957. DOI: https://doi.org/10.1039/F29848000957.

(88) Ferracci, V.; Rowley, D. M. Kinetic studies of the BrO + ClO cross-reaction over the range T = 246–314 K. *Physical Chemistry Chemical Physics* **2014**, *16* (3), 1182-1196, 10.1039/C3CP53440E. DOI: https://doi.org/10.1039/C3CP53440E.

(89) von Glasow, R.; Bobrowski, N.; Kern, C. The effects of volcanic eruptions on atmospheric chemistry. *Chemical Geology* **2009**, *263* (1), 131-142. DOI: https://doi.org/10.1016/j.chemgeo.2008.08.020.

(90) Liu, Y.; Fan, Q.; Chen, X.; Zhao, J.; Ling, Z.; Hong, Y.; Li, W.; Chen, X.; Wang, M.; Wei, X. Modeling the impact of chlorine emissions from coal combustion and prescribed waste incineration on tropospheric ozone formation in China. *Atmos. Chem. Phys.* **2018**, *18* (4), 2709-2724. DOI: https://doi.org/10.5194/acp-18-2709-2018.

(91) Zhai, S.; Wang, X.; McConnell, J. R.; Geng, L.; Cole-Dai, J.; Sigl, M.; Chellman, N.; Sherwen, T.; Pound, R.; Fujita, K.; et al. Anthropogenic Impacts on Tropospheric Reactive Chlorine Since the Preindustrial. *Geophysical Research Letters* **2021**, *48* (14), e2021GL093808. DOI: https://doi.org/10.1029/2021GL093808.

(92) McCulloch, A.; Aucott, M. L.; Benkovitz, C. M.; Graedel, T. E.; Kleiman, G.; Midgley, P. M.; Li, Y.-F. Global emissions of hydrogen chloride and chloromethane from coal combustion, incineration and industrial activities: Reactive Chlorine Emissions Inventory. *Journal of Geophysical Research: Atmospheres* **1999**, *104* (D7), 8391-8403. DOI: https://doi.org/10.1029/1999jd900025.

(93) Yin, S.; Yi, X.; Li, L.; Huang, L.; Ooi, M. C. G.; Wang, Y.; Allen, D. T.; Streets, D. G. An Updated Anthropogenic Emission Inventory of Reactive Chlorine Precursors in China. *ACS Earth and Space Chemistry* **2022**, *6* (7), 1846-1857. DOI: https://doi.org/10.1021/acsearthspacechem.2c00096.

(94) Fu, X.; Wang, T.; Wang, S.; Zhang, L.; Cai, S.; Xing, J.; Hao, J. Anthropogenic Emissions of Hydrogen Chloride and Fine Particulate Chloride in China. *Environmental Science & Technology* **2018**, *52* (3), 1644-1654. DOI: https://doi.org/10.1021/acs.est.7b05030.

(95) Ren, X.; Sun, R.; Chi, H.-H.; Meng, X.; Li, Y.; Levendis, Y. A. Hydrogen chloride emissions from combustion of raw and torrefied biomass. *Fuel* **2017**, *200*, 37-46. DOI: https://doi.org/10.1016/j.fuel.2017.03.040.

(96) Lobert, J. M.; Keene, W. C.; Logan, J. A.; Yevich, R. Global chlorine emissions from biomass burning: Reactive Chlorine Emissions Inventory. *Journal of Geophysical Research: Atmospheres* **1999**, *104* (D7), 8373-8389. DOI: https://doi.org/10.1029/1998jd100077.

(97) Odabasi, M. Halogenated Volatile Organic Compounds from the Use of Chlorine-Bleach-Containing Household Products. *Environmental Science & Technology* **2008**, *42* (5), 1445-1451. DOI: https://doi.org/10.1021/es702355u.

(98) Odabasi, M.; Elbir, T.; Dumanoglu, Y.; Sofuoglu, S. C. Halogenated volatile organic compounds in chlorine-bleach-containing household products and implications for their use. *Atmospheric Environment* **2014**, *92*, 376-383. DOI: https://doi.org/10.1016/j.atmosenv.2014.04.049.

(99) Stubbs, A. D.; Lao, M.; Wang, C.; Abbatt, J. P. D.; Hoffnagle, J.; VandenBoer, T. C.; Kahan, T. F. Near-source hypochlorous acid emissions from indoor bleach cleaning. *Environmental Science: Processes & Impacts* **2023**, *25* (1), 56-65, 10.1039/D2EM00405D. DOI: https://doi.org/10.1039/D2EM00405D.

(100) Angelucci, A. A.; Crilley, L. R.; Richardson, R.; Valkenburg, T. S. E.; Monks, P. S.; Roberts, J. M.; Sommariva, R.; VandenBoer, T. C. Elevated levels of chloramines and chlorine detected near an indoor sports complex. *Environmental Science: Processes & Impacts* **2023**, *25* (2), 304-313, 10.1039/D2EM00411A. DOI: https://doi.org/10.1039/D2EM00411A.

(101) Moravek, A.; VandenBoer, T. C.; Finewax, Z.; Pagonis, D.; Nault, B. A.; Brown, W. L.; Day, D. A.; Handschy, A. V.; Stark, H.; Ziemann, P.; et al. Reactive Chlorine Emissions from Cleaning and Reactive Nitrogen Chemistry in an Indoor Athletic Facility. *Environmental Science & Technology* **2022**, *56* (22), 15408-15416. DOI: https://doi.org/10.1021/acs.est.2c04622.

(102) Mattila, J. M.; Lakey, P. S. J.; Shiraiwa, M.; Wang, C.; Abbatt, J. P. D.; Arata, C.; Goldstein, A. H.; Ampollini, L.; Katz, E. F.; DeCarlo, P. F.; et al. Multiphase Chemistry Controls Inorganic Chlorinated and Nitrogenated Compounds in Indoor Air during Bleach Cleaning. *Environmental Science & Technology* **2020**, *54* (3), 1730-1739. DOI: https://doi.org/10.1021/acs.est.9b05767.

(103) Wong, J. P. S.; Carslaw, N.; Zhao, R.; Zhou, S.; Abbatt, J. P. D. Observations and impacts of bleach washing on indoor chlorine chemistry. *Indoor Air* **2017**, *27* (6), 1082-1090. DOI: https://doi.org/10.1111/ina.12402.

(104) Dawe, K. E. R.; Furlani, T. C.; Kowal, S. F.; Kahan, T. F.; VandenBoer, T. C.; Young, C. J. Formation and emission of hydrogen chloride in indoor air. *Indoor Air* **2019**, *29* (1), 70-78. DOI: https://doi.org/10.1111/ina.12509.

(105) Eger, P. G.; Helleis, F.; Schuster, G.; Phillips, G. J.; Lelieveld, J.; Crowley, J. N. Chemical ionization quadrupole mass spectrometer with an electrical discharge ion source for atmospheric trace gas measurement. *Atmos. Meas. Tech.* **2019**, *12* (3), 1935-1954. DOI: https://doi.org/10.5194/amt-12-1935-2019.

(106) Toth, R. A.; Hunt, R. H.; Plyler, E. K. Line strengths, line widths, and dipole moment function for HCl. *Journal of Molecular Spectroscopy* **1970**, *35* (1), 110-126. DOI: https://doi.org/10.1016/0022-2852(70)90169-4.

(107) Hagen, C. L.; Lee, B. C.; Franka, I. S.; Rath, J. L.; VandenBoer, T. C.; Roberts, J. M.; Brown, S. S.; Yalin, A. P. Cavity ring-down spectroscopy sensor for detection of hydrogen chloride. *Atmos. Meas. Tech.* **2014**, *7* (2), 345-357. DOI: https://doi.org/10.5194/amt-7-345-2014.

(108) Furlani, T. C.; Veres, P. R.; Dawe, K. E. R.; Neuman, J. A.; Brown, S. S.; VandenBoer, T. C.; Young, C. J. Validation of a new cavity ring-down spectrometer for measuring tropospheric gaseous hydrogen chloride. *Atmos. Meas. Tech.* **2021**, *14* (8), 5859-5871. DOI: https://doi.org/10.5194/amt-14-5859-2021.

(109) Halfacre, J. W.; Stewart, J.; Herndon, S. C.; Roscioli, J. R.; Dyroff, C.; Yacovitch, T. I.; Flynn, M.; Andrews, S. J.; Brown, S. S.; Veres, P. R.; et al. Using tunable infrared laser direct absorption spectroscopy for ambient hydrogen chloride detection: HCl-TILDAS. *Atmos. Meas. Tech.* **2023**, *16* (5), 1407-1429. DOI: https://doi.org/10.5194/amt-16-1407-2023.

(110) Furlani, T. C.; Ye, R.; Stewart, J.; Crilley, L. R.; Edwards, P. M.; Kahan, T. F.; Young, C. J. Development and validation of a new in situ technique to measure total gaseous chlorine in air. *Atmos. Meas. Tech.* **2023**, *16* (1), 181-193. DOI: https://doi.org/10.5194/amt-16-181-2023.

(111) Goldstein, A.; Galbally, I. Known and Unexplored Organic Constituents in the Earth's Atmosphere. *Environmental Science and Technology* **2007**, *41*. DOI: https://doi.org/10.1021/es072476p.

(112) Hansen, R. F.; Griffith, S. M.; Dusanter, S.; Gilman, J. B.; Graus, M.; Kuster, W. C.; Veres, P. R.; de Gouw, J. A.; Warneke, C.; Washenfelder, R. A.; et al. Measurements of Total OH Reactivity During CalNex-LA. *Journal of Geophysical Research: Atmospheres* **2021**, *126* (11), e2020JD032988. DOI: https://doi.org/10.1029/2020JD032988.

(113) Dolgorouky, C.; Gros, V.; Sarda-Esteve, R.; Sinha, V.; Williams, J.; Marchand, N.; Sauvage, S.; Poulain, L.; Sciare, J.; Bonsang, B. Total OH reactivity measurements in Paris during the 2010 MEGAPOLI winter campaign. *Atmos. Chem. Phys.* **2012**, *12* (20), 9593-9612. DOI: https://doi.org/10.5194/acp-12-9593-2012.

(114) Yang, Y.; Shao, M.; Keßel, S.; Li, Y.; Lu, K.; Lu, S.; Williams, J.; Zhang, Y.; Zeng, L.; Nölscher, A. C.; et al. How the OH reactivity affects the ozone production efficiency: case studies in Beijing and

Heshan, China. *Atmos. Chem. Phys.* **2017**, *17* (11), 7127-7142. DOI: https://doi.org/10.5194/acp-17-7127-2017.

(115) Whalley, L. K.; Stone, D.; Bandy, B.; Dunmore, R.; Hamilton, J. F.; Hopkins, J.; Lee, J. D.; Lewis, A. C.; Heard, D. E. Atmospheric OH reactivity in central London: observations, model predictions and estimates of in situ ozone production. *Atmos. Chem. Phys.* **2016**, *16* (4), 2109-2122. DOI: https://doi.org/10.5194/acp-16-2109-2016.

(116) Kovacs, T. A.; Brune, W. H. Total OH Loss Rate Measurement. *Journal of Atmospheric Chemistry* **2001**, *39* (2), 105-122. DOI: https://doi.org/10.1023/A:1010614113786.

(117) Kaufman, F. Kinetics of elementary radical reactions in the gas phase. *The Journal of Physical Chemistry* **1984**, *88* (21), 4909-4917. DOI: https://doi.org/10.1021/j150665a024.

(118) Donahue, N. M.; Clarke, J. S.; Demerjian, K. L.; Anderson, J. G. Free-radical kinetics at high pressure: a mathematical analysis of the flow reactor. *The Journal of Physical Chemistry* **1996**, *100* (14), 5821-5838. DOI: https://doi.org/10.1021/jp9525503.

(119) Seeley, J. V.; Jayne, J. T.; Molina, M. J. High pressure fast-flow technique for gas phase kinetics studies. *International journal of chemical kinetics* **1993**, *25* (7), 571-594. DOI: https://doi.org/10.1002/kin.550250706.

(120) Mao, J.; Ren, X.; Brune, W. H.; Olson, J. R.; Crawford, J. H.; Fried, A.; Huey, L. G.; Cohen, R. C.; Heikes, B.; Singh, H. B.; et al. Airborne measurement of OH reactivity during INTEX-B. *Atmos. Chem. Phys.* **2009**, *9* (1), 163-173. DOI: https://doi.org/10.5194/acp-9-163-2009.

(121) Ingham, T.; Goddard, A.; Whalley, L. K.; Furneaux, K. L.; Edwards, P. M.; Seal, C. P.; Self, D. E.; Johnson, G. P.; Read, K. A.; Lee, J. D.; et al. A flow-tube based laser-induced fluorescence instrument to measure OH reactivity in the troposphere. *Atmos. Meas. Tech.* **2009**, *2* (2), 465-477. DOI: https://doi.org/10.5194/amt-2-465-2009.

(122) Hansen, R. F.; Griffith, S. M.; Dusanter, S.; Rickly, P. S.; Stevens, P. S.; Bertman, S. B.; Carroll, M. A.; Erickson, M. H.; Flynn, J. H.; Grossberg, N.; et al. Measurements of total hydroxyl radical reactivity during CABINEX 2009 - Part 1: field measurements. *Atmos. Chem. Phys.* **2014**, *14* (6), 2923-2937. DOI: https://doi.org/10.5194/acp-14-2923-2014.

(123) Heard, D. E.; Pilling, M. J. Measurement of OH and HO_2 in the Troposphere. *Chemical Reviews* **2003**, *103* (12), 5163-5198. DOI: https://doi.org/10.1021/cr020522s.

(124) Shirley, T. R.; Brune, W. H.; Ren, X.; Mao, J.; Lesher, R.; Cardenas, B.; Volkamer, R.; Molina, L. T.; Molina, M. J.; Lamb, B.; et al. Atmospheric oxidation in the Mexico City Metropolitan Area (MCMA) during April 2003. *Atmos. Chem. Phys.* **2006**, *6* (9), 2753-2765. DOI: https://doi.org/10.5194/acp-6-2753-2006.

(125) Calpini, B.; Jeanneret, F.; Bourqui, M.; Clappier, A.; Vajtai, R.; van den Bergh, H. Direct measurement of the total reaction rate of OH in the atmosphere. *Analusis* **1999**, *27*. DOI: https://doi.org/10.1051/analusis:1999270328.

(126) Sadanaga, Y.; Yoshino, A.; Watanabe, K.; Yoshioka, A.; Wakazono, Y.; Kanaya, Y.; Kajii, Y. Development of a measurement system of OH reactivity in the atmosphere by using a laser-induced pump and probe technique. *Review of Scientific Instruments* **2004**, *75* (8), 2648-2655. DOI: https://doi.org/10.1063/1.1775311.

(127) Lou, S.; Holland, F.; Rohrer, F.; Lu, K.; Bohn, B.; Brauers, T.; Chang, C. C.; Fuchs, H.; Häseler, R.; Kita, K.; et al. Atmospheric OH reactivities in the Pearl River Delta – China in summer 2006: measurement and model results. *Atmos. Chem. Phys.* **2010**, *10* (22), 11243-11260. DOI: https://doi.org/10.5194/acp-10-11243-2010.

(128) Stone, D.; Whalley, L. K.; Ingham, T.; Edwards, P. M.; Cryer, D. R.; Brumby, C. A.; Seakins, P. W.; Heard, D. E. Measurement of OH reactivity by laser flash photolysis coupled with laser-induced fluorescence spectroscopy. *Atmos. Meas. Tech.* **2016**, *9* (7), 2827-2844. DOI: https://doi.org/10.5194/amt-9-2827-2016.

(129) Sinha, V.; Williams, J.; Crowley, J. N.; Lelieveld, J. The Comparative Reactivity Method - a new tool to measure total OH Reactivity in ambient air. *Atmos. Chem. Phys.* **2008**, *8* (8), 2213-2227. DOI: https://doi.org/10.5194/acp-8-2213-2008.

(130) Yang, G.; Huo, J.; Wang, L.; Wang, Y.; Wu, S.; Yao, L.; Fu, Q.; Wang, L. Total OH Reactivity Measurements in a Suburban Site of Shanghai. *Journal of Geophysical Research: Atmospheres* **2022**, *127* (11), e2021JD035981. DOI: https://doi.org/10.1029/2021JD035981.

(131) Kim, S.; Guenther, A.; Karl, T.; Greenberg, J. Contributions of primary and secondary biogenic VOC tototal OH reactivity during the CABINEX (Community Atmosphere-Biosphere INteractions Experiments)-09 field campaign. *Atmos. Chem. Phys.* **2011**, *11* (16), 8613-8623. DOI: https://doi.org/10.5194/acp-11-8613-2011.

(132) Wang, W.; Qi, J.; Zhou, J.; Yuan, B.; Peng, Y.; Wang, S.; Yang, S.; Williams, J.; Sinha, V.; Shao, M. The improved comparative reactivity method (ICRM): measurements of OH reactivity under high-NO_x conditions in ambient air. *Atmos. Meas. Tech.* **2021**, *14* (3), 2285-2298. DOI: https://doi.org/10.5194/amt-14-2285-2021.

(133) Hansen, R. F.; Blocquet, M.; Schoemaecker, C.; Léonardis, T.; Locoge, N.; Fittschen, C.; Hanoune, B.; Stevens, P. S.; Sinha, V.; Dusanter, S. Intercomparison of the comparative reactivity method (CRM) and pump–probe technique for measuring total OH reactivity in an urban environment. *Atmos. Meas. Tech.* **2015**, *8* (10), 4243-4264. DOI: https://doi.org/10.5194/amt-8-4243-2015.

(134) Kato, S.; Sato, T.; Kajii, Y. "A method to estimate the contribution of unidentified VOCs to OH reactivity". *Atmospheric Environment* **2011**, *45* (31), 5531-5539. DOI: https://doi.org/10.1016/j.atmosenv.2011.05.074.

(135) Nölscher, A. C.; Sinha, V.; Bockisch, S.; Klüpfel, T.; Williams, J. Total OH reactivity measurements using a new fast Gas Chromatographic Photo-Ionization Detector (GC-PID). *Atmos. Meas. Tech.* **2012**, *5* (12), 2981-2992. DOI: https://doi.org/10.5194/amt-5-2981-2012.

(136) Michoud, V.; Hansen, R. F.; Locoge, N.; Stevens, P. S.; Dusanter, S. Detailed characterizations of the new Mines Douai comparative reactivity method instrument via laboratory experiments and modeling. *Atmos. Meas. Tech.* **2015**, *8* (8), 3537-3553. DOI: https://doi.org/10.5194/amt-8-3537-2015.

(137) Sinha, V.; Custer, T. G.; Kluepfel, T.; Williams, J. The effect of relative humidity on the detection of pyrrole by PTR-MS for OH reactivity measurements. *International Journal of Mass Spectrometry* **2009**, *282* (3), 108-111. DOI: https://doi.org/10.1016/j.ijms.2009.02.019.

(138) de Gouw, J.; Warneke, C. Measurements of volatile organic compounds in the earth's atmosphere using proton-transfer-reaction mass spectrometry. *Mass Spectrometry Reviews* **2007**, *26* (2), 223-257. DOI: https://doi.org/10.1002/mas.20119.

(139) Fuchs, H.; Novelli, A.; Rolletter, M.; Hofzumahaus, A.; Pfannerstill, E. Y.; Kessel, S.; Edtbauer, A.; Williams, J.; Michoud, V.; Dusanter, S.; et al. Comparison of OH reactivity measurements in the atmospheric simulation chamber SAPHIR. *Atmos. Meas. Tech.* **2017**, *10* (10), 4023-4053. DOI: https://doi.org/10.5194/amt-10-4023-2017.

(140) Lindinger, W.; Jordan, A. Proton-transfer-reaction mass spectrometry (PTR–MS): on-line monitoring of volatile organic compounds at pptv levels. *Chemical Society Reviews* **1998**, *27* (5), 347-375, 10.1039/A827347Z. DOI: https://doi.org/10.1039/A827347Z.

(141) Hansel, A.; Jordan, A.; Holzinger, R.; Prazeller, P.; Vogel, W.; Lindinger, W. Proton transfer reaction mass spectrometry: on-line trace gas analysis at the ppb level. *International Journal of Mass Spectrometry and Ion Processes* **1995**, *149-150*, 609-619. DOI: https://doi.org/10.1016/0168-1176(95)04294-U.

(142) Byliński, H.; Gębicki, J.; Dymerski, T.; Namieśnik, J. Direct Analysis of Samples of Various Origin and Composition Using Specific Types of Mass Spectrometry. *Critical Reviews in Analytical Chemistry* **2017**, *47* (4), 340-358. DOI: https://doi.org/10.1080/10408347.2017.1298986.

(143) Smith, D.; Španěl, P. Selected ion flow tube mass spectrometry (SIFT-MS) for on-line trace gas analysis. *Mass Spectrometry Reviews* **2005**, *24* (5), 661-700. DOI: https://doi.org/10.1002/mas.20033.

(144) Guelachvili, G.; Niay, P.; Bernage, P. Infrared bands of HCl and DCl by Fourier transform spectroscopy: Dunham coefficients for HCl, DCl, and TCl. *Journal of Molecular Spectroscopy* **1981**, *85* (2), 271-281. DOI: https://doi.org/10.1016/0022-2852(81)90200-9.

(145) Gordon, I. E.; Rothman, L. S.; Hill, C.; Kochanov, R. V.; Tan, Y.; Bernath, P. F.; Birk, M.; Boudon, V.; Campargue, A.; Chance, K. V.; et al. The HITRAN2016 molecular spectroscopic database. *Journal of Quantitative Spectroscopy and Radiative Transfer* **2017**, *203*, 3-69. DOI: https://doi.org/10.1016/j.jqsrt.2017.06.038.

(146) Fountoukis, C.; Nenes, A. ISORROPIA II: a computationally efficient thermodynamic equilibrium model for K^+-Ca^{2+}-Mg^{2+}-NH_4^+-Na^+-SO_4^{2-}-NO_3^--Cl^--H_2O aerosols. *Atmos. Chem. Phys.* **2007**, *7* (17), 4639-4659. DOI: https://doi.org/10.5194/acp-7-4639-2007.

(147) Nenes, A.; Pandis, S. N.; Pilinis, C. ISORROPIA: A New Thermodynamic Equilibrium Model for Multiphase Multicomponent Inorganic Aerosols. *Aquatic Geochemistry* **1998**, *4* (1), 123-152. DOI: https://doi.org/10.1023/A:1009604003981.

(148) Thames, A. B.; Brune, W. H.; Miller, D. O.; Allen, H. M.; Apel, E. C.; Blake, D. R.; Bui, T. P.; Commane, R.; Crounse, J. D.; Daube, B. C.; et al. Missing OH reactivity in the global marine boundary layer. *Atmos. Chem. Phys.* **2020**, *20* (6), 4013-4029. DOI: https://doi.org/10.5194/acp-20-4013-2020.

(149) Di Carlo, P.; Brune, W. H.; Martinez, M.; Harder, H.; Lesher, R.; Ren, X.; Thornberry, T.; Carroll, M. A.; Young, V.; Shepson, P. B.; et al. Missing OH Reactivity in a Forest: Evidence for Unknown Reactive Biogenic VOCs. *Science* **2004**, *304* (5671), 722-725. DOI: https://doi.org/10.1126/science.1094392.

(150) Edwards, P. M.; Evans, M. J.; Furneaux, K. L.; Hopkins, J.; Ingham, T.; Jones, C.; Lee, J. D.; Lewis, A. C.; Moller, S. J.; Stone, D.; et al. OH reactivity in a South East Asian tropical rainforest during the Oxidant and Particle Photochemical Processes (OP3) project. *Atmos. Chem. Phys.* **2013**, *13* (18), 9497-9514. DOI: https://doi.org/10.5194/acp-13-9497-2013.

(151) Nölscher, A. C.; Williams, J.; Sinha, V.; Custer, T.; Song, W.; Johnson, A. M.; Axinte, R.; Bozem, H.; Fischer, H.; Pouvesle, N.; et al. Summertime total OH reactivity measurements from boreal forest during HUMPPA-COPEC 2010. *Atmos. Chem. Phys.* **2012**, *12* (17), 8257-8270. DOI: https://doi.org/10.5194/acp-12-8257-2012.

(152) Nölscher, A. C.; Yañez-Serrano, A. M.; Wolff, S.; de Araujo, A. C.; Lavrič, J. V.; Kesselmeier, J.; Williams, J. Unexpected seasonality in quantity and composition of Amazon rainforest air reactivity. *Nature Communications* **2016**, *7* (1), 10383. DOI: https://doi.org/10.1038/ncomms10383.

(153) Kovacs, T. A.; Brune, W. H.; Harder, H.; Martinez, M.; Simpas, J. B.; Frost, G. J.; Williams, E.; Jobson, T.; Stroud, C.; Young, V.; et al. Direct measurements of urban OH reactivity during Nashville

SOS in summer 1999. *Journal of Environmental Monitoring* **2003**, *5* (1), 68-74, https://doi.org/10.1039/B204339D. DOI: 10.1039/B204339D.

(154) Bemand, P. P.; Clyne, M. A. A. Atomic resonance fluorescence spectrometry for rate constants of rapid bimolecular reactions. Part 4.—Chlorine atom fluorescence 4s2,4P–3p52P. *Journal of the Chemical Society, Faraday Transactions 2: Molecular and Chemical Physics* **1975**, *71* (0), 1132-1144, 10.1039/F29757101132. DOI: https://doi.org/10.1039/F29757101132.

(155) Boothroyd, J.; Dillon, T. J. Efficient generation of atomic chlorine by a low-temperature plasma and application to atmospheric chemistry. PhD thesis, University of York, 2021. https://etheses.whiterose.ac.uk/28408/ (accessed 01/03/2023).

(156) Sommariva, R.; Cox, S.; Martin, C.; Borońska, K.; Young, J.; Jimack, P. K.; Pilling, M. J.; Matthaios, V. N.; Nelson, B. S.; Newland, M. J.; et al. AtChem (version 1), an open-source box model for the Master Chemical Mechanism. *Geosci. Model Dev.* **2020**, *13* (1), 169-183. DOI: https://doi.org/10.5194/gmd-13-169-2020.

(157) Saunders, S. M.; Jenkin, M. E.; Derwent, R. G.; Pilling, M. J. Protocol for the development of the Master Chemical Mechanism, MCM v3 (Part A): tropospheric degradation of non-aromatic volatile organic compounds. *Atmos. Chem. Phys.* **2003**, *3* (1), 161-180. DOI: https://doi.org/10.5194/acp-3-161-2003.

(158) Jenkin, M. E.; Saunders, S. M.; Pilling, M. J. The tropospheric degradation of volatile organic compounds: a protocol for mechanism development. *Atmospheric Environment* **1997**, *31* (1), 81-104. DOI: https://doi.org/10.1016/S1352-2310(96)00105-7.

(159) Atkinson, R.; Baulch, D. L.; Cox, R. A.; Hampson, R. F., Jr.; Kerr, J. A.; Rossi, M. J.; Troe, J. Evaluated Kinetic and Photochemical Data for Atmospheric Chemistry, Organic Species: Supplement VII. *Journal of Physical and Chemical Reference Data* **1999**, *28* (2), 191-393. DOI: https://doi.org/10.1063/1.556048.

(160) Atkinson, R. Gas-Phase Tropospheric Chemistry of Volatile Organic Compounds: 1. Alkanes and Alkenes. *Journal of Physical and Chemical Reference Data* **1997**, *26* (2), 215-290. DOI: https://doi.org/10.1063/1.556012.

(161) Kwok, E. S. C.; Atkinson, R. Estimation of hydroxyl radical reaction rate constants for gas-phase organic compounds using a structure-reactivity relationship: An update. *Atmospheric Environment* **1995**, *29* (14), 1685-1695. DOI: https://doi.org/10.1016/1352-2310(95)00069-B.

(162) Taatjes, C. A.; Christensen, L. K.; Hurley, M. D.; Wallington, T. J. Absolute and Site-Specific Abstraction Rate Coefficients for Reactions of Cl with CH3CH2OH, CH3CD2OH, and CD3CH2OH between 295 and 600 K. *The Journal of Physical Chemistry A* **1999**, *103* (48), 9805-9814. DOI: https://doi.org/10.1021/jp992465l.

(163) Carr, S. A.; Blitz, M. A.; Seakins, P. W. Site-Specific Rate Coefficients for Reaction of OH with Ethanol from 298 to 900 K. *The Journal of Physical Chemistry A* **2011**, *115* (15), 3335-3345. DOI: https://doi.org/10.1021/jp200186t.

(164) Tully, F. P.; Goldsmith, J. E. M.; Droege, A. T. Hydrogen atom abstraction from alkanes by hydroxyl. 4. Isobutane. *The Journal of Physical Chemistry* **1986**, *90* (22), 5932-5937. DOI: https://doi.org/10.1021/j100280a095.

(165) Choi, N.; Pilling, M. J.; Seakins, P. W.; Wang, L. Studies of site selective hydrogen atom abstractions by Cl atoms from isobutane and propane by laser flash photolysis/IR diode laser spectroscopy. *Physical Chemistry Chemical Physics* **2006**, *8* (18), 2172-2178, 10.1039/B516531H. DOI: https://doi.org/10.1039/B516531H.

(166) Hess, W. P.; Tully, F. P. Hydrogen-atom abstraction from methanol by hydroxyl radical. *The Journal of Physical Chemistry* **1989**, *93* (5), 1944-1947. DOI: https://doi.org/10.1021/j100342a049.

(167) Renbaum-Wolff, L.; Smith, G. D. "Virtual Injector" Flow Tube Method for Measuring Relative Rates Kinetics of Gas-Phase and Aerosol Species. *The Journal of Physical Chemistry A* **2012**, *116* (25), 6664-6674. DOI: https://doi.org/10.1021/jp303221w.

(168) Crawford, M. A.; Li, Z.; Heuerman, H. A.; Kinscherff, D. A kinetic and product study of reaction of chlorine atom with CH_3CH_2OD. *International Journal of Chemical Kinetics* **2004**, *36* (11), 584-590. DOI: https://doi.org/10.1002/kin.20025.

(169) Mellouki, A.; Teton, S.; Le Bras, G. Kinetics of OH radical reactions with a series of ethers. *International Journal of Chemical Kinetics* **1995**, *27* (8), 791-805. DOI: https://doi.org/10.1002/kin.550270806.

(170) McLoughlin, P.; Kane, R.; Shanahan, I. A relative rate study of the reaction of chlorine atoms (Cl) and hydroxyl radicals (OH) with a series of ethers. *International Journal of Chemical Kinetics* **1993**, *25* (3), 137-149. DOI: https://doi.org/10.1002/kin.550250302.

(171) Whalley, L. K.; Stone, D.; Dunmore, R.; Hamilton, J.; Hopkins, J. R.; Lee, J. D.; Lewis, A. C.; Williams, P.; Kleffmann, J.; Laufs, S.; et al. Understanding in situ ozone production in the summertime through radical observations and modelling studies during the Clean air for London project (ClearfLo). *Atmos. Chem. Phys.* **2018**, *18* (4), 2547-2571. DOI: https://doi.org/10.5194/acp-18-2547-2018.

(172) Whalley, L. K.; Furneaux, K. L.; Goddard, A.; Lee, J. D.; Mahajan, A.; Oetjen, H.; Read, K. A.; Kaaden, N.; Carpenter, L. J.; Lewis, A. C.; et al. The chemistry of OH and HO₂ radicals in the boundary layer over the tropical Atlantic Ocean. *Atmos. Chem. Phys.* **2010**, *10* (4), 1555-1576. DOI: https://doi.org/10.5194/acp-10-1555-2010.

(173) Xue, L. K.; Saunders, S. M.; Wang, T.; Gao, R.; Wang, X. F.; Zhang, Q. Z.; Wang, W. X. Development of a chlorine chemistry module for the Master Chemical Mechanism. *Geosci. Model Dev.* **2015**, *8* (10), 3151-3162. DOI: https://doi.org/10.5194/gmd-8-3151-2015.

(174) Ezell, M. J.; Wang, W.; Ezell, A. A.; Soskin, G.; Finlayson-Pitts, B. J. Kinetics of reactions of chlorine atoms with a series of alkenes at 1 atm and 298 K: structure and reactivity. *Physical Chemistry Chemical Physics* **2002**, *4* (23), 5813-5820, 10.1039/B207529F. DOI: https://doi.org/10.1039/B207529F.

(175) Orlando, J. J.; Tyndall, G. S.; Apel, E. C.; Riemer, D. D.; Paulson, S. E. Rate coefficients and mechanisms of the reaction of cl-atoms with a series of unsaturated hydrocarbons under atmospheric conditions. *International Journal of Chemical Kinetics* **2003**, *35* (8), 334-353. DOI: https://doi.org/10.1002/kin.10135.

(176) Morozov, I. I.; Nielsen, C.; Morozova, O. S.; Vasiliev, E. S.; Loukhovitskaya, E. E. Reactions of chloroethenes with atomic chlorine in air at atmospheric pressure. *Russian Chemical Bulletin* **2010**, *59* (4), 754-760. DOI: http://doi.org/10.1007/s11172-010-0158-4.

(177) Shi, J.; Bernhard, M. J. Kinetic studies of Cl-atom reactions with selected aromatic compounds using the photochemical reactor-FTIR spectroscopy technique. *International Journal of Chemical Kinetics* **1997**, *29* (5), 349-358, https://doi.org/10.1002/(SICI)1097-4601(1997)29:5<349::AID-KIN5>3.0.CO;2-U. DOI: https://doi.org/10.1002/(SICI)1097-4601(1997)29:5<349::AID-KIN5>3.0.CO;2-U (acccessed 2023/03/02).

(178) Finlayson-Pitts, B. J.; Keoshian, C. J.; Buehler, B.; Ezell, A. A. Kinetics of reaction of chlorine atoms with some biogenic organics. *International Journal of Chemical Kinetics* **1999**, *31* (7), 491-499. DOI: https://doi.org/10.1002/(SICI)1097-4601(1999)31:7<491::AID-KIN4>3.0.CO;2-E.

(179) Burkholder, J. B.; Sander, S. P.; Abbatt, J.; Barker, J. R.; Cappa, C.; Crounse, J. D.; Dibble, T. S.; Huie, R. E.; Kolb, C. E.; Kurylo, M. J.; et al. *"Chemical Kinetics and Photochemical Data for Use in Atmospheric Studies, Evaluation No. 19," JPL Publication 19-5, Jet Propulsion Laboratory, Pasadena* **2019, http://jpldataeval.jpl.nasa.gov.**

(180) Vijayakumar, S.; Rajakumar, B. Experimental and Theoretical Investigations on the Reaction of 1,3-Butadiene with Cl Atom in the Gas Phase. *The Journal of Physical Chemistry A* **2017**, *121* (9), 1976-1984. DOI: https://doi.org/10.1021/acs.jpca.6b12227.

(181) Stevens, P. S.; Anderson, J. G. Kinetic measurements of the ClO + O3 → ClOO + O2 reaction. *Geophysical Research Letters* **1990**, *17* (9), 1287-1290. DOI: 10.1029/GL017i009p01287.

(182) Toohey, D. W.; Brune, W. H.; Anderson, J. G. Rate constant for the reaction Br + O_3 → BrO + O_2 from 248 to 418 K: Kinetics and mechanism. *International Journal of Chemical Kinetics* **1988**, *20* (2), 131-144. DOI: https://doi.org/10.1002/kin.550200206.

(183) Gutleben, H.; Bechtold, E. Adsorption of chlorine on the Pt(100) face: structural aspects and desorption kinetics. *Surface Science* **1990**, *236* (3), 313-324. DOI: https://doi.org/10.1016/0039-6028(90)90476-O.

(184) Schennach, R.; Bechtold, E. Chlorine adsorption on Pt(111) and Pt(110). *Surface Science* **1997**, *380* (1), 9-16. DOI: https://doi.org/10.1016/S0039-6028(96)01593-2.

(185) Hutton, E.; Wright, M. Photoemissive and recombination reactions of atomic chlorine. *Transactions of the Faraday Society* **1965**, *61* (0), 78-89, 10.1039/TF9656100078. DOI: https://doi.org/10.1039/TF9656100078.

(186) Linnett, J. W.; Booth, M. H. Recombination of Chlorine Atoms. *Nature* **1963**, *199* (4899), 1181-1182. DOI: https://doi.org/10.1038/1991181a0.

(187) Bader, L. W.; Ogryzlo, E. A. Recombinations of Chlorine Atoms. *Nature* **1964**, *201* (4918), 491-492. DOI: https://doi.org/10.1038/201491a0.

(188) Lindemann, F. A.; Arrhenius, S.; Langmuir, I.; Dhar, N. R.; Perrin, J.; McC. Lewis, W. C. Discussion on "the radiation theory of chemical action". *Transactions of the Faraday Society* **1922**, *17* (0), 598-606, https://doi.org/10.1039/TF9221700598. DOI: 10.1039/TF9221700598.

(189) Hippler, H.; Troe, J. Flash photolysis study of the recombination of chlorine atoms in the presence of various inert gases and NO. *International Journal of Chemical Kinetics* **1976**, *8* (4), 501-510. DOI: https://doi.org/10.1002/kin.550080404.

(190) Simpson, W. R.; Rakitzis, T. P.; Kandel, S. A.; Orr-Ewing, A. J.; Zare, R. N. Reaction of Cl with vibrationally excited CH_4 and CHD_3: State-to-state differential cross sections and steric effects for the HCl product. *The Journal of Chemical Physics* **1995**, *103* (17), 7313-7335. DOI: https://doi.org/10.1063/1.470305.

(191) Blanco, M. B.; Bejan, I.; Barnes, I.; Wiesen, P.; Teruel, M. A. Temperature-dependent rate coefficients for the reactions of Cl atoms with methyl methacrylate, methyl acrylate and butyl methacrylate at atmospheric pressure. *Atmospheric Environment* **2009**, *43* (38), 5996-6002. DOI: https://doi.org/10.1016/j.atmosenv.2009.08.032.

(192) Hass, S. A.; Andersen, S. T.; Nielsen, O. J. Trichloroacetyl chloride, CCl_3COCl, as an alternative Cl atom precursor for laboratory use and determination of Cl atom rate coefficients for n-CH_2=CH(CH_2)xCN (x = 3–4). *Environmental Science: Processes & Impacts* **2020**, *22* (6), 1347-1354, 10.1039/D0EM00105H. DOI: https://doi.org/10.1039/D0EM00105H.

(193) Sharma, A.; Pushpa, K. K.; Dhanya, S.; Naik, P. D.; Bajaj, P. N. Rate coefficients and products for gas-phase reactions of chlorine atoms with cyclic unsaturated hydrocarbons at 298 K. *International Journal of Chemical Kinetics* **2010**, *42* (2), 98-105. DOI: https://doi.org/10.1002/kin.20467.

(194) Baklanov, A. V.; Krasnoperov, L. N. Oxalyl Chloride - A Clean Source of Chlorine Atoms for Kinetic Studies. *The Journal of Physical Chemistry A* **2001**, *105* (1), 97-103. DOI: https://doi.org/10.1021/jp0019456.

(195) Imwinkelried, G.; Gaona-Colmán, E.; Teruel, M. A.; Blanco, M. B. Kinetics, mechanism and $CH_3C(O)CH_3$ formation in the Cl-initiated oxidation of 1,8-cineole at 298 K and atmospheric pressure. *Chemical Physics Letters* **2020**, *739*, 136901. DOI: https://doi.org/10.1016/j.cplett.2019.136901.

(196) Qian, H.-B.; Turton, D.; Seakins, P. W.; Pilling, M. J. A laser flash photolysis/IR diode laser absorption study of the reaction of chlorine atoms with selected alkanes. *International Journal of Chemical Kinetics* **2002**, *34* (2), 86-94. DOI: https://doi.org/10.1002/kin.10025.

(197) Dash, M. R.; Rajakumar, B. Reaction kinetics of Cl atoms with limonene: An experimental and theoretical study. *Atmospheric Environment* **2014**, *99*, 183-195. DOI: https://doi.org/10.1016/j.atmosenv.2014.09.066.

(198) Hiroshi, T.; Katsumi, K.; Koji, K.; Jiro, T.; Saburo, N. Vacuum Ultraviolet Absorption Spectra of Saturated Organic Compounds with Non-bonding Electrons. *Bulletin of the Chemical Society of Japan* **1964**, *37* (3), 417-423. DOI: https://doi.org/10.1246/bcsj.37.417.

(199) Holmes, J. R.; O'Brien, R. J.; Crabtree, J. H.; Hecht, T. A.; Seinfeld, J. H. Measurement of ultraviolet radiation intensity in photochemical smog studies. *Environmental Science & Technology* **1973**, *7* (6), 519-523. DOI: https://doi.org/10.1021/es60078a002.

(200) Harvey, R. B.; Stedman, D. H.; Chameides, W. Determination of the Absolute Rate of Solar Photolysis of NO_2. *Journal of the Air Pollution Control Association* **1977**, *27* (7), 663-666. DOI: https://doi.org/10.1080/00022470.1977.10470469.

(201) Kley, D.; McFarland, M. Chemiluminescence detector for NO and NO_2. *Atmos. Technol.* **1980**, *12*, 63-69.

(202) Atkinson, R.; Baulch, D. L.; Cox, R. A.; Crowley, J. N.; Hampson, R. F.; Hynes, R. G.; Jenkin, M. E.; Rossi, M. J.; Troe, J. Evaluated kinetic and photochemical data for atmospheric chemistry: Volume I - gas phase reactions of O_x, HO_x, NO_x and SO_x species. *Atmos. Chem. Phys.* **2004**, *4* (6), 1461-1738. DOI: https://doi.org/10.5194/acp-4-1461-2004.

(203) Ragains, M. L.; Finlayson-Pitts, B. J. Kinetics and Mechanism of the Reaction of Cl Atoms with 2-Methyl-1,3-butadiene (Isoprene) at 298 K. *The Journal of Physical Chemistry A* **1997**, *101* (8), 1509-1517. DOI: https://doi.org/10.1021/jp962786m.

(204) Fantechi, G.; Jensen, N. R.; Saastad, O.; Hjorth, J.; Peeters, J. Reactions of Cl Atoms with Selected VOCs: Kinetics, Products and Mechanisms. *Journal of Atmospheric Chemistry* **1998**, *31* (3), 247-267. DOI: https://doi.org/10.1023/A:1006033910014.

(205) Canosa-Mas, C. E.; Hutton-Squire, H. R.; King, M. D.; Stewart, D. J.; Thompson, K. C.; Wayne, R. P. Laboratory Kinetic Studies of the Reactions of Cl Atoms with Species of Biogenic Origin: δ3-Carene, Isoprene, Methacrolein and Methyl Vinyl Ketone. *Journal of Atmospheric Chemistry* **1999**, *34* (1), 163-170. DOI: https://doi.org/10.1023/A:1006214423298.

(206) Španěl, P.; Smith, D. Selected ion flow tube studies of the reactions of H_3O^+, NO^+, and O_2^+ with several aromatic and aliphatic hydrocarbons. *International Journal of Mass Spectrometry* **1998**, *181* (1), 1-10. DOI: https://doi.org/10.1016/S1387-3806(98)14114-3.

(207) Knížek, A.; Dryahina, K.; Španěl, P.; Kubelík, P.; Kavan, L.; Zukalová, M.; Ferus, M.; Civiš, S. Comparative SIFT-MS, GC–MS and FTIR analysis of methane fuel produced in biogas stations and in artificial photosynthesis over acidic anatase TiO2 and montmorillonite. *Journal of Molecular Spectroscopy* **2018**, *348*, 152-160. DOI: https://doi.org/10.1016/j.jms.2017.10.002.

(208) Hooshiyar, P. A.; Niki, H. Rate constants for the gas-phase reactions of Cl-atoms with C2-C8 alkanes at T = 296 ± 2 K. *International Journal of Chemical Kinetics* **1995**, *27* (12), 1197-1206. DOI: https://doi.org/10.1002/kin.550271206.

(209) Rowley, D. M.; Lesclaux, R.; Lightfoot, P. D.; Noziere, B.; Wallington, T. J.; Hurley, M. D. Kinetic and mechanistic studies of the reactions of cyclopentylperoxy and cyclohexylperoxy radicals with hydroperoxy radical. *The Journal of Physical Chemistry* **1992**, *96* (12), 4889-4894. DOI: https://doi.org/10.1021/j100191a031.

(210) Atkinson, R. Kinetics and mechanisms of the gas-phase reactions of the hydroxyl radical with organic compounds under atmospheric conditions. *Chemical Reviews* **1986**, *86* (1), 69-201. DOI: https://doi.org/10.1021/cr00071a004.

(211) Byrne, F. P.; Forier, B.; Bossaert, G.; Hoebers, C.; Farmer, T. J.; Hunt, A. J. A methodical selection process for the development of ketones and esters as bio-based replacements for traditional hydrocarbon solvents. *Green Chemistry* **2018**, *20* (17), 4003-4011, 10.1039/C8GC01132J. DOI: https://doi.org/10.1039/C8GC01132J.

(212) Mapelli, C.; Donnelly, J. K.; Hogan, Ú. E.; Rickard, A. R.; Robinson, A. T.; Byrne, F.; McElroy, C. R.; Curchod, B. F. E.; Hollas, D.; Dillon, T. J. Atmospheric oxidation of new 'green' solvents part II: methyl pivalate and pinacolone. *EGUsphere* **2023**, *2023*, 1-23. DOI: https://doi.org/10.5194/egusphere-2023-282.

(213) Wennberg, P. O.; Bates, K. H.; Crounse, J. D.; Dodson, L. G.; McVay, R. C.; Mertens, L. A.; Nguyen, T. B.; Praske, E.; Schwantes, R. H.; Smarte, M. D.; et al. Gas-Phase Reactions of Isoprene and Its Major Oxidation Products. *Chemical Reviews* **2018**, *118* (7), 3337-3390. DOI: https://doi.org/10.1021/acs.chemrev.7b00439.

(214) Lei, W.; Zhang, D.; Zhang, R.; Molina, L. T.; Molina, M. J. Rate constants and isomeric branching of the Cl–isoprene reaction. *Chemical Physics Letters* **2002**, *357* (1), 45-50. DOI: https://doi.org/10.1016/S0009-2614(02)00437-2.

(215) Bedjanian, Y.; Laverdet, G.; Le Bras, G. Low-Pressure Study of the Reaction of Cl Atoms with Isoprene. *The Journal of Physical Chemistry A* **1998**, *102* (6), 953-959. DOI: https://doi.org/10.1021/jp973336c.

(216) Xing, J.-H.; Takahashi, K.; Hurley, M. D.; Wallington, T. J. Kinetics of the reaction of chlorine atoms with isoprene (2-methyl 1,3-butadiene, $CH_2C(CH_3)CHCH_2$) at 297±2K. *Chemical Physics Letters* **2009**, *472* (1), 39-43. DOI: https://doi.org/10.1016/j.cplett.2009.03.002.

(217) Suh, I.; Zhang, R. Kinetic Studies of Isoprene Reactions Initiated by Chlorine Atom. *The Journal of Physical Chemistry A* **2000**, *104* (28), 6590-6596. DOI: https://doi.org/10.1021/jp000605h.

(218) Kaiser, E. W.; Pala, I. R.; Wallington, T. J. Kinetics and Mechanism of the Reaction of Methacrolein with Chlorine Atoms in 1−950 Torr of N_2 or N_2/O_2 Diluent at 297 K. *The Journal of Physical Chemistry A* **2010**, *114* (25), 6850-6860. DOI: https://doi.org/10.1021/jp103317c.

(219) Peeters, J.; Nguyen, T. L.; Vereecken, L. HOx radical regeneration in the oxidation of isoprene. *Physical Chemistry Chemical Physics* **2009**, *11* (28), 5935-5939, 10.1039/B908511D. DOI: https://doi.org/10.1039/B908511D.

(220) Molina, L. T.; Molina, M. J. Absolute absorption cross sections of ozone in the 185- to 350-nm wavelength range. *Journal of Geophysical Research: Atmospheres* **1986**, *91* (D13), 14501-14508. DOI: https://doi.org/10.1029/JD091iD13p14501.

(221) Martinez, R. D.; Buitrago, A. A.; Howell, N. W.; Hearn, C. H.; Joens, J. A. The near U.V. absorption spectra of several aliphatic aldehydes and ketones at 300 K. *Atmospheric Environment. Part A. General Topics* **1992**, *26* (5), 785-792. DOI: https://doi.org/10.1016/0960-1686(92)90238-G.

(222) Chen, Y.; Zhu, L.; Francisco, J. S. Wavelength-Dependent Photolysis of n-Butyraldehyde and i-Butyraldehyde in the 280−330-nm Region. *The Journal of Physical Chemistry A* **2002**, *106* (34), 7755-7763. DOI: https://doi.org/10.1021/jp014544e.

(223) Gierczak, T.; Burkholder, J. B.; Talukdar, R. K.; Mellouki, A.; Barone, S. B.; Ravishankara, A. R. Atmospheric fate of methyl vinyl ketone and methacrolein. *Journal of Photochemistry and Photobiology A: Chemistry* **1997**, *110* (1), 1-10. DOI: https://doi.org/10.1016/S1010-6030(97)00159-7.

(224) Gierczak, T.; Burkholder, J. B.; Bauerle, S.; Ravishankara, A. R. Photochemistry of acetone under tropospheric conditions. *Chemical Physics* **1998**, *231* (2), 229-244. DOI: https://doi.org/10.1016/S0301-0104(98)00006-8.

(225) Blitz, M. A.; Heard, D. E.; Pilling, M. J.; Arnold, S. R.; Chipperfield, M. P. Pressure and temperature-dependent quantum yields for the photodissociation of acetone between 279 and 327.5 nm. *Geophysical Research Letters* **2004**, *31* (6). DOI: https://doi.org/10.1029/2003GL018793.

(226) Pinho, P. G.; Pio, C. A.; Jenkin, M. E. Evaluation of isoprene degradation in the detailed tropospheric chemical mechanism, MCM v3, using environmental chamber data. *Atmospheric Environment* **2005**, *39* (7), 1303-1322. DOI: https://doi.org/10.1016/j.atmosenv.2004.11.014.

(227) Volkamer, R.; Spietz, P.; Burrows, J.; Platt, U. High-resolution absorption cross-section of glyoxal in the UV–vis and IR spectral ranges. *Journal of Photochemistry and Photobiology A: Chemistry* **2005**, *172* (1), 35-46. DOI: https://doi.org/10.1016/j.jphotochem.2004.11.011.

(228) Tadić, J.; Moortgat, G. K.; Wirtz, K. Photolysis of glyoxal in air. *Journal of Photochemistry and Photobiology A: Chemistry* **2006**, *177* (2), 116-124. DOI: https://doi.org/10.1016/j.jphotochem.2005.10.010.

(229) Meller, R.; Raber, W.; Crowley, J. N.; Jenkin, M. E.; Moortgat, G. K. The UV-visible absorption spectrum of methylglyoxal. *Journal of Photochemistry and Photobiology A: Chemistry* **1991**, *62* (2), 163-171. DOI: https://doi.org/10.1016/1010-6030(91)87017-P.

(230) Chen, Y.; Wang, W.; Zhu, L. Wavelength-Dependent Photolysis of Methylglyoxal in the 290−440 nm Region. *The Journal of Physical Chemistry A* **2000**, *104* (47), 11126-11131. DOI: https://doi.org/10.1021/jp002262t.

(231) Horowitz, A.; Meller, R.; Moortgat, G. K. The UV–VIS absorption cross sections of the α-dicarbonyl compounds: pyruvic acid, biacetyl and glyoxal. *Journal of Photochemistry and Photobiology A: Chemistry* **2001**, *146* (1), 19-27. DOI: https://doi.org/10.1016/S1010-6030(01)00601-3.

(232) Plum, C. N.; Sanhueza, E.; Atkinson, R.; Carter, W. P. L.; Pitts, J. N. Hydroxyl radical rate constants and photolysis rates of .alpha.-dicarbonyls. *Environmental Science & Technology* **1983**, *17* (8), 479-484. DOI: https://doi.org/10.1021/es00114a008.

(233) Miyoshi, A.; Matsui, H.; Washida, N. Detection and reactions of the HOCO radical in gas phase. *The Journal of Chemical Physics* **1994**, *100* (5), 3532-3539. DOI: https://doi.org/10.1063/1.466395.

(234) Mellouki, A.; Ammann, M.; Cox, R. A.; Crowley, J. N.; Herrmann, H.; Jenkin, M. E.; McNeill, V. F.; Troe, J.; Wallington, T. J. Evaluated kinetic and photochemical data for atmospheric chemistry: volume VIII – gas-phase reactions of organic species with four, or more, carbon atoms (≥ C4). *Atmos. Chem. Phys.* **2021**, *21* (6), 4797-4808. DOI: https://doi.org/10.5194/acp-21-4797-2021.

(235) Kim, Y. P.; Seinfeld, J. H. Atmospheric Gas–Aerosol Equilibrium: III. Thermodynamics of Crustal Elements Ca^{2+}, K^{+}, and Mg^{2+}. *Aerosol Science and Technology* **1995**, *22* (1), 93-110. DOI: https://doi.org/10.1080/02786829408959730.

(236) Ansari, A. S.; Pandis, S. N. Prediction of multicomponent inorganic atmospheric aerosol behavior. *Atmospheric Environment* **1999**, *33* (5), 745-757. DOI: https://doi.org/10.1016/S1352-2310(98)00221-0.

(237) Metzger, S.; Dentener, F.; Pandis, S.; Lelieveld, J. Gas/aerosol partitioning: 1. A computationally efficient model. *Journal of Geophysical Research: Atmospheres* **2002**, *107* (D16), ACH 16-11-ACH 16-24. DOI: https://doi.org/10.1029/2001JD001102.

(238) Trebs, I.; Metzger, S.; Meixner, F. X.; Helas, G.; Hoffer, A.; Rudich, Y.; Falkovich, A. H.; Moura, M. A. L.; da Silva Jr., R. S.; Artaxo, P.; et al. The NH_4^{+}-NO3^{-}-Cl^{-}-SO_4^{2-}-H_2O aerosol system and its gas phase precursors at a pasture site in the Amazon Basin: How relevant are mineral cations and soluble organic acids? *Journal of Geophysical Research: Atmospheres* **2005**, *110* (D7). DOI: https://doi.org/10.1029/2004JD005478.

(239) Dasgupta, P. K.; Campbell, S. W.; Al-Horr, R. S.; Ullah, S. M. R.; Li, J.; Amalfitano, C.; Poor, N. D. Conversion of sea salt aerosol to $NaNO_3$ and the production of HCl: Analysis of temporal behavior of aerosol chloride/nitrate and gaseous HCl/HNO_3 concentrations with AIM. *Atmospheric Environment* **2007**, *41* (20), 4242-4257. DOI: https://doi.org/10.1016/j.atmosenv.2006.09.054.

(240) Clegg, S. L.; Brimblecombe, P.; Wexler, A. S. Thermodynamic Model of the System H^{+}–NH_4^{+}–SO_4^{2-}–NO_3^{-}–H_2O at Tropospheric Temperatures. *The Journal of Physical Chemistry A* **1998**, *102* (12), 2137-2154. DOI: https://doi.org/10.1021/jp973042r.

(241) Sudheer, A. K.; Rengarajan, R. Time-resolved inorganic chemical composition of fine aerosol and associated precursor gases over an urban environment in western India: Gas-aerosol equilibrium characteristics. *Atmospheric Environment* **2015**, *109*, 217-227. DOI: https://doi.org/10.1016/j.atmosenv.2015.03.028.

(242) Watson, N.; Allan, J.D.; Flynn, M. (2023): Mass Concentration of the Non-Refractory Component of Ambient Aerosol Particles in Air Data from Aerosol Chemical Species Monitor (ACSM) at Manchester Air Quality Site, 2019-present. NERC EDS Centre for Environmental Data Analysis. https://catalogue.ceda.ac.uk/uuid/8d8613a3d67a4e76adfe94c94ede6a4f (accessed 2023/05/11).

(243) Watson, N. (2023): Ammonia and Water Abundance Measurements from Los Gatos Research Ammonia Analyzer Instrument at Manchester Air Quality Site 2019 onwards. https://catalogue.ceda.ac.uk/uuid/5fc811f707f54415b129882a38889501 (accessed 2023/05/11).

(244) Watson, N. (2023): NO and NOy Abundance Data from Thermo Model 42i-Y NOY Analyzer Instrument at the Manchester Air Quality Site, 2019 onwards. NERC EDS Centre for Environmental

Data Analysis. https://catalogue.ceda.ac.uk/uuid/1d58f2f5e7874e55a83ca57311dcfb9a (accessed 2023/05/11).

(245) Watson, N. (2023): Nitrogen Dioxide Abundance Data from Teledyne Model T500U Instrument at the Manchester Air Quality Site, 2019 onwards. NERC EDS Centre for Environmental Data Analysis. https://catalogue.ceda.ac.uk/uuid/f60761f3279042859e5c2902dfa0f2ef (accessed 2023/05/11).

(246) Watson, N.; Allan, J.D.; Flynn, M. (2023): Number concentration and size distribution of ambient aerosol particles in air measurements from a Cloud Particle Condenser instrument (SMPS) at the Manchester Air Quality Site, 2019 onwards. https://catalogue.ceda.ac.uk/uuid/6f6366eb78c44875b2c92d3b8fe403c1 (accessed 2023/06/12).

(247) Watson, N.; Allan, J.D.; Flynn, M. (2023): Elemental Composition Data of Ambient PM2.5 and PM10 Aerosol Particles in Air from a Cooper XACT 625i Instrument at the Manchester Air Quality Site, 2019 onwards. NERC EDS Centre for Environmental Data Analysis. https://catalogue.ceda.ac.uk/uuid/21723af1f2a640c6990ce9cb3b70aaef (accessed 2023/06/13).

(248) Malm, W. C.; Day, D. E. Estimates of aerosol species scattering characteristics as a function of relative humidity. *Atmospheric Environment* **2001**, *35* (16), 2845-2860. DOI: https://doi.org/10.1016/S1352-2310(01)00077-2.

(249) von Glasow, R.; Sander, R. Variation of sea salt aerosol pH with relative humidity. *Geophysical Research Letters* **2001**, *28* (2), 247-250. DOI: https://doi.org/10.1029/2000GL012387.

(250) Liakakou, E.; Fourtziou, L.; Paraskevopoulou, D.; Speyer, O.; Lianou, M.; Grivas, G.; Myriokefalitakis, S.; Mihalopoulos, N. High-Resolution Measurements of SO_2, HNO_3 and HCl at the Urban Environment of Athens, Greece: Levels, Variability and Gas to Particle Partitioning. *Atmosphere* **2022**, *13* (2), 218. DOI: https://doi.org/10.3390/atmos13020218.

(251) Crilley, L. R.; Lucarelli, F.; Bloss, W. J.; Harrison, R. M.; Beddows, D. C.; Calzolai, G.; Nava, S.; Valli, G.; Bernardoni, V.; Vecchi, R. Source apportionment of fine and coarse particles at a roadside and urban background site in London during the 2012 summer ClearfLo campaign. *Environmental Pollution* **2017**, *220*, 766-778. DOI: https://doi.org/10.1016/j.envpol.2016.06.002.

(252) Visser, S.; Slowik, J. G.; Furger, M.; Zotter, P.; Bukowiecki, N.; Dressler, R.; Flechsig, U.; Appel, K.; Green, D. C.; Tremper, A. H.; et al. Kerb and urban increment of highly time-resolved trace elements in PM_{10}, $PM_{2.5}$ and $PM_{1.0}$ winter aerosol in London during ClearfLo 2012. *Atmos. Chem. Phys.* **2015**, *15* (5), 2367-2386. DOI: https://doi.org/10.5194/acp-15-2367-2015.